UAB
Universitat Autònoma de Barcelona

# Novel chronokine-based approaches to tackle multiple pathways in Alzheimer's disease: secreted Klotho and newly designed chimeric HEBE

**Jon Esandi Jauregui**

**ADVERTIMENT.** L'accés als continguts d'aquesta tesi queda condicionat a l'acceptació de les condicions d'ús establertes per la següent llicència Creative Commons: https://creativecommons.org/licenses/?lang=ca

**ADVERTENCIA.** El acceso a los contenidos de esta tesis queda condicionado a la aceptación de las condiciones de uso establecidas por la siguiente licencia Creative Commons: https://creativecommons.org/licenses/?lang=es

**WARNING.** The access to the contents of this doctoral thesis it is limited to the acceptance of the use conditions set by the following Creative Commons license: https://creativecommons.org/licenses/?lang=en

UAB
Universitat Autònoma de Barcelona

Department of Biochemistry and Molecular Biology

PhD Program in Biochemistry, Molecular Biology and Biomedicine

DOCTORAL THESIS

# Novel chronokine-based approaches to tackle multiple pathways in Alzheimer's disease: secreted Klotho and newly designed chimeric HEBE

**Jon Esandi Jauregui**

2024

Supervisor: Miguel Chillón Rodríguez




# Novel chronokine-based approaches to tackle multiple pathways in Alzheimer's disease: secreted Klotho and newly designed chimeric HEBE

Presented by

**Jon Esandi Jauregui**

To obtain the degree in

**PhD in Biochemistry, Molecular Biology and Biomedicine**

by *Universitat Autònoma de Barcelona*

**PhD Candidate,**

Jon Esandi Jauregui

**Supervisor,**

Miguel Chillón Rodríguez

The research described in this doctoral thesis was performed in the Gene Therapy for the Central Nervous System laboratory at the Department of Biochemistry and Molecular Biology, *Institut de Neurociències*, *Universitat Autònoma de Barcelona*, under the supervision of Dr Miguel Chillón.

Jon Esandi Jauregui was recipient of a *Ajuts de Suport a Departaments i Unitats de Recerca Universitaris per a la Contractació de Personal Investigador Predoctoral en Formació* Fellowship (2020 FI-SDUR 00037) from *Generalitat de Catalunya*.



Generalitat de Catalunya
**Departament de Recerca i Universitats**

# SUMMARY

Alzheimer's disease (AD) is the most common form of dementia worldwide. This neurodegenerative disorder is characterized by amyloid-β and Tau protein depositions in the brain, alongside dysregulated pathways and cellular processes. Despite numerous proposed therapeutic approaches, no definitive treatment has been approved to cure or prevent AD due to its multifaceted nature, rendering single-target strategies inefficient. Therefore, pleiotropic proteins like chronokines offer a potential alternative for effective AD therapy. Chronokines are proteins that determine systemic functions and biological aging processes, and they can be employed to develop a therapy aiming to combat the cognitive decline observed in AD.

Klotho is a pleiotropic protein that plays an important anti-aging and neuroprotective role in the brain. The secreted isoform (sKL) has demonstrated cognitive enhancement and memory improvement in aged mice. The decline in sKL expression with age or in AD pathology positions it as a promising therapeutic candidate for AD.

In the present thesis, the systemic administration of recombinant human sKL was tested in a mouse model of AD. Five-month-old APP/Tau mice received daily intraperitoneal injections of recombinant sKL over 6 weeks. Notably, sKL treatment did not impact the weight or locomotor activity of AD mice. Despite the relatively mild AD phenotype in the mice, particularly among females, a modest enhancement in recognition memory was observed in male AD mice following sKL treatment. Transcriptomic analysis suggested that this cognitive improvement might involve enhanced glutamate neurotransmission, although the precise mechanism remains unclear due to sKL's inability to cross the blood-brain barrier.

Despite sKL's pleiotropic properties, it may not be sufficient as a standalone AD treatment. Consequently, a combination of various chronokines could represent a more potent therapeutic strategy. In the present thesis, a novel chimeric chronokine, HEBE, was engineered by integrating sKL's neuroprotective effects, sTREM2's microglial function improvements, and TIMP2's neuronal differentiation and synapse density promotion. *In vitro* testing of HEBE revealed new functions derived from the assembly of the proteins, while the TIMP2 subunit in HEBE was not able to inhibit MMPs. Subsequently, HEBE was

evaluated *in vivo* via gene therapy using an AAV9P31 vector in 24-week-old APP/Tau mice, and behavioral and cognitive tests were performed at 36 weeks of age. AD mice showed a marked phenotype, and HEBE significantly improved recognition memory and spatial learning, without toxic effects. These improvements coincided with reduced pTau depositions in the hippocampus and modest transcriptional enhancements in the hippocampus and entorhinal cortex.

A second version of HEBE was also generated, called HEBE2, to overcome the lack of MMP inhibition by TIMP2 in HEBE, and to achieve more sustained expression of the protein via promoter modification. Future studies will assess HEBE2's efficacy *in vitro* and *in vivo* to ascertain its potential for improved functional outcomes compared to HEBE.

# INDEX

ABBREVIATIONS ..... 1

INTRODUCTION ..... 6

**1. Alzheimer's disease ..... 7**

1.1. Risk factors ..... 7

1.2. Pathophysiology of Alzheimer's disease ..... 8

1.2.1. Amyloid-β ..... 9

1.2.2. Tau ..... 11

1.2.3. Neuroinflammation ..... 12

1.2.4. Autophagy ..... 13

1.3. Alzheimer's disease stages ..... 14

1.3.1. Preclinical Alzheimer's disease ..... 14

1.3.2. Mild Cognitive Impairment ..... 15

1.3.3. Alzheimer's dementia ..... 15

1.4. Anatomical progression of AD ..... 16

1.5. Diagnostics for AD and biomarkers ..... 17

1.5.1. Neuroimaging ..... 18

1.5.2. Fluid biomarkers ..... 19

1.6. Treatments for AD ..... 21

1.6.1. Symptomatic treatments ..... 21

1.6.2. Disease-modifying treatments ..... 22

**2. Chronokines ..... 23**

2.1. Klotho ..... 23

2.1.1. Klotho transcripts and isoforms ..... 23

2.1.2. Klotho expression and protein distribution ..... 24

2.1.3. Klotho functions ..... 25

2.1.4. sKL as a therapeutic agent ..... 30

2.2. TREM2 ..... 31

2.2.1. TREM2 transcripts and isoforms ..... 31

2.2.2. TREM2 expression ..... 31

2.2.3. TREM2 variants in AD ..... 31

2.2.4. TREM2 functions ..... 32

2.2.5. sTREM2 as a therapeutic agent ..... 35

2.3. TIMP2 ..... 36

2.3.1. TIMP2 expression and protein distribution ..... 36

2.3.2. TIMP2 functions ..... 37

**3. Gene therapy ..... 38**

3.1. Vectors ..... 39

3.2. Viral vectors ..... 40

3.2.1. Adeno-associated viral vectors ..... 42

**4. Experimental models for AD ..... 48**

4.1. *In vivo* models ..... 48

4.1.1. APP/Tau mouse model ..... 49

**HYPOTHESIS AND OBJECTIVES ..... 51**

**1. Hypothesis ..... 52**

**2. Objectives ..... 52**

**MATERIALS AND METHODS ..... 53**

**1. Materials ..... 54**

1.1. Animals ..... 54

1.2. Plasmids and viral vectors ..... 54

1.3. Cell lines ..... 55

1.4. Bacterial strains ..... 56

1.5. Oligonucleotides ..... 56

1.5.1. Primers for mice genotyping ..... 56

1.5.2. Primers for qPCR analysis ..... 56

1.5.3. TaqMan sets for gene expression analysis ..... 56

**2. Methods ..... 57**

2.1. Transgenic mice genotyping ..... 57

2.1.1. Genomic DNA extraction ..... 57

2.1.2. Transgene detection by PCR ..... 57

2.2. Plasmid vector generation ..... 57

2.2.1. Digestions with restriction enzymes ..... 57

2.2.2. Cloning ..... 58

2.2.3. Transformation of chemically competent bacteria ..... 60

2.3. DNA obtention and analysis ..... 60

2.3.1. DNA minipreps ..... 60

2.3.2. DNA maxipreps ..... 61

2.3.3. Tissue DNA extraction ..... 61

2.3.4. Electrophoresis in agarose gel ..... 61

2.3.5. DNA purification from agarose gel ..... 62

2.3.6. DNA quantification ..... 62

2.3.7. DNA sequencing ..... 62

2.4. RNA obtention and analysis ..... 62

2.4.1. Tissue RNA isolation ..... 62

2.4.2. RNA quantification ..... 63

2.4.3. DNase treatment and reverse transcription ..... 63

2.4.4. Real-Time quantitative PCR (qPCR) ..... 63

2.4.5. qPCR data analysis ..... 65

2.4.6. RNA-seq ..... 65

2.5. Protein obtention and analysis ..... 65

2.5.1. Protein extraction ..... 65

2.5.2. Protein quantification ..... 65

2.5.3. Denaturing electrophoresis (SDS-PAGE) ..... 66

2.5.4. Transference ..... 67

2.5.5. Immunodetection ..... 67

2.5.6. sKL quantification through ELISA ..... 68

2.5.7. sKL half-life determination ..... 68

2.6. Cell culture techniques ..... 68

2.6.1. HEK293 cell line ..... 69

2.6.2. CHO cell line ..... 69

2.6.3. BV2 cell line ..... 70

2.7. Viral vectors ..... 70

2.7.1. AAV vector production and purification ..... 70

2.7.2. Adenoviral vector production and purification ..... 73

2.8. Recombinant protein production and purification ..... 76
2.8.1. Recombinant protein production through cell line infection ..... 76
2.8.2. Recombinant protein purification ..... 76
2.9. Recombinant protein activity studies ..... 76
2.9.1. β-glucuronidase activity study ..... 76
2.9.2. MMP1 inhibition study ..... 77
2.9.3. Phagocytic activity study ..... 77
2.10. *In vivo* studies ..... 78
2.10.1. Viral vector injections ..... 78
2.10.2. Recombinant protein injections ..... 78
2.10.3. Blood-brain barrier penetration study ..... 79
2.10.4. Behavioral and memory tests ..... 80
2.10.5. Euthanasia and sample collection ..... 83
2.10.6. Blood sample analysis ..... 85
2.11. Statistical analyses ..... 85
2.12. Bioinformatic studies ..... 86
2.12.1. All-atom models. ..... 86
2.12.2. All-atom MD simulations. ..... 86
2.12.3. Analysis of all-atom MD simulations. ..... 87
2.12.4. Construction of models of the united proteins. ..... 87
2.12.5. Coarse-grained MD simulations. ..... 88
2.12.6. AlphaFold analysis ..... 88

**RESULTS ..... 89**

**Chapter 1: Recombinant human sKL as a therapeutic strategy for AD ..... 90**

1.1. Production and purification of recombinant sKL ..... 90
1.2. *In vitro* testing of biological activity ..... 91
1.3. Blood-brain barrier penetration ..... 92
1.4. Setup for sKL detection ..... 93
1.5. Recombinant human sKL's half-life determination ..... 93
1.5.1. Protein half-life with intravenous administration ..... 94
1.5.2. Protein half-life with intraperitoneal administration ..... 95
1.6. *In vivo* study ..... 96

1.6.1. Administration interval and dose determination ..... 96
1.6.2. Experimental design ..... 98
1.6.3. Weight evolution ..... 99
1.6.4. Behavioral and cognitive tests ..... 100
1.6.5. Gene expression analysis ..... 107
1.6.6. Histopathology ..... 115

**Chapter 2: Design, generation, and proof of concept of HEBE ..... 118**

2.1. Bioinformatic analysis ..... 118
2.1.1. Analyses of individual chronokines ..... 118
2.1.2. Analyses of HEBE candidates ..... 123

2.2. *In vitro* functional characterization of HEBE ..... 125
2.2.1. Cloning and production of HEBE ..... 125
2.2.2. Production of recombinant proteins ..... 125
2.2.3. Testing of biological activity ..... 126

2.3. *In vivo* therapeutic approach with HEBE ..... 132
2.3.1. AAV9P31 setup ..... 132
2.3.2. Experimental design ..... 132
2.3.3. Viral vector verification ..... 134
2.3.4. HEBE toxicity ..... 136
2.3.5. Body weights ..... 138
2.3.6. Behavioral and cognitive tests ..... 139
2.3.7. RNA-seq analysis ..... 148
2.3.8. Histopathology ..... 155

2.4. HEBE2 generation ..... 159
2.4.1. Bioinformatic analysis ..... 159
2.4.2. Cloning and production of recombinant HEBE2 ..... 160

**DISCUSSION ..... 161**

**1. Recombinant sKL as a therapy for Alzheimer's disease ..... 162**

1.1. Recombinant sKL production and characterization ..... 163

1.2. *In vivo* assessment of sKL's effects ..... 165

1.3. sKL-induced changes at a molecular level ..... 167

1.4. Final remarks ..... 168

**2. HEBE as a therapy for Alzheimer's disease..... 170**

2.1. HEBE design..... 171

2.2. *In vitro* functional characterization..... 172

2.3. *In vivo* assessment of HEBE's activities..... 173

2.4. HEBE-induced changes at a molecular level..... 176

2.5. HEBE2 generation..... 179

2.6. HEBE versus sKL..... 180

2.7. Final remarks..... 180

**CONCLUSIONS..... 182**

**REFERENCES..... 184**

**PATENT..... 211**

# ABBREVIATIONS

| | |
|---|---|
| **AAP** | Assembly-activating protein |
| **AAV** | Adeno-associated virus |
| **Aβ** | Amyloid-β |
| **Ab** | Antibody |
| **ACh** | Acetylcholine |
| **AChEI** | Acetylcholinesterase inhibitors |
| **AD** | Alzheimer's disease |
| **Ad** | Adenovirus |
| **APOE** | Apolipoprotein E |
| **APP** | Amyloid precursor protein |
| **AUC** | Area under the curve |
| **BBB** | Blood-brain barrier |
| **BCA** | Bicinchoninic acid |
| **bp** | Base pairs |
| **BSA** | Bovine serum albumin |
| **CA3** | Cornu Ammonis 3 |
| **CAR** | Coxsackievirus and adenovirus receptor |
| **cDNA** | Complementary DNA |
| **CG** | Coarse-grained |
| **CHO** | Chinese hamster ovary |
| **CMV** | Cytomegalovirus |
| **CNS** | Central nervous system |
| **Cq** | Quantification cycle |
| **CsCl** | Caesium chloride |
| **CSF** | Cerebrospinal fluid |
| **Ctrl** | Control |
| **CycB** | Cyclin B |
| **DAM** | Disease-associated microglia |
| **DG** | Dentate gyrus |
| **DMEM** | Dulbecco's Modified Eagle's Medium |
| **DMEM/F-12** | Dulbecco's Modified Eagle's Medium/Ham's F-12 |
| **DNA** | Deoxyribonucleic acid |

| | |
|---|---|
| **dNTP** | Deoxynucleotide triphosphate |
| **dsDNA** | Double-stranded DNA |
| **EGFP** | Enhanced green fluorescent protein |
| **ELISA** | Enzyme-linked immunosorbent assay |
| **EtOH** | Ethanol |
| **FBS** | Fetal bovine serum |
| **FDA** | Food and drug administration |
| **FGF23** | Fibroblast growth factor |
| **g** | Relative centrifugal force |
| **GAPDH** | Glyceraldehyde 3-phosphate dehydrogenase |
| **GFAP** | Glial fibrillary acidic protein |
| **GFP** | Green fluorescent protein |
| **GO** | Gene ontology |
| **GOI** | Gene of interest |
| **h** | Hours |
| **HC** | Hippocampus |
| **HEK** | Human embryonic kidney |
| **His** | Histidine |
| **Ig** | Immunoglobulin |
| **IGF-1** | Insulin-like growth factor 1 |
| **i.p.** | Intraperitoneal |
| **iPSC** | Induced pluripotent stem cells |
| **IU** | Infective units |
| **i.v.** | Intravenous |
| **ITR** | Inverted terminal repeat |
| **Kb** | Kilobase |
| **kDa** | Kilodalton |
| **KL** | Klotho |
| **LB** | Luria broth |
| **LPS** | Lipopolysacharide |
| **LTP** | Long-term potentiation |
| **MAPK** | Mitogen-activated protein kinase |

| | |
|---|---|
| **MCI** | Mild cognitive impairment |
| **MD** | Molecular dynamics |
| **MFI** | Mean fluorescence intensity |
| **min** | Minutes |
| **mKL** | Transmembrane Klotho |
| **mL** | Mililiter |
| **MMP** | Matrix metalloproteinase |
| **MnSOD** | Manganese superoxide dismutase |
| **MOI** | Multiplicity of infection |
| **MRI** | Magnetic resonance imaging |
| **mRNA** | Messenger RNA |
| **NAbs** | Neutralizing antibodies |
| **NFT** | Neurofibrillary tangles |
| **NMDA** | N-methyl-D-aspartate |
| **NMDAR** | NMDA receptor |
| **NORT** | Novel object recognition test |
| **OF** | Open field |
| **O/N** | Overnight |
| **ORF** | Open reading frame |
| **PCA** | Principal component analysis |
| **P/S** | Penicillin-Streptomycin |
| **PBS** | Phosphate-buffered saline |
| **PCR** | Polymerase chain reaction |
| **PEI** | Polyethyleneimine |
| **PEG** | Polyetilenglycol |
| **PET** | Positron emission tomography |
| **pKL** | Processed Klotho |
| **PolyA** | Polyadenylation signal |
| **PSEN** | Presenilin |
| **P/T Ratio** | Peak-Trough ratio |
| **pTau** | Phosphorylated Tau |
| **qPCR** | Real-time quantitative polymerase chain reaction |

| | |
|---|---|
| **R** | Accumulation index |
| **rAAV** | Recombinant adeno-associated virus |
| **RMSD** | Root-mean-square deviation |
| **RMSF** | Root-mean-square fluctuations |
| **RNA** | Ribonucleic acid |
| **rpm** | Revolutions per minute |
| **ROS** | Reactive oxygen species |
| **RT** | Room temperature |
| **s** | Seconds |
| **SEM** | Standard error of the mean |
| **sKL** | Secreted Klotho |
| **SN** | Supernatant |
| **ssDNA** | Single-stranded DNA |
| **sTREM2** | Soluble triggering receptor expressed on myeloid cells 2 |
| **SUV** | Standardized uptake value |
| **Tau** | Tubulin associated unit |
| **TEMED** | Tetramethylethylenediamine |
| **TFGβ** | Transforming growth factor β |
| **TIMP2** | Tissue inhibitor of metalloproteinases 2 |
| **TNFα** | Tumor necrosis factor α |
| **TREM2** | Triggering receptor expressed on myeloid cells 2 |
| **U** | Units |
| **UV** | Ultraviolet |
| **Vg** | Viral genomes |
| **Vs** | Versus |
| **WT** | Wild type |
| **wtAAV** | Wild-type AAV |

# INTRODUCTION

# 1. Alzheimer's disease

Alzheimer's disease (AD) is the most common form of dementia worldwide, accounting for 60-80% of all cases [1]. This neurodegenerative disease is characterized by the depositions of amyloid-β (Aβ) and Tau proteins in the brain [2], ultimately leading to synaptic loss, neuronal death, and cognitive decline in patients suffering from the disease [3]. Estimations suggest that dementia cases worldwide will increase from 57.4 million in 2019 to 152.8 million by 2050 [4], impacting patients and caregivers and underscoring the urgent need for effective therapeutic interventions, which have so far remained elusive.

## 1.1. Risk factors

Age represents a primary risk factor for AD. Most individuals affected by the disease are aged 65 and above (late-onset AD), with the risk of onset doubling every five years beyond this age [5]. Only around 5.5% of all AD cases develop at young ages, before 65 (early-onset AD) [6]. Nonetheless, other risk factors, including genetic mutations, gender, lifestyle, pre-existing medical conditions, and environmental factors, also contribute to AD development [7].

AD presents high heritability, suggesting a significant role for genetics in the development of the pathology [8]. Patients with early-onset AD, also referred to as familial AD, may carry rare autosomal dominant mutations in the *APP* and *PSEN1/2* genes [9]. Mutations in the Amyloid Precursor Protein (*APP)* gene generally lead to an increase in the production of the toxic $A\beta_{42}$ peptide, which tends to form fibrils and aggregate into pathological amyloid plaques [10,11]. Mutations in the Presenilin 1 and 2 (*PSEN1/2*) genes, on the other hand, typically lead to an increased $A\beta_{42}/A\beta_{40}$ ratio by decreasing $A\beta_{40}$ levels [12,13] and an early onset of the symptoms. However, the aforementioned mutations represent less than 1% of all AD cases.

In late-onset AD, also referred to as sporadic AD, various genetic mutations are found, which confer an increased risk of developing the disease. Among them, one of the most prevalent is the *APOE* ε4 allele of the ApoE protein involved in lipid metabolism, which can increase the chances of developing AD by up to 3-fold in heterozygotes, and 15-fold

in homozygotes [14]. In contrast, the *APOE* ε2 allele reduces the risk of AD by almost half and promotes longevity [15].

Although the *APOE* ε4 allele has commonly been associated with a higher risk for developing AD, more recent studies have revealed additional genes whose mutations can exert similar effects. One of them is *TREM2*, which encodes a receptor expressed on microglial cells in the brain and possesses anti-inflammatory properties. Rare variants of this gene can increase the risk of developing late-onset AD by 2 to 4-fold [16,17].

Gender represents another risk factor for Alzheimer's disease, with women being more likely to develop the disease compared to men. In the United States, two-thirds of AD patients are women [1]. The reasons for this disparity are still not fully understood, but several factors could be influencing the impact of AD on gender. The longer life-expectancy for women could be an important factor increasing the likelihood to develop AD [18]. However, this factor alone is not enough to explain the differences observed between men and women. The menopause transition in women is said to be a major contributor to the development of AD, disrupting the estrogen-regulated systems and leading to neurological dysfunction [19].

## 1.2. Pathophysiology of Alzheimer's disease

Alzheimer's disease was first described by Alois Alzheimer in 1906 in a patient exhibiting cognitive disturbance, disorientation, delusions, and other behavioral changes. Neuropathologic evaluation revealed diffuse brain atrophy, but it was not until the 1980s that amyloid-β plaques and hyperphosphorylated Tau were identified. Despite the disease being identified over a century ago, the pathogenesis of AD remains incompletely understood.

It is commonly accepted that an interplay of misfolded proteins in the brain is the driver of this disease. Intracellular Aβ plaques and extracellular hyperphosphorylated Tau neurofibrillary tangles lead to the loss of connections between nerve cells, causing their death and subsequent loss of brain tissue [2]. These alterations, along with

neuroinflammation, ultimately lead to a progressive cognitive decline in affected individuals.

### 1.2.1. Amyloid-β

Aβ plaques are comprised of Aβ peptides derived from the sequential cleavage of the transmembrane amyloid precursor protein (APP) by β and γ-secretases [20]. The APP protein can undergo processing through two different pathways: the non-amyloidogenic pathway and the amyloidogenic pathway (Fig. 1).

In the non-amyloidogenic pathway, APP is cleaved by the α-secretase in the middle, releasing a soluble N-terminal fragment (sAPPα) and a C-terminal fragment that is further cleaved by γ-secretase, releasing a C-terminal fragment (p3). The cleavage of APP by α-secretase occurs within the region containing the Aβ peptide, preventing its release [21].

In the amyloidogenic pathway, the BACE1 β-secretase may cleave the APP protein, releasing a soluble N-terminal fragment (sAPPβ) and leaving a transmembrane fragment (β-CTF) [22]. Two mutations at the β-secretase cleavage site of APP are linked to a stronger affinity of BACE1 to APP, releasing higher levels of sAPPβ [23,24]. The β-CTF fragment is further cleaved by γ-secretase, releasing Aβ into the extracellular space. γ-secretase is a membrane protein complex, with presenilin 1 (PSEN1) and presenilin 2 (PSEN2) serving as its catalytic elements. Mutations in the genes encoding these proteins are considered to be risk factors for AD, as discussed previously.

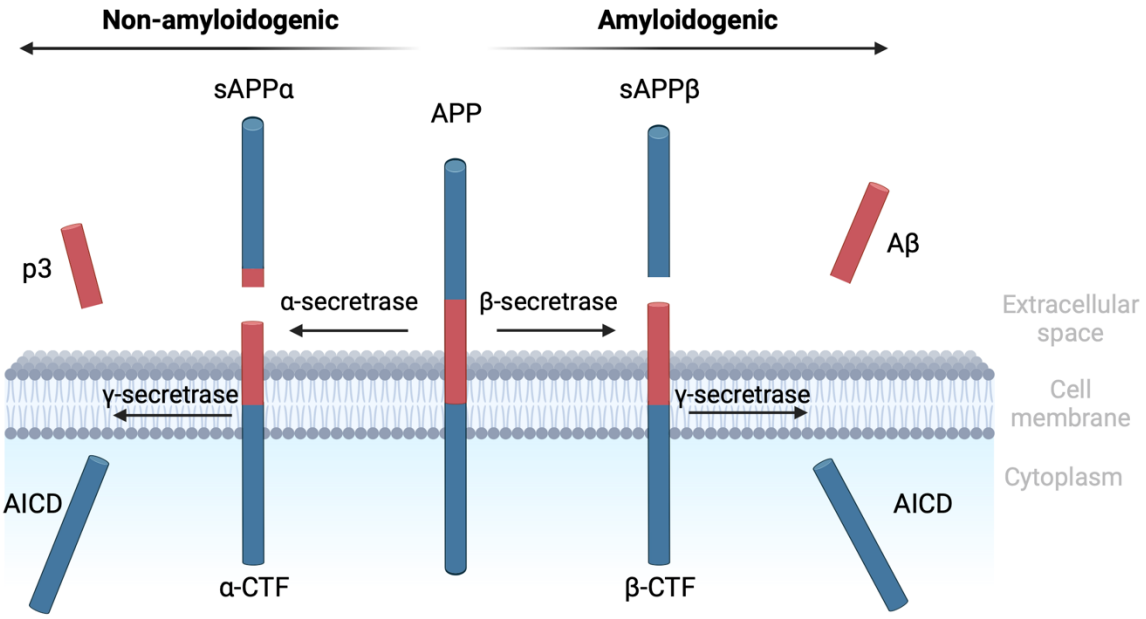



Figure 1. Proteolytic cleavage of APP in the non-amyloidogenic and amyloidogenic pathways. Adapted from [20].

Several Aβ peptide species exist, the ones with 40 and 42 amino acids ($A\beta_{40}$ and $A\beta_{42}$ respectively) being the most relevant in AD. $A\beta_{42}$ is more prone to aggregation and fibrilization compared to $A\beta_{40}$ due to its reduced solubility, with $A\beta_{42}$ being the most toxic species, while neuroprotective effects have been attributed to $A\beta_{40}$ [25]. Aβ species are initially produced as monomers, which progressively aggregate into oligomers, protofibrils, and eventually fibrils, culminating in the formation of amyloid plaques [26]. The aggregation of Aβ is the result of interconnected processes, where a primary nucleation step leads to the formation of oligomers that can then elongate into insoluble fibrils [27]. Among the different aggregation states of Aβ, the oligomers are considered the most toxic [28], as they interact with neurons and glial cells, activating inflammatory responses and oxidative stress [29], while also promoting Tau hyperphosphorylation. Consequently, these alterations lead to further dysfunction in APP metabolism, creating a positive feedback loop in which more Aβ depositions occur.

The amyloid cascade hypothesis was proposed in 1991 [30]. According to it, Aβ is the main driver of the pathology, as AD starts in the brain with Aβ peptide aggregation, followed by Tau phosphorylation and neuronal death. For years, the search for a treatment has been based on this hypothesis. However, more recently, it has been observed that the

progression of AD does not correlate with amyloid formation, and treatments aimed at reducing brain Aβ levels have not been fully successful [31]. These observations suggest that Aβ may not be the only cause of the disease, calling for further research into its etiology.

### 1.2.2. Tau

Tau is a microtubule-associated protein that is highly expressed in the nervous system. This protein has a microtubule binding domain, involved in the stabilization of the microtubule assembly to maintain the integrity of the cytoskeleton in neurons [32].

Tau's interaction with microtubules is regulated by phosphorylation at specific serine/threonine residues by various kinases, including CDK5 [33]. The balance between phosphorylation and dephosphorylation of these epitopes promotes conformational changes that regulate interactions between Tau proteins and tubulin, as well as microtubule stabilization [32]. In the context of AD, Aβ activates calpain and dysregulates p35, an activator of CDK5 [34]. This dysregulation leads to hyperactivation of CDK5 and subsequent hyperphosphorylation of Tau (pTau). Hyperphosphorylated Tau loses its affinity for microtubules, forming oligomers, filaments, and ultimately neurofibrillary tangles (NFTs) (Fig. 2). These are insoluble aggregates in the cytosol that impair cell structure maintenance, leading to disrupted communication between neurons and signal processing, culminating in neuronal death [35]. Furthermore, mutations in the *Tau* gene can also contribute to Tau hyperphosphorylation [36].

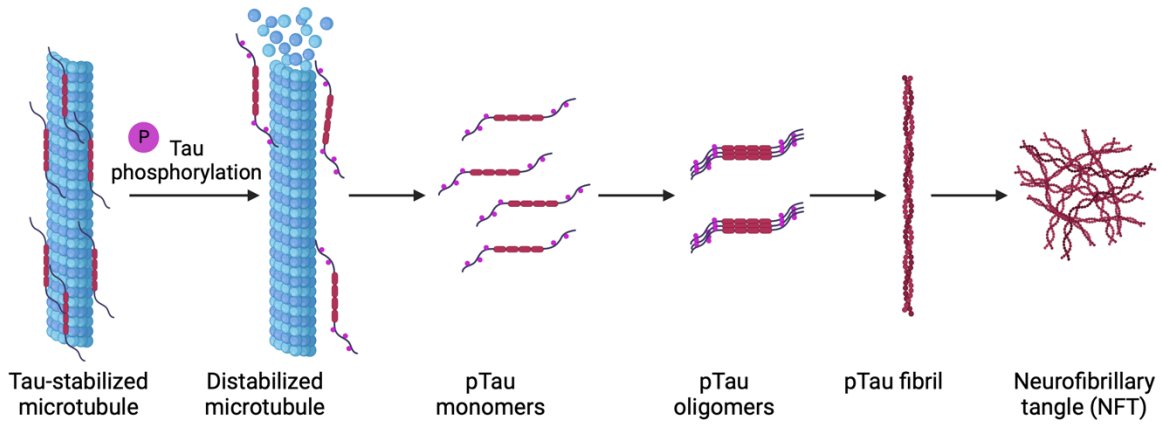



Figure 2. Tau protein hyperphosphorylation and aggregation process. Adapted from [21].

### 1.2.3. Neuroinflammation

Neuroinflammation is defined as the activation of glial cells such as microglia and astrocytes, which increase the production of pro-inflammatory cytokines that can lead to synaptic dysfunction, neuronal death, and inhibition of neurogenesis [37]. This process plays an important role in the pathogenesis of AD, as it can exacerbate both Aβ and Tau pathologies.

#### 1.2.3.1. Microglia

Microglia are innate immune cells found throughout the central nervous system (CNS), distributed across the entire brain [38]. These cells play a role in immune surveillance by clearing pathogens and cellular debris through phagocytosis [39]. Additionally, they provide factors for tissue maintenance, remodeling synapses and maintaining neuronal plasticity [40].

Upon detecting damage such as neuronal death or protein aggregates, microglia undergo activation, leading to the production of either pro-inflammatory (M1 phenotype) or anti-inflammatory cytokines (M2 phenotype), and they migrate to the lesion site. Anti-inflammatory factors aid in tissue healing and repair, while pro-inflammatory factors assist in clearing cellular debris and aggregated misfolded proteins. A balance between these two types of factors is necessary for preserving a healthy CNS [41].

However, in AD, overactivation of microglia triggered by neuron death and Aβ and Tau protein aggregates results in excessive production of pro-inflammatory cytokines by M1 microglia, exacerbating the neuroinflammation and accelerating disease progression. Aβ is believed to activate microglial cells, which in turn secrete pro-inflammatory cytokines and recruit additional microglial cells to Aβ sites. As a response to receptor binding, microglia start engulfing soluble Aβ forms and fibrils, directing them to the lysosomal/endosomal pathway for degradation [42]. Initially, microglial activation may effectively eliminate Aβ and serve to prevent disease progression, but chronic activation resulting in sustained elevation of pro-inflammatory cytokine levels impairs microglial phagocytic activity, ultimately leading to neurodegeneration [43].

#### 1.2.3.2. Astrocytes

Astrocytes, the most abundant cell type in the CNS, play crucial roles in regulating neuronal maturation and maintaining their function by preserving synaptic transmission, preventing excitotoxicity, and providing neuroprotection [44].

Under pathological conditions, these cells become activated in a process known as astrogliosis, accumulating around Aβ plaques and aiding in Aβ clearance during early disease stages [45]. Astrocyte activation may occur even before Aβ depositions begin appearing in patients. While beneficial initially for protein aggregate clearance, chronic astrocyte activation can lead to excessive release of GABA and glutamate, resulting in synaptic loss during advanced disease stages [46]. Additionally, these cells can contribute to the disruption of the blood-brain barrier (BBB), increasing Aβ accumulation and releasing pro-inflammatory cytokines that exacerbate neuroinflammation [47].

In conclusion, neuroinflammation in AD is not merely a consequence of Aβ and Tau depositions but also plays a pivotal role in contributing to disease development and progression. While acute inflammation may aid in protein aggregate clearance at initial stages, excessive neuroinflammation proves detrimental, aggravating the neurodegeneration observed in AD.

### 1.2.4. Autophagy

Autophagy is a cellular process in which defective proteins and organelles are degraded in lysosomes of eukaryotic cells [48]. The nervous system relies on autophagy to clear insoluble protein aggregates to maintain protein homeostasis [49], and evidence indicates that impairment of this process contributes to the pathogenesis of AD.

Autophagy in the early stages of the disease is protective, aiding in the clearance of Aβ and Tau aggregates in the brain. This process is involved in Aβ metabolism, enhancing APP degradation and hindering Aβ secretion [50]. However, as the disease progresses, autophagic flux becomes compromised, leading to increased accumulation of insoluble protein aggregates and exacerbating disease progression [51]. Recent studies suggest that

autophagy dysfunction may be a causative factor for developing the pathology [52], highlighting it as a potential therapeutic target.

## 1.3. Alzheimer's disease stages

AD is a progressive disease involving a complex interplay of various mechanisms, as discussed earlier. This complexity makes it challenging to categorize the different stages of the disease due to diverse progression patterns among individuals. Several classifications have been proposed, with one of the most commonly used being the NIA-AA, based on the interactions among different pathologic processes and cognitive symptoms [53]. This classification includes a biologically based definition of the disease, including the preclinical phase to facilitate the discovery of interventions aimed at preventing the initial onset of the pathology.

This NIA-AA classification defines stages based on the severity grading using biomarkers and cognitive impairment levels. Three main stages are identified: preclinical AD, mild cognitive impairment (MCI) and Alzheimer's dementia, with the latter further divided into mild, moderate, and severe (Fig. 3). It is worth noting that the duration of each phase may vary among patients [54].

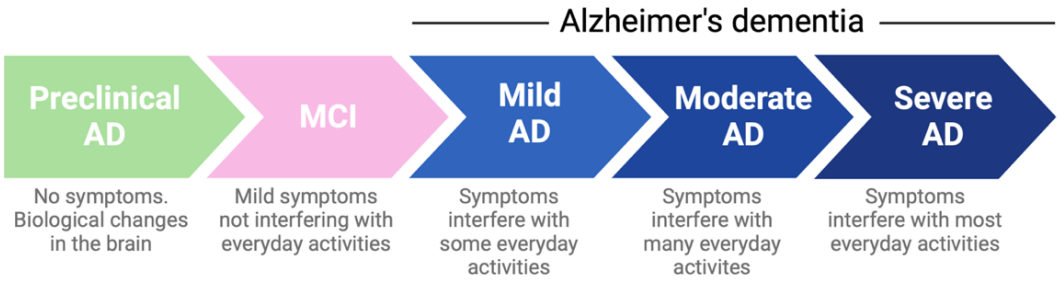



Figure 3. Alzheimer's disease stages. Adapted from [1].

### 1.3.1. Preclinical Alzheimer's disease

In this phase, patients may present biomarker levels indicative of early brain changes associated with AD [55]. However, during these early stages, the brain is capable of compensating for these changes, resulting in no noticeable cognitive impairment. It is also important to note that not all patients presenting early signs of AD will eventually develop the disease [56].

### 1.3.2. Mild Cognitive Impairment

Individuals with MCI exhibit biomarkers indicating changes in the brain and mild cognitive symptoms such as alterations in thinking, memory, and language. However, these changes may not affect their ability to carry a normal daily life. This phase begins when the organism is no longer able to fully compensate for the changes that are occurring in the brain. Although all patients with AD experience MCI, only around 15% of individuals with MCI progress to dementia [57].

### 1.3.3. Alzheimer's dementia

Patients in this phase are characterized by significant impairments in memory, language, and behavioral symptoms that interfere with their ability to lead a normal life. Symptoms worsen progressively, reflecting the extent of brain damage, with varying rates of progression among patients [1].

#### 1.3.3.1. Mild Alzheimer's dementia

In this stage, most patients can perform many tasks independently, although some degree of assistance may be required in certain areas. Individuals with mild dementia may take longer to complete some everyday tasks.

#### 1.3.3.2. Moderate Alzheimer's dementia

This stage is typically the longest, characterized by increasing difficulties with memory and language. Multistep tasks may become more difficult, and personality and behavioral changes are common. Difficulty recognizing other people is also a trait of moderate dementia.

#### 1.3.3.3. Severe Alzheimer's dementia

In this stage of the disease, patients often struggle to communicate verbally and require constant care. Brain damage affects areas involved in locomotor activity, often resulting in patients being confined to bed. Physical complications arise from the immobility of the patients, including blood clots, skin infections and sepsis. Organ failure derived from these conditions or aspiration pneumonia can lead to death in patients with severe dementia.

## 1.4. Anatomical progression of AD

Despite extensive investigations into the processes underlying the appearance and progression of Aβ plaques and NFTs in the brain, there is still controversy regarding the etiology of AD, underscoring the need for further research.

Regarding Aβ, spatiotemporal evolution has been observed using neuroimaging techniques. Aβ accumulation starts before symptom onset and can first be observed in areas with neuronal populations that have a high metabolic rate, such as association cortices. Subsequently, these accumulations spread from the neocortex to the allocortex (entorhinal cortex, hippocampus, and subiculum) and the brainstem, eventually reaching the cerebellum (Fig. 4) [58].

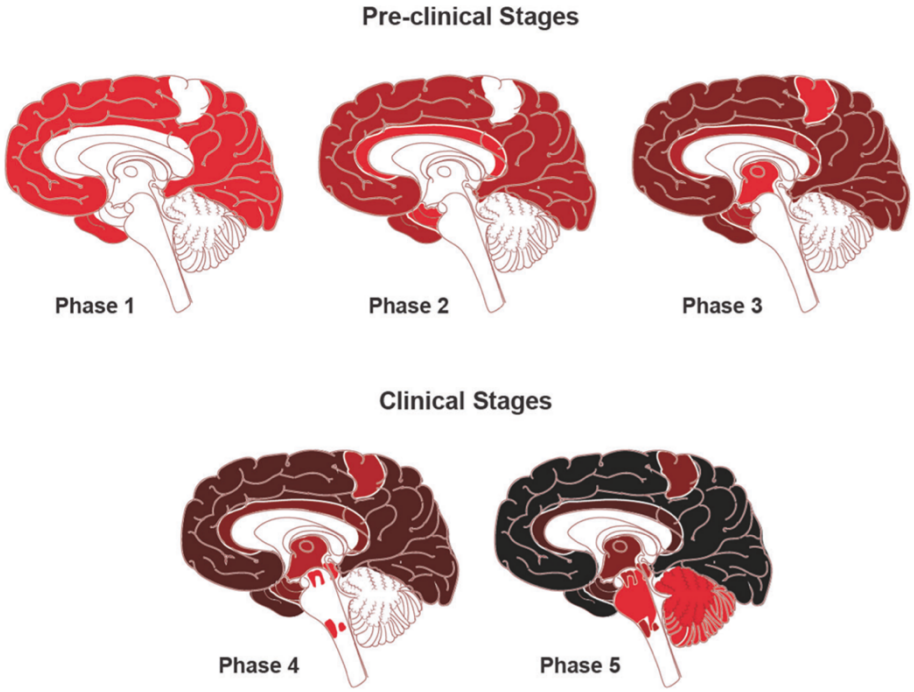



Figure 4. Spatiotemporal spread of Aβ in the human brain [22]. The red color in phase 1 represents initial accumulation of Aβ. As more Aβ depositions appear in an area, the color gets more intense.

NFTs start appearing after Aβ plaques, and their spread presents six stages that can be summarized in three (Fig. 5) [59]. The first NFTs appear in the allocortex of the medial temporal lobe (entorhinal cortex and hippocampus), followed by their spread to the associative isocortex. Ultimately, the isocortical areas are affected by NFTs. Notably,

unlike Aβ, the levels and distribution of NFTs are associated with cognitive status and disease progression in patients [60].

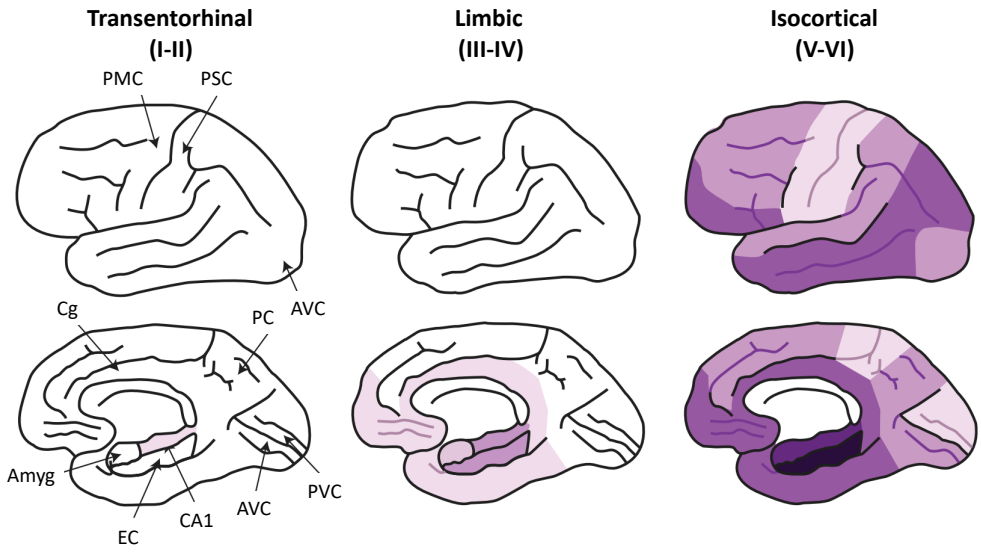



Figure 5. Spatiotemporal spread of NFTs. Purple shades indicate the distribution of NFTs, darker colors representing an increase in accumulation. PMC: Primary motor cortex. PSC: Primary sensory cortex. AVC: Associative visual cortex. PC: Precuneus. Cg: Cingulate cortex. Amyg: Amygdala. EC: Entorhinal cortex. CA1: Cornus ammonis 1. PVC: Primary visual cortex. Adapted from [61].

## 1.5. Diagnostics for AD and biomarkers

Until recently, the diagnosis for AD relied on neuropsychological testing [62]. However, studies have revealed that pathological changes begin up to two decades before symptom onset [63]. Consequently, diagnosing the disease at symptom onset is inadequate for effective treatment, as pathological changes are already progressing rapidly. The only conclusive way to confirm AD is by analyzing patients' brains *postmortem* [64]. This highlights the urgent need for diagnostic techniques capable of identifying AD at earlier stages to facilitate more effective therapeutic interventions.

Biomarkers are defined as measurable indicators in a patient that can aid in assessing the progression of AD. Given that pathological changes precede symptoms, biomarkers hold promise for early detection of preclinical AD and for determining the phase of the disease continuum, as they are dynamic and change depending on the stage (Fig. 6). These biomarkers are usually measured using neuroimaging techniques or by analyzing biological fluids.

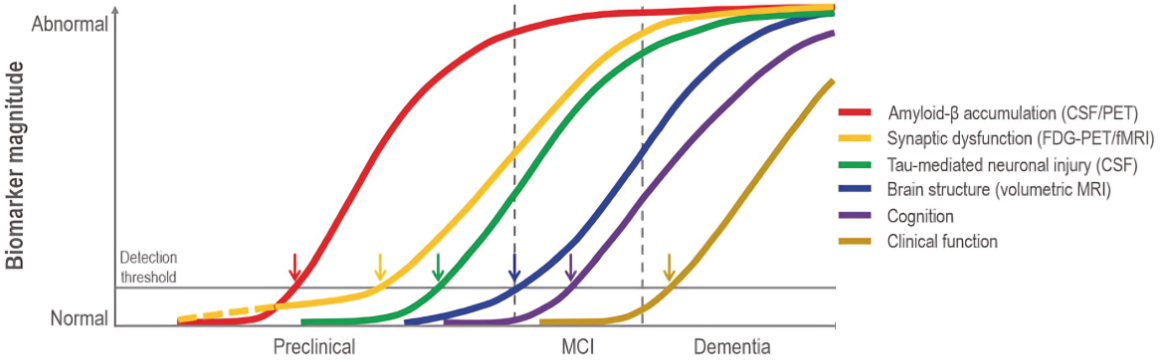



Figure 6. Evolution of biomarkers along the AD continuum, and correlation with cognitive impairment [22].

### 1.5.1. Neuroimaging

Neuroimaging is useful for the determination of anatomical and functional changes in the brain, employing various techniques.

#### 1.5.1.1. Positron emission tomography (PET)

PET measures changes in metabolism using various radioactive tracers. These tracers are analogous to different biological molecules like glucose, peptides, and proteins. Upon injection into a subject, they participate in metabolic processes that release gamma rays, which are then detected and used to determine the metabolic activity of the brain [65].

There is evidence suggesting that AD patients can present metabolic changes in the brain before protein deposition and symptom onset [66], indicating that these changes could be used to diagnose AD at preclinical stages. $^{18}$F-fluorodeoxyglucose (FDG) is used as a tracer to detect brain hypometabolism [67], as AD patients display a more significant decline in glucose metabolism compared to healthy individuals [68]. This decrease in glucose metabolism precedes the clinical diagnosis of the disease in patients, making it a reliable predictor.

The $^{11}$C-PiB tracer, on the other hand, binds efficiently to Aβ plaques, allowing discrimination between patients with very mild AD and healthy controls [69]. Another tracer suitable for detecting Tau via PET is $^{18}$F-flortaucipir [70], as it can detect and quantify early Tau pathological changes that occur in the brain. Studies have demonstrated that Tau-PET might be more sensitive than Aβ-PET to discriminate between

AD and other neurodegenerative diseases, with a sensitivity and specificity of over 90% in predicting cognitive decline when the Tau-PET signal is elevated [71].

#### 1.5.1.2. Magnetic resonance imaging (MRI)

Structural MRI is a technique used to visualize the anatomy of the brain [72]. AD is characterized by structural changes caused by neurodegeneration, including volumetry and cortical thickness [73]. Grey matter atrophy begins in the preclinical stage of AD, affecting areas like the entorhinal cortex and hippocampus [74]. These areas have been the main target in MRI analysis due to the volumetric reduction observed. Additionally, this technique can measure cortical thickness and ventricular enlargement in correlation with Aβ plaques and NFTs, which are helpful for predicting and classifying AD [75,76].

### 1.5.2. Fluid biomarkers

Biomarkers can also be measured in biological fluids such as blood and cerebrospinal fluid (CSF), aiding in the diagnosis and prediction of disease progression.

#### 1.5.2.1. Cerebrospinal fluid

CSF offers the advantage of its proximity to the brain parenchyma, receiving proteins secreted by the brain and reflecting its biochemical changes. Three main biomarkers typically measured in the CSF are Aβ, total Tau and pTau [77].

In AD, $A\beta_{42}$ levels in the CSF decrease significantly with disease progression, reflecting an increase in Aβ deposition, which hinders the peptide's release into the CSF [78]. However, measuring the $A\beta_{42}/A\beta_{40}$ ratio is considered more reliable than assessing $A\beta_{42}$ levels alone due to individual fluctuation compensations [79]. Given interindividual variability in Aβ production, most studies investigate Aβ levels alongside Tau and pTau levels to increase accuracy [80].

Due to the hyperphosphorylation of Tau in AD, higher levels of total Tau and pTau are secreted to the CSF. In AD patients, an increase of around 200-300% in total Tau has been observed, alongside a moderate increase in pTau levels [81], indicative of NFT formation.

However, the most effective strategy for a biomarker-based diagnostic tool is to combine both Aβ and Tau, as Tau levels do not begin to increase until later disease stages [82].

#### 1.5.2.2. Blood

CSF collection has drawbacks due to the invasive nature of the lumbar puncture required for obtaining samples. In contrast, blood collection is less invasive and more cost-effective, making it a promising source for biomarker analysis [83]. However, detecting biomarkers in blood presents challenges because these molecules must traverse the blood-brain barrier to reach the bloodstream [84]. Additionally, given the volume ratio between the CSF and blood, significant biomarker dilution occurs. Nevertheless, significant dysfunction of the BBB has been described in AD, leading to increased protein exchange [83]. As a result of the aforementioned challenges, blood biomarker analysis has not been widely implemented in AD diagnosis yet, as further validation studies in clinical trials need to be conducted.

A correlation between CSF and blood Aβ levels has been observed in recent studies, showing a decrease in blood $A\beta_{42}$ levels correlating with disease progression [85]. Additionally, elevated levels of total Tau and pTau have been observed in the blood of AD patients [86], although more accurate results have been obtained by analyzing enzymes involved in Tau hyperphosphorylation, such as GSK-3β. Levels of this enzyme are significantly increased in patients with AD and MCI, making it an appropriate biomarker for disease diagnosis [87].

In conclusion, while PET neuroimaging and CSF biomarker analyses are the most used techniques for AD diagnosis, they are invasive, time-consuming, and expensive. Consequently, there is a need to develop accurate biomarker analyses capable of detecting the disease in its early stages, in a cost-effective, non-invasive, and accessible manner. Machine learning and artificial intelligence technologies are being used to address this challenge, aiming to identify new biomarkers for enhanced diagnostic accuracy [88].

## 1.6. Treatments for AD

When discussing treatments for Alzheimer's disease, two groups of treatments can be differentiated: symptomatic treatments and disease-modifying treatments [89]. Symptomatic treatments aim to alleviate the symptoms experienced by patients without addressing the underlying causes of the pathology. In contrast, disease-modifying treatments seek to modify the causes of the disease, preventing or decelerating the progression of the disease. However, it is noteworthy that no effective cure for AD has been developed yet.

### 1.6.1. Symptomatic treatments

As the disease progresses, patients experience loss of cholinergic neurons in the basal forebrain, leading to a decrease in acetylcholine (ACh) levels and subsequent cognitive dysfunction [90]. Three acetylcholinesterase inhibitors (AChEI) have been approved by the Food and Drug Administration (FDA) with the goal of reducing ACh breakdown and increasing its availability at synapses [91]. These drugs are donepezil, galantamine and rivastigmine, which have demonstrated effectiveness in delaying cognitive decline in patients with mild to moderate AD [64,92].

The only other FDA-approved symptomatic treatment is memantine, an N-methyl-D-aspartate (NMDA) receptor antagonist. Memantine binds to NMDA receptors, partially blocking the ion influx and counteracting the detrimental effects of elevated glutamate levels that lead to neuronal dysfunction, while preserving the physiological actions of glutamate on learning on memory [93]. This drug has demonstrated efficacy in patients with moderate to severe AD [89].

However, it is important to note that these symptomatic treatments do not alter the course of the disease, as neurodegeneration continues in the brain, ultimately resulting in the drugs' inability to relieve symptoms. Hence, disease-modifying treatments are being developed.

### 1.6.2. Disease-modifying treatments

The primary targets for disease-modifying treatments are Aβ and Tau. At the time of writing this thesis, only two drugs have received FDA approval: aducanumab and lecanemab [94]. Aducanumab is a human IgG1 monoclonal antibody that binds to the N-terminal of Aβ fibrils, blocking amyloid aggregation [95]. This antibody is infused every month, and a dose- and time-dependent reduction in Aβ is observed after one year of infusions [96]. Clinical trials showed a slow cognitive decline and decrease in biomarkers indicating amyloid removal in patients with MCI or mild dementia [94]. However, further research is required to determine the effects of the drug, as improvements are modest, and other regulatory agencies have not approved its use due to side effects [97].

Lecanemab is a humanized IgG1 antibody that selectively binds to soluble Aβ protofibrils. Clinical trials involving patients with MCI or mild dementia demonstrated a dose-dependent reduction of amyloid plaques, leading to its recent approval by the FDA in January 2023 [98]. This drug is infused intravenously every two weeks, and less cognitive decline is observed in patients as early as 6 months after treatment initiation [99].

In addition, as of the beginning of 2023, there were 187 ongoing clinical trials evaluating 141 different treatments for AD. Among these, 55 were in phase III, 99 in phase II, and 33 in phase I. Disease-modifying strategies accounted for 78% of all studies, indicating a trend towards prioritizing these approaches over symptomatic treatments [100].

However, many of the drugs tested fail in clinical trials, likely due to late initiation of therapies in the disease course, incorrect main target, and an incomplete understanding of the AD pathophysiology [89]. In this context, a therapeutic approach targeting multiple underlying causes of the disease may be more beneficial, given its multifactorial nature. For instance, in a parabiosis experiment between young and aged mice, a rejuvenation effect was observed in old mice, suggesting that blood contains factors that could be beneficial for the treatment of aging-associated pathologies like Alzheimer's [101]. These factors have been called chronokines due to their ability to alter aging phenotypes, and can be an innovative tool for developing more effective therapeutic strategies for AD.

## 2. Chronokines

Chronokines are defined as proteins that determine systemic functions and biological aging processes [102]. These are typically present in plasma and can exert either detrimental or beneficial effects. In this study, we have selected a combination of three beneficial chronokines capable of addressing various aspects of AD, aiming to develop an effective therapeutic strategy for aging-related diseases.

### 2.1. Klotho

In 1997, Kuro-o *et al*. [103] reported on a mutant mouse exhibiting an accelerated aging phenotype similar to premature aging in humans. These mice presented a shorter lifespan, multiple organ degeneration, vascular calcification, and cardiovascular disease. This phenotype was attributed to the abolished expression of the *Klotho* gene, responsible for encoding the αKlotho protein (hereafter referred to as Klotho). In contrast, overexpression of the gene has been observed to have the opposite effect in mice, extending lifespan [104], prompting extensive research on the potential anti-aging effects of the Klotho protein.

Furthermore, in humans, the *KL*-VS allele increases soluble Klotho levels [105,106]. Studies have also revealed that *KL*-VS in heterozygosity protects against age-associated cognitive decline and even enhances cognition [107], as it is associated with a larger brain volume [108] and increased Aβ clearance [109], thereby reducing the risk of AD.

#### 2.1.1. Klotho transcripts and isoforms

The *Klotho* gene contains five exons and encodes a 130 kDa type I transmembrane protein, known as mKL [103]. This protein consists of an N-terminal signal sequence, an extracellular domain composed of two subunits (KL1 and KL2), a single transmembrane domain, and a short intracellular domain [110]. The extracellular domain of the full-length protein can be cleaved by the ADAM10 and ADAM17 secretases [111], releasing a soluble form of the protein named processed Klotho (pKL). Further cleavage of the pKL protein can result in the separation of the two domains, generating pKL1 and pKL2 [112].

Within the third exon of the gene, there is an alternative splicing donor that produces a 70 kDa secreted form of the protein, due to the presence of a premature stop codon [110]. This protein is known as secreted Klotho (sKL) and contains the KL1 domain, along with a 15 amino acid tail in the C-terminal absent in the mKL transcript (Fig. 7) [113]. Both sKL and pKL are referred to as soluble Klotho, as they can be found in body fluids like serum, urine, and CSF [114,115].

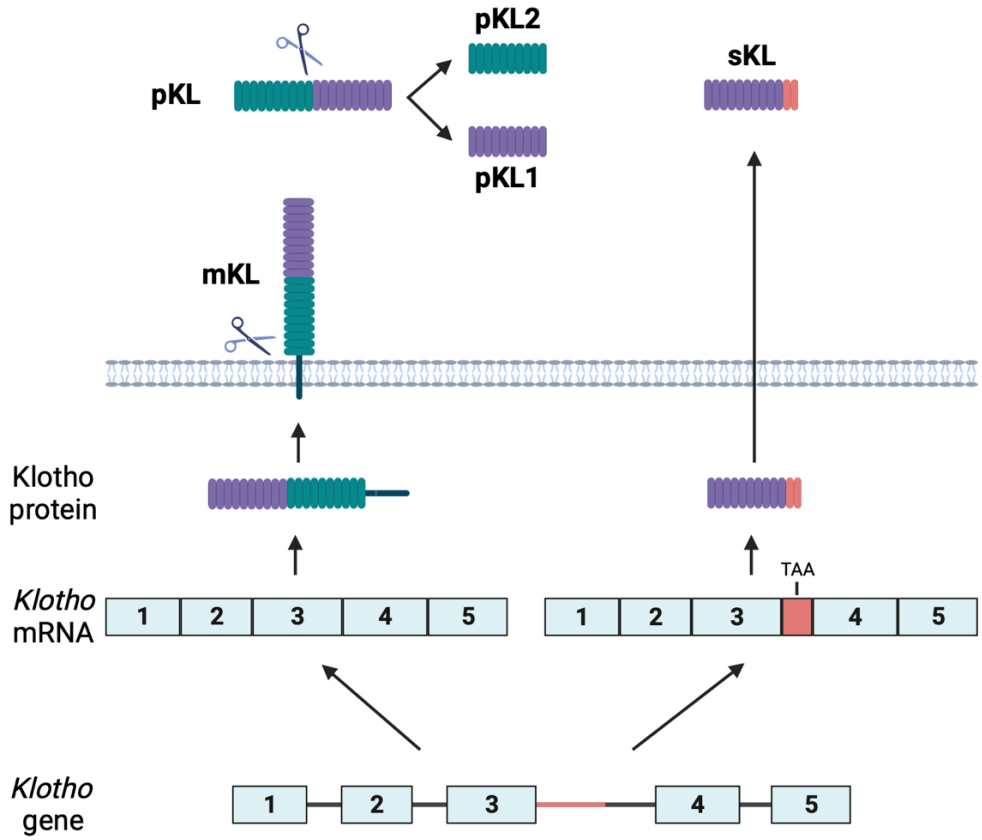



Figure 7. *Klotho* gene and its transcript variants, along with protein isoforms and their formation pathway.

### 2.1.2. Klotho expression and protein distribution

*Klotho* is primarily expressed in the kidney and brain, and to a lesser extent in pancreatic β cells, blood vessels, and skin [116]. The kidney is the main source of soluble Klotho in the blood, produced by the proximal and distal convoluted renal tubules. Within the brain, *Klotho* is highly expressed in ependymal cells of the choroid plexus, which secrete soluble Klotho into the CSF [103]. Additionally, *Klotho* is expressed in Purkinje cells and hippocampal neurons [117].

The expression of mKL compared to sKL varies among tissues and species. In mice, while sKL expression in the brain is higher than in other organs [118], mKL expression is around ten times higher in both the kidney and brain [113]. In contrast, in the human brain, sKL expression is reported to be higher than that of mKL [110]. However, *Klotho* expression levels have been observed to decline with age and in cases of AD, both in animals [119] and humans [120].

Despite these variations in mRNA expression, the differences in protein expression remain unclear, as no available antibody can distinguish between pKL and sKL. Consequently, the contribution of sKL to soluble Klotho levels remains uncertain. Nonetheless, soluble Klotho has been detected in both humans and mice, both in tissues and biological fluids [114–116].

### 2.1.3. Klotho functions

The different Klotho isoforms are believed to serve distinct functions in the organism. It can be found as a membrane-bound coreceptor for fibroblast growth factor 23 (FGF23) [121] and as a soluble endocrine mediator with diverse systemic effects (Fig. 8) [122].

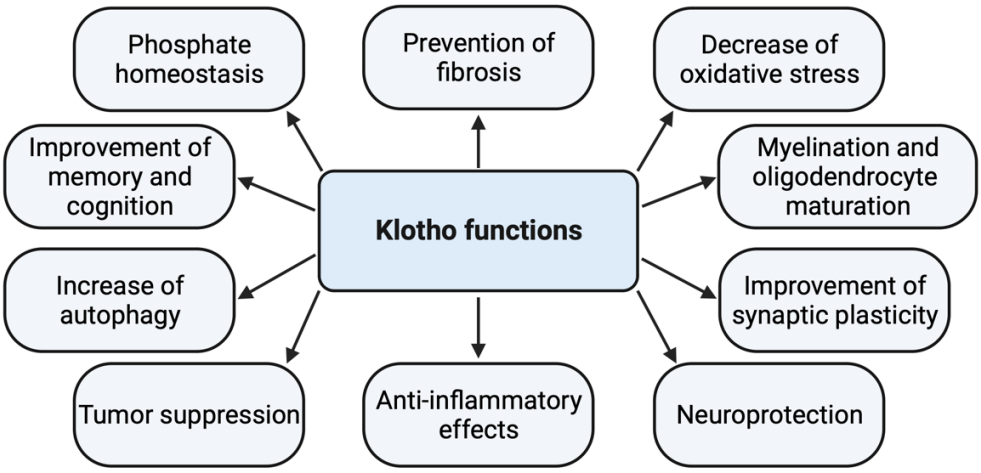



Figure 8. Main Klotho functions.

#### 2.1.3.1. Phosphate homeostasis

The extracellular domain of mKL can bind to FGFR1c, -3c, or -4 forming a receptor for FGF23 [121,123]. FGF23 is a bone-derived hormone that regulates renal phosphate homeostasis when it is bound to Klotho; otherwise, the affinity of FGF23 for the receptor

is low [124]. The binding of mKL to FGF23 and FGFR1c activates the MAPK cascade, regulating phosphate and calcium exchange in renal proximal tubule cells. This occurs through the inhibition of sodium-phosphate transporters, leading to a reduced phosphate reabsorption [125]. When mKL binds to FGF23 and FGFR3c or -4, an inhibition of the synthesis of active vitamin D occurs, which is involved in kidney calcium metabolism [126]. A deficiency in either mKL or FGF23 results in excessive production of vitamin D, along with hyperphosphatemia and hypercalcemia, contributing to an accelerated aging phenotype in mice [127]. The fact that mKL binds to FGF23 through its extracellular domain suggests that soluble Klotho isoforms could also be involved in the regulation of these functions [128].

#### 2.1.3.2. Prevention of fibrosis

One of soluble Klotho's functions is the prevention of renal, cardiac, and pulmonary fibrosis by inhibiting TGF-β [129,130]. TGF-β is a cytokine associated with aging, as it promotes cellular senescence, stem cell decline, immunologic impairment, and fibrosis [131]. Klotho binds to the TGF-β receptor, preventing TFG-β from binding to it, thereby blocking the activation of the signaling cascade [132]. Given that this cytokine is involved in various biologic processes altered during aging, soluble Klotho may act at multiple levels to protect against alterations caused by TFG-β.

#### 2.1.3.3. Decrease of oxidative stress

Klotho serves as a potent suppressor of oxidative stress, an important driver of aging in the organism. FOXO3a negatively regulates mitochondrial reactive oxygen species (ROS) generation through the upregulation of manganese superoxide dismutase (MnSOD) expression, which helps eliminate ROS [133]. Klotho increases the phosphorylation of FOXO3a by inhibiting the insulin/IGF-1 pathway [104], leading to increased MnSOD expression and aiding in ROS elimination, thus reducing oxidative stress [134]. Mice overexpressing Klotho exhibit lower levels of markers associated with oxidative DNA damage, $H_2O_2$-induced apoptosis, and mitochondrial DNA fragmentation [135]. Additionally, Klotho has been observed to decrease superoxide production, oxidative damage, and apoptosis through the regulation of the cAMP/PKA pathway [136].

In the context of the CNS, induction of the redox system was observed in the HT22 hippocampus-derived cell line and primary hippocampal neurons treated with recombinant Klotho [137], as well as in dopaminergic neurons of mice with elevated Klotho levels [117,138], thereby preventing neuronal damage.

#### 2.1.3.4. Tumor suppression

Klotho may act as a tumor suppressor through the regulation of two pathways. Firstly, the insulin/IGF-1 pathway plays a crucial role in cancer, as its dysregulation can lead to cancer development [139]. Klotho acts as an inhibitor of this pathway, suppressing downstream signaling and preventing the development of various cancer types [140–142]. Additionally, dysregulation of the Wnt signaling pathway is involved in various degenerative conditions and cancer [143], as Wnt induces the activity of transcription factors that promote the expression of oncogenic genes [144]. Klotho also blocks the Wnt signaling cascade by acting as an antagonist, binding to its ligands [145]. Inhibition of the Wnt pathway by Klotho has been observed to reduce cancer cell invasiveness and proliferation while promoting cancer cell apoptosis [146–148].

#### 2.1.3.5. Anti-inflammatory effects

Inflammation is a key driver of aging, as chronic inflammation can cause tissue damage and contribute to the development of neurodegenerative diseases like AD [149]. Klotho inhibits the NF-κB pathway involved in this process [150], stimulates the production of the anti-inflammatory cytokine IL-10, and suppresses production of the pro-inflammatory tumor necrosis factor α (TNFα) [151]. In this manner, Klotho functions to reduce the inflammatory environment.

#### 2.1.3.6. Klotho functions in the central nervous system

Aside from its systemic functions that may also have an impact on the brain, Klotho's specific roles in the CNS are believed to be crucial for the aging brain and associated neurodegenerative diseases. The downregulation of Klotho expression in the brains of aged humans and animals [120,152] suggests that this decline may hinder its neuroprotective effects, potentially contributing to the progression of various pathologies.

#### 2.1.3.6.1. Myelination and oligodendrocyte maturation

Klotho is believed to play an important role in myelination, as evidenced by decreased Klotho expression observed in the white matter of aged rhesus monkeys [119], along with impaired myelination in Klotho-deficient mice [153]. Studies suggest that Klotho enhances the maturation of primary oligodendrocyte progenitor cells [154], while also increasing the expression of myelin-associated proteins [155]. These findings indicate that Klotho may offer protective effects against myelin-related diseases like multiple sclerosis.

#### 2.1.3.6.2. Improvement of synaptic plasticity

NMDAR-dependent long-term potentiation (LTP) in the hippocampus is crucial for learning and different modalities of memory, such as spatial or temporal [156,157]. LTP is initiated when glutamate binds to NMDA receptors (NMDARs), allowing calcium to enter the cell and initiating a complex intracellular signaling cascade [158]. This process ultimately alters synaptic strength, thereby enhancing synaptic connectivity. Klotho has been found to increase the abundance of the GluN2B subunit of NMDARs in postsynaptic densities, enhancing LTP. Several studies involving different Klotho isoforms have supported these findings [107,159,160], suggesting that Klotho's action of improving cognition may be mediated by an enhancement in synaptic plasticity.

#### 2.1.3.6.3. Neuroprotection and reduction of neuroinflammation

In the context of AD, the aggregation of Aβ stimulates cerebral inflammation by activating microglia, as previously discussed [161]. Aβ activates NLRP3, a protein complex that contains caspase-1, responsible for the release of the pro-inflammatory cytokine IL-1β [162–164]. IL-1β, in turn, regulates the expression of other pro-inflammatory cytokines, amplifying the inflammatory response, leading to further Aβ depositions, cell death and neuronal injury [165]. Additionally, NLRP3 induces Tau hyperphosphorylation and aggregation [166]. Klotho is known to inhibit the NLRP3/caspase-1 pathway, thereby reducing the production of pro-inflammatory cytokines and associated neuroinflammation, exerting a neuroprotective effect, and aiding in the prevention of cognitive decline [167]. Furthermore, Klotho overexpression has also been shown to promote the differentiation of microglia into the anti-inflammatory M2 phenotype, thereby suppressing neuroinflammation [167,168].

#### 2.1.3.6.4. Increase of autophagy

Klotho has also been described to promote autophagy, suppressing the development and progression of AD by eliminating Aβ plaques and inhibiting the formation of NFTs [169]. Klotho-deficient mice exhibit impaired autophagy [170], suggesting that Klotho may help stimulate the impaired autophagy observed in AD [171].

#### 2.1.3.6.5. Improvement of memory and cognition

The effects of Klotho on cognition have been extensively studied. As mentioned earlier, human carriers of the *KL*-VS allele in heterozygosis, which leads to increased secretion of Klotho, present enhanced short-term memory, executive functions, and higher information processing rates [108,172–174]. However, individuals with the mutation in homozygosis experience cognitive decline and a reduced lifespan [106]. This effect may be attributed to the mutation enhancing one function of Klotho while impairing another one. In this context, when only one allele is present, the benefits of the gained function outweigh the drawbacks of the partially compromised function. However, when two copies are present, the loss of function appears too significant to compensate for [175].

Overexpression of Klotho in mice has also been shown to enhance cognition and memory. Aged mice injected with an sKL-expressing AAV vector displayed improved working memory, learning, and memory formation [176,177]. Furthermore, an enhancement in spatial and working memory was observed after systemic administration of recombinant pKL in mice, although the mechanism remains unclear, as pKL does not cross the BBB [160]. Overexpression of the full-length Klotho has also demonstrated improvements in cognitive deficits [107]. Similar effects have been observed in mouse models of AD, where Klotho overexpression, either through viral vectors or genetic modifications, led to improvements in memory and alleviation of the pathology hallmarks [159,167,169].

Collectively, these studies suggest that Klotho has the potential to improve cognitive deficits associated with aging and neurodegenerative diseases. Its pleiotropic nature, acting at all the pathways described earlier, positions it as a promising therapeutic agent.

### 2.1.4. sKL as a therapeutic agent

Most therapeutic strategies developed for AD often fail because they target only one aspect and cannot address all the neuropathological changes that occur in the brain. Therefore, strategies based on pleiotropic proteins like Klotho may offer greater efficacy. Klotho's multiple functions suggest that it could be used as a multitarget therapeutic strategy with broad effects in AD.

However, several questions remain unanswered. In most of the studies, the contribution of each Klotho isoform to the neuroprotective properties is unclear, as a distinction between them is usually not made. This lack of clarity may arise from the use of KL1 to assess Klotho levels and properties, which is common across all Klotho isoforms. Consequently, the term "soluble Klotho" is often used to encompass both pKL and sKL, without specifying which isoform is responsible for the observed properties. Additionally, apart from the lipid rafts through which some of its functions may be exerted [178], no specific receptor for Klotho has been identified in the brain, posing challenges in understanding the mechanisms underlying Klotho's effects on cognition and memory.

In a previous study conducted by our group in both wild-type mice and a mouse model of AD, it was observed that the expression of sKL is almost exclusively limited to the brain, exhibiting a distinct temporal and spatial expression pattern compared to mKL [118]. Furthermore, in a different study, the administration of an AAV viral vector expressing sKL in aged mice resulted in an improvement in age-dependent cognitive decline [177]. This was corroborated by another group, which demonstrated enhanced memory formation in mice overexpressing sKL in the hippocampus [176].

These findings point to the importance of further research on sKL as a potential therapeutic agent for preventing or treating aging-associated pathologies.

## 2.2. TREM2

Genetics plays a crucial role as a risk factor for the development of AD, as discussed earlier. A rare mutation in the gene encoding Triggering Receptor Expressed on Myeloid Cells 2 (TREM2) has been found to increase the risk of AD by approximately threefold, comparable to carrying one copy of the *APOE* ε4 allele [17,179]. This discovery prompted further investigation into the function of this protein in AD pathology, revealing its essential role in CNS homeostasis [180].

### 2.2.1. TREM2 transcripts and isoforms

TREM2 is a 35 kDa type I transmembrane glycoprotein with an extracellular V-type Ig ectodomain, a transmembrane region, and an intracellular C-terminal tail [181]. The ectodomain can be cleaved by ADAM10 and ADAM17 secretases at the H158-S158 peptide bond [182], releasing the 18 kDa soluble TREM2 (sTREM2) into the CSF and bloodstream [183]. Additionally, sTREM2 may be produced via an alternative transcript lacking the transmembrane domain [184], and it has been shown to function independently of transmembrane TREM2 [185].

### 2.2.2. TREM2 expression

*TREM2* is almost exclusively expressed by microglial cells in the CNS. This expression is predominantly concentrated in microglial cells in the hippocampus, the spinal cord and white matter [186]. *TREM2* expression appears to be regulated by inflammation *in vitro*, as pro-inflammatory cytokines such as TNFα, IL1β, and lipopolysaccharide downregulate its expression, while anti-inflammatory molecules upregulate it [187–189]. However, *in vivo* findings seem to contradict these observations, as an upregulation of TREM2 expression is noted in neurodegenerative diseases associated with neuroinflammation [190]. Thus, TREM2 overexpression has been detected in AD patients, likely associated with the recruitment of microglia to Aβ plaques [191].

### 2.2.3. TREM2 variants in AD

Multiple TREM2 variants with varying impacts on AD pathology have been identified. Among these variants, the R47H mutation has been extensively studied and is associated with a threefold increase in AD risk [179,192]. Carriers of this variant typically exhibit

earlier disease onset and more rapid progression due to impaired ligand binding capacity, which disrupts normal protein function [193]. Further investigation into other TREM2 variants could provide insights into the mechanisms through which this protein functions in the brain. For instance, the H157Y variant has been observed to ameliorate Aβ pathology and synaptic function, despite also increasing the risk of AD [194].

### 2.2.4. TREM2 functions

TREM2 is a pattern recognition receptor. Upon activation by various ligands such as phospholipids, lipoproteins, and Aβ peptides, it induces an innate immune response characterized by processes such as phagocytosis, chemotaxis, and transcriptional changes (Fig. 9) [195].

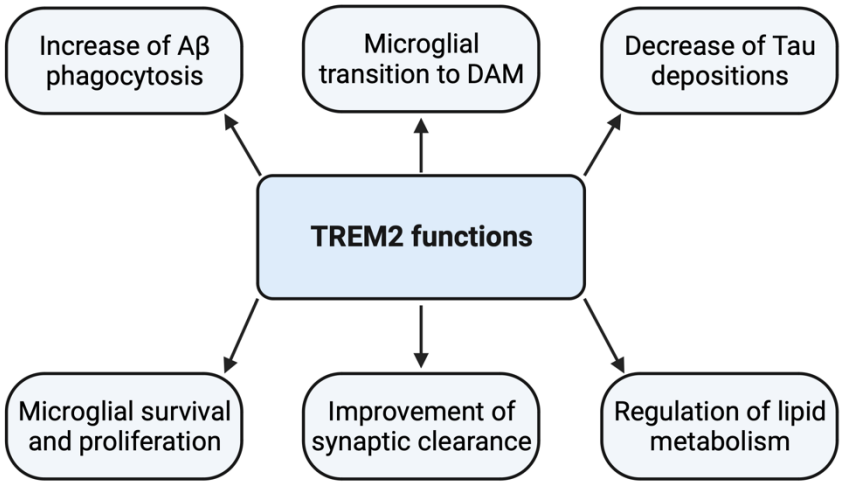



Figure 9. Main TREM2 functions.

#### 2.2.4.1. Increase of Aβ phagocytosis

TREM2 plays an important role in microglial phagocytosis. Studies in mice and *in vitro* demonstrate that *Trem2* deletion results in reduced phagocytosis of apoptotic cells, cellular debris, lipoproteins, Aβ plaques and bacteria [196–199], whereas overexpression has the opposite effect [200]. TREM2 also aids in microglial clustering around Aβ plaques, trimming and compacting them [201]. However, the role of TREM2 in Aβ elimination is controversial, as contradictory results have been observed. Deletion of *Trem2* appears to decrease Aβ deposition in young mice but increases it in older mice [202]. The consensus is that the effect of TREM2 on Aβ deposition is dependent on disease progression: in early stages of AD, TREM2 may promote Aβ seeding and plaque aggregation, whereas when

the disease progresses and plaques have already been formed, TREM2's plaque trimming action becomes more prevalent, reducing Aβ pathology.

#### 2.2.4.2. Decrease of Tau depositions

TREM2 is also involved in Tau depositions in AD, although the mechanism of action remains unclear, and conflicting findings have emerged. In mouse models of pure tauopathy, loss of TREM2 function appears to ameliorate the pathology by reducing brain atrophy and microgliosis in the hippocampus, thereby leading to reduced neurodegeneration [203,204]. However, in a mouse model with both tauopathy and Aβ pathology, the opposite effect was observed. In this model, *Trem2* deletion exacerbated Tau accumulation and brain atrophy, suggesting that TREM2 may slow AD progression by affecting Tau spreading, but only in the presence of Aβ pathology [205–207]. Nonetheless, further research is needed to clarify the effects of TREM2 on Tau depositions and determine whether therapeutic interventions targeting TREM2 could yield beneficial outcomes in AD patients.

#### 2.2.4.3. Microglial survival and proliferation

TREM2 influences myeloid cell survival and proliferation, as evidenced by reduced microglial proliferation observed in TREM2-deficient mice and primary microglia under stress conditions such as inflammation and Aβ exposure [208–210]. Moreover, decreased survival rates have been observed in primary microglia and cell lines when TREM2 is decreased [211], while dendritic cell survival increases upon TREM2 activation [212]. The decline in survival rates may be associated with metabolic defects, as functional TREM2 deficiency leads to reduced glucose use, dysfunctional glycolysis, and lower ATP levels in microglia [208,213].

#### 2.2.4.4. Regulation of lipid metabolism

TREM2 is an immune receptor that regulates cholesterol and phospholipid metabolism in the CNS [214]. It has been reported that TREM2 can bind to all ApoE isoforms [215,216], which mediate the endocytosis and efflux of lipids and cholesterol [217]. Therefore, the regulation of lipid metabolism by TREM2 is likely mediated through its interaction with ApoE. Studies in mice lacking TREM2 have demonstrated a deficiency in cholesterol efflux,

resulting in cholesterol ester accumulation [214]. Additionally, TREM2-deficient cells exhibited elevated levels of several lipid types, including cholesterol, ceramides, sulfatides, phospholipids, triacylglycerols, and diacylglycerol [218]. Lipid metabolism is also regulated by the PLCγ2 enzyme, located downstream of the TREM2 signaling pathway, indicating that mutations in TREM2 may increase the risk of AD by disrupting lipid metabolism, although the exact mechanism remains unclear [218].

TREM2 also participates in microglial responses to myelin damage. Microglia deficient in TREM2 present impaired clearance of myelin debris, fewer oligodendrocytes, axonal dystrophy, and persistent demyelination [219,220], all of which can be reversed with the administration of a TREM2-activating antibody [221].

#### 2.2.4.5. Microglial transition to DAM

TREM2 may promote the transition of microglia into a disease-associated microglia (DAM) subtype, characterized by enhanced phagocytic activity and the ability to limit Aβ plaque growth by forming a physical barrier around Aβ aggregates [222]. One of the steps in DAM activation involves TREM2-mediated induction of phagocytic pathways and lipid metabolism, leading to the transition of microglia to an anti-inflammatory DAM subset that exerts beneficial effects in AD [222,223]. Through this mechanism, TREM2 can ameliorate the neuroinflammation observed in AD [180,224,225].

#### 2.2.4.6. Improvement of synaptic clearance

Synaptic clearance is the process for eliminating unnecessary synapses to maintain the morphological and functional maturation of remaining synapses, which is essential for synaptic plasticity involved in learning and memory [226]. This process is mediated by the classical complement cascade, where redundant synapses express the C1q protein, recognized by microglia to initiate synaptic clearance [227]. It is proposed that TREM2 interacts with both ApoE and the C1q protein during synaptic clearance [228,229], as this process is compromised in TREM2-deficient mice [230].

### 2.2.5. sTREM2 as a therapeutic agent

In addition to the membrane-bound form, the soluble form of TREM2 (sTREM2) also plays a pivotal role in AD. sTREM2 can be detected in the CSF and serves as a biomarker of microglial activation in response to neurodegeneration [231–233]. sTREM2 levels in the CSF are low in early asymptomatic stages of AD, when only Aβ pathology is present. sTREM2 levels peak during early symptomatic phases when microglial activation begins, and subsequently decline in dementia stages [234,235]. Thus, sTREM2 has been proposed as a biomarker for diagnosing AD and determining disease stage. Furthermore, individuals with higher sTREM2 levels have been observed to progress at a slower rate through MCI and dementia [236,237], suggesting an important neuroprotective role for sTREM2.

Some actions mediated by sTREM2 overlap with those of membrane-bound TREM2, but differences may exist. For instance, TREM2 is believed to have anti-inflammatory effects, while studies haves shown that sTREM2 activates microglia and induces the expression of pro-inflammatory cytokines, both *in vitro* and *in vivo* [238,239]. However, this increase in pro-inflammatory cytokines does not appear to exacerbate cognitive impairment in mice, as improvements could be observed after sTREM2 delivery to the hippocampus [239].

sTREM2 also promotes microglial survival by inhibiting apoptosis [238], and enhances Aβ phagocytosis [240]. Additionally, sTREM2 can bind to oligomeric Aβ, preventing fibrilization [241,242] and even disaggregating oligomers [243]. This mechanism helps prevent neuronal loss *in vitro*. Moreover, sTREM2 is proposed to act as a chaperone for Aβ, preventing it from folding as an aggregable protein and degrading misfolded forms. This is supported by findings in *Trem2* knockout mice, which show more Aβ plaques due to impaired inhibition of Aβ aggregation by sTREM2 [244].

All the improvements observed in neuropathology translate to enhanced memory and cognitive skills in AD mice. Overexpression of sTREM2 via an AAV viral vector in the brains of mice overexpressing Aβ led to enhanced spatial memory, accompanied by a reduction in Aβ plaque load and improved long-term potentiation [240]. In a recent study, memory and cognition improvements were observed in a mouse model of tauopathy with sTREM2

overexpression, along with attenuation of Tau hyperphosphorylation in the hippocampus [245].

Taken together, the effects of sTREM2 suggest it presents potential as a therapeutic target for addressing neuropathological alterations in AD. Further investigation into its impact on cognition in mouse models of AD is necessary to assess the feasibility of sTREM2 as a therapeutic approach for humans.

## 2.3. TIMP2

In a heterochronic parabiosis experiment where the circulatory systems of young and aged mice were connected, a rejuvenation effect was observed in the older mice [246]. This effect was later confirmed by injecting young plasma into aged mice [247]. Furthermore, the administration of human umbilical cord plasma improved cognition and synaptic plasticity in aged rodents [248]. One of the key enriched factors found in both human umbilical plasma and young mouse plasma is Tissue Inhibitor of Metalloproteinases 2 (TIMP2), which is believed to be responsible for the observed rejuvenation effects in aged mice [248]. Similar improvements were noted in aging mice when recombinant TIMP2 was administered, further confirming its significance as a potential anti-aging factor.

### 2.3.1. TIMP2 expression and protein distribution

TIMP2 is a 24 kDa soluble protein expressed in a variety of tissues, including lymph nodes, brain, heart, arteries, colon, kidneys, liver, breast, ovaries, prostate, and testes [249–251]. It is highly expressed in hippocampal neurons, and its levels decline with age, suggesting an important role of this protein in maintaining brain homeostasis [248]. TIMP2 inhibits matrix metalloproteinases (MMPs) through reversible blockage, thereby affecting extracellular matrix degradation. Additionally, it exhibits MMP-independent functions through receptor binding [252].

### 2.3.2. TIMP2 functions

TIMP2 is a pleiotropic protein with diverse functions. Its involvement in cancer and potential therapeutic applications are subject of extensive research [253], and it is also being studied as a biomarker for acute kidney injury [254]. However, this thesis will focus solely on its functions related to the brain and neurodegenerative diseases (Fig. 10).

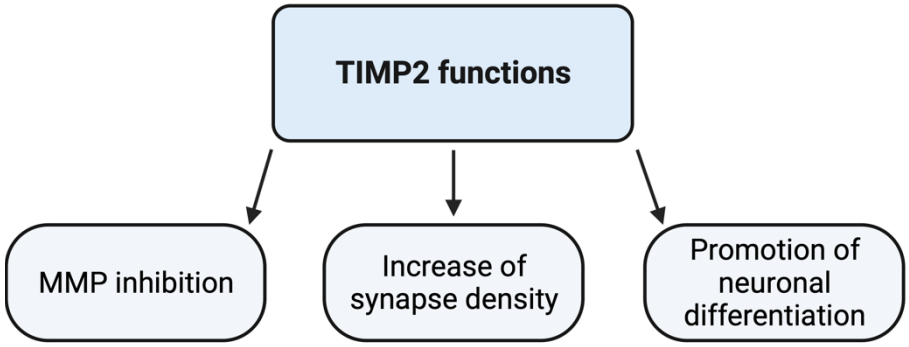



Figure 10. Main TIMP2 functions.

#### 2.3.2.1. MMP inhibition

Matrix metalloproteinases 2 and 9 (MMP2 and MMP9) are substrates for TIMP2. Increased MMP9 levels in cortical regions have been observed in early stages of AD, correlating with cognitive decline associated with the proteolytic degradation of the nerve growth factor [255], demonstrating MMP9's neurotoxic effect on hippocampal neurons [256]. Moreover, the presence of the *APOE* ε4 allele leads to the activation of MMP9, which in turn activates the pro-inflammatory cyclophilin A pathway, resulting in blood-brain barrier breakdown [257], observed in both animal models [258] and humans [259]. Similarly, MMP2 upregulation has been linked to this effect [260], suggesting that both MMPs contribute detrimentally to AD by inducing BBB breakdown and subsequent chronic neuroinflammation. Additionally, MMP2 upregulation in early stages of AD has been associated with promoting pTau aggregation [261]. These observations indicate that inhibition of MMP2 and MMP9 by TIMP2 could potentially mitigate some of the pathological changes present in AD [262].

#### 2.3.2.2. Promotion of neuronal differentiation

One of TIMP2's functions is promoting neuronal differentiation. Through cell-cycle arrest, TIMP2 can promote neuronal differentiation and neurite outgrowth, as demonstrated

both *in vitro* and *in vivo* in *Timp2* knockout mice, where incomplete neuronal differentiation is observed [263]. These functions are independent of MMP inhibition, although the precise mechanism remains unknown and requires further research.

#### 2.3.2.3. Increase of synapse density

The decline in excitatory synapse density during aging and in AD is closely associated with cognitive impairment. TIMP2 promotes an increase in excitatory synapse density in the hippocampus, without affecting inhibitory synapse density. This increase in excitatory synapse density leads to enhanced hippocampal-dependent spatial memory and learning through TIMP2's MMP-independent effects directly on neurons, with no impact on microglial cells [264,265]. Additionally, TIMP2 regulates the accumulation of extracellular matrix around synapses, affecting synaptic plasticity and memory. In contrast, loss of TIMP2 results in an accumulation of extracellular matrix proteins, leading to fewer dendritic spines and reduced neurogenesis [265].

In summary, despite the limited number of studies on TIMP2 in AD, a beneficial effect is evident. Further research is necessary to elucidate its exact mechanisms of action and functions, although it represents a promising candidate for AD treatment, along with sKL and sTREM2.

## 3. Gene therapy

Gene therapy is defined as the transfer of genetic material to a patient for the treatment of a disease, enabling the patient's own cells to synthetize the encoded genetic product [266]. Initially focused on monogenic diseases, providing a correct copy of the mutated gene to correct the disease, gene therapy has expanded its applications to a wide range of conditions since its first clinical investigation in 1990 (Fig. 11). As of March 2023, there were 3826 ongoing clinical trials using gene therapy, with cancer representing the most prevalent target, accounting for 68,5% of all global clinical trials [267]. Additionally, a total of 27 gene therapy strategies have been approved worldwide for treating various diseases [268].

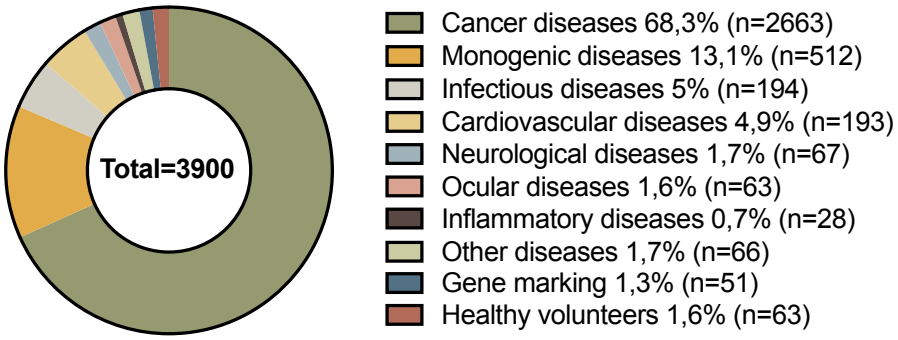



Figure 11. Gene therapy clinical trials classified according to the treated disease [267].

## 3.1. Vectors

The gene transfer is mediated by the vector, which can be viral or non-viral. The vector can be administered directly into the patient (*in vivo* gene therapy) or into cultured cells extracted from the patient (*ex vivo* gene therapy), with the choice of vector varying based on the application (Fig. 12). In *ex vivo* gene therapy approaches, stem cells or progenitor cells are isolated from the patient, and integrative vectors like lentiviral vectors are used to integrate the DNA into the genome. This ensures that when the cells are reintroduced into the patient and undergo division, the genetic material is passed on to daughter cells. In contrast, in *in vivo* gene therapy strategies, post-mitotic cells are typically targeted, and long-term expression of the therapeutic gene can be achieved if the transferred DNA remains stable within the cells. Adeno-associated viral vectors are preferred for *in vivo* strategies, as the transferred DNA remains stable as an episome [266].

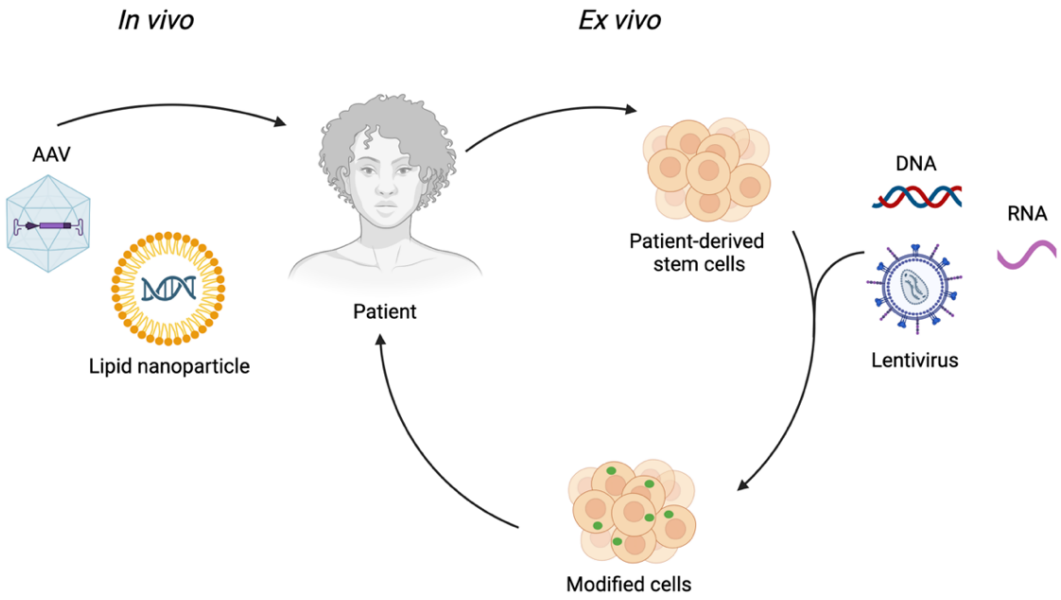



Figure 12. Types of gene therapy and most used vector for each type.

Non-viral vectors typically consist of DNA or RNA molecules that are delivered within a lipidic or polymeric envelope. These vectors offer several advantages, including the ability to deliver large amounts of genetic material, lower immunogenicity compared to viral vectors, and ease of preparation [269]. However, the expression achieved with these vectors is usually transient, and effectively targeting specific cell types can be challenging. Therefore, viral vectors are predominantly employed in gene therapy applications due to their superior cell transduction capabilities and ability to sustain long-term expression of the transgene. Among them, adenovirus (Ad), lentivirus, and adeno-associated virus (AAV) can be highlighted, which collectively represent approximately 60% of all current clinical trials involving viral vectors, and are also extensively used in preclinical studies (Fig. 13) [267].

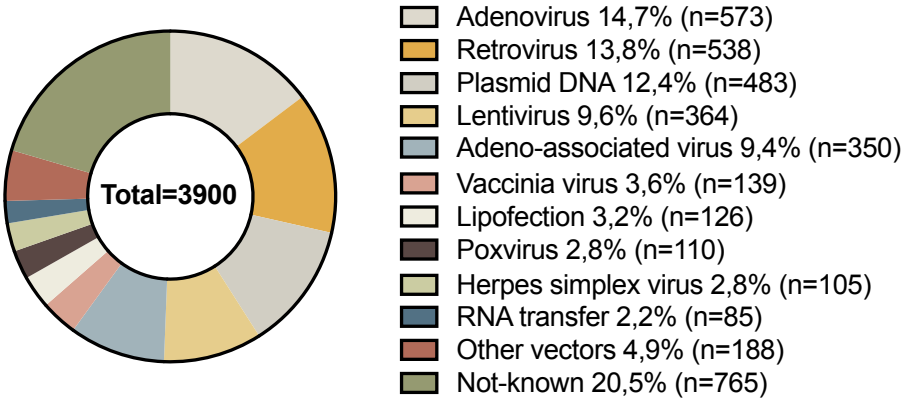



Figure 13. Gene therapy clinical trials classified according to the vector used [267].

## 3.2. Viral vectors

Viruses are agents that have naturally evolved to infect cells, deliver their genetic material, and exploit the host cell's machinery for their own replication. Gene therapy strategies leverage their ability to infect cells to deliver therapeutic genes. This is accomplished by replacing the virus' replication genes with the therapeutic transgene, thereby rendering it unable to replicate while retaining its infectivity, making them safe and effective therapeutic vectors.

A diverse range of viral vectors is available for gene therapy strategies, and the selection of a specific vector depends on the intended application (Table 1). Other considerations include immunogenicity, cell tropism, packaging capacity, carcinogenic potential, and

scalability. The ideal viral vector for most applications should possess the ability to specifically transduce the target tissue or cell type, elicit minimal immunogenic response, and be producible in high titers. Currently, the most widely used viral vector in *in vivo* gene therapy strategies is the adeno-associated virus (AAV) due to its low immunogenic profile, ability to sustain long-term expression of therapeutic transgenes, and high transduction efficiency in a variety of tissues [270].

Table 1. Most used viral vectors in gene therapy. Adapted from [271].

| Vector | Packaging capacity | Immunogenicity | Advantages | Disadvantages |
|---|---|---|---|---|
| **Enveloped** | | | | |
| **Retrovirus** | 8 kb (RNA) | Low | Persistent gene transfer in dividing cells | Integration might induce oncogenesis |
| **Lentivirus** | 8 kb (RNA) | Low | Persistent gene transfer in most tissues | Integration might induce oncogenesis |
| **HSV-1** | 40-150 kb (dsDNA) | High | Large packaging capacity | Inflammatory; transient transgene expression |
| **Non-enveloped** | | | | |
| **AAV** | 4.7 kb (ssDNA) | Low | Non-inflammatory; non-pathogenic | Small packaging capacity |
| **Adenovirus** | 8-30 kb (dsDNA) | High | Efficient transduction of most tissues | Potent inflammatory response (can be an advantage for cancer) |

HSV-1: Herpes simplex virus type 1, AAV: adeno-associated virus, ssDNA: single-stranded DNA, dsDNA: double-stranded DNA.

### 3.2.1. Adeno-associated viral vectors

AAVs are non-pathogenic viruses belonging to the *Parvoviridae* family, with a 4.7 kb ssDNA genome enclosed within a non-enveloped icosahedral capsid. These viruses require co-infection with a helper virus, such as adenoviruses, herpesviruses, or papillomaviruses, for replication [272]. In the absence of a helper virus, wild-type AAVs (wtAAV) can still infect cells but are unable to replicate and produce new particles. Instead, they integrate into the host genome at the AAVS1 locus on chromosome 19 [273].

Several therapeutic strategies using AAVs have been approved for their use in human patients. The first one was Glybera in 2012, designed to treat lipoprotein lipase deficiency [274]. Since then, additional gene therapy treatments based on AAVs have received approval [275], underscoring the potential of this vector for treating a variety of diseases.

#### 3.2.1.1. Genome and engineering

The wtAAV genome is flanked by two inverted terminal repeats (ITRs), each 145 bp in length, serving as the viral origin of replication and genome packaging signal. The AAV genome comprises three open reading frames (ORF): the *rep* ORF encodes four non-structural proteins (Rep78, Rep68, Rep52 and Rep48) involved in viral replication, transcription, genomic integration, and virion assembly. The *cap* ORF encodes the three structural proteins (VP1-3) that form the capsid [276]. Lastly, an ORF present as an alternative reading frame within the *cap* gene encodes the assembly-activating protein (AAP), responsible for capsid assembly [277].

For recombinant AAV (rAAV) production using the triple transfection method, the *rep* and *cap* genes are replaced by the transgene of interest, flanked by the two ITRs within a single plasmid [278]. This plasmid also includes the promoter and regulatory sequences. The ITRs are the only elements that are required in *cis*, while *rep* and *cap* can be provided in *trans* using another plasmid (pRepCap). The helper virus necessary for AAV replication is also replaced by a third plasmid (pHelper) containing adenoviral genes: E1a, E1b, E2a, E4orf6 and VA [279,280]. Alternatively, the E1a and E1b may be provided by the producer cells, as is the case for HEK293 cells. rAAVs produced through the co-transfection of these three plasmids contain the expression cassette, including the promoter, transgene, and

regulatory sequences, flanked by two ITR sequences. Notably, wtAAVs integrate into the host cell's genome, whereas rAAVs lose this capability due to the deletion of *rep78/68* involved in this process [281]. The DNA packaging capacity of rAAVs is constrained to the wtAVV genome size. Therefore, the cassette including the promoter, transgene, regulatory sequences, and ITRs should not exceed 4.7 kb (Fig. 14).

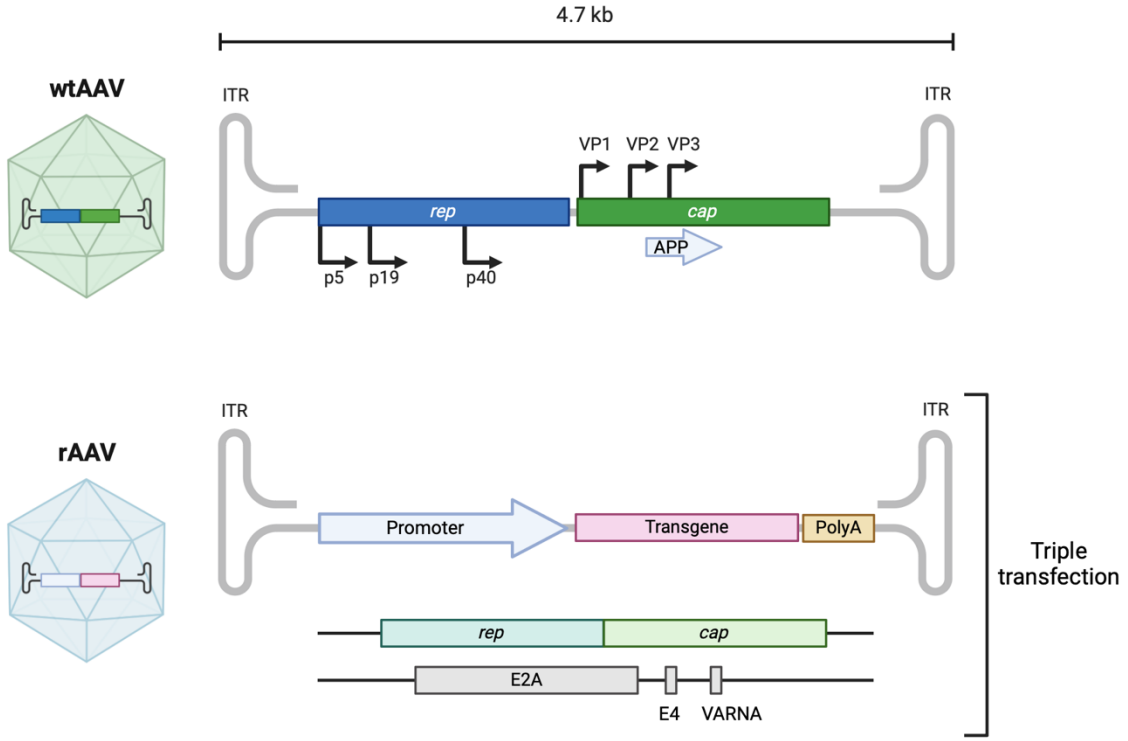



Figure 14. Genomic structure of a wtAAV and a rAAV.

### 3.2.1.2. rAAV transduction mechanism

rAAV's transduction into the host cell begins with binding to cell surface receptors [282]. Various receptors have been identified for AAV binding, resulting in different tropisms for each serotype. Following receptor binding, the rAAV is internalized via endocytosis toward the cell nucleus. Once inside the cell, the rAAV undergoes pH-mediated structural changes within endosomes, which are necessary for cell transduction and trafficking through the cytosol. Subsequent endosomal escape is triggered by a drop in pH, allowing the free rAAV to travel through the cytosol to enter the nuclear pore complex. Upon nuclear entry, the rAAV undergoes capsid uncoating, releasing its genome. Then, the ITR sequences serve as the origin of transcription to start the conversion of the ssDNA genome into dsDNA. The synthesis of the second DNA strand may occur either via the host cell's DNA polymerases or through an alignment of the anti-sense strands that coexist in the nucleus. Then, the

dsDNA undergoes intra- or inter-molecular circularization via ITR recombination. This yields double-stranded circular concatemeric episomal forms that stabilize the viral genome, leading to gene expression in postmitotic cells. The viral genome can also integrate into the host cell's genome, although this event is rare [281,283] (Fig. 15).

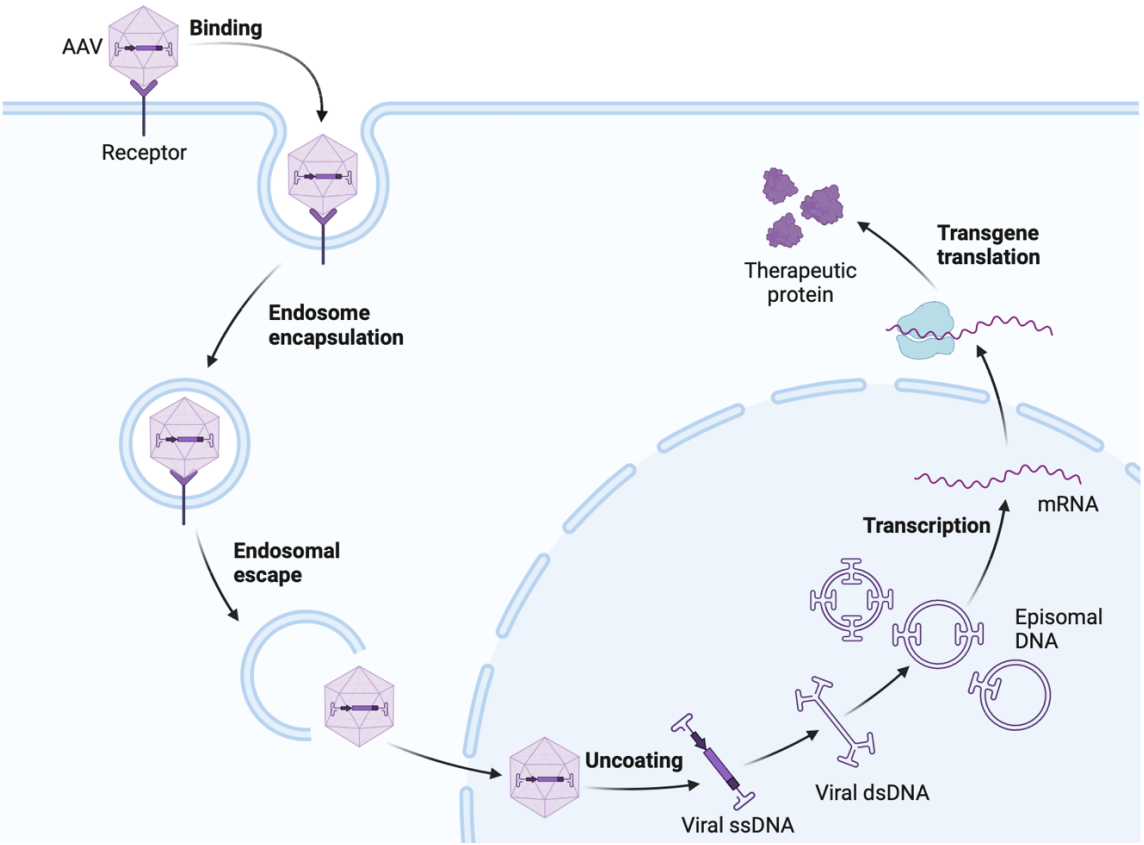



Figure 15. rAAV transduction mechanism. Figure adapted from [283].

### 3.2.1.3. Tropism

The AAV capsid determines the receptors it binds to on the cell surface, thereby dictating the cell types it transduces. Numerous AAV serotypes exhibit diverse tropisms due to differences in capsid composition. This confers them distinct tropisms, defined as the preference for a specific cell type [284]. Twelve serotypes have been identified in humans and non-human primates, and over 100 AAV variants have been tested as gene therapy vectors (Table 2) [285].

The AAV2 was the first discovered serotype to be extensively characterized [286,287]. Consequently, rAAVs are commonly produced using the AAV2's ITR and *rep* sequences. By incorporating *cap* genes from other serotypes, rAAVs with different tropisms can be

generated [288]. Recently, new technologies have been developed to generate new variants not found in nature by modifying the capsids, aiming to enhance transduction of specific cell types or reduce immunogenicity. These technologies include rational design, directed evolution, and computationally designed ancestral capsid libraries [285].

Table 2. AAV serotypes, their receptors and tropism. Adapted from [285].

| Serotype | Primary receptor | Co-receptor | Tropism |
|---|---|---|---|
| **AAV1** | Sialic acid | AAVR | Muscle, heart, CNS |
| **AAV2** | Heparin | Integrin, FGFR, HGFR, LamR, AAVR | Liver, muscle, CNS |
| **AAV3** | Heparin | FGFR, HGFR, LamR, AAVR | Muscle, stem cells |
| **AAV4** | Sialic acid | Unknown | Eye, CNS |
| **AAV5** | Sialic acid | PDGFR, AAVR | SNC, lung, eye |
| **AAV6** | Heparin Sialic acid | EGFR, AAVR | Muscle, SNC, heart, lung |
| **AAV7** | Unknown | Unknown | Muscle, CNS |
| **AAV8** | Unknown | LamR, AAVR | Liver, muscle, pancreas, CNS |
| **AAV9** | Galactose | LamR, AAVR | Every tissue |
| **AAV10** | Unknown | Unknown | Muscle |
| **AAV11** | Unknown | Unknown | Unknown |
| **AAV12** | Unknown | Unknown | Nasal |

#### 3.2.1.3.1. AAV9

The AAV9 serotype is widely used in preclinical and clinical studies as a gene therapy vector targeting the CNS [289], as it can transduce all major cell types in the brain, including neurons, microglia, astrocytes, and oligodendrocytes [290,291]. This leads to a widespread expression of the transgene of interest when the vector is locally administered. However, although the AAV9 has been shown to cross the BBB, this process is not very efficient [292], making the local administration route of this vector too invasive for practical use in clinical studies.

#### 3.2.1.3.2. AAV9P31

Recently, a new AAV9 variant has been developed through directed evolution. A library of AAVs with a random 7 amino acid insertion in the hypervariable region of the AAV9 Cap protein was generated, and the variants that more efficiently crossed the BBB were selected. One of them is the so-called AAV9P31 variant, showing a 385-fold increase in expression in the CNS following systemic administration compared to AAV9 [293]. This suggests that the random peptide insertion confers this variant the ability to efficiently penetrate the BBB, enabling wide expression of the transgene of interest while also eliminating the need for invasive local CNS administrations.

### 3.2.1.4. Advantages and disadvantages

Currently, AAVs are the most widely used viral vectors for *in vivo* gene therapy, as they present major advantages. They are non-pathogenic to humans, replication-defective in the absence of a helper virus, and exhibit low immunogenicity, making them safe vectors. The absence of viral coding sequences dramatically reduces the immune response against transduced cells, allowing for sustained expression of the transgene of interest following a single administration [270]. Furthermore, the diverse array of AAV serotypes and variants offers versatility for targeting specific tissues or cell types in different diseases [285].

However, these vectors also present some drawbacks. The previously discussed expression cassette size limitation of 4.4 kb needs to be taken into consideration. Nonetheless, new technologies are being developed to overcome this limitation, including dual vector strategies [294,295]. Additionally, transgene expression does not start immediately after the administration of the vector, as the ssDNA genome must be converted to dsDNA before transcription initiation. Peak expression *in vivo* is usually achieved around two weeks post-administration, making rAAVs relatively slow vectors [296]. Hepatic toxicity caused by rAAVs is also a concern, although this effect is believed to be dose-dependent and only observed at high rAAV doses [297,298]. Translatability to humans is another drawback of rAAVs, as preclinical data obtained in animal models may not always be directly applicable to humans, necessitating new models like human organoids to overcome challenges in preclinical data translation [299]. Large-scale

manufacturing of rAAVs poses challenges, as large amounts of vector are necessary to treat humans, unlike animal models. Consequently, the current economic cost of a rAAV-based therapy is very high due to the manufacturing expenses [283]. This highlights the need for improved manufacturing techniques to increase the rAAV yield and reduce costs.

#### 3.2.1.5. Immune response against rAAVs

Despite one of rAAV's advantages being their low immunogenicity, it is noteworthy that the protein capsid may produce the activation of the host immune system under certain conditions.

In humans, neutralizing antibodies (NAbs) against capsid proteins constitute the first immunologic barrier. Studies have shown that 30-60% of humans have naturally acquired NAbs against all AAV serotypes due to prior wtAAV infections [300]. This presents a potential challenge for rAAV therapy, as individuals with these antibodies may neutralize the administered vector, hindering its interaction with target cells and transgene expression. This is especially significant when the rAVV vector needs to be administered multiple times, as the humoral response generated after the initial administration could impede subsequent treatments. Strategies to overcome this include increasing vector dose or pharmacologically immunosuppressing patients using agents like rapamycin to induce immune tolerance [301,302]. Additionally, the capsid may elicit a cytotoxic response mediated by $CD8^+$ T-cells, resulting in the elimination of transduced cells and loss of transgene expression. However, this cytotoxic response only occurs at high vector doses. Consequently, this response only affects the therapeutic strategy beyond a critical threshold where vector elimination occurs [302,303] (Fig. 16).

The innate immune system may also get activated shortly after vector administration through stimulation mediated by TLR receptors (TLR2 and TLR9) when either the capsid proteins or the genome comes into contact with these receptors. This activation leads to the expression of pro-inflammatory cytokines, which in turn activate the adaptative immune response [304].

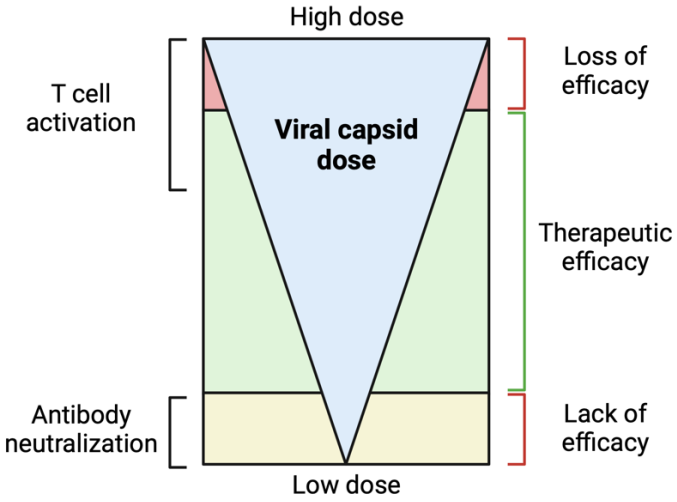



Figure 16. Relationship between the viral capsid dose and the immune response generated after rAAV systemic administration. The therapeutic efficacy can be affected by NAbs at low doses. Efficacy is achieved by increasing the dose, although a cytotoxic effect may appear at high doses, leading to the vector elimination when a threshold is reached, and the consequent loss of efficacy. Figure adapted from [302].

## 4. Experimental models for AD

Experimental models are essential for studying AD pathology and underlying mechanisms involved, as well as for identifying biomarkers and testing therapeutic approaches. However, the generation of a model that recapitulates all pathological characteristics observed in human patients has proven challenging, resulting in a vast number of *in vivo* and *in vitro* models depending on the intended application.

For instance, induced pluripotent stem cells (iPSC) derived from patient's fibroblasts [305] offer a valuable platform for generating two- or three-dimensional *in vitro* models for studying AD [306]. These pluripotent cells can differentiate into various cell types, including neurons and microglia, generating cell cultures that have enabled the study of sporadic AD, which affects more human patients, and is normally not replicated in *in vivo* animal models.

### 4.1. *In vivo* models

While numerous *in vitro* models are being generated for the study of AD, animal models still remain one of the most widely used tools to understand the pathophysiology and to

test therapeutic strategies. Over the years, a wide range of vertebrate and invertebrate models have been developed, spanning from yeast to non-human primates [307]. However, mouse models remain the most extensively used, with a total of 221 models as of 2023 [308].

Mice offer several advantages over other animal models. It is a well characterized species, small in size, with a high birth rate, and they can be easily housed in animal facilities at a relatively low cost [309]. Additionally, they provide insights into cognitive impairment that cannot be obtained from other models [310].

Animal models can either be spontaneous, interventional, or genetically modified. In the case of mouse models, the majority are genetically modified transgenic models, as mice do not naturally develop AD [307]. Hence, mutations associated with early-onset AD in humans are introduced into mice to generate transgenic AD mice. Typically, mutations in *APP* or *PSEN* genes are introduced to increase Aβ levels, enabling mice to develop Aβ plaques. The human *Tau* gene may also be introduced to induce NFT depositions, as mice do not naturally express Tau. However, a limitation of mouse models is that they usually present either Aβ plaques or NFTs, whereas patients present both features [311]. Therefore, the APP/Tau mouse model may serve as a viable alternative, presenting both hallmarks of AD pathology.

### 4.1.1. APP/Tau mouse model

The APP/Tau mouse model, developed by Dr Saura's group at Universitat Autònoma de Barcelona [312], is a transgenic model that overexpresses mutated human *APP* and *Tau* genes, reflecting synaptic, behavioral, and molecular alterations characteristic of AD.

The APP/Tau model exhibits Tau accumulation in the hippocampus, and Aβ accumulation in the amygdala by 6 months of age. Notably, gender differences exist, with females displaying higher Aβ and Tau levels in the entorhinal cortex and the CA3 region of the hippocampus. Females also present higher anxiety levels, while this behavior is not visible in males. In this model, Aβ and Tau synergistically act to impair hippocampal synaptic transmission and plasticity, which coincides with a reduction in presynaptic and

postsynaptic proteins. Both male and female mice display spatial learning and memory deficits associated with Tau accumulation. Furthermore, these mice present transcriptional alterations that are linked to AD. These observations in the APP/Tau mouse model suggest its suitability for investigating the effects of therapeutic interventions.

In conclusion, advancements in models for AD and its pathophysiology, along with the ever-expanding search for new therapeutic molecules have paved the way for researchers to develop innovative strategies that depart from conventional treatments for Alzheimer's disease.

# HYPOTHESIS AND OBJECTIVES

## 1. Hypothesis

The systemic administration of recombinant human sKL may be a potential therapeutic approach for Alzheimer's disease, counteracting cognitive deficits. Furthermore, the generation of a novel chimeric chronokine by combining three proteins, named HEBE, could hold promise for enhanced efficacy for the treatment of Alzheimer's disease.

## 2. Objectives

1. To produce a biologically active recombinant human sKL protein *in vitro.*

2. To assess the impact of systemic administration of recombinant sKL on cognitive impairment in a mouse model of Alzheimer's disease.

3. To generate a bioinformatic model for HEBE and assess its stability and biological activity *in vitro.*

4. To produce HEBE-expressing AAV vectors and evaluate their therapeutic potential in a mouse model of Alzheimer's disease.

5. To explore and enhance the features of HEBE based on findings and needs identified during the project's development.

# MATERIALS AND METHODS

# 1. Materials

## 1.1. Animals

The APP/Tau mouse model of Alzheimer's disease was generated by Dr Carlos Saura's group (UAB, Spain). APP/Tau transgenic mice and non-transgenic control littermates (WT) were obtained by crossing heterozygous $APP_{Sw,Ind}$ (J9 line, C57BL/6) [313] and Tau P301S (PS19 line, C57BL/6) [314] mice expressing the familial AD-linked K670N/M671L and V717F APP, plus frontotemporal dementia-linked P301S Tau mutations. Our own APP/Tau colony was maintained after Dr Carlos Saura's group kindly provided us with breeder mice.

## 1.2. Plasmids and viral vectors

The general and backbone plasmid vectors used for the thesis were the following: pTG6600 [315], pKP1.4ΔCMV [315,316], pXX6 [279], pRep2Cap9, pRep2Cap9P31, pGG2, pGG2-Null, pGG2-eGFP, pGV, pGVΔCMV.

The plasmid vectors generated in this thesis are represented in Table 3, with the human isoforms of each protein.

Table 3. Plasmid vectors generated in the thesis.

| Plasmid vector | Description |
|---|---|
| pGG2-HEBE | HEBE-expressing vector for AAV production |
| pTG6600-HEBE | HEBE-expressing shuttle vector for Ad production |
| pTG6600-HEBE-His | HEBE-His-expressing shuttle vector for Ad production |
| pKP1.4ΔCMV-HEBE-His | HEBE-His-expressing vector for Ad production |
| pGV-CBh-HEBE2 | HEBE2-expressing vector for AAV production |
| pGV-sKL | sKL-expressing vector for AAV production |
| pTG6600-sKL | sKL-expressing shuttle vector for Ad production |
| pTG6600-sKL-His | sKL-His-expressing shuttle vector for Ad production |
| pKP1.4ΔCMV-sKL-His | sKL-His-expressing vector for Ad production |
| pGV-sTREM2 | sTREM2-expressing vector for AAV production |
| pTG6600-sTREM2 | sTREM2-expressing shuttle vector for Ad production |
| pTG6600-sTREM2-His | sTREM2-His-expressing shuttle vector for Ad production |
| pKP1.4ΔCMV-sTREM2-His | sTREM2-His-expressing vector for Ad production |

| | |
|---|---|
| pGV-TIMP2 | TIMP2-expressing vector for AAV production |
| pTG6600-TIMP2 | TIMP2-expressing shuttle vector for Ad production |
| pTG6600-TIMP2-His | TIMP2-His-expressing shuttle vector for Ad production |
| pKP1.4ΔCMV-TIMP2-His | TIMP2-His-expressing vector for Ad production |

Adenoviral vectors and adeno-associated viral vectors were generated in this thesis, represented in Table 4.

Table 4. Viral vectors generated in the thesis.

| Viral vector | Description |
|---|---|
| Ad5-sKL-His | Adenovirus for recombinant sKL production |
| Ad5-sTREM2-His | Adenovirus for recombinant sTREM2 production |
| Ad5-TIMP2-His | Adenovirus for recombinant TIMP2 production |
| Ad5-HEBE-His | Adenovirus for recombinant HEBE production |
| AAV9P31-Null | Control AAV vector for *in vivo* experiment |
| AAV9P31-HEBE | HEBE-expressing AAV vector for *in vivo* experiment |
| AAV9-eGFP | eGFP-expressing AAV9 vector for setup experiment |
| AAV9P31-eGFP | eGFP-expressing AAV9P31 vector for setup experiment |

### 1.3. Cell lines

Various cell lines were employed in this thesis, each serving specific experimental objectives.

Two clones derived from HEK293 were used, a human embryonic kidney immortalized cell line, which contains the adenovirus' E1 region (early 1), necessary for AAV production. HEK293-AAV (Strategene) cells were used for AAV vector production, while HEK293-QB (Q-Biogene) were used for adenoviral vector production and *in vitro* studies.

BV2 cells are microglial cells derived from C57BL/6 mice (CLS 305156), used to test the phagocytic activity in the present thesis.

The CHO cell line is derived from Chinese hamster ovary cells. A clone of this cell line expressing the CAR receptor (CHO-CAR) was used for recombinant protein production.

## 1.4. Bacterial strains

Chemically competent *E. coli* bacteria were used. The TOP10R (Invitrogen) strain was used to obtain a high number of plasmid copies, and the BJ5183R (Stratagene) strain was used to perform the homologous recombination cloning procedures.

## 1.5. Oligonucleotides

### 1.5.1. Primers for mice genotyping

Table 5. Primer pairs used for mice genotyping, for each transgene and the housekeeping.

| Primer name | Forward primer | Reverse primer |
|---|---|---|
| **APP** | 5'-CGTGAGTTTGTAAGTGATGCC-3' | 5'-TCTTCTTCTTCCACCTCAGC-3' |
| **Tau** | 5'-GGCATCTCAGCAATGTCTCC-3' | 5'-GGTATTAGCCTATGGGGGACAC-3' |
| **oIMR1544** | 5'-CAAATGTTGCTTGTCTGGTG-3' | 5'-GTCAGTCGAGTGCACAGTTT-3' |

### 1.5.2. Primers for qPCR analysis

Table 6. Primer pairs used for qPCR analysis of viral genomes and transgene expression levels.

| Gene | Forward primer | Reverse primer |
|---|---|---|
| ***HEBE*** | 5'-AATGGCTTCCCTCCTTTACC-3' | 5'-CTCGAAGCATTAACCCTCACT-3' |
| ***Gapdh*** | 5'-AGGTCGGTGTGAACGGATTTG-3' | 5'-TGTAGACCATGTAGTTGAGGTC-3' |
| ***CycB*** | 5'-TCAACCTCTCCTCTCCTGCC-3' | 5'-GGTTTCTCCACTTCGATCTTGC-3' |

### 1.5.3. TaqMan sets for gene expression analysis

Table 7. TaqMan probes used for gene expression analyses.

| Gene | Identification | Reference | Manufacturer |
|---|---|---|---|
| ***Gapdh*** | Mm99999915_g1 | 4331182 | ThermoFisher |
| ***Rpl7*** | Mm02342562_gH | 4331182 | ThermoFisher |
| ***Slc17a7*** | Mm00812886_m1 | 4331182 | ThermoFisher |
| ***Homer1*** | Mm00516275_m1 | 4331182 | ThermoFisher |
| ***Foxo3*** | Mm01185722_m1 | 4331182 | ThermoFisher |
| ***Def8*** | Mm00459823_m1 | 4331182 | ThermoFisher |

Fluorophore: FAM; quencher: MGB

# 2. Methods

## 2.1. Transgenic mice genotyping

### 2.1.1. Genomic DNA extraction

Mice were genotyped using genomic DNA extracted from tail biopsies. Tail biopsies were incubated in Eppendorf tubes with 200 μL of 50 mM NaOH (Panreac) at 55 °C for 3 h. Samples were then vortexed until complete homogenization and centrifuged at 12000 g for 10 min, and the supernatants containing the DNA were transferred to new tubes. Samples were stored at -20 °C until the genotyping.

### 2.1.2. Transgene detection by PCR

A single PCR reaction was used for the detection of both transgenes and the reference gene, using the primers indicated in Table 5. PCR reactions of a volume of 25 μL contained 2 μL of genomic DNA solution, 0.5 mM of each primer, 25 mM of dNTPs (ThermoScientific), 10x Taq buffer including $MgCl_2$ (ThermoScientific), 5 U/μL DreamTaq Polymerase (ThermoScientific) and MiliQ water (Braun). PCR reactions were performed in a thermocycler as follows: 94 °C for 4 min, followed by 40 cycles of 94 °C for 1 min, 60 °C for 1 min, and 72 °C for 1 min.

PCR products were run on a 2% agarose electrophoresis gel, using 15 μL of product and 1.66 μL of Xylene Cyanol loading buffer. The gel was run for 1 h at 120 V, and amplicons were visualized using a UV transilluminator (Syngene).

## 2.2. Plasmid vector generation

### 2.2.1. Digestions with restriction enzymes

Plasmid DNA enzymatic digestions were performed in an aqueous medium, in a final volume of 20 μL containing 2-10 enzymatic units per 1 μg of DNA (Fermentas or New England Biolabs). Both the temperature and necessary buffer were stablished by the manufacturer. Digestion times varied between 2-18 h depending on enzymatic units, DNA quantity and enzyme type.

### 2.2.2. Cloning

The aim of this technique was to unite two plasmid DNA fragments to obtain a DNA molecule capable of autonomous replication within a bacterial cell.

#### 2.2.2.1. Ligation

To prevent vector religation, dephosphorylation was performed using FastAP phosphatase (Fermentas). Dephosphorylation involved adding 1 μL of enzyme to the vector and incubating for 1 h at 37 °C, followed by inactivation for 5 min at 75 °C. Ligation reactions were then carried out using T4DNA ligase (New England Biolabs), with 50 ng of vector per reaction. Various conditions were performed, including one with an excess of insert (1:3), and a condition without insert (1:0) as a control of the background. Ligation reactions were incubated O/N at 16 °C. The products of the ligation were transformed into *E. coli* TOP10 bacteria for DNA extraction and ligation verification.

#### 2.2.2.2. Homologous recombination

This technique was used for the generation of plasmid vectors for Ad production, given that the pKP plasmid's big size renders traditional ligation techniques inefficient. First, the pKP1.4ΔCMV was linearized using the SwaI enzyme, while the shuttle vector pTG600 carrying the gene of interest was digested with enzymes that have targets outside the recombination sequence. For the recombination reaction, 50 ng of the pKP1.4ΔCMV plasmid was used, with an excess of insert (1:2). This mixture was transformed into *E. coli* BJ5183 bacteria, DNA from isolated colonies was extracted and the size of the DNA was analyzed without any digestions. Colonies exhibiting larger DNA sizes were presumed positive and their DNA was transformed into TOP10 bacteria to yield increased DNA quantities. This DNA was then subjected to enzymatic digestions to confirm successful cloning.

#### 2.2.2.3. Overlapping PCR

This technique was used to introduce a small polyhistidine tag into the plasmids to facilitate protein purification. The process consisted of two steps (Fig. 17).

In the first step, a PCR was performed with specific primers to obtain a megaprimer. The forward primer was a conventional primer that overlapped with the 3' end of the gene of interest (GOI). The reverse primer, however, overlapped with the gene of interest's end and a segment of the plasmid backbone, incorporating a sequence encoding the polyhistidine tag in between. The reaction was prepared as follows: 10 ng of the pTG600-GOI plasmid, 25 μM of each primer, 0.2 μM of dNTPs (ThermoScientific), 0.02 U/μL of Q5 DNA polymerase (New England Biolabs), 1x reaction buffer in a final volume of 50 μL. PCR reactions were performed in a thermocycler as follows: 98 °C for 30 s, followed by 30 cycles of 98 °C for 15 s, 58 °C for 20 s and 72 °C for 30 s/kb. The resulting 400-600 bp megaprimer was run in an agarose gel, and the band was purified.

Then, this megaprimer was used for the generation of the final plasmid, where the plasmid was amplified introducing the polyhistidine tag. The reaction was prepared as follows: 10 ng of the pTG600-GOI plasmid, 0.2 μM of dNTPs (ThermoScientific), 0.02 U/μL of Q5 DNA polymerase (New England Biolabs), 500 equimolar concentration of megaprimer relative to the plasmid, 1x reaction buffer in a final volume of 25 μL. PCR reactions were performed in a thermocycler as follows: 98 °C for 2 min, followed by 30 cycles of 98 °C for 30 s, 50 °C for 1 min and 72 °C for 90 s/kb. The PCR product was digested with DpnI (New England Biolabs) to degrade the initial plasmid that was methylated, and the product was then transformed into TOP10 bacterial cells for plasmid amplification and verification.

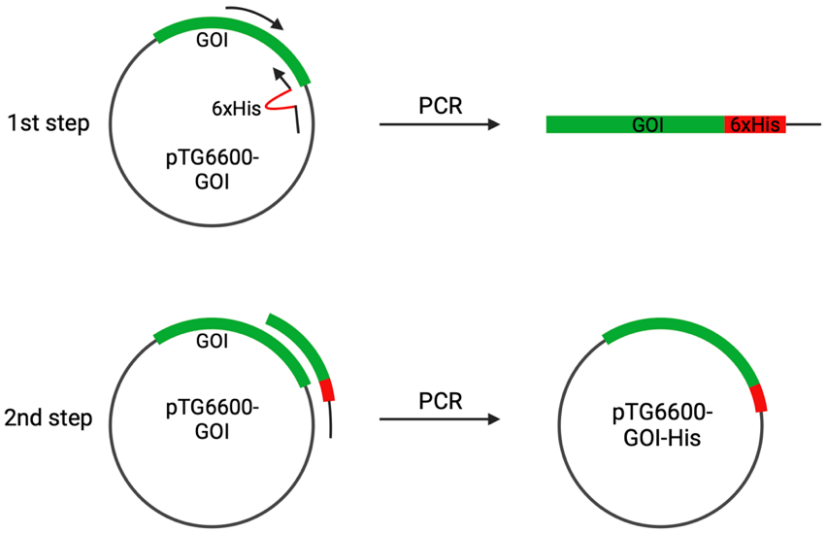



Figure 17. Schematic representation of the overlapping PCR cloning. In the first step, the megaprimer is generated and purified, which is used in the second step to generate the plasmid with the insertion.

### 2.2.3. Transformation of chemically competent bacteria

Transformation is the process through which chemically competent bacteria internalize plasmid DNA via the heat shock method. A vial of chemically competent bacteria was thawed on ice for 10 min, and 7 μL of a minipreparation or ligation was added. Bacteria were incubated with the DNA on ice for 20 min, followed by a heat shock for 90 s at 42 °C. The vials were then immediately placed on ice for 2 min, and 500 μL of LB (Conda) without antibiotics was added. Bacteria were incubated for 1 h at 37 °C to allow for growth. Then, the bacteria were plated onto LB-agar (Panreac) plates (Nunc) with ampicillin (USB) to select for plasmid-carrying bacteria. Plates were incubated O/N at 37 °C to facilitate colony growth.

## 2.3. DNA obtention and analysis

### 2.3.1. DNA minipreps

This technique is used for the obtention of plasmid DNA via alkaline lysis of a bacterial culture, and subsequent precipitation with isopropanol. 3 mL of selective media inoculated with isolated bacterial colonies grown on LB-agar plates with antibiotic was used. This technique yields low amounts of plasmid DNA (<15 μg) and of low purity, although enough for enzymatic digestions.

The 3 mL of bacterial cultures were centrifuged for 1 min at 12000 g, supernatants were discarded, and pellets were resuspended in 200 μL of solution I. Then, 400 μL of solution II was added for lysis, and tubes were incubated for 5 min at RT. The pH was neutralized by adding 200 μL of solution III and mixing. Samples were incubated on ice for 10 min, followed by centrifugation for 10 min at 12000 g. The supernatants were transferred to new tubes, and 0.6 volumes of isopropanol (Panreac) was added for DNA precipitation, with a 10 min incubation. Samples were centrifuged for 10 min at 12000 g and supernatants were discarded. The DNA pellets were washed with 70% EtOH (Panreac) and allowed to dry. Finally, the pellets were resuspended in 30 μL of MiliQ water with RNase (Sigma).

Solution I: 50 mM Tris-HCl (Sigma) pH 8, 10 mM EDTA (USB)
Solution II: 200 mM NaOH (Panreac), 1% SDS (USB)
Solution III: 3 M KAc (Panreac) pH 5.5

### 2.3.2. DNA maxipreps

This technique enables the extraction of large amounts of pure plasmid DNA (~1000 μg) from bacterial cultures, suitable for cloning or transfection into cell lines. The HiPure PureLink (Invitrogen) kit was used following manufacturer's instructions, after transformed bacteria had been growing in 250 mL of LB with antibiotics O/N at 37 °C.

### 2.3.3. Tissue DNA extraction

DNA from brain and liver tissues was extracted using the QIAamp DNA Mini Kit (Qiagen), following the manufacturer's instructions.

### 2.3.4. Electrophoresis in agarose gel

Agarose gels were prepared by dissolving agarose (Amresco) in TAE 1x in a microwave to a final concentration of 1% or 2% (w/v). After agarose was dissolved, the solution was cooled and RedSafe Nucleic Acid Staining Solution 20000x (iNtRON) was added for DNA visualization. After the gel polymerized in a gel tray (BioRad), it was placed in an electrophoresis cuvette. The gel was covered by TAE 1x, and samples were loaded with loading buffer 10x. Depending on the DNA fragment size, GeneRuler 1 kb or 100 bp

(ThermoFisher Scientific) was loaded. Electrophoresis was conducted at 100 V for 60 min, followed by visualization under a UV transilluminator (Syngene). Gel images were analyzed using GeneSnap software (Syngene).

TAE 1X: 40 mM Tris-acetate pH 8, 0.1 mM EDTA (Calbiochem)
Loading buffer 10x: 50% glycerol (Panreac), 100 mM EDTA pH 8 (USB), 1% SDS (USB) and 0.1% Bromophenol Blue (Sigma) or Xylene Cyanol (Sigma).

#### 2.3.5. DNA purification from agarose gel

DNA purification from agarose gel bands was performed using the Wizard SV and PCR Clean-Up System (Promega) commercial kit, following the manufacturer's protocol.

#### 2.3.6. DNA quantification

DNA obtained through different procedures was quantified in a NanoDrop (NanoDrop Technologies) at a 260 nm wavelength. This system facilitated determination of DNA concentration, as well as the purity by measuring absorbance at 280 nm.

#### 2.3.7. DNA sequencing

For plasmid verification, Sanger sequencing was performed by the Genomics and Bioinformatics service in the Biotechnology and Biomedicine Institute (IBB, Bellaterra).

### 2.4. RNA obtention and analysis

#### 2.4.1. Tissue RNA isolation

To prevent RNA degradation, RNase-free conditions were ensured by cleaning surfaces and materials with EtOH 70% and RNaseZap (Ambion). RNAse-free solutions and filter tips were used, and samples were kept on ice.

##### 2.4.1.1. Brain

Tissue samples were homogenized by sonication using the ultrasonic processor (Vibra-cell, Sonics & Material Inc) at 40 Hz and three pulses of 10 s, while maintaining samples on ice to prevent RNA degradation. RNA was then isolated using the RNeasy Plus Mini Kit (Qiagen) following manufacturer's instructions.

#### 2.4.1.2. Liver

QIAzol (Qiagen) was added to samples at a ratio of 1 mL per 100 mg of tissue, followed by sonication using the ultrasonic processor at 40 Hz and three pulses of 10 s. Homogenates were then centrifuged at 12000 g for 10 min at 4 °C, and supernatants were transferred to new tubes. After an incubation of 5 min at RT, chloroform (Panreac) was added at a 0.2 mL/mL QIAzol ratio, and after vortexing and an incubation of 3 min at RT, samples were centrifuged at 12000 g for 10 min at 4 °C. The aqueous phase was recovered, and isopropanol (Panreac) was added at a 0.5 mL/mL QIAzol ratio. After a 10 min incubation at RT, samples were centrifuged at 12000 g for 10 min at 4 °C for RNA precipitation. After discarding the supernatants, RNA pellets were washed with 75% EtOH (Panreac) (1 mL/mL QIAzol) and centrifuged for 5 min. The dry RNA pellets were then resuspended in 20 μL of MiliQ water, quantified, and stored at -80 °C.

### 2.4.2. RNA quantification

RNA concentration was determined using the NanoDrop (NanoDrop Technologies) by measuring the optical density at a 260 nm wavelength. Purity was also assessed measuring absorbance at 280 and 230 nm.

### 2.4.3. DNase treatment and reverse transcription

RNA samples were treated with DNaseI (Sigma) to prevent genomic DNA amplification, especially in samples where viral expression was assessed, as the cDNA of the transgene has the same sequence as the viral genome. 1 μg of RNA was incubated with 1 U of DNaseI at 37 °C for 30 min. The enzyme was then inactivated by incubation at 65 °C for 10 min in the presence of 50 mM EDTA. The reverse transcription to obtain cDNA was done using the SensiFAST cDNA Synthesis Kit (Bioline), following the manufacturer's instructions.

### 2.4.4. Real-Time quantitative PCR (qPCR)

The qPCR technique allows to detect differences in mRNA expression among samples. Two fluorescent probes were used in this thesis, depending on the aim of the expression study.

#### 2.4.4.1. qPCR with SybrGreen

SybrGreen, a dsDNA-binding molecule, emits fluorescence during strand elongation in the thermocycler, proportional to the initial cDNA quantity. This technique was used to evaluate the presence and expression of the viral vector.

Reactions were prepared with 50 ng of cDNA, 5 μL of iTaq Universal SYBR Green Supermix (BioRad), 0.3 mM of each oligonucleotide and MiliQ water to a final volume of 10 μL. A Hard-Shell Whin-Wall 384-Well Skirted PCR plate (BioRad) was filled with samples and sealed with Microseal Adhesive Seal (BioRad). Each sample was analyzed in triplicates using the specific oligonucleotide pair for each gene (Table 6). The program used in the CFX384 Thermocycler (BioRad) was the same in all cases: 2 min at 98 °C for polymerase activation and cDNA denaturation, followed by 40 cycles of 5 s at 95 °C for denaturation and 30 s at 58 °C for annealing and extension.

#### 2.4.4.2. qPCR with TaqMan probes

TaqMan probes consist of two oligonucleotides that act as primers for the amplification, and a probe that contains a fluorophore covalently linked to the 5' end and a quencher in the 3'. This technology is based on the Taq polymerase's exonuclease activity that releases the fluorophore from the probe that is hybridized to the target sequence. The advantage of these probes is their high specificity of detection, for which they were used for gene expression analyses.

Reactions were prepared with 50 ng of cDNA, 0.5 μL of the TaqMan probe (Invitrogen, table 7), 5 μL of SensiFast Probe No-ROX Kit (Bioline), and MiliQ water to a final volume of 10 μL. A Hard-Shell Whin-Wall 384-Well Skirted PCR plate (BioRad) was filled with triplicates and sealed with Microseal Adhesive Seal (BioRad). Reactions were performed in the CFX384 Thermocycler (BioRad) with the following program: 5 min at 95 °C followed by 40 cycles of 15 s at 95 °C for denaturation and 1 min at 60 °C for annealing and elongation.

### 2.4.5. qPCR data analysis

For each reaction, the cycle threshold (Cq) was measured and used for gene expression quantification. Replicates exhibiting a Cq difference greater than 1 were considered outliers. The gene expression quantification relative to two reference genes was calculated using the Hellemans' quantification model [317].

### 2.4.6. RNA-seq

RNA-seq analysis was performed by BGI Genomics with RNA samples from mouse hippocampus and entorhinal cortex. Data was analyzed using the Dr. Tom platform provided by BGI.

## 2.5. Protein obtention and analysis

### 2.5.1. Protein extraction

This technique was used to extract total proteins from cell cultures. The cell pellet was resuspended in 100 µL of RIPA and homogenized by sonication using the ultrasonic processor (Vibra-cell, Sonics & Material Inc) at 40 Hz and three pulses of 10 s, while maintaining samples on ice to prevent protein degradation. Samples were then centrifuged for 15 min at 12000 g and 4 °C to eliminate cell debris, and resulting supernatants were transferred to new tubes and stored at -80 °C.

RIPA: 50 mM Tris-HCl (Sigma) pH 7.4, 150 mM NaCl (Panreac), 1 mM EDTA (USB), 1% NP-40 (Panreac), 0.25% sodium deoxycholate (Sigma), 50 mM NaF (Sigma), 1 mM sodium ortovanadate (Sigma), 10 mM Na-beta glycerophosphate (Sigma), 5 mM sodium pyrophosphate, protease inhibitors (Calbiochem).

### 2.5.2. Protein quantification

Protein concentrations in the extracts were determined using the Pierce BCA Protein Assay Kit (Thermo Scientific), based on the chelating capacity of the bicinchoninic acid (BCA) with the $Cu^{+}$ ions resulting from the reduction of $Cu^{2+}$ to $Cu^{+}$ by the peptide bonds of proteins in an alkaline medium, known as Biuret reaction. This reaction produces a water-soluble complex that exhibits absorbance at 562 nm.

A standard curve consisting of serial dilutions of Bovine Serum Albumin (BSA) was used, ranging from 0.625 mg/mL to 2 mg/mL. Samples were also diluted, normally a 1/10 dilution, and all samples were mixed with the working solution provided in the kit. The reaction was incubated for 30 min at 37 °C, and the absorbance at 562 nm was measured in a Spark plate reader (Tecan). Total protein concentrations in each sample were calculated by interpolating the absorbance values on the standard curve.

### 2.5.3. Denaturing electrophoresis (SDS-PAGE)

This technique is based on the migration capacity of charged proteins when an electric field is applied. The presence of an anionic detergent like SDS makes proteins denature, allowing them to migrate according to their molecular weight.

A resolving gel was prepared with a 10% acrylamide concentration (Amresco) in resolving buffer, and a stacking gel with a 3.9% acrylamide concentration in stacking buffer. For gel polymerization, APS (Amresco) and TEMED (Sigma) were added. Protein extracts were diluted in MiliQ water and loading buffer to a final concentration of 1x to obtain 30 μg of diluted protein, and samples were incubated for 10 min at 98 °C for denaturation. The polymerized gel was placed in the electrophoresis chamber Mini Protean Tetra Cell (BioRad) and filled with electrophoresis buffer. Samples and the molecular weight marker Page-Ruler Pre-stained Protein Ladder (Fermentas) were loaded into the stacking gel, and the following voltage program was applied: 25 min at 100 V for proteins to concentrate before entering the resolving gel, and 1 h at 130 V for proteins to migrate and separate according to their molecular weight.

Resolving buffer: 1.5 M Tris-HCl (Sigma) pH 8.8, 0.4% SDS (USB)
Stacking buffer: 0.5 M Tris-HCl (Sigma) pH 6.8, 0.4% SDS (USB)
Loading buffer 5x: 20% glycerol (Panreac), 10% SDS, 0.32% 2-β-mercaptoethanol (Sigma), 0.02% bromophenol blue (Sigma)
Electrophoresis buffer: 25 mM Tris-HCl, 192 mM glycine (Serva), 1% SDS (USB)

### 2.5.4. Transference

The proteins in the acrylamide gel were transferred onto a previously activated PVDF membrane (GE Healthcare) with 10 s in methanol (Panreac), 5 min in distilled water and 15 min in transference buffer. The acrylamide gel was also equilibrated in transference buffer for 15 min, as well as the two Extra Thick Wester Blotting Filter Papers (Thermo Scientific). The order of the layers for the transference from bottom to top was as follows: paper, membrane, gel, and paper. The transference was carried out for 45 min at 25 V in the Transblot Turbo Transfer Cell (Bio Rad).

Transference buffer: 25 mM Tris (Sigma), 190 mM glycine (Serva), 20% methanol (Panreac)

### 2.5.5. Immunodetection

The transferred membrane was blocked by submersion in blocking solution for 1 h at RT in constant shaking to prevent non-specific bindings of primary antibodies. Next, 5 mL of primary antibody solution in blocking buffer was added, and the membrane was incubated O/N at 4 °C with agitation (Table 8). The following day, the membrane was washed three times in TBS-T for 10 min, and the secondary antibody diluted in blocking buffer was added and incubated for 1 h at RT. After three washes in TBS-T protein detection was carried out. The luminol and peroxidase substrates provided in the Westar Eta C Ultra 2.0 Western-Blot kit (Cyanagen) were mixed, and the membrane was covered with this mixture for 90 s in the dark. The luminol reacted with the secondary antibody's peroxidase emitting light that can be detected by the ChemiDoc chemiluminescence system (BioRad).

Table 8. Antibodies used for immunodetection.

| Primary antibody | Reference | Manufacturer | Dilution | Secondary antibody |
|---|---|---|---|---|
| **sKL** | MABN1807 | Sigma | 1/1000 | Rat[1] |
| **TREM2** | AF1828 | R&D Systems | 1/1000 | Goat[2] |
| **TIMP2** | AF971 | R&D Systems | 1/1000 | Goat[2] |
| **His** | Ab18184 | Abcam | 1/1000 | Mouse[3] |

[1]Sheep anti-rat Ig HRP (PA1-28642, Thermofisher) [2]Rabbit anti-goat Ig HRP (P0160, Dako) [3]Goat anti-mouse Ig HRP (31430, Thermofisher)

TBS-T buffer: 50 mM Tris (Sigma) pH 7.5, 136 mM NaCl (Panreac), 40 mM KCl (Panreac), 0.1% Tween20 (Sigma)

Blocking solution: TBS-T, 5% BSA

### 2.5.6. sKL quantification through ELISA

The soluble α-Klotho ELISA (Tecan JP27998) was used to quantify human sKL in mouse serum samples, following the manufacturer's instructions.

### 2.5.7. sKL half-life determination

Recombinant sKL was administered to mice at a dose of 50 µg/kg, either intravenously or intraperitoneally. Blood samples were collected at specified time points, as indicated in the results section, and the previously described ELISA was used for sKL quantification. Concentration data were plotted, and the pseudo-equilibrium phase was identified, representing the phase where the decrease in protein concentration is attributed to drug elimination rather than plasma clearance. Concentrations during this pseudo-equilibrium phase were represented on a logarithmic scale, and the following equation was used for the determination of the protein's terminal half-life [318]:

$$t_{1/2} = \frac{0.693}{\lambda_z}$$

where 0.693 is the natural logarithm of 2 and $\lambda_z$ is the slope of the terminal phase.

## 2.6. Cell culture techniques

General equipment: vertical laminar flow cabinet (Telstar), $CO_2$ cell incubator (Forma Scientific) with controlled atmosphere (5% $CO_2$, 95% $O_2$, 95% relative humidity and 37 °C), -80°C freezer (Forma Scientific).

Fungible material: Plastic sterile pipettes (Cultek), 10 and 15 cm culture dishes, 6, 12, 48 and 96 well plates, 15 and 50 mL conical tubes (Falcon), cryotubes (Corning), scrappers (Biologix).

### 2.6.1. HEK293 cell line

#### 2.6.1.1. Cell line maintenance

Maintenance of the cell line was done in 15 cm dishes. First, cells were resuspended in their own medium by mechanic action with the pipette and were then transferred to a Falcon tube. Cells were centrifuged at 200 g for 5 min, the supernatant was discarded, and the cell pellet was resuspended in an appropriate volume for the desired passage. One 15 cm dish with 16 mL of growth medium was seeded and incubated until further use.

Growth medium: Dulbecco's modified Eagle's medium (DMEM) with high glucose (4.5 mg/mL) (Lonza), supplemented with 10% fetal bovine serum (FBS) (Sigma) and 1% penicillin/streptomycin (P/S) (Sigma).

#### 2.6.1.2. Plasmid DNA introduction through transfection

At the time of transfection, cells should be at around 60-70% confluence. Transfections were typically carried out in 6-well plates, using 3 µg of plasmid dissolved in 200 µL of 0.9% NaCl (B.Braun). In a separate tube, 2.25 µL of polyethylenimine (PEI) (Sigma) per µg of DNA was diluted in 200 µL of NaCl. The DNA dilution was slowly mixed with the PEI solution and left at RT for 20 min to form the DNA/PEI complexes. Then, the growth medium from each plate well was discarded and 500 µL of transfection medium was added, along with 240 µL of the DNA/PEI mixture. Plates were incubated at 37 °C and 5% $CO_2$ for 3 h, the medium was discarded, and 3 mL of fresh growth medium was added.

Transfection medium: DMEM (Lonza), 1% FBS (Sigma), 1% P/S (Sigma)

### 2.6.2. CHO cell line

#### 2.6.2.1. Cell line maintenance

Maintenance of the cell line was done in 15 cm dishes. First, the medium was discarded, and cells were washed with PBS. After discarding the PBS, 3 mL of trypsin-EDTA (Sigma) was added, and the dish was incubated at 37 °C for 4 min. Then, 7 mL of growth medium was added for trypsin inactivation and cells were transferred to a Falcon tube. Cells were centrifuged at 200 g for 5 min, the supernatant was discarded, and the cell pellet was

resuspended in an appropriate volume for the desired passage. One 15 cm dish with 16 mL of growth medium was seeded and incubated until further use.

Growth medium: DMEM/F-12 (Gibco), 10% FBS (Sigma), 1% P/S (Sigma)

### 2.6.3. BV2 cell line

#### 2.6.3.1. Cell line maintenance

Maintenance of the cell line was done in 10 cm dishes. First, cells were resuspended in their own medium by mechanic action with the pipette and were then transferred to a Falcon tube. Cells were centrifuged at 200 g for 5 min, the supernatant was discarded, and the cell pellet was resuspended in an appropriate volume for the desired passage. One 10 cm dish with 7 mL of growth medium was seeded and incubated until further use.

Growth medium: DMEM (Lonza), 10% FBS (Sigma), 1% P/S (Sigma)

#### 2.6.3.2. Cell counting

Cell counting was performed using a Neubauer chamber to determine the appropriate seeding density for the phagocytosis assay. A volume of 10 µL of cells in suspension was loaded into the chamber, and the number of cells in the outer four squares was counted manually in a microscope, obtaining the concentration as cells/mL.

## 2.7. Viral vectors

### 2.7.1. AAV vector production and purification

#### 2.7.1.1. AAV production through triple transfection

The AAV production was performed following the triple transfection protocol [279], in which each plasmid serves a specific function: pRepCap expresses the necessary proteins for viral replication and provides the capsid proteins, pXX6 provides the adenoviral genes necessary for AAV replication, and lastly, the pGV or pGG2 plasmid contains the viral ITR sequences and the transgene.

Sixty HEK293-AAV dishes at a 70% confluence were used for the transfection. The growth medium was discarded, and 12 mL of transfection medium was added to each dish. The DNA solution was prepared with 25 µg of pXX6, 12.5 µg of pRepCap and 12.5 µg of the transgene plasmid per dish in a final volume of 1 mL of 0.9% NaCl (B.Braun) per dish. Simultaneously, the PEI solution (Sigma) was prepared at a ratio of 2.25 µL per µg of DNA in 1 mL of 0.9% NaCl (B.Braun). The DNA solution was mixed with the PEI solution and left at RT for 20 min to form the DNA/PEI complexes. Then, 2 mL of the mixture was added to each cell dish, and dishes were incubated at 37 °C and 5% $CO_2$ for 6 h. After this time, a medium change was performed to add fresh growth medium. Cells were harvested using a scrapper 48 h post-transfection, and centrifuged for 15 min at 200 g. The supernatant was separated for purification, and cells were resuspended in a final volume of 60 mL of lysis buffer. The supernatant was stored at -20 °C and cells at -80 °C until purification.

Growth medium: DMEM (Lonza), 10% FBS (Sigma), 1% P/S (Sigma)
Transfection medium: DMEM (Lonza), 1% FBS (Sigma), 1% P/S (Sigma)
Lysis buffer: 50 mM Tris (Sigma), 20 mM NaCl (Panreac), 2 mM $MgCl_2$ (Panreac)

#### 2.7.1.2. AAV purification through iodixanol gradient

The protocol was based on precipitation of viral particles, followed by an iodixanol gradient (non-ionic inert medium). During the production, AAV vectors are partially released to the supernatant, so the cells and the supernatant need to be purified separately.

First, three freeze-thaw cycles were performed to release the viral particles from cells, and cell debris was discarded after a 10 min centrifugation at 2000 g. The supernatant was recovered, 6 µL of benzonase nuclease (50 U/mL) (Merck) was added to degrade DNA and RNA outside of viral capsids, and it was incubated for 1 h at 37 °C. Then, it was centrifuged for 20 min at 3000 g and the supernatant was recovered, to which PEG 40% (Sigma) was added at a ratio of 1 mL/4mL lysate, and 5 M NaCl at a ratio of 36.7 µL/mL of lysate. This way, the precipitation of viral particles occurred O/N at 4 °C. The viral precipitate was centrifuged for 15 min at 8000 g and 4 °C, and then resuspended in 5 mL of lysis buffer.

The supernatant of the production was also processed, adding PEG 40% and 5 M NaCl at the same proportion as for the lysate, to precipitate the viral particles O/N at 4 °C. The next day, it was centrifuged for 30 min at 3000 g and 4 °C, the supernatant was discarded, and the pellet was resuspended in 5 mL of lysis buffer. Then, 1 µL of benzonase (50 U/mL) was added and incubated for 1 h at 37 °C. Finally, the 5 mL of this resuspension and the 5 mL of resuspension from the cell pellet were mixed for them to be purified together in an iodixanol gradient.

For gradient preparation, the following iodixanol (Axis-Shield) concentrations were used: 15% (in PBSMK-NaCl), 25% (in PBSMK with 20 µL of phenol red (Sigma)), 40% (in PBSMK) and 60% (in PBSMK with 2 µL of phenol red). The different solutions were placed on an ultracentrifuge tube (Optiseal Polypropilene Tube, Beckman), from the less dense to the densest, crossing the previously placed solution. Finally, the viral solution was placed above the iodixanol solutions. The tube was centrifuged at 55000 rpm in a 70Ti Beckman rotor for 2 h at 18 °C, and viral fractions were collected after perforation of the bottom of the tube (Fig 18).

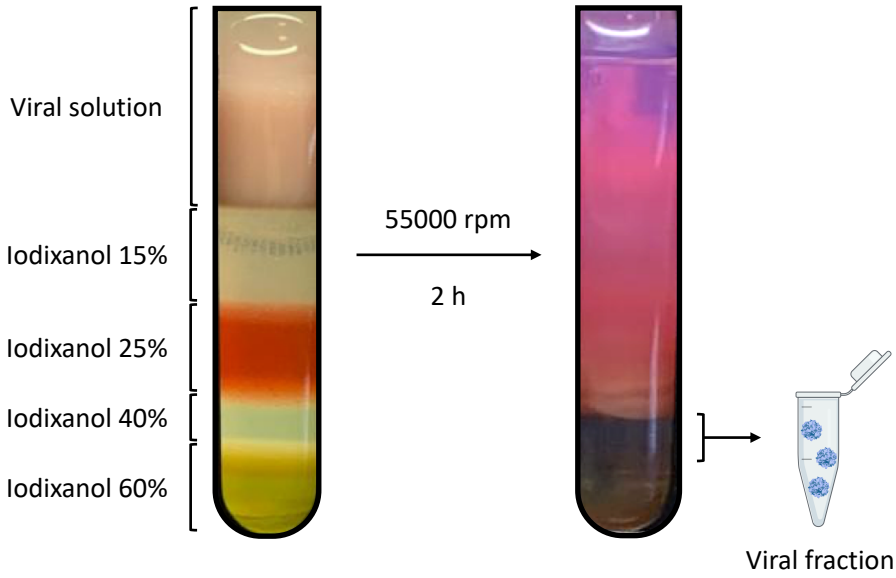



Figure 18. Iodixanol gradient for AAV purification. The picture on the left is the gradient before the ultracentrifugation, and the picture on the right is the gradient after the ultracentrifugation, from which the viral fraction is collected.

Lysis buffer: 50 mM Tris (Sigma), 20 mM NaCl (Panreac), 2 mM $MgCl_2$ (Panreac)

PBSMK: PBS, 1 mM $MgCl_2$ (Panreac), 2.5 mM KCl (Panreac)

PBSMK-NaCl: PBSMK, 1 M NaCl (Panreac)

#### 2.7.1.3. AAV vector titration

Titration of AAV productions was performed using a molecule called picogreen (Invitrogen), which intercalates into dsDNA, enabling quantification of genomes based on fluorescence [319].

First, 2 µL of each viral fraction was diluted in 18 µL of lysis buffer and subjected to thermal lysis in a thermocycler at 70 °C for 1 h, followed by a slow decrease in temperature of 5 °C/min until reaching 25 °C. In parallel, 2 µL of each sample was also diluted in 18 µL of TE buffer, which were not lysed. Subsequently, the 20 µL of each sample was loaded into a black 96-well plate (Nunc), followed by the addition of 180 µL of a 1/600 dilution of picogreen. Additionally, a calibration curve spanning from 0 to 40 ng of DNA was included. By correlating the fluorescence values obtained from the samples with the calibration curve, the amount of DNA (ng) in each sample was determined. Viral genomes (vg) were calculated with the following equation:

$$vg = \frac{A \cdot 1.82 \cdot 10^{12}}{B}$$

**A**: ng/mL of DNA = ng in well·1000/C

**B**: AAV genome length (distance between ITRs)

**C**: µL of viral fraction analyzed

The final AAV titer was determined by subtracting the number of AAV viral genomes from the non-lysed samples from those of the lysed samples.

Lysis buffer: 20 mM Tris (Sigma) pH 7.4, 200 mM NaCl (Panreac), 0.2% SDS (USB)
TE buffer: 10 mM Tris (Sigma) pH 8, 1 mM EDTA (USB)

### 2.7.2. Adenoviral vector production and purification

The production of adenoviral vectors was based on the transfection of the linearized plasmid into HEK293-QB cells to produce a conditioned medium that was used for further amplification of the viral vectors. The viral genomes used lacked the E1 gene, which was provided in *trans* by the HEK293 cell line, producing replication-deficient adenoviral vectors.

#### 2.7.2.1. Adenoviral genome preparation for transfection

First, 100 µg of the viral genome plasmid was linearized with 50 U of PacI (New England Biolabs) in a final volume of 200 µL to remove the bacterial origin of replication and the ampicillin resistance gene. Then, the linearized plasmid was precipitated with 1/10 volumes of 3 M KAc (Panreac) and 2.5 volumes of cold ethanol (Panreac). It was incubated at -80 °C for 30 min and centrifuged at 16000 g for 25 min at 4 °C, discarding the supernatant. The precipitated plasmid was washed with 70% EtOH and left to dry at RT. Finally, the plasmid was resuspended in 100 µL of TE and incubated for 1 h at 37 °C.

TE buffer: 10 mM Tris (Sigma) pH 8, 1 mM EDTA (USB)

#### 2.7.2.2. Transfection and vector amplification

The transfection of the linearized plasmid was conducted in 6-well plates of HEK293-QB cells, following the protocol described in section 2.6.1.2. Three days post-transfection, cells were harvested, and three freeze-thaw cycles were performed to release the virus. The lysate was centrifuged for 5 min at 2000 g to remove cell debris and obtain the supernatant, which was then used to infect a 10 cm HEK293-QB dish in infection medium. Ten days after the infection, when cytopathic effect was observed, cells were harvested, and three freeze-thaw cycles were performed to release the virus. The lysate was centrifuged for 4 min at 3000 g and the supernatant was obtained. Subsequently, this supernatant was used to infect twenty 15 cm HEK293-QB dishes in infection medium, and 40 h after the infection, when cytopathic effect was observed, cells were harvested. These cells were centrifuged for 5 min at 200 g and were then resuspended in 19 mL of infection medium. Three freeze-thaw cycles were performed, and it was centrifuged for 10 min at 3000 g to obtain the supernatant for virus purification.

Infection medium: DMEM (Lonza), 2% FBS (Sigma), 1%P/S (Sigma)

#### 2.7.2.3. Purification through CsCl gradients

For the preparation of the first gradient, 10 mL of CsCl (Sigma) 1.25 mg/mL was placed in the ultracentrifugation tube (344058, Beckman). Then, 10 mL of CsCl 1.4 mg/mL was placed at the bottom of the tube, crossing the first solution. Finally, the lysate containing the virus was placed above the solutions. The tube was centrifuged in a SW32 Beckman

rotor at 32000 rpm for 1 h 42 min at 18 °C. The band corresponding to the virus was extracted through lateral perforation of the tube with a hypodermic needle. For the second gradient, 5 mL of CsCl 1.34 mg/mL was placed in the ultracentrifugation tube (331374, Beckman) and the sample obtained from the first gradient was placed above it. The tube was centrifuged in a SW40 Beckman rotor at 35000 rpm for 18 h at 18 °C. In this second gradient, empty capsids with a lower density were separated, and the band corresponding to full capsids was extracted through lateral perforation of the tube with a hypodermic needle. Finally, the CsCl was removed, as it is toxic for cells, through a Sephadex PD-10 column (Amersham Biosciences), exchanging the CsCl with PBS. Viral fractions were collected and 10% of glycerol (Sigma) was added as a cryoprotectant. Fractions were stored at -80 °C until titration (Fig. 19).

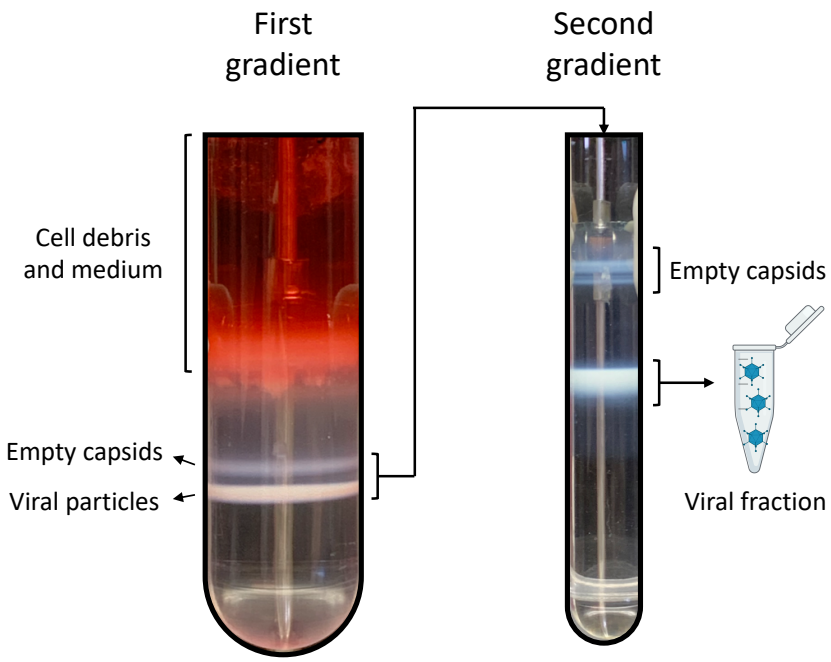



Figure 19. CsCl gradients for adenoviral purification. The picture on the left is the first gradient, from where the viral fraction is collected. The picture on the right is the second gradient, where empty and full capsids are separated, and the final viral fraction is obtained.

#### 2.7.2.4. Infective particle titration

The titration of infective adenoviral particles (IU/mL) was performed in HEK293-QB cells via a serial dilution of the virus ranging from $10^{-3}$ to $10^{-10}$, in 96-well plates and duplicates. The result of the titration was obtained using the AdEasy Viral Titer Kit (Stratagene) following manufacturer's instructions.

## 2.8. Recombinant protein production and purification

### 2.8.1. Recombinant protein production through cell line infection

For protein production, 100 CHO-CAR dishes were seeded. When cells reached approximately 80% confluence, they were infected with adenoviral vectors expressing each protein, at a multiplicity of infection (MOI) of 150 particles/cell in infection medium. The medium was removed 3 h post-infection, and fresh infection medium was added. Cell culture supernatants were harvested 72 h post-infection, centrifuged at 1000 rpm for 5 min, and supernatants were stored at -80 °C until the purification.

Infection medium: DMEM/F-12 (Gibco), 2% FBS (Sigma), 1% P/S (Sigma)

### 2.8.2. Recombinant protein purification

Supernatants containing the proteins were purified by the Protein Technologies Unit (CRG, Barcelona), using a nickel affinity chromatography. Purified proteins were aliquoted and stored at -80 °C to prevent degradation.

## 2.9. Recombinant protein activity studies

### 2.9.1. β-glucuronidase activity study

sKL (10 or 20 µg) and equimolar amounts of the other indicated proteins diluted in 0.1 M citrate buffer were incubated with 0.5 mM of substrate 4-methylumbelliferyl β-D-glucuronide hydrate (Sigma M9130). The reaction was allowed to occur for 2 h at 37 °C, and the fluorescence of the reaction product was measured with an excitation wavelength of 360 nm and an emission wavelength of 470 nm in a Spark plate reader (Tecan). Bovine β-glucuronidase (Sigma G0251) served as a positive control, while PBS was used as a negative control.

Citrate buffer: 0.1 M sodium citrate (Panreac) pH 5.5, 0.05 M NaCl (Panreac), 0.01% Tween20 (Sigma)

### 2.9.2. MMP1 inhibition study

In a 96-well plate, 1.6 µg/mL of MMP1 (PeproTech 420-01) was incubated with 30 µM of substrate (Sigma SCP0193), 1 µg/mL of TIMP2, and equimolar concentrations of the other indicated proteins. The mixture was incubated for 30 min at RT and fluorescence was measured with an excitation wavelength of 324 nm and an emission wavelength of 400 nm in a Spark plate reader (Tecan). The activity of TIMP2 was measured as the reduction in fluorescence due to the inhibition of MMP1 enzymatic activity on the substrate that yielded the fluorescent product. In the positive control, TIMP2 was omitted, and in the negative control MMP1 was not added.

### 2.9.3. Phagocytic activity study

BV2 cells (CLS 305156) were seeded in 96-well plates (2000 cells/well). After 16 h of incubation with 2 µg/mL of sTREM2 and equimolar concentrations of the other indicated proteins, cells were exposed to 3 µM of FITC-A$\beta_{1\text{-}42}$ (Bachem 4095738) or 15 µg/mL of myelin-pHrodo for 3 h. Following trypsinization of the cells and an incubation with a PerCP Rat Anti-Mouse CD45 antibody (BD 557235) for 30 min at 4 °C to label activated microglial cells, phagocytic activity was measured as the increase in intracellular fluorescence by flow cytometry in a CytoFLEX cytometer (Beckman) following manufacturer's instructions.

#### 2.9.3.1. Amyloid-β peptide preparation

Lyophilized FITC-A$\beta_{1\text{-}42}$ (Bachem 4095738) was re-suspended in cold HFIP (Sigma) to a 1 mM solution and was left for to 2 h to obtain Aβ monomers. HFIP was then evaporated using a SpeedVac centrifuge, and vials containing the Aβ film were stored at -80 °C until the day of the experiment. One film was re-suspended in DMSO (Sigma) to a final concentration of 5 mM, and further diluted in PBS to a final concentration of 0.25 mM. The vial was then incubated at 4 °C for 24 h to obtain Aβ oligomers.

#### 2.9.3.2. Myelin-pHrodo preparation

First, 500 µg of lyophilized amine-reactive pHrodo Green STP ester (ThermoFisher P35369) was re-suspended in 75 µL of DMSO. Then, 18.5 µL of purified myelin at a 15 mg/mL concentration (Sigma M1891) was mixed with 25 µL of pHrodo and re-suspended in 206.5 µL of PBS. The reaction was incubated for 45 min at RT protected from light,

followed by centrifugation at 4000 g for 10 min at 4 °C. The supernatant was discarded, and the pellet was re-suspended in 950 µL of PBS to a final concentration of 0.3 µg/µL of purified myelin-pHrodo.

## 2.10. *In vivo* studies

These studies were carried out in strict accordance with the current National regulations in the animal facilities of the UAB. The Committee on the Ethic of Animal Experiments of the Universitat Autònoma de Barcelona approved the procedures described (protocol number: CEEAH 4882). Mice were bred in Macrolon cages, fed *ad libitum* with standard diet, and kept under controlled temperature (22±2 °C) and light-dark cycles (12 h).

### 2.10.1. Viral vector injections

Animals received intravenous injections via the lateral tail vein. Mice were placed in a mouse restraint (MH-100 Ibi scientific), and the tail was exposed to ultraviolet light for 15 s to induce vasodilation of the tail vein. Subsequently, the viral vector diluted in NaCl was injected in a total volume of 200 µL, using a 1 mL syringe (9161798V Braun) and 30Gx1/2" needles (4646300 Braun).

### 2.10.2. Recombinant protein injections

#### 2.10.2.1. Intravenous administration

Animals received intravenous injections via the lateral tail vein. Mice were placed in a mouse restraint (MH-100 Ibi scientific), and the tail was exposed to ultraviolet light for 15 s to induce vasodilation of the tail vein. Subsequently, the PBS-diluted sKL was injected at a dose of 50 µg/kg in a total volume of 200 µL, using a 1 mL syringe (9161798V Braun) and 30Gx1/2" needles (4646300 Braun).

#### 2.10.2.2. Intraperitoneal administration

Animals were intraperitoneally injected, alternating sides daily to prevent injuries. PBS-diluted sKL was injected at a dose of 50 µg/kg in 200 µL for half-life determination, or 10 µg/kg in a volume of 10 µL/g for the *in vivo* experiment, using a 1 mL syringe (9161798V Braun) and 30Gx1/2" needles (4646300 Braun).

### 2.10.3. Blood-brain barrier penetration study

#### 2.10.3.1. Bioconjugation and radiolabeling

sKL was conjugated to the chelating agent *p*-SCN-Bz-Deferoxamine (DFO) at a protein/chelator ratio of 1:10 at 37 °C for 1 h under stirring. Quality control was performed by mass spectrometry (MALDI-TOF), gel electrophoresis and SEC-HPLC (isocratic method, 200 mM monopotassium phosphate + 250 mM potassium chloride, pH 6.2). Radiolabeling was carried out by incubating the protein conjugates with zirconium-89 ($^{89}$Zr) chloride at a 1:5 ratio at RT for 1 h at pH 7. The resulting radioconjugates were purified with a PD-10 desalting column in formulation buffer (20 mM HEPES, 100 mM NaCl, 5% sucrose, pH 7). Radiochemical purity was determined by SEC-HPLC (≥95%, $R_t$=6.8 min).

#### 2.10.3.2. *In vivo* PET/CT imaging

[$^{89}$Zr]$^{89}$Zr-sKL (10 µg, 0.9 MBq, 200 µL) was injected intravenously into the lateral tail vein of 12-week-old male and female C57BL6/J WT mice (Charles River). At 24, 48, and 72 h post-injection, mice were anaesthetized by isoflurane inhalation (4-2.5% [v/v] and placed on the scanning bed in a prone position. PET/CT imaging was performed using a SuperArgus PET/CT scanner (Sedecal). PET images were acquired statically for 10-15 min using a 400-700 keV energy window (whole-body mode, 2 beds), followed by a CT scan (360 projections, 45 kVp, standard resolution) for anatomical reference and attenuation correction. At the end of the imaging experiment, animals were sacrificed by cervical dislocation.

CT reconstruction was performed using the FeldKamp method with binning 2. PET data was reconstructed using a 2DOSEM iterative reconstruction method (2 iterations, 16 subsets). Reconstructed CT images were used to derive an attenuation map for PET attenuation correction. Random and scatter correction were also applied to PET images. For quantitative analysis of tracer uptake, PET/CT images were analyzed using the Pmod 4.3 software (Bruker Corporation). Spherical volumes of interest (VOIs) were delineated in organs of interest and $SUV_{mean}$ values were obtained.

### 2.10.4. Behavioral and memory tests

In all tests described below, male and female mice were assessed separately to prevent behavioral changes.

#### 2.10.4.1. Sensorimotor tests

Prior to conducting behavioral and memory assessments, the sensorimotor abilities of mice were evaluated. The tail suspension test was used to assess motor and visual reflexes. Mice were suspended by their tail 30 cm above a flat black surface. After 3 s in suspension, mice were slowly lowered towards the black surface. Mice extending their extremities when nearing the surface were considered to exhibit correct reflexes and scored 1, while those not extending their extremities scored 0. The test was repeated a total of three times, and an average above 0.6 was indicative of correct reflexes.

Motor coordination and equilibrium were assessed by measuring the distance traveled and latency to fall from a horizontal wooden rod (1.3 cm wide) on two consecutive 20 s trials. Motor coordination was also evaluated based on the distance traveled in the wire hang test. Mice were allowed to cling from the middle of a horizontal wire (2 mm diameter, 40 cm length) with their forepaws for 60 s. Muscle strength was measured by the time it took for them to fall from the wire.

#### 2.10.4.2. Open Field

The Open Field test was conducted to assess the exploratory activity of mice. Mice were placed in a square wall-enclosed 40x40 cm white box, and were allowed to freely explore for 5 min. The test was done using two identical boxes and two mice at a time. A fixed digital camera was used to record the test, and was later analyzed with the Any-Maze software (version 7.20). At the end of each test, the box was thoroughly cleaned with 70% EtOH before the next mice was tested.

In the Any-Maze software, a 5x5 grid was painted over the box for the determination of thigmotaxis (Fig. 20), calculated as the percentage of time mice spent in the area close to the walls.

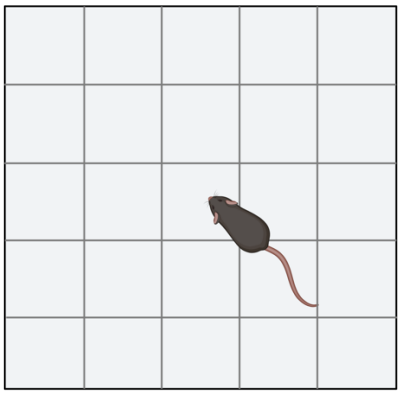


Figure 20. Open Field box, with an area of 40x40 cm, and the grid used for the determination of thigmotaxis. The outer 16 blocks were counted as the area close to the walls, while the inner 9 blocks were counted as the center area.

#### 2.10.4.3. Novel Object Recognition Test

The Novel Object Recognition Test is used to assess recognition memory in mice, based on their natural preference to explore new objects. The test was conducted over three consecutive days, encompassing three distinct tasks: habituation, familiarization, and memory (Fig. 21). The same 40x40 cm white box used for the Open Field was employed. The Open Field test served as the habituation day, where mice were placed in the center of the box and explored it for 5 min. On the familiarization day, two identical objects were placed inside the box, and mice had 10 min to explore them, expecting them to explore each object for the same amount of time. The objects consisted of two tower-like pieces, with green and grey strips and a rectangular form, and they were placed 5 cm away from the sides, and 7 cm away from the wall. On the memory day, one of the objects was replaced with a novel one, and mice had 10 min to explore both objects. The new object consisted of a cylindrical black tube, wider than the first object, and were placed in the same positions as the previous day. The side in which the new object was placed was randomized to avoid any possible bias, and both the objects and the box were thoroughly cleaned with 70% EtOH after each test.

A fixed camera was used to record the tests, and subsequent analyses were conducted using Any-Maze software. Parameters such as speed, traveled distance, exploration time for each object, and preference index were measured. Preference index is defined as the percentage of time spent exploring the new object relative to the total exploration time.

A score of 50% indicates no preference for any of the objects, while a score over 50% indicates preference for the new object.

The total exploration time in the familiarization and memory days was used as an inclusion criterion. Only mice that spent more than 5 s exploring objects were included in the analysis, as exploring for less time is considered as insufficient to remember the objects.

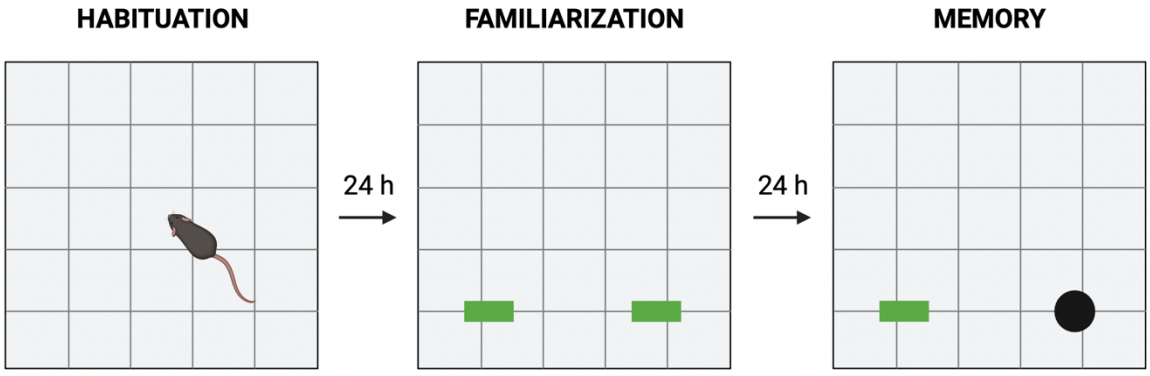



Figure 21. Schematic representation of the NORT.

#### 2.10.4.4. Morris Water Maze

The Morris Water Maze is a widely used test for the assessment of hippocampal-dependent spatial memory and learning. The test is based on mice locating and reaching a platform (7 cm in diameter, placed 1.5 cm beneath the water surface) in a circular pool (120 cm in diameter, 60 cm in height) filled with opaque water at 25 °C (Fig. 22).

The first day of the test (Cue) consisted of the visual perceptual learning, where mice performed four trials of a maximum of 60 s to locate the platform that was visible above the water surface, marked by a small flag serving as a visual clue. During the following four days (Learning), mice were trained to find the platform that was 1.5 cm beneath the surface with the help of four visual clues positioned around the pool for orientation. Each mouse performed four trials of a maximum of 60 s every day. If a mouse failed to reach the platform, it was manually placed on it for 10 s. Throughout the learning phase, the platform remained fixed in position, and mice entered the pool from different starting locations in each trial to encourage spatial learning facilitated by the visual cues. Improvement in spatial learning was measured as a decrease in the latency to reach the platform and the traveled distance to reach it.

To assess spatial memory, mice performed two probe trials, 2 h and 24 h after the last learning trial. For these tests, the platform was removed from the pool, and a single trial of 60 s was performed for each mouse. With the help of the Any-Maze software, a target zone was defined as the spot where the platform was in the learning trials. Mice entered the pool from different spots for the two probe trials. The latency to reach the target was measured, alongside the number of times they crossed the target, and the traveled distance. Mice that did not enter the target zone were assigned a latency of 60 s. The Any-Maze software was used to analyze the results, and improvement in spatial memory was defined as a decrease in the latency to reach the target and a preference for the target quadrant.

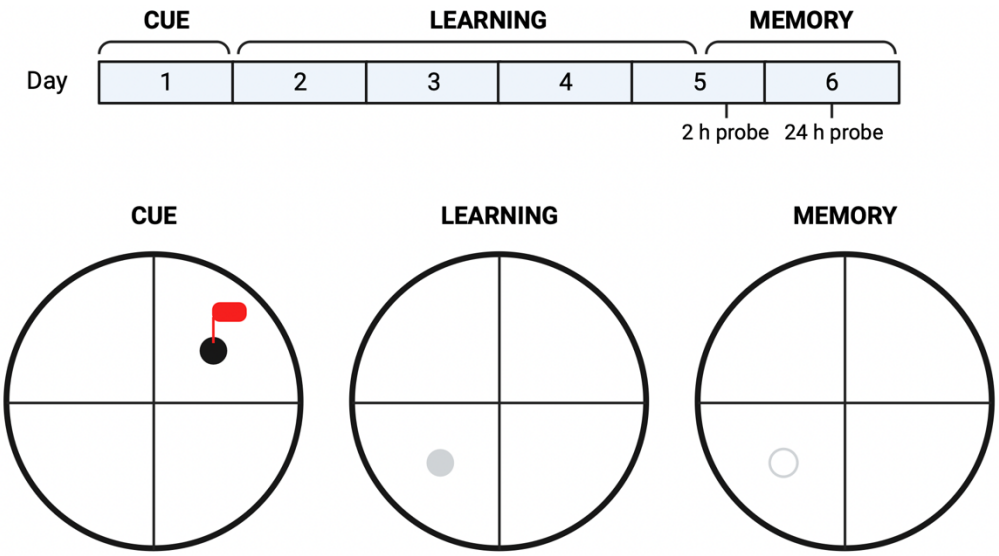



Figure 22. MWM timeline and schematic representation. In the cue day, the platform is visible and marked with a flag. In the learning phase, the platform is under the water, and in the memory phase the platform is removed, its position is marked with a grey circle.

### 2.10.5. Euthanasia and sample collection

Mice were anesthetized by inhalation of Isoflurane (IsoFlo, Esteve) in a closed chamber, followed by cervical dislocation and decapitation. Blood was collected from the neck of mice. One liver lobe and one kidney were collected from each mouse in an Eppendorf tube. The brain was extracted and bisected into two hemispheres. One hemisphere was immersed in 4% paraformaldehyde (PFA) (Casa Álvarez) for fixation and subsequent immunofluorescence studies. The other hemisphere was dissected, and the following brain areas were separated: olfactory bulbs, hippocampus, entorhinal cortex, and

cerebellum. Each brain area was collected into different tubes, and all samples were stored at -80 °C until further processing.

#### 2.10.5.1. Brain fixation

One brain hemisphere was fixed in 4% paraformaldehyde (PFA) (Casa Álvarez) for 24 h at 4 °C. Following fixation, brains were washed three times with PBS and incubated in PBS containing 10% sucrose (Panreac) for at least three days. Brains were then embedded in OCT (ThermoFisher) and frozen at -80 °C. Sagittal sections of 14 µm thickness were obtained using a cryostat.

#### 2.10.5.2. Brain immunofluorescence

Slides containing brain slices were allowed to thaw at RT for 30 min, and were then placed on a heating plate at 42 °C for 20 min to ensure proper adhesion of the samples. Samples for Aβ immunofluorescence underwent antigen retrieval through an incubation of 30 min in citrate buffer at 55 °C, followed by 30 min at RT in 80% formic acid (Panreac) solution. Samples were then permeabilized with cold methanol (Panreac) for 10 s for GFAP, Iba1 and Aβ immunofluorescence, or 30 min in PBS-Tween 0.3% for pTau. After three washes with washing solution, samples were blocked for 1 h at RT with blocking solution. Then, 200 µL of primary antibody in blocking solution was added (Table 9), and samples were incubated O/N at 4 °C. The following day, after three washes, 200 µL of secondary antibody in blocking solution was added, and samples were incubated at RT for 1 h. Following three washes, samples were incubated for 10 min with Hoechst (ThermoScientific) to label cell nuclei. Samples were mounted with Fluoromount (ThermoScientific), immunofluorescence images were captured in an Eclipse 90i microscope (Nikon) and analyzed using the Fiji software. Results were expressed as the percentage of positive fluorescent area, and two sections were analyzed per animal.

Citrate buffer: 10 mM sodium citrate (Panreac), Tween20 0.05% (Sigma), pH 6

PBS: pH 7.4, 137 mM NaCl (Panreac), 3 mM KCl (Panreac), 10 mM $Na_2HPO_4 \cdot 7H_2O$ (Panreac), 1.7 mM $KH_2PO_4$ (Panreac)

Washing solution: PBS-Tween20 0.05% (Sigma)

Blocking solution: PBS-Tween20 0.05% (Sigma), BSA 1% (Sigma)

Table 9. Antibodies used for immunofluorescence.

| Labeling | Primary antibody | Reference | Manufacturer | Secondary antibody |
|---|---|---|---|---|
| **Astrocytes** | GFAP | Z0034 | Dako | Rabbit[1] |
| **Microglia** | Iba1 | Ab5076 | Abcam | Goat[2] |
| **NFTs** | pTau | MN1020 | ThermoScientific | Mouse[3] |
| **Aβ** | $A\beta_{1\text{-}16}$ | 803001 | Taper | Mouse[3] |

[1]Alexa 568 goat anti-rabbit (A11011, Invitrogen) [2]Alexa 568 donkey anti-goat (A11057, Invitrogen) [3]Goat anti-mouse Biotin (62-6540, Invitrogen) + Streptavidin-alexa 488 (S11223, Invitrogen)

### 2.10.6. Blood sample analysis

Serum samples were analyzed by the Veterinary Clinical Biochemistry Service (UAB, Barcelona). A complete profile was selected for the analysis of serum samples.

#### 2.10.6.1. Blood serum collection

Mice were anesthetized with isoflurane (IsoFlo, Esteve), followed by decapitation and blood collection into BD Microtainer tubes. After allowing samples to coagulate for 30min, they were centrifuged for 10 min at 1600 g and 4 °C. The supernatant (serum) was transferred to new tubes and stored at -80 °C.

## 2.11. Statistical analyses

Results are expressed as the mean of the obtained values ± standard error of the mean (SEM). Statistical analyses were performed using the GraphPad software (version 9.0.1), with a parametric analysis, which was also used for the generation of graphs. Differences among more than two groups were evaluated using either One-way ANOVA (for one variable) or Two-way ANOVA (for two variables), followed by Tukey's post-hoc test. Differences between two means among test days in the MWM were evaluated using a t-test. In all cases, a two-tailed hypothesis analysis was performed, and a p-value below 0.05 was considered statistically significant.

## 2.12. Bioinformatic studies

### 2.12.1. All-atom models.

For Klotho, sTREM2 and TIMP2, all-atom models were built from the crystal structures in PDB entries 5W21, 5UD7 and 1BR9, respectively. The model for Klotho included residues E34-V534 of chain A of 5W21.pdb. A stretch of 18 residues (L98-S115) absent from the crystal was included using Modeller [320]. For sTREM2, all residues (T21-A157) of the chain F of 5UD7.pdb were retained. For TIMP2, all residues (C1-A182) in 1BR9.pdb were included (12 C-terminal residues not seen in the crystal structure were not added to the model).

### 2.12.2. All-atom MD simulations.

For each protein, titratable residues were attributed their dominant protonation state at pH 7.4. Neutral groups were added to cap the N- and C-termini of each protein chain. The software HTMD [321] was employed to solvate and ionize the proteins. Each protein was inserted in a water box whose edges were at a minimum distance of 12 Å from the solute. Ions were added to neutralize charges and up to a concentration of 0.15 M NaCl.

After 500 steps of energy minimization with the conjugated gradient method, systems were equilibrated for 3 ns in the NPT ensemble, with temperature of 300 K and pressure of 1 atm. Harmonic position restraints of 1.0 kcal·mol$^{-1}$·Å$^{-2}$ were applied to the Cα atoms, while restraints of 0.1 kcal·mol$^{-1}$·Å$^{-2}$ were applied to the remaining heavy atoms of the protein. These restraints were progressively released during equilibration. Production simulations of 520 ns were performed in the NVT ensemble, at 300 K. In all stages, temperature was controlled by a Langevin thermostat, a 9.0 Å cut-off was used for non-bonded interactions, and long-range electrostatic interactions were calculated with the particle-mesh Ewald (PME) method. Hydrogen mass repartitioning allowed a timestep of 4 fs. The ff14SB [322] force field was used for proteins, and water was described by the TIP3P model [323]. We employed the Acemd 2 [324] software to run the trajectories.

### 2.12.3. Analysis of all-atom MD simulations.

Principal component analysis (PCA) consisted in the diagonalization of the covariance matrix, whose elements are:

$$C_{ij} = \langle (r_i - \langle r_i \rangle) \cdot (r_j - \langle r_j \rangle) \rangle$$

where i and j denote all pairs of the 3N Cartesian coordinates of the N Cα atoms in the protein. The vector $r_i$ indicates the instantaneous value of coordinate i and $\langle r_i \rangle$ is the average value of this coordinate in the ensemble of conformations. The coordinates of the Cα atoms in each individual trajectory were projected on the space of the respective first two principal components. These analyses were performed with the Gromacs software [325].

Root-mean-square fluctuations (RMSF) were also calculated with Gromacs, according to the expression:

$$\text{RMSF}_i = \sqrt{\langle (r_i - \langle r_i \rangle)^2 \rangle}$$

where $r_i$ denotes the coordinates of atom i.

Root-mean-square deviations (RMSD) were also calculated with Gromacs, according to the expression:

$$\text{RMSD} = \sqrt{\frac{1}{N} \sum_{i=1}^{N} (r_i - r_i^{ref})^2}$$

Where $r_i$ is the set of coordinates of an atom, and $r_i^{ref}$ represents the set of coordinates of the i atom in the reference structure.

### 2.12.4. Construction of models of the united proteins.

These models were built by homology modeling using Modeller [320]. A single sequence, consisting of the sequences of the three proteins and the linkers arranged in the desired order, was defined as the target, and the structures of Klotho, sTREM2 and TIMP2 were used as templates. Additional restrictions were added to enforce the helical secondary structure of the linkers.

### 2.12.5. Coarse-grained MD simulations.

The all-atom models of the united proteins were converted to coarse-grained (CG) representation using the "Martini Maker" functionality of the Charmm-gui webserver [326]. The systems were described by the Martini 2.2 force field [327], with the addition of an elastic network composed of harmonic springs between interacting sites (elnedyn) to preserve the secondary and overall tertiary structures of each protein [328]. However, it is important to note that there were no inter-protein springs, so the relative motions of the three components were not restrained. The CG models were solvated and ionized up to a 0.15 M NaCl concentration. Each system was submitted to two independent simulation replicas. In each replica, after energy minimization with the steepest descent algorithm, equilibration in the NPT ensemble, with progressive release of position restraints on the protein, was run for 20 ns. Equilibration was followed by a 10 μs production in the NPT ensemble, with temperature of 300 K and pressure of 1 atm. Temperature was controlled with the v-rescale thermostat, and pressure was controlled with the Berendsen (during equilibration) and Parrinello-Rahman (during production) barostats. A dielectric constant of 15 was adopted, and electrostatic interactions as well as van der Waals interactions were shifted to zero between 0 and 11 Å. In equilibration and production, the timestep was 20 fs. All CG simulations were performed with the Gromacs software (version 2019) [325]. Trajectories were visually inspected for an assessment on protein aggregation.

### 2.12.6. AlphaFold analysis

The AlphaFold software was used to accurately predict the structure of HEBE2 from the amino acid sequence, as originally described [329].

# RESULTS

# Chapter 1

## Recombinant human sKL as a therapeutic strategy for Alzheimer's disease

### 1.1. Production and purification of recombinant sKL

To develop a therapeutic strategy using recombinant sKL, the protein needed to be produced first. An efficient and rapid method for protein production is the transduction of cells with an adenoviral vector capable of generating large quantities of protein. Accordingly, an adenoviral vector encoding human sKL was generated. To facilitate downstream purification of the protein, a polyhistidine tag was incorporated at the 3' end of the gene via overlapping PCR (Fig. 23).

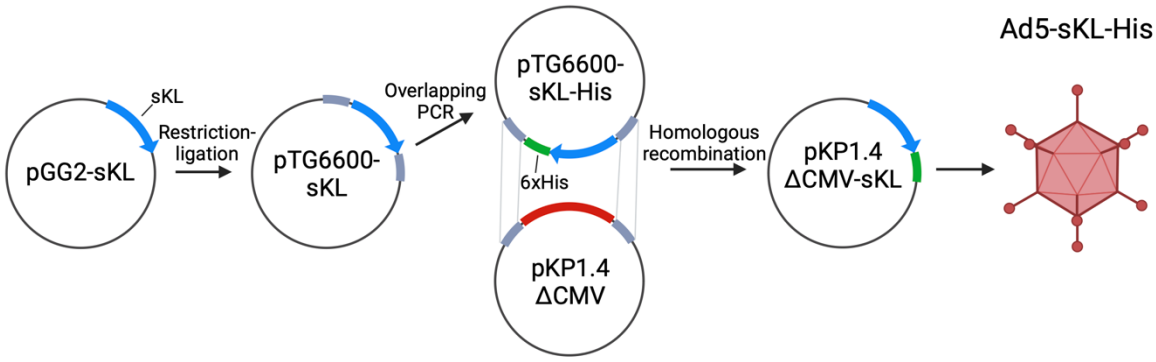



Figure 23. Schematic representation of the adenoviral vector generation for sKL. The human *sKL* gene was cloned into a pTG6600 shuttle vector through a restriction enzyme cloning. A C-terminal polyhistidine tag was introduced through an overlapping PCR reaction, and the resulting *sKL*-His cassette was introduced into the pKP plasmid through homologous recombination. This last plasmid encodes all the genes necessary for the production of adenoviral vectors when transfected into HEK293 cells.

This adenoviral vector was later used to transduce CHO cells *in vitro*. Correct protein expression and secretion were confirmed through Western Blot analysis of transduced cells, where a band of ~70 kDa was detected using antibodies against sKL and the polyhistidine tag (Fig. 24). The supernatant containing the secreted protein was purified, as intracellular protein was expected to lack the necessary posttranslational modifications for biological activity, resulting in highly purified recombinant human sKL suitable for subsequent assays.

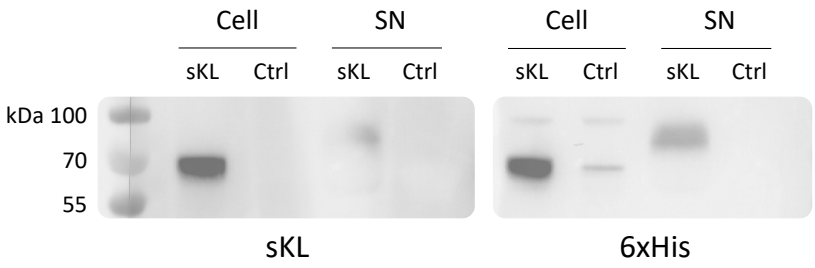



Figure 24. Western Blot of CHO cells transduced with an adenoviral vector encoding human sKL-His or Null as a control. Both cell lysates (Cell) and supernatants (SN) were loaded, and the immunodetection was performed using antibodies against Klotho and the His tag, as indicated below each membrane. Theoretical molecular weight of sKL-His without posttranslational modifications is 63,4 kDa.

## 1.2. *In vitro* testing of biological activity

The produced recombinant sKL needed to be biologically active to be suitable for an *in vivo* experimental setting. To assess the activity of the recombinant protein, a straightforward enzymatic assay was employed, as sKL possesses β-glucuronidase activity, allowing it to hydrolyze a substrate and generate a fluorescent product. The biological activity of the produced recombinant protein was confirmed using this enzymatic assay, demonstrating a significant increase in fluorescence comparable to that of the positive control (Fig. 25).

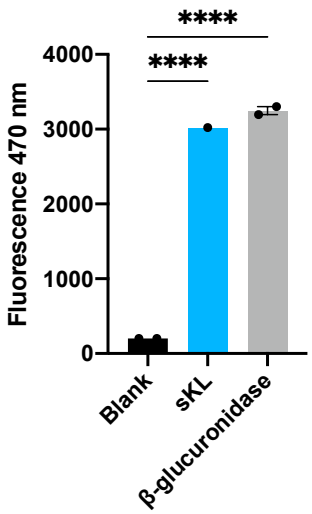



Figure 25. β-glucuronidase activity assay. 20 μg of sKL was used with two replicates per condition. Bovine β-glucuronidase was used as a positive control, while the blank did not contain any protein. Data are shown as Mean ± SEM, One-way ANOVA and Tukey post-hoc (****p<0.0001).

### 1.3. Blood-brain barrier penetration

Given the intended intravenous administration of the protein aimed at improving cognition, it was crucial to investigate its ability to traverse the BBB and reach the brain. To assess this, sKL was radiolabeled with zirconium ($^{89}$Zr) and administered intravenously to mice for biodistribution analysis by Dr Raúl Herance's group from Vall d'Hebron Institut de Recerca. Notably, no detectable levels of the protein were observed in the brains of the mice across all examined time points (Fig. 26A-D). These findings strongly indicate that sKL does not penetrate the BBB but instead accumulates primarily in the liver. Consequently, any observed cognitive enhancements following systemic administration of sKL cannot be attributed to a direct action of sKL within the brain.

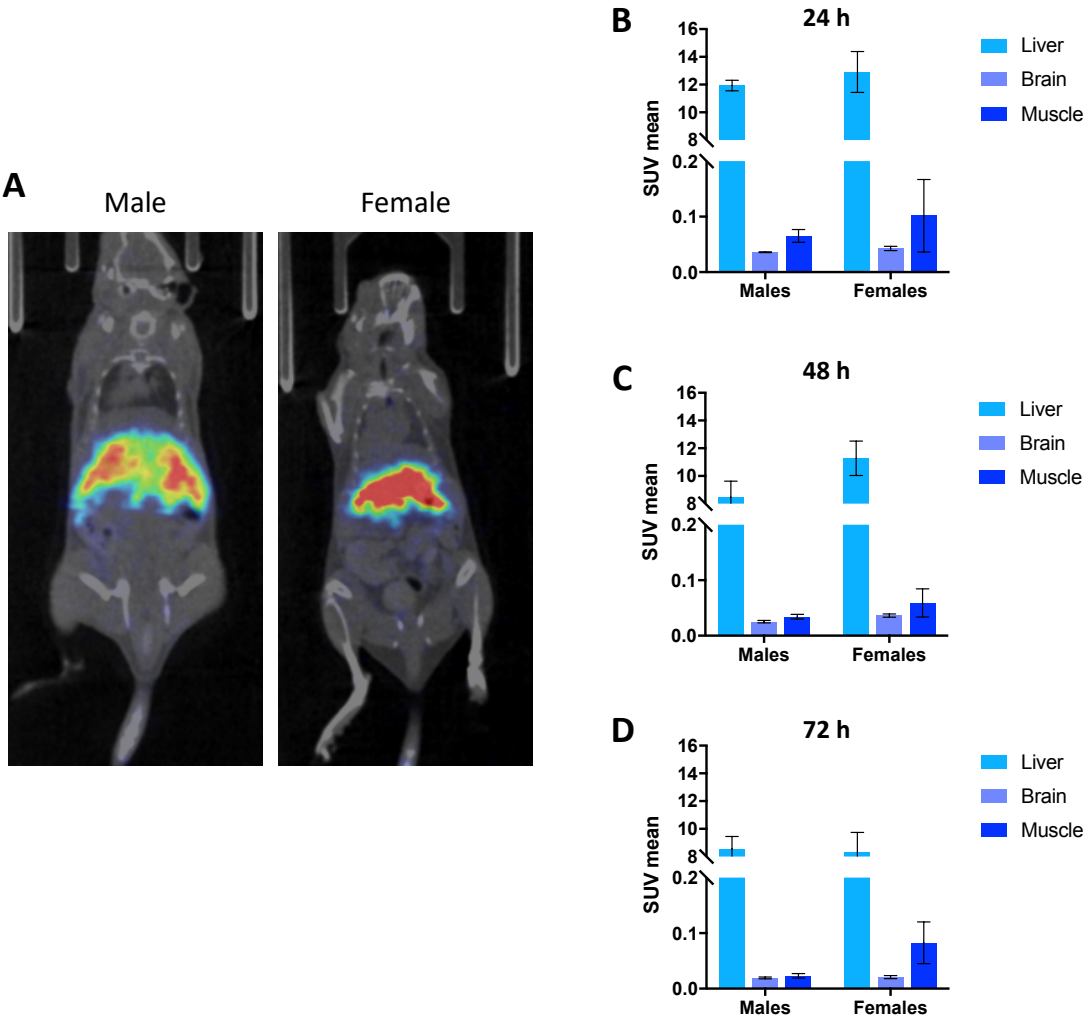



Figure 26. Blood-brain barrier penetration experiment. (A) Representative PET/CT images of male and female mice injected with [$^{89}$Zr]Zr-sKL. Color intensity reflects protein accumulation, with red indicating the highest concentration. (B-D) Standardized uptake value (SUV) of labeled sKL in the liver, brain, and muscle at different timepoints. Data are shown as Mean ± SEM. Sample size: 3 mice per sex.

## 1.4. Setup for sKL detection

To determine the half-life of recombinant sKL in mouse serum, a human Klotho ELISA was planned to be used. However, this ELISA had not previously been used to quantify human sKL in mouse serum. Therefore, a small pilot experiment was conducted (Fig. 27). Various samples containing recombinant human sKL or conditioned media were tested. The ELISA successfully detected human sKL in the samples, while no mouse sKL was detected, as evidenced by the serum-only sample. Nonetheless, the measured sKL levels in both serum and PBS were lower than the theoretical concentration of 5000 pg/mL for reasons that remain unclear. Notably, the protein concentration detected in PBS was even lower than that in serum, indicating that the dilution medium influences the outcome of the ELISA measurement. Overall, these results suggest that this ELISA can detect human recombinant sKL in mouse serum samples without cross-reactivity for murine sKL.

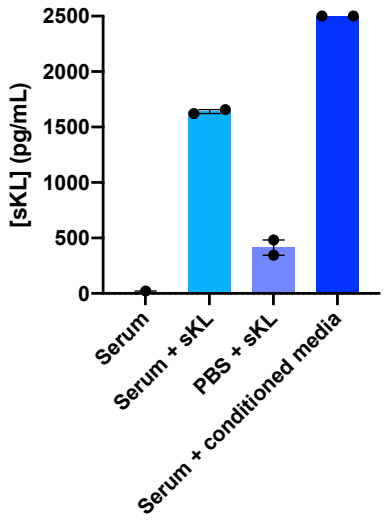



Figure 27. Human sKL ELISA test with different samples; mouse serum as a negative control, mouse serum with 5000 pg/mL recombinant human sKL, PBS with 5000 pg/mL recombinant human sKL, mouse serum with conditioned media from HEK293 cells transduced with a human sKL-expressing adenoviral vector as a positive control. Data are shown as Mean ± SEM.

## 1.5. Recombinant human sKL's half-life determination

Determining the protein's half-life was essential for designing a therapeutic approach, as recombinant proteins degrade in the bloodstream, requiring repeated administrations. The half-life of human sKL in mouse serum had not been previously determined, prompting the design of an experiment to elucidate this parameter.

### 1.5.1. Protein half-life with intravenous administration

Three-month-old wild-type (WT) mice were intravenously injected with a high dose of the protein and subsequently euthanized at various timepoints to collect serum for protein quantification using the previously described ELISA (Fig. 28).

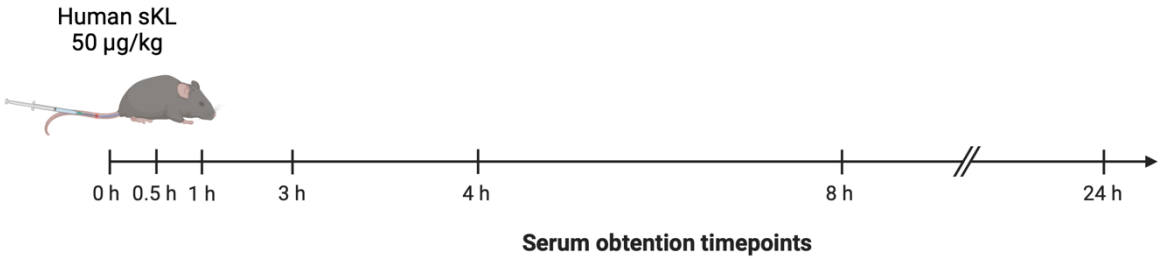



Figure 28. Experimental design for the determination of human sKL's half-life via an intravenous administration. Mice were injected with 50 µg/kg of recombinant sKL, euthanized at different timepoints, and serum was obtained for subsequent ELISA quantification.

Serum sKL concentrations were quantified and plotted (Fig. 29A). The resulting graph revealed two distinct phases: an initial rapid plasma clearance of the protein, where the concentration fell abruptly (0-1 h), followed by a drug elimination phase, during which the concentration of the protein decreased slowly once a pseudo-equilibrium was reached (1-24 h). The terminal half-life is calculated when concentrations reach pseudo-equilibrium [318], with a logarithmic scale of the concentrations (Fig. 29B) (details in methods). From this analysis, a serum terminal half-life of 8.65 h was calculated for intravenously administered recombinant human sKL in mice.

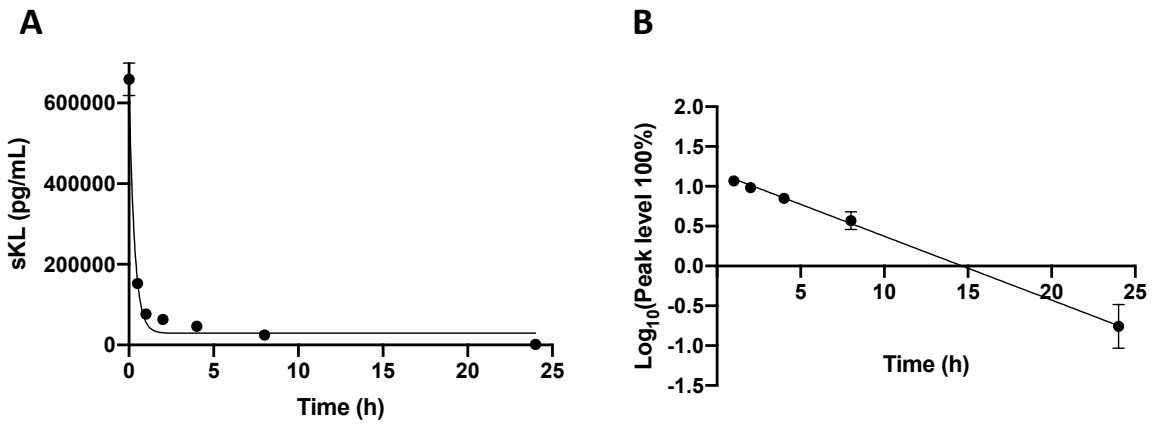



Figure 29. (A) Plot of serum sKL concentrations along the experiment. (B) Logarithmic plot of sKL concentrations in the pseudo-equilibrium phase. Data are shown as Mean ± SEM. Sample size: 3 mice per timepoint.

### 1.5.2. Protein half-life with intraperitoneal administration

While intravenous administration provides the most accurate method for determining the true half-life of a protein, this route is impractical for *in vivo* experiments due to its time-consuming nature and inability to facilitate repeated administrations over an extended period. Therefore, the intraperitoneal route was selected, understanding that this might result in a different half-life due to the slower absorption of the protein into the bloodstream. Consequently, the previous experiment was repeated with the administration route changed to intraperitoneal (Fig. 30).

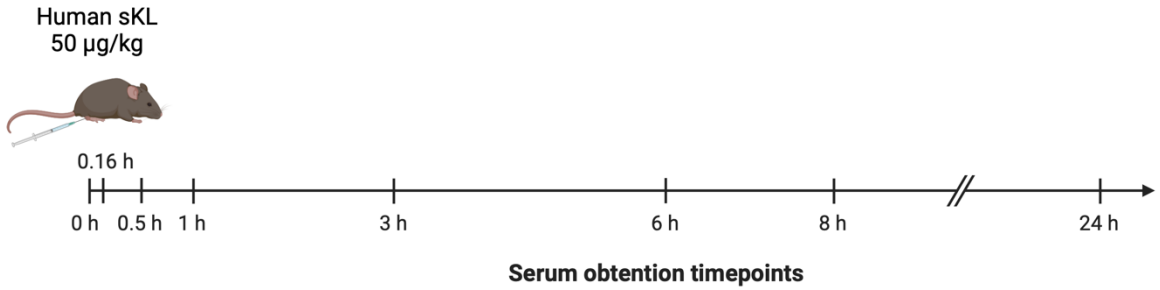



Figure 30. Experimental design for the determination of human sKL's half-life via an intraperitoneal administration. Mice were injected with 50 µg/kg of recombinant sKL, euthanized at different timepoints, and serum was obtained for subsequent ELISA quantification.

Serum sKL concentrations were quantified using the previous ELISA (Fig. 31A). In this case, the evolution of protein concentrations differed from that observed with intravenous administration. Initially, an increase in sKL concentration was noted up to 6 h post-administration, although the concentration reached at 6 h was significantly lower than that achieved with intravenous administration. This is likely due to the sum of two effects: first, the slow absorption of the protein into the bloodstream, and second, the rapid plasma clearance of the protein upon entering the bloodstream. Following this phase, pseudo-equilibrium was reached, enabling the calculation of the terminal half-life of the protein (Fig. 31B). In this case, a serum terminal half-life of 10.53 h was determined for intraperitoneally administered recombinant human sKL in mice, which was moderately longer than that calculated for intravenous administration.

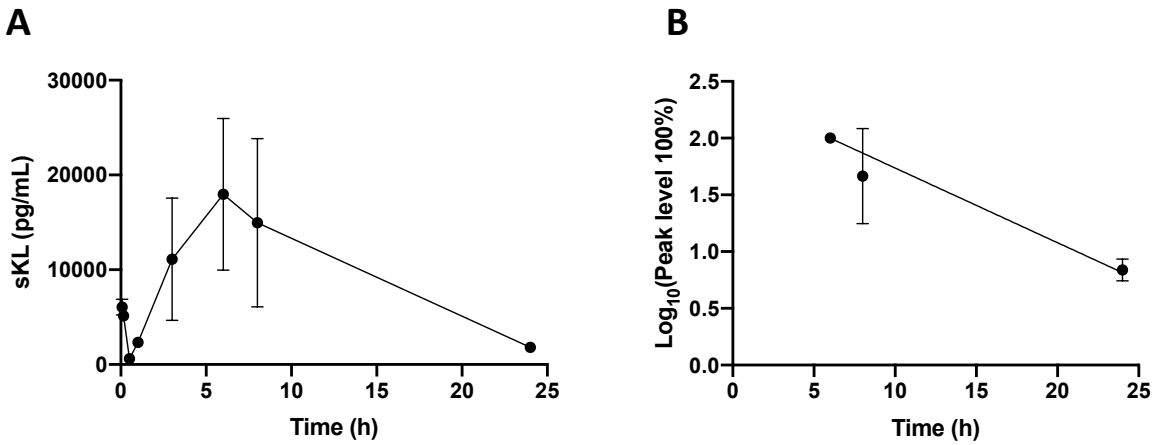



Figure 31. (A) Plot of serum sKL concentrations along the experiment. (B) Logarithmic plot of sKL concentrations in the pseudo-equilibrium phase. Data are shown as Mean ± SEM. Sample size: 2 mice per timepoint.

## 1.6. *In vivo* study

### 1.6.1. Administration interval and dose determination

The administration interval and the protein dose were calculated based on the protein's half-life data prior to conducting the *in vivo* experiment. Considering this data, the evolution of plasma concentrations following repeated protein dosing would likely resemble the pattern represented in Fig. 32. After the initial protein administration, plasma concentration would rapidly decline to the pseudo-equilibrium phase upon completion of protein clearance. Subsequent dosing would occur before complete depletion of the protein from the previous dose, resulting in higher plasma concentrations compared to the initial pseudo-equilibrium phase. These concentrations would progressively rise with each dose until reaching a steady-state, where the amount of administered drug exactly compensates for the amount of eliminated drug over the dosing interval.

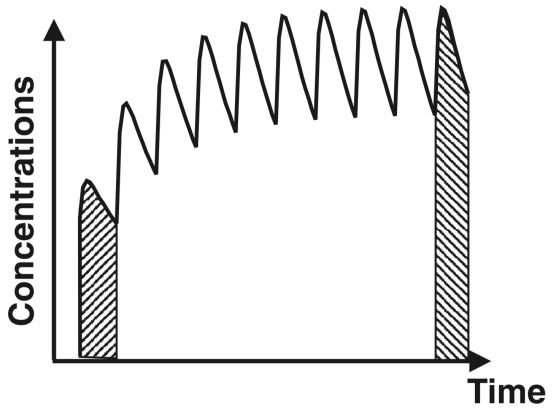



Figure 32. Theoretical evolution of the protein's plasma concentration after repeated administrations. After repeated administrations, a steady-state is reached, in which the amount of administered drug exactly compensates for the amount of eliminated drug over the dosing interval. Figure taken from [318].

The administration interval was determined using the accumulation index (R), which represents the ratio of the average amount of drug in the body under steady-state conditions to the average amount in the body after the first administration. This index was calculated using the following equation [318]:

$$R = \frac{1}{1 - e^{-(\frac{0.693}{Half-life} \cdot Admin.\ interval)}}$$

Assuming an administration interval of 24 h, the accumulation index would be:

$$R = \frac{1}{1 - e^{-(\frac{0.693}{10.53} \cdot 24)}} = 1.259$$

This indicates that the protein concentration in the steady-state would be 1.259 times higher than the concentration reached after the initial administration. With a 48-h administration interval, the accumulation index would decrease to 1.04, indicating complete depletion of the protein from the first dose by the time the second dose is administered, which would not maintain sustained protein levels in the bloodstream. Therefore, a 24-h administration interval was selected.

For determining the appropriate dosage, the Peak-Trough (P/T) ratio was calculated to assess protein concentration fluctuations during the steady-state phase. The following equation was used [318]:

$$\frac{P}{T}\ Ratio = \frac{C_{max}}{C_{min}} = 2^{\frac{\tau}{t_{1/2}}} = 2^{24/10.53} = 4.85$$

This indicates that the fluctuation between maximum and minimum protein concentrations would be approximately five-fold in the steady-state. Our goal was to ensure that blood sKL concentrations remained above physiological levels consistently. In healthy young humans, plasma soluble Klotho levels are around 1500 pg/mL [330,331]. Assuming a dose of 10 μg/kg for our experiment and extrapolating the data obtained from the protein's half-life experiment, we would expect a $C_{max}$ of around 14500 pg/mL and a $C_{min}$ of around 3000 pg/mL. Therefore, this dose is expected to maintain Klotho levels above physiological thresholds in humans.

### 1.6.2. Experimental design

In this study, we investigated the effects of recombinant human sKL on the APP/Tau transgenic mouse model of AD. Male and female APP/Tau mice and WT littermate controls were used, resulting in six distinct experimental groups as outlined in Table 10.

Table 10. Experimental groups of the experiment, and number of animals used.

| | | Males | Females |
|---|---|---|---|
| **WT** | **PBS** | 6 | 5 |
| **AD** | **PBS** | 5 | 6 |
| | **sKL** | 5 | 5 |

Five-month-old mice were injected with a dose of 10 μg/kg of PBS-diluted recombinant human sKL or PBS alone as a control (Fig. 33). Administrations were performed daily via intraperitoneal injection over a six-week period. Behavioral and cognitive assessments were conducted during the final two weeks of treatment, with injections performed in the afternoon to minimize stress-induced effects during testing. Evaluation of learning and memory functions was performed using the Open Field, Novel Object Recognition Test, and Morris Water Maze. Following behavioral testing, mice were euthanized, and tissue samples were collected for subsequent biochemical and histological analyses.

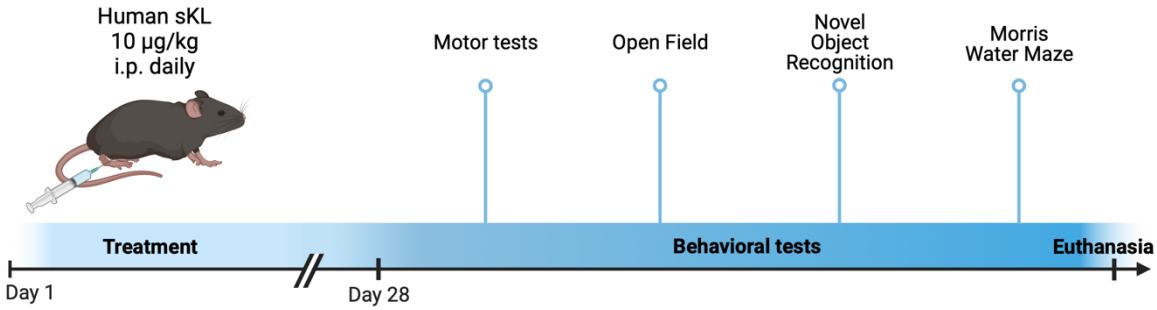



Figure 33. Experimental design of the *in vivo* experiment for recombinant human sKL in APP/Tau mice.

### 1.6.3. Weight evolution

Daily monitoring of body weight was conducted (Fig. 34). Interestingly, both male and female mice exhibited a declining trend in body weight over the study duration (Fig. 34A, B), likely attributed to injection-associated stress. Nonetheless, statistical analysis revealed no significant differences in body weight changes among experimental groups (Fig. 34C, D). These findings suggest that sKL treatment did not induce significant alterations in body weight compared to WT and AD mice.

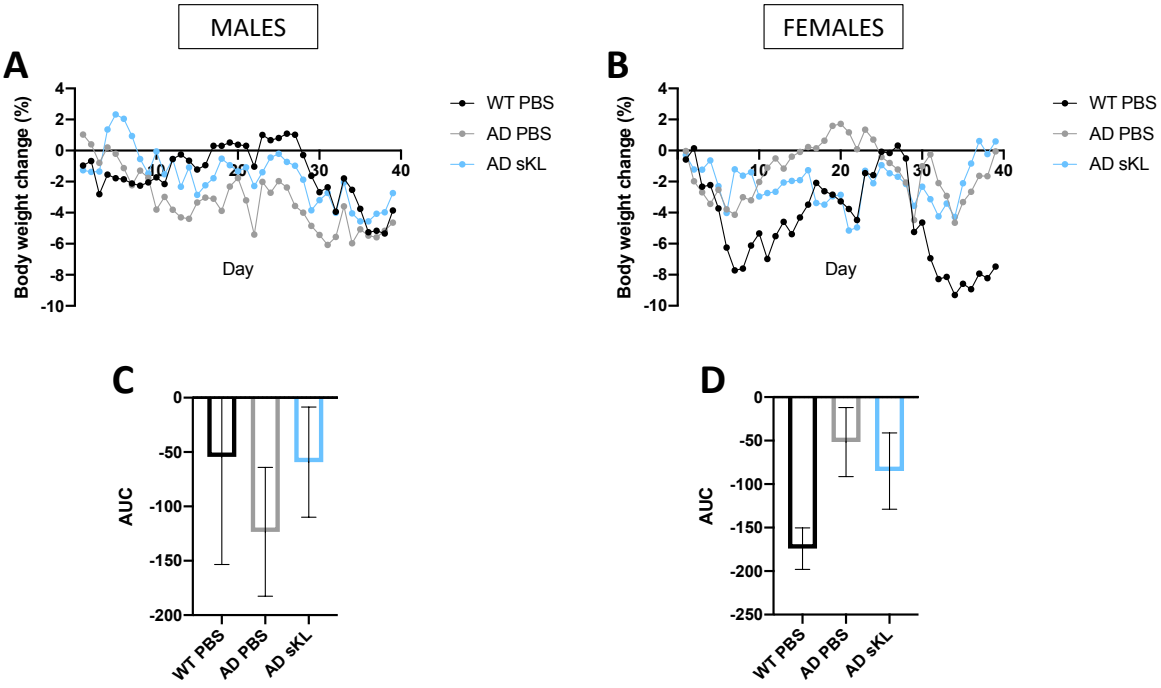



Figure 34. Weight evolution in males (A, B) and females (C, D) along the study. (A, C) Body weight change as percentage compared to the first day. (B, D) Area under the curve (AUC) of body weight for each group. Data are shown as Mean ± SEM, One-way ANOVA and Tukey post-hoc. Sample size for males: WT-PBS=6, AD-PBS=5, AD-sKL=4. Sample size for females: WT-PBS=5, AD-PBS=6, AD-sKL=5.

### 1.6.4. Behavioral and cognitive tests

Prior to behavioral and cognitive assessments, mice underwent evaluations of sensorimotor functions encompassing visual and hindlimb reflexes, equilibrium, and strength. Notably, no discernible differences were observed across experimental groups, indicating that neither genotype nor sKL treatment had notable effects on sensorimotor capabilities (results not shown). Therefore, it was assumed that all groups presented similar physical conditions, and any difference observed in the behavioral tests could be attributed to behavioral and/or cognitive functions.

#### 1.6.4.1. Open Field

The Open Field (OF) test was used to assess locomotor activity and anxiety-like behaviors in mice. The traveled distance and mean speed were analyzed as indicators of general locomotor activity. In males, no differences were found among groups, suggesting the absence of locomotor deficits in 6-month-old AD animals, and indicating that sKL treatment did not induce impairments (Fig. 35A, B).

Additionally, the percentage of time spent in motion was recorded as an indicator of anxiety-like behaviors, given that immobility might be a sign of fear. Males displayed no differences among groups, with approximately 85% of the time spent in motion (Fig. 35C). Another commonly used measurement is thigmotaxis, which refers to the time that mice spend close to the outer walls of the maze; the more anxiety, the more time mice spend around the walls. Male AD mice did not display increased thigmotaxis, with all groups spending approximately 80% of the time close to the walls (Fig. 35D).

Collectively, these findings indicate that at 6 months of age, male AD mice did not manifest locomotor impairments or heightened anxiety levels, and treatment with sKL did not alter the evaluated parameters.

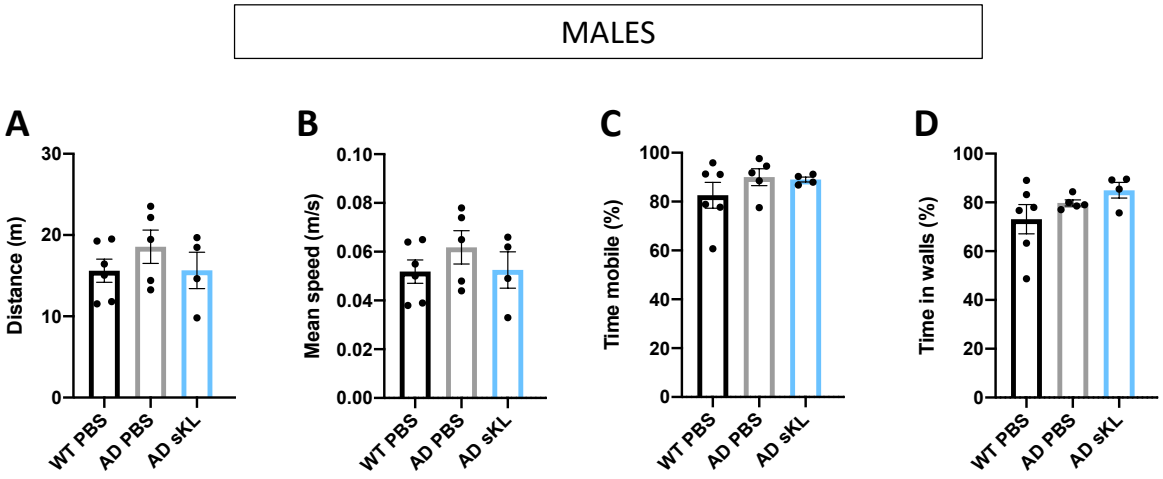



Figure 35. Open Field test in males. (A) Distance traveled in the Open Field. (B) Mean speed in the Open Field. (C) Percentage of time mice spend mobile during the test. (D) Percentage of time mice spend around the walls of the Open Field. Data are shown as Mean ± SEM, One-way ANOVA and Tukey post-hoc. Sample size after discarding outliers: WT-PBS=6, AD-PBS=5, AD-sKL=4.

In the case of female mice, no significant disparities in locomotor activity were detected, as evidenced by similar traveled distances and mean speeds across experimental groups (Fig. 36A, B). Similarly, no discernible differences were observed in the percentage of time spent in motion (Fig. 36C). However, a moderate increase in thigmotaxis was noted in sKL-treated mice compared to WT mice (Fig. 36D), with a shift from 75 to 85% of the time spent close to the walls. These results suggest that female mice did not display locomotor impairment, but sKL may slightly increase anxiety-like behaviors.

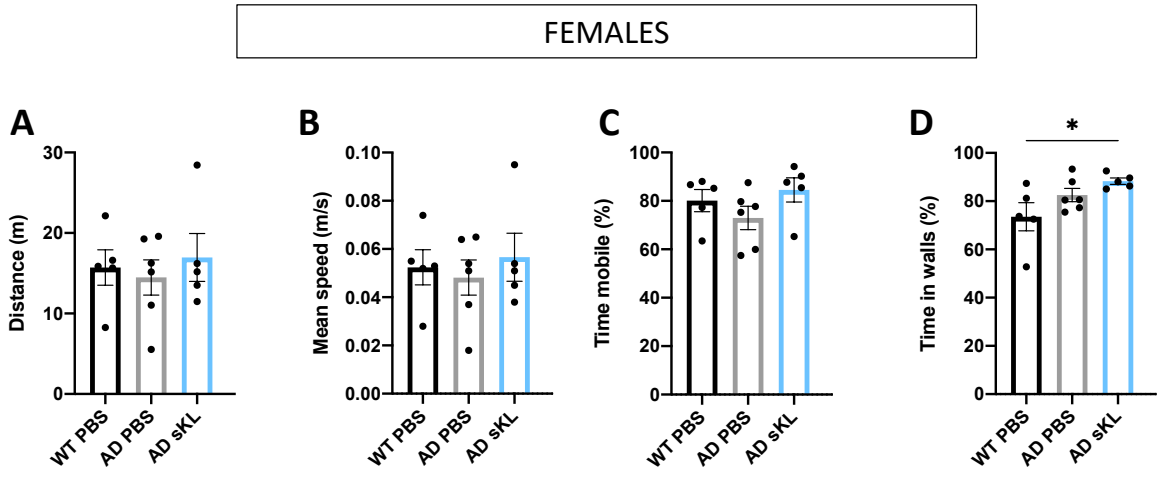



Figure 36. Open Field test in females. (A) Distance traveled in the Open Field. (B) Mean speed in the Open Field. (C) Percentage of time mice spend mobile during the test. (D) Percentage of time mice spend around the walls of the Open Field. Data are shown as Mean ± SEM, One-way ANOVA and Tukey post-hoc (*p<0.05). Sample size after discarding outliers: WT-PBS=5, AD-PBS=6, AD-sKL=5.

### 1.6.4.2. Novel Object Recognition Test

Recognition memory in mice was assessed using the Novel Object Recognition Test (NORT). The total exploration time served as an exclusion criterion, requiring mice to explore the objects for a minimum of 5 seconds to be included in the analysis. Consequently, only mice meeting this criterion were included in subsequent analyses.

In the case of male mice, no differences were observed in the preference index among groups on the first day of the test, when both objects were identical (Fig. 37A). On the second day, however, when one of the objects was replaced with a novel item, WT mice exhibited an expected increase in the preference for the new object, whereas AD mice did not display this behavior, indicative of impaired memory retention of the object explored on the preceding day (Fig. 37B). Notably, sKL-treated AD mice displayed a trend toward increased preference for the novel object, albeit not achieving statistical significance. The observed changes in preference index were independent of variations in exploration time, as all groups spent comparable times interacting with the objects (Fig. 37C). Comparison of preference indexes between the first and second day revealed a substantial increase in WT mice, contrasting with the absence of improvement in AD mice and a moderate enhancement observed in sKL-treated mice (Fig. 37D). Collectively, these findings suggest that sKL-treated mice presented enhanced recognition memory compared to control AD mice.

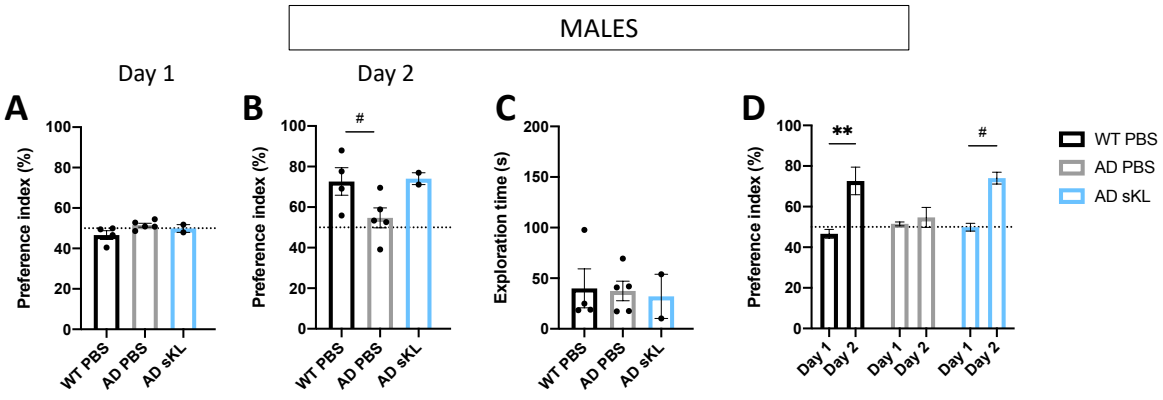



Figure 37. Novel Object Recognition Test for males. (A) Preference index on the first day of the test, when both objects are identical. (B) Preference index for the new object on the second day of the test. (C) Total time mice spend exploring the objects. (D) Comparison of the preference index between both test days. Data are shown as Mean ± SEM, One-way ANOVA and Tukey post-hoc, comparisons between days analyzed by 2-way ANOVA and Tukey post-hoc (**p<0.01, #<0.1). Sample size after discarding outliers: WT-PBS=4, AD-PBS=5, AD-sKL=2.

In the case of female mice, no differences in the preference index were observed on the first day of the test, as expected (Fig. 38A). On the second day, a moderate increase in the preference for the new object was observed in WT mice, although no statistically significant differences were discerned among groups (Fig. 38B). Interestingly, a trend towards an increase in exploration time was noted in sKL-treated mice (Fig. 38C). Upon comparing the preference indexes between the first and second day, no statistically significant increase in the preference for the novel object was observed, despite a notable trend in WT mice (Fig. 38D). These results suggest that, unlike in males, sKL does not distinctly enhance recognition memory in females.

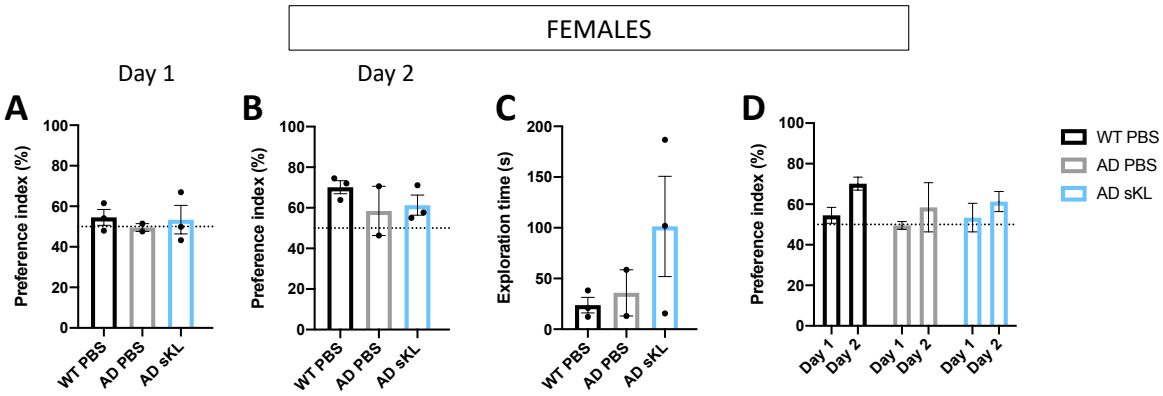



Figure 38. Novel Object Recognition Test for females. (A) Preference index on the first day of the test, when both objects are identical. (B) Preference index for the new object on the second day of the test. (C) Total time mice spend exploring the objects. (D) Comparison of the preference index between both test days. Data are shown as Mean ± SEM, One-way ANOVA and Tukey post-hoc, comparisons between days analyzed by 2-way ANOVA and Tukey post-hoc. Sample size after discarding outliers: WT-PBS=3, AD-PBS=2, AD-sKL=3.

### 1.6.4.3. Morris Water Maze

The Morris Water Maze (MWM) was used to assess spatial learning and memory in mice. Male WT mice performed well from the first learning day, evidenced by a short time to reach the hidden platform (Fig. 39A), a high number of platform entries (Fig. 39B), and a short swimming distance to the platform (Fig. 39C). In contrast, control AD mice initially displayed prolonged latency to reach the platform and a low number of entries. However, they showed learning by progressively improving throughout the experiment, achieving comparable performance to WT mice by the final test day, with reduced latency (day 2 vs day 5, p=0.0487) and distance (day 2 vs day 5, p=0.0234). sKL-treated AD mice, on the other hand, did not present significant improvement across the experiment in any of the

assessed parameters. Notably, the observed differences were not attributed to locomotor abilities, as all three groups demonstrated similar swimming speeds (Fig. 39D). These results indicate that male AD mice did not manifest significant spatial learning impairments, and consequently, treatment with sKL did not lead to observable improvements.

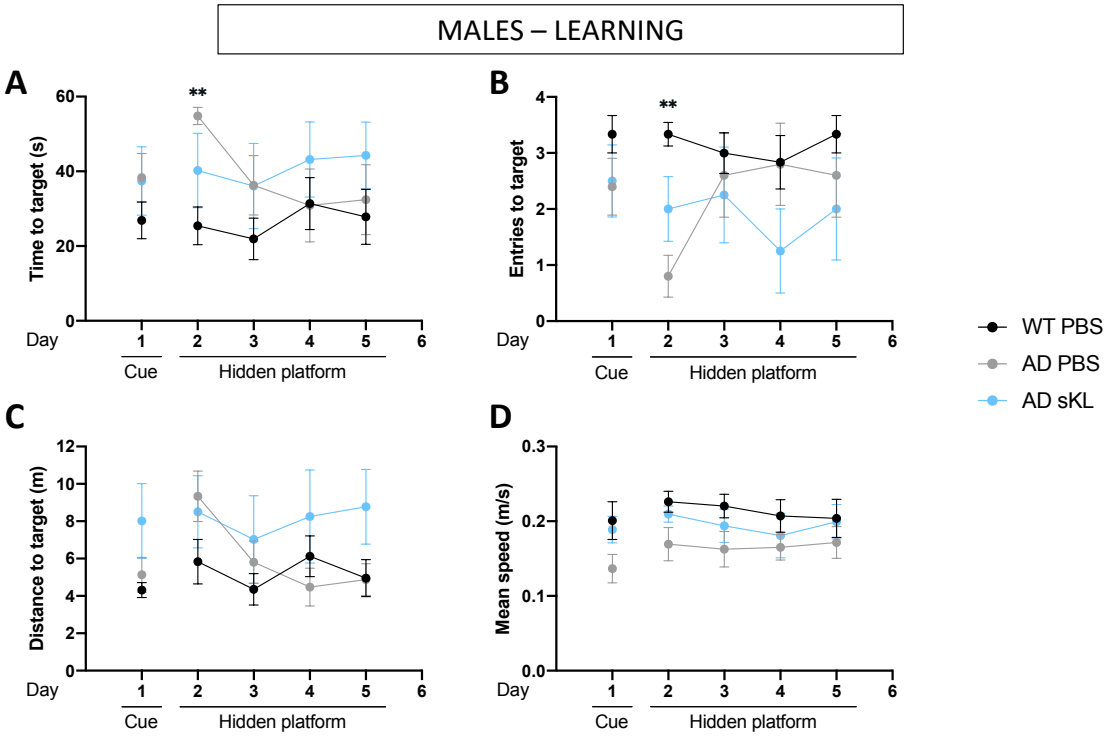



Figure 39. Learning phase of the Morris Water Maze for males. (A) Time to reach the target platform inside the pool. (B) Average of entries to the platform in each training day. (C) Distance traveled to reach the platform. (D) Mean swimming speed. Data are shown as Mean ± SEM, 2-way ANOVA and Tukey post-hoc (**p<0.01). T-test for comparisons of means within groups among test days. Sample size after discarding outliers: WT-PBS=6, AD-PBS=5, AD-sKL=4.

Short-term memory was assessed two hours after the last learning trial in the 2 h probe test, by removing the platform and recording the animals for 60 seconds (Fig. 40A-D). In males, no significant differences were detected in the number of entries into the target zone among groups (Fig. 40A) or the latency to reach the platform zone (Fig. 40B). The time spent in each of the pool's quadrants was also analyzed to determine if mice spent more time in the quadrant where the platform was (Fig. 40C). However, no differences were observed among groups, and swimming speeds were also consistent among them (Fig. 40D). This suggests that male AD mice did not exhibit impairments in short-term memory.

Long-term memory was assessed 24 hours after the last learning trial in the 24 h probe test (Fig. 40E-H). The same parameters as before were analyzed. In male mice, a trend toward reduced number of entries was observed in both AD groups (Fig. 40E), along with a trend toward increased latency to reach the target zone (Fig. 40F). However, no differences were observed in the time spent in the target quadrant (Fig. 40G) or swimming speed (Fig. 40H). These results suggest that male AD may present moderate impairment in long-term memory, which was not mitigated by the treatment with sKL.

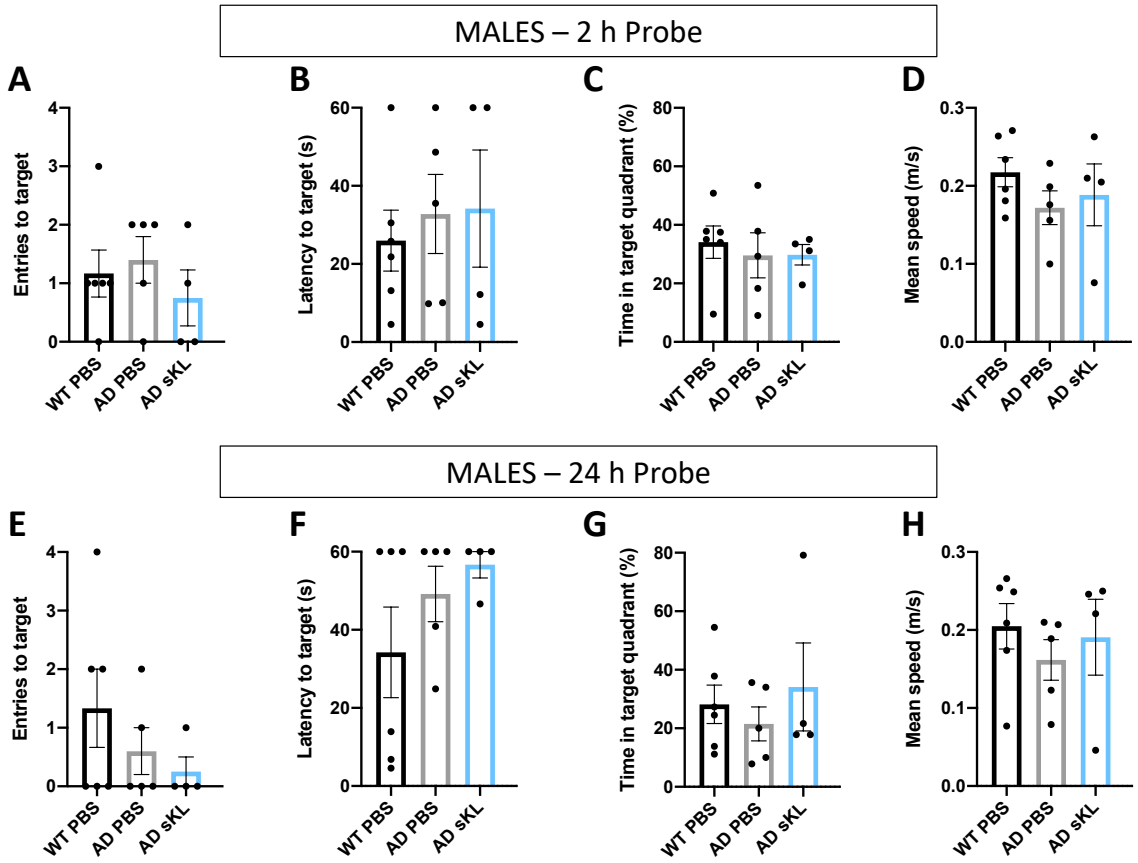



Figure 40. Probe phase of the MWM for males, 2 h probe (A-D) and 24 h probe (E-H). (A, E) Number of entries to the area where the platform was. (B, F) Latency to the first entry into the target area. (C, G) Percentage of time in the target quadrant were the platform used to be. (D, H) Mean swimming speed along the test. Data are shown as Mean ± SEM, 2-way ANOVA and Tukey post-hoc. Sample size after discarding outliers for males: WT-PBS=6, AD-PBS=5, AD-sKL=4.

In the case of females, WT mice performed well from the first learning day, as evidenced by the low latency to reach the platform (Fig. 41A), high number of entries to the platform (Fig. 41B), and short swimming distance to reach the platform (Fig. 41C). However, both AD groups appeared to demonstrate inferior performance compared to WT counterparts on the first day of testing, without displaying a clear learning curve throughout the

experiment. By the final day of testing, both groups showed significantly poorer performance relative to WT mice in the latency to reach the target. These differences among groups were not due to locomotor impairments, as they all exhibited similar swimming speeds (Fig. 41D). These results suggest that female AD mice experienced spatial learning impairments, which were not alleviated by sKL.

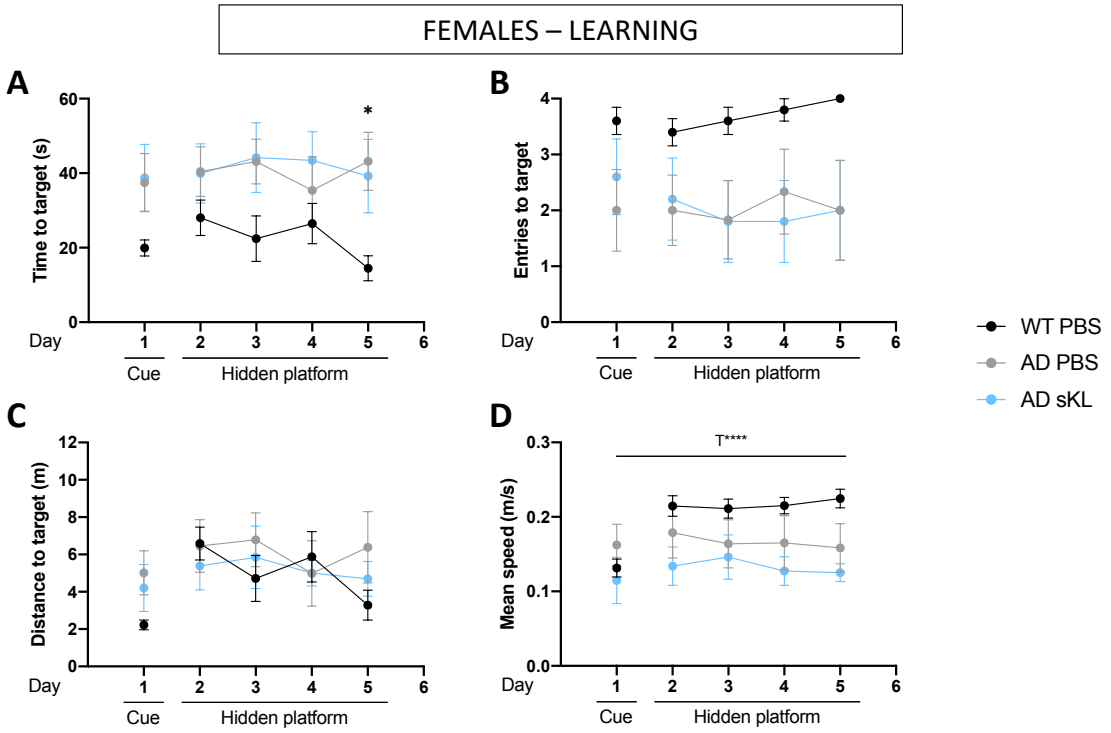



Figure 41. Learning phase of the Morris Water Maze for females. (A) Time to reach the target platform inside the pool. (B) Average of entries to the platform in each training day. (C) Distance traveled to reach the platform. (D) Mean swimming speed. Data are shown as Mean ± SEM, 2-way ANOVA and Tukey post-hoc (*p<0.05, ****p<0.0001). T: time factor. Sample size after discarding outliers: WT-PBS=5, AD-PBS=6, AD-sKL=5.

In the 2 h probe test (Fig. 42A-D), a modest trend toward decreased entries into the platform zone (Fig. 42A) and increased latency (Fig. 42B) were observed in both AD groups. However, no significant differences were noted in the time spent in the target quadrant (Fig. 42C) or mean swimming speed (Fig. 42D). These results indicate a potential moderate short-term memory impairment in female AD mice, which was not alleviated by sKL.

Similarly, in the 24 h probe test (Fig. 42E-H), a comparable trend towards increased latency (Fig. 42F) was observed in both AD groups. Nevertheless, no differences were

observed in the time spent in the target quadrant (Fig. 42G) or mean swimming speed (Fig. 42H). These results suggest the presence of slight long-term memory impairment in female AD mice, which was not ameliorated by sKL.

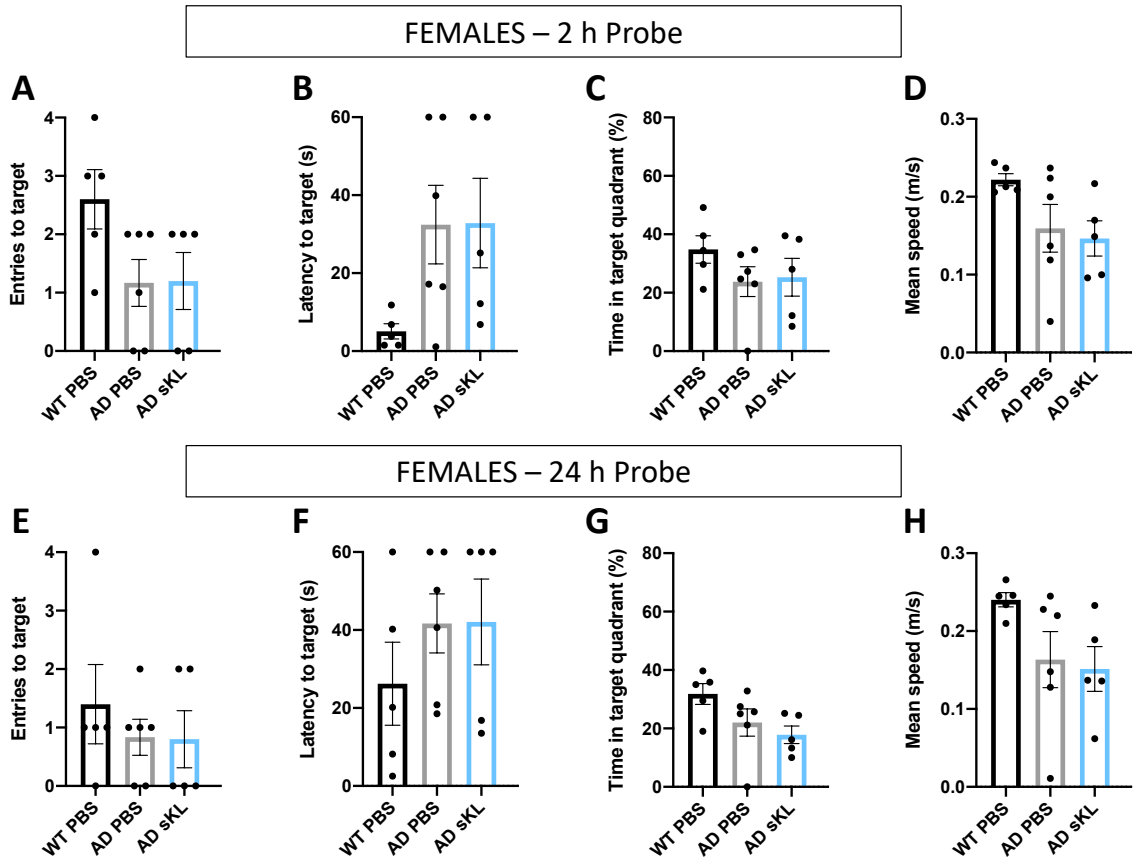



Figure 42. Probe phase of the MWM for females, 2 h probe (A-D) and 24 h probe (E-H). (A, E) Number of entries to the area where the platform was. (B, F) Latency to the first entry into the target area. (C, G) Percentage of time in the target quadrant were the platform used to be. (D, H) Mean swimming speed along the test. Data are shown as Mean ± SEM, 2-way ANOVA and Tukey post-hoc. Sample size after discarding outliers for males: WT-PBS=5, AD-PBS=6, AD-sKL=5.

### 1.6.5. Gene expression analysis

#### 1.6.5.1. qPCR

A gene expression analysis was conducted in four cerebral regions affected to varying extents in Alzheimer's disease: the hippocampus, entorhinal cortex, cerebellum, and olfactory bulbs. Four candidate genes were selected based on prior investigations from our group using an AAV9-sKL viral vector. *Slc17a7* encodes the Vesicular Glutamate Transporter 1, a protein involved in transporting L-glutamate into synaptic vesicles at presynaptic nerve terminals of excitatory neural cells. *Homer1* encodes a protein involved

in the scaffolding of the postsynaptic density, and necessary for the structural integrity of dendritic spines, along with glutamate neurotransmission. *Foxo3* encodes a protein that regulates different processes including apoptosis and autophagy. *Def8* encodes a protein that positively regulates lysosome peripheral distribution.

In the hippocampus (Fig. 43), a consistent trend was observed in both male and female mice regarding the expression of *Slc17a7* (Fig. 43A, E). Notably, a trend towards a decrease in *Slc17a7* expression was evident in AD mice, which appeared to be restored with sKL treatment. The *Homer1* gene displayed a significant decrease in expression specifically in male AD mice (Fig. 43B), with expression levels restored following treatment; however, no such difference was observed in females (Fig. 43F). There were no significant differences among groups in the expression of *Foxo*3 (Fig. 43C, G) or *Def8* (Fig. 43D, H) in the hippocampus.

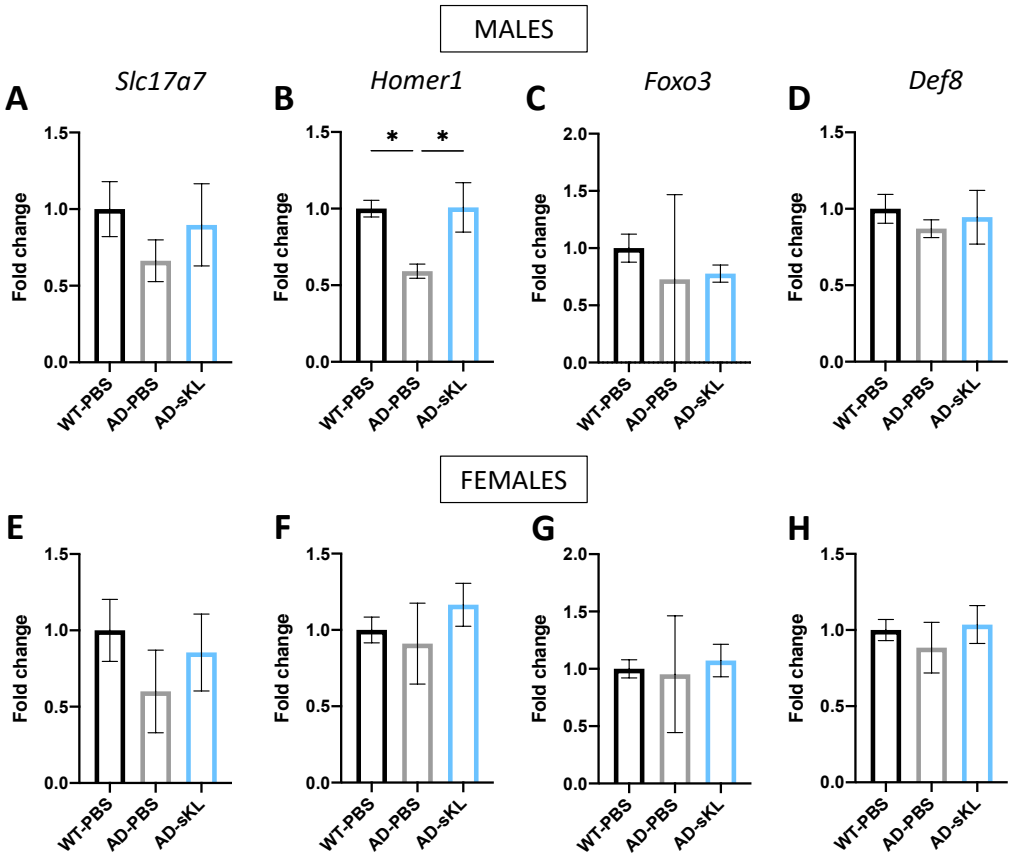



Figure 43. Gene expression analysis in the hippocampus of males (A-D) and females (E-H), represented as fold change normalized to the WT group. (A, E) Expression of *Slc17a7*. (B, F) Expression of *Homer1*. (C, G) Expression of *Foxo3*. (D, H) Expression of *Def8*. Data are shown as Mean ± SEM, One-way ANOVA and Tukey post-hoc (*p<0.05). Sample size for males after discarding outliers: WT-PBS=6, AD-PBS=5, AD-sKL=4. Sample size for females after discarding outliers: WT-PBS=5, AD-PBS=3, AD-sKL=5.

In the entorhinal cortex (Fig. 44), results differed for the *Slc17a7* gene. Notably, there was no apparent decrease in expression observed in male AD mice, although a moderate increase was noted in sKL-treated mice (Fig. 44A). In contrast, females exhibited a trend towards decreased expression in both AD groups (Fig. 44E). *Homer1* expression significantly decreased in AD males, and the treatment with sKL appeared to rescue the expression levels of WT mice (Fig. 44B). However, no such differences were observed in females (Fig. 44F). Regarding *Foxo3* (Fig. 44C, G) and *Def8* (Fig. 44D, H), no significant differences were observed among groups.

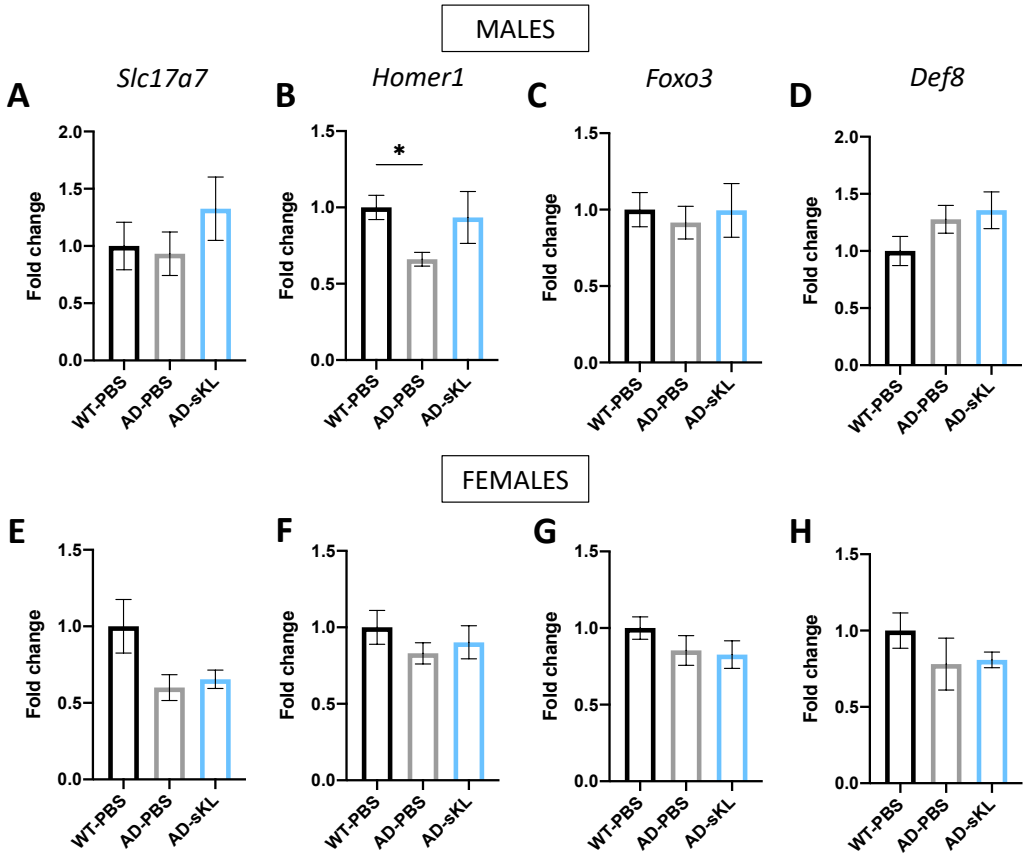



Figure 44. Gene expression analysis in the entorhinal cortex of males (A-D) and females (E-H), represented as fold change normalized to the WT group. (A, E) Expression of *Slc17a7*. (B, F) Expression of *Homer1*. (C, G) Expression of *Foxo3*. (D, H) Expression of *Def8*. Data are shown as Mean ± SEM, One-way ANOVA and Tukey post-hoc (*p<0.05). Sample size for males after discarding outliers: WT-PBS=6, AD-PBS=5, AD-sKL=3. Sample size for females after discarding outliers: WT-PBS=5, AD-PBS=6, AD-sKL=5.

In the cerebellum (Fig. 45), no significant differences were observed in any of the analyzed genes. This suggests that this cerebral area was not significantly affected in the animal model and remained unaltered by the treatment.

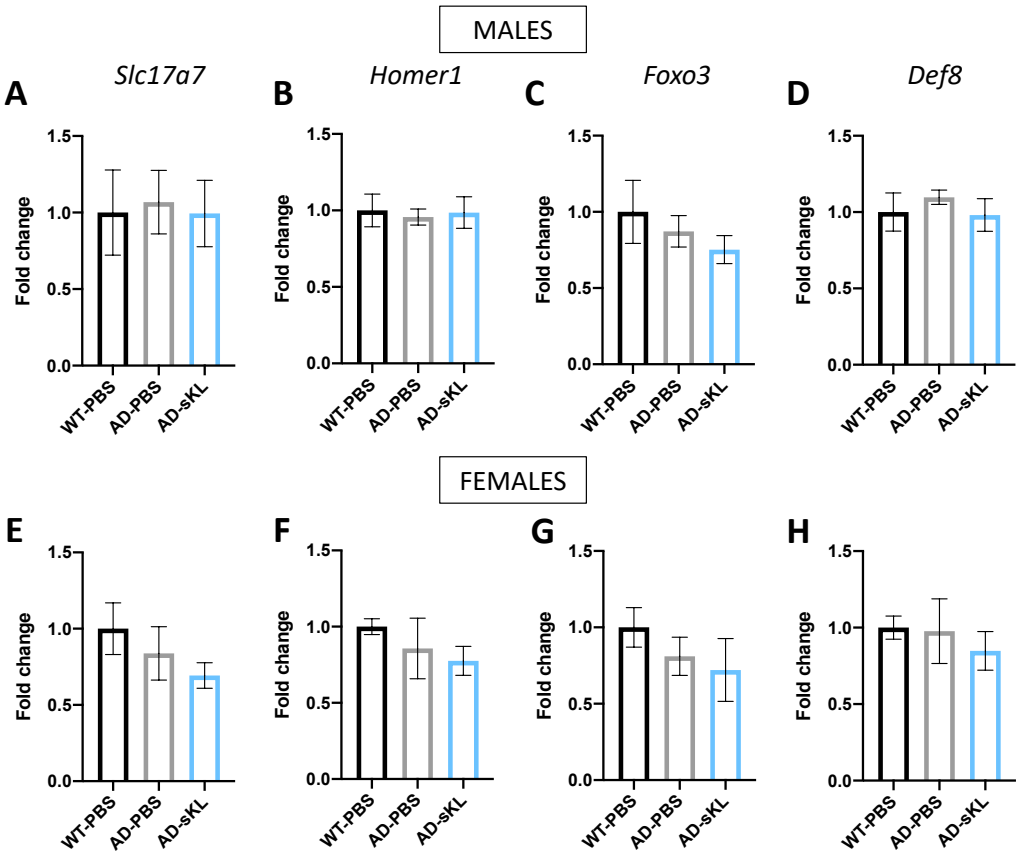



Figure 45. Gene expression analysis in the cerebellum of males (A-D) and females (E-H), represented as fold change normalized to the WT group. (A, E) Expression of *Slc17a7*. (B, F) Expression of *Homer1*. (C, G) Expression of *Foxo3*. (D, H) Expression of *Def8*. Data are shown as Mean ± SEM, One-way ANOVA and Tukey post-hoc. Sample size for males after discarding outliers: WT-PBS=6, AD-PBS=5, AD-sKL=4. Sample size for females after discarding outliers: WT-PBS=5, AD-PBS=6, AD-sKL=5.

In the olfactory bulbs (Fig. 46), differences were only observed in the *Homer1* gene. In males, a significant decrease was observed in AD mice, which was not recovered by sKL (Fig. 46B). In females, a similar trend was noted, although statistical significance was not achieved (Fig. 46F). No significant differences were observed among groups for the other analyzed genes in the olfactory bulbs.

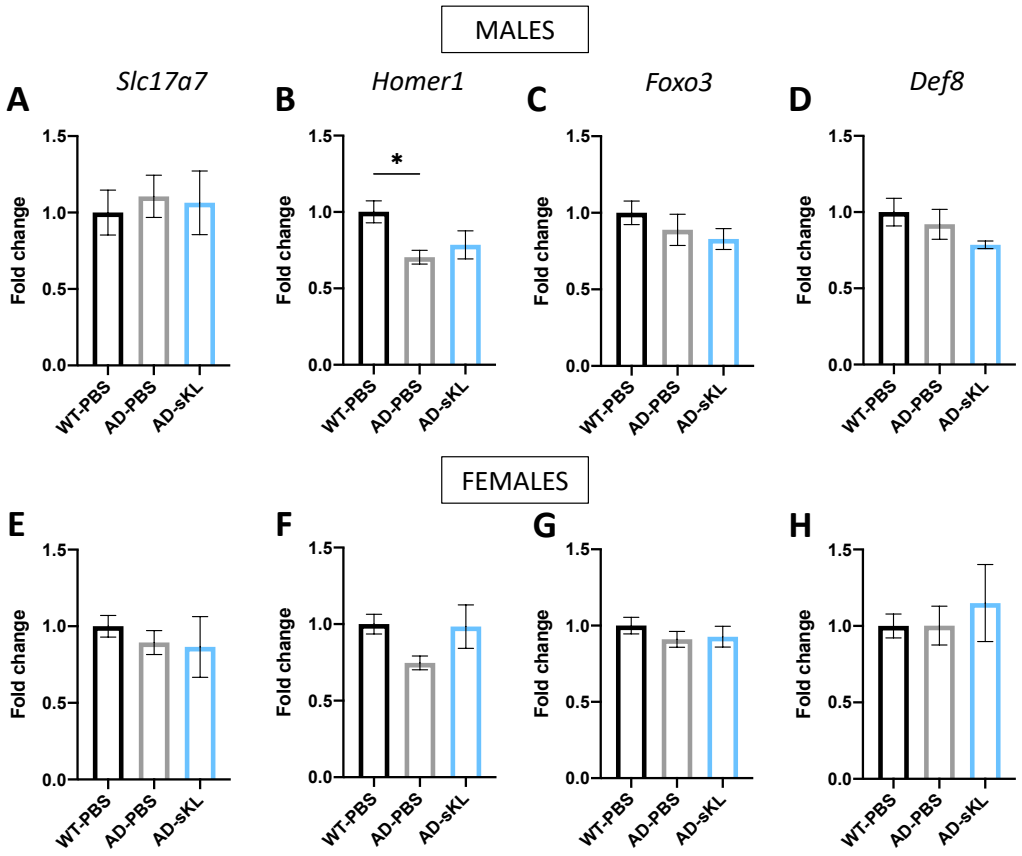



Figure 46. Gene expression analysis in the olfactory bulb of males (A-D) and females (E-H), represented as fold change normalized to the WT group. (A, E) Expression of *Slc17a7*. (B, F) Expression of *Homer1*. (C, G) Expression of *Foxo3*. (D, H) Expression of *Def8*. Data are shown as Mean ± SEM, One-way ANOVA and Tukey post-hoc (*p<0.05). Sample size for males after discarding outliers: WT-PBS=5, AD-PBS=5, AD-sKL=4. Sample size for females after discarding outliers: WT-PBS=5, AD-PBS=6, AD-sKL=4.

#### 1.6.5.2. RNA-seq

An RNA-seq analysis was conducted to further explore potentially affected pathways in the animal model and assess whether sKL treatment mitigated these changes, with a focus on hippocampal samples due to their significant involvement in AD pathology.

Initially, a principal component analysis (PCA) plot was used to discern the expression patterns among the experimental groups. In males, no clear differences were observed in expression patterns among groups (Fig. 47A), whereas in females, distinct groupings were evident (Fig. 48A). With the aim of understanding the changes between the control AD mouse model and the WT group, a KEGG pathway enrichment plot was used (Fig. 47B, C, Fig. 48B, C). A total of 4635 differentially expressed genes (DEGs) were identified in males,

while only 438 were detected in females. These upregulated and downregulated DEGs were subsequently assigned to various biological pathways.

In males, upregulation was observed in pathways related to “lysosome”, “phagosome”, “Fcγ R-mediated phagocytosis”, “apoptosis” and “cellular senescence” (Fig. 47B), alongside downregulation of various synapse types and the long-term potentiation involved in memory formation (Fig. 47C). However, no significant pathological traits were identified in female AD mice, likely due to the low number of DEGs (Fig. 48B, C). These results suggest that male AD mice exhibit key molecular characteristics of the disease, while females may not have developed a strong phenotype by 6 months of age.

In terms of differences between sKL-treated mice and AD mice, a total of 1032 DEGs were identified in males, and 440 in females. Once again, these were assigned to biological pathways. Notably, in males, sKL treatment primarily impacted neuronal regulation and synaptic transmission improvement (Fig. 47D), accompanied by reductions in Aβ and pTau formation (Fig. 47E). However, conclusive interpretations were challenging for female mice, as the animal model did not present significant differences compared to WT mice (Fig. 48D, E).

Overall, these results suggest that the animal model displays clear signs of pathology only in males and not in females, at least by 6 months of age. Furthermore, sKL treatment appears to ameliorate specific pathological pathways altered in males through pronounced transcriptional effects.

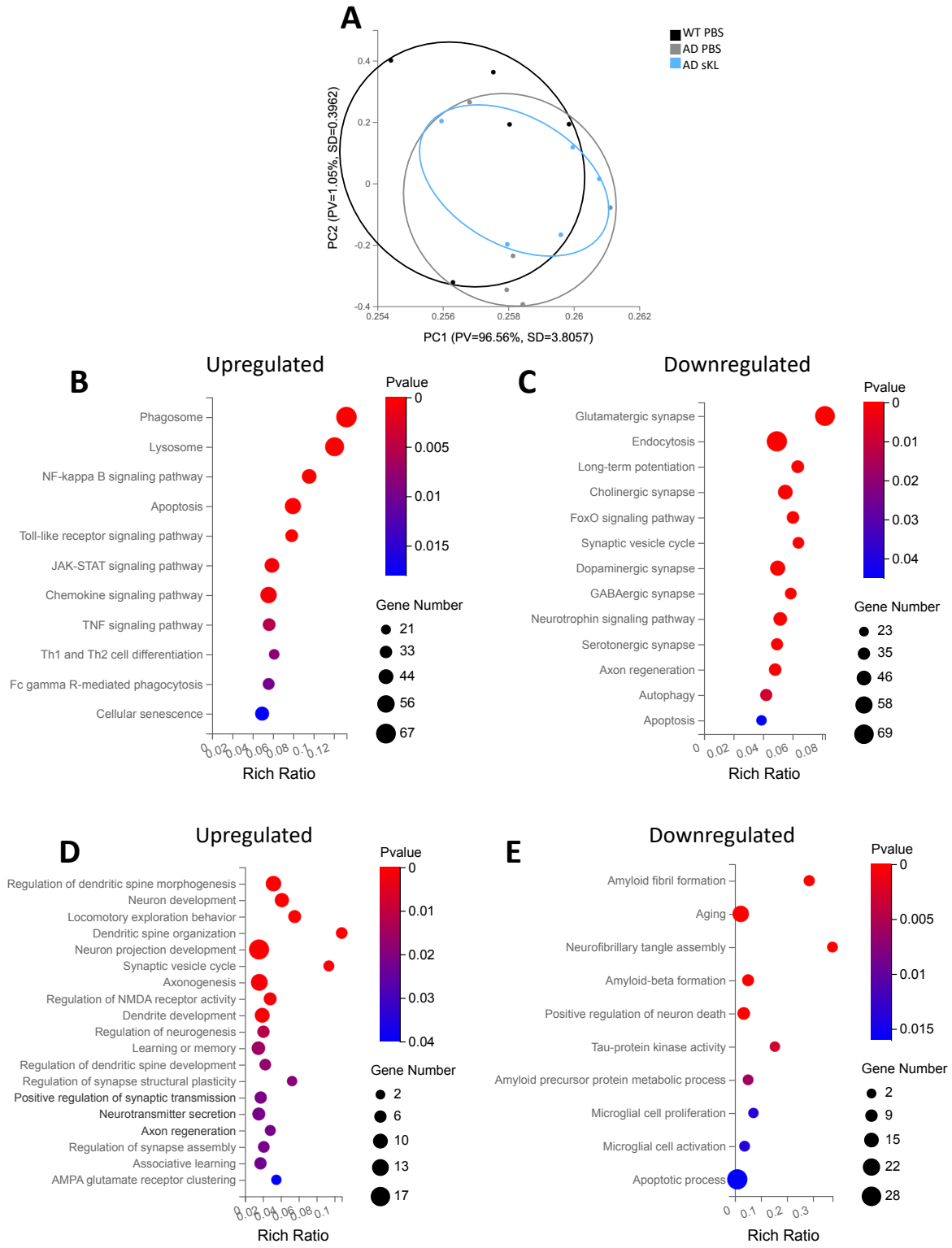



Figure 47. RNA-seq analysis of hippocampus samples for males. (A) Principal component analysis (PCA) plot. (B) KEGG pathways enriched in AD-PBS vs WT-PBS upregulated genes. (C) KEGG pathways enriched in AD-PBS vs WT-PBS downregulated genes. (D) GO pathways enriched in AD-sKL vs AD-PBS upregulated genes. (E) GO pathways enriched in AD-sKL vs AD-PBS downregulated genes. The abscissa represents the rich ratio, indicating the proportion of DEGs in each pathway. The number of DEGs in each pathway is represented by the circle area, and the color represents the corrected p-value. Sample size of 5 per group.

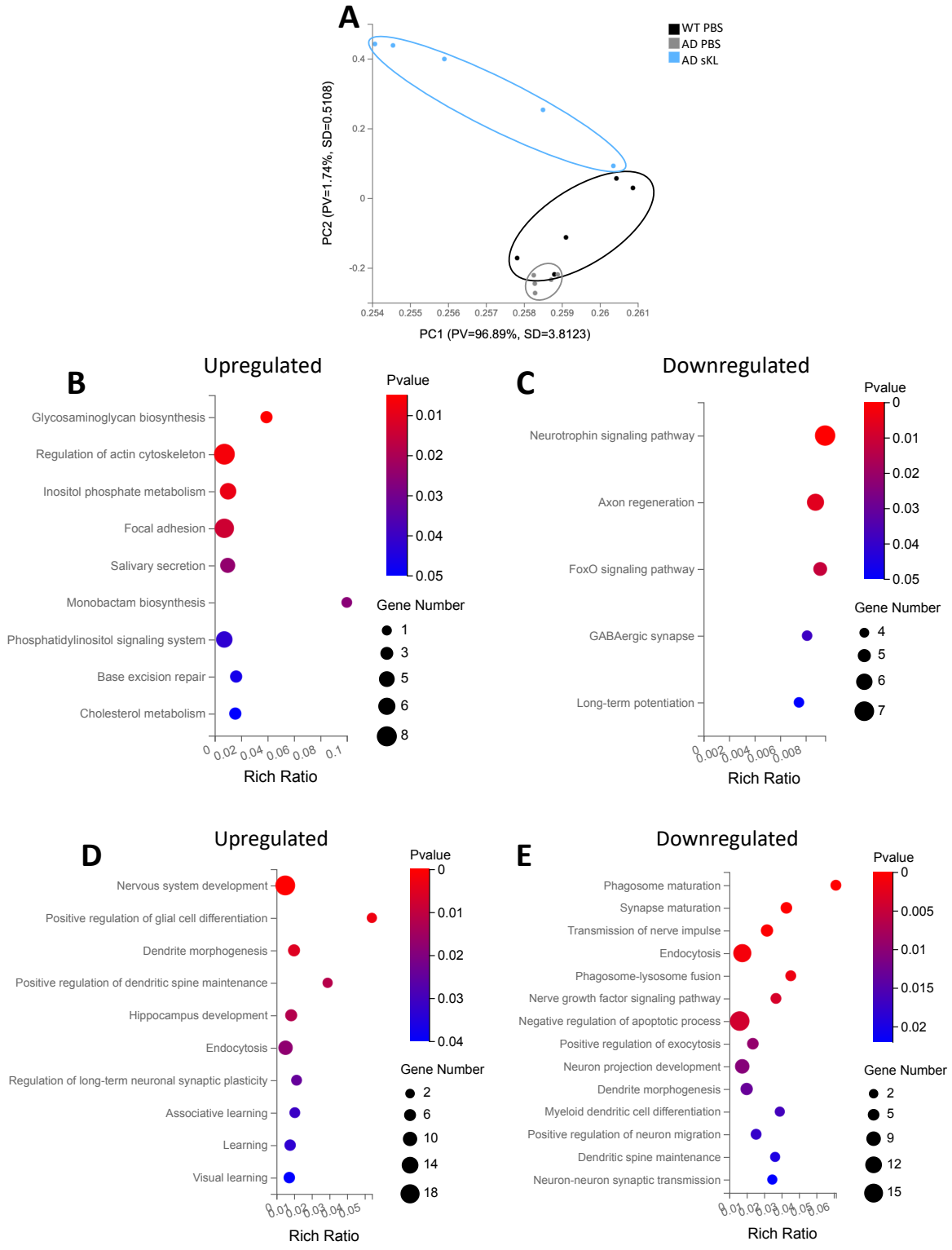



Figure 48. RNA-seq analysis of hippocampus samples for males. (A) Principal component analysis (PCA) plot. (B) KEGG pathways enriched in AD-PBS vs WT-PBS upregulated genes. (C) KEGG pathways enriched in AD-PBS vs WT-PBS downregulated genes. (D) GO pathways enriched in AD-sKL vs AD-PBS upregulated genes. (E) GO pathways enriched in AD-sKL vs AD-PBS downregulated genes. The abscissa represents the rich ratio, indicating the proportion of DEGs in each pathway. The number of DEGs in each pathway is represented by the circle area, and the color represents the corrected p-value. Sample size of 5 per group.

### 1.6.6. Histopathology

Histopathological studies are valuable for visually assessing changes in tissues. In this study, we analyzed the brains of mice through immunofluorescence imaging, focusing on the hippocampus, a brain region crucial for memory and learning and affected early in AD.

#### 1.6.6.1. GFAP

GFAP serves as an astrocytic marker, aiding in the assessment of reactive astrogliosis in the brain (Fig. 49A). Notably, only sKL-treated males showed an increase in astrogliosis in the dentate gyrus (DG) (Fig. 49B) and the CA3 area (Fig. 49D), while females did not present significant differences among groups (Fig. 49C, E).

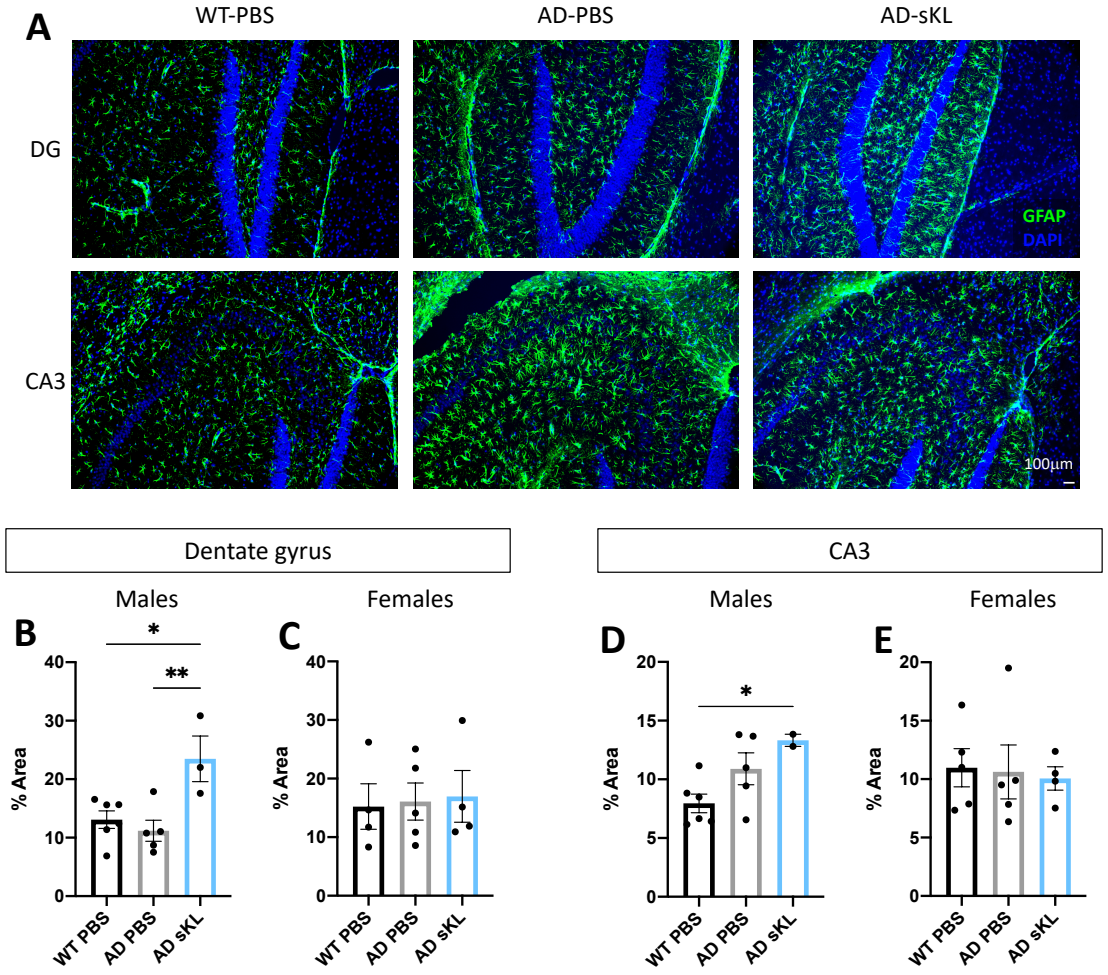



Figure 49. GFAP immunofluorescence in hippocampus, dentate gyrus (B, C) and CA3 (D, E). (A) Representative images for immunofluorescence with GFAP antibody. Green: GFAP labeling, blue: DAPI. (B, C) Quantification of positive GFAP area in the dentate gyrus, in males and females, respectively. (E, F) Quantification of positive GFAP area in the CA3 region, in males and females, respectively. Data are shown as Mean ± SEM, One-way ANOVA and Tukey post-hoc (*p<0.05, **p<0.01). Sample size for males: WT-PBS=6, AD-PBS=5, AD-sKL=3. Sample size for females: WT-PBS=4, AD-PBS=5, AD-sKL=4.

### 1.6.6.2. Iba1

Iba1 is a microglial marker, used to assess microglial activation in the brain (Fig. 50A). No significant differences in microglial activation were observed among groups in either sex or hippocampal areas (Fig. 50B-E), indicating that microglial activation was not prominent in mice of this age.

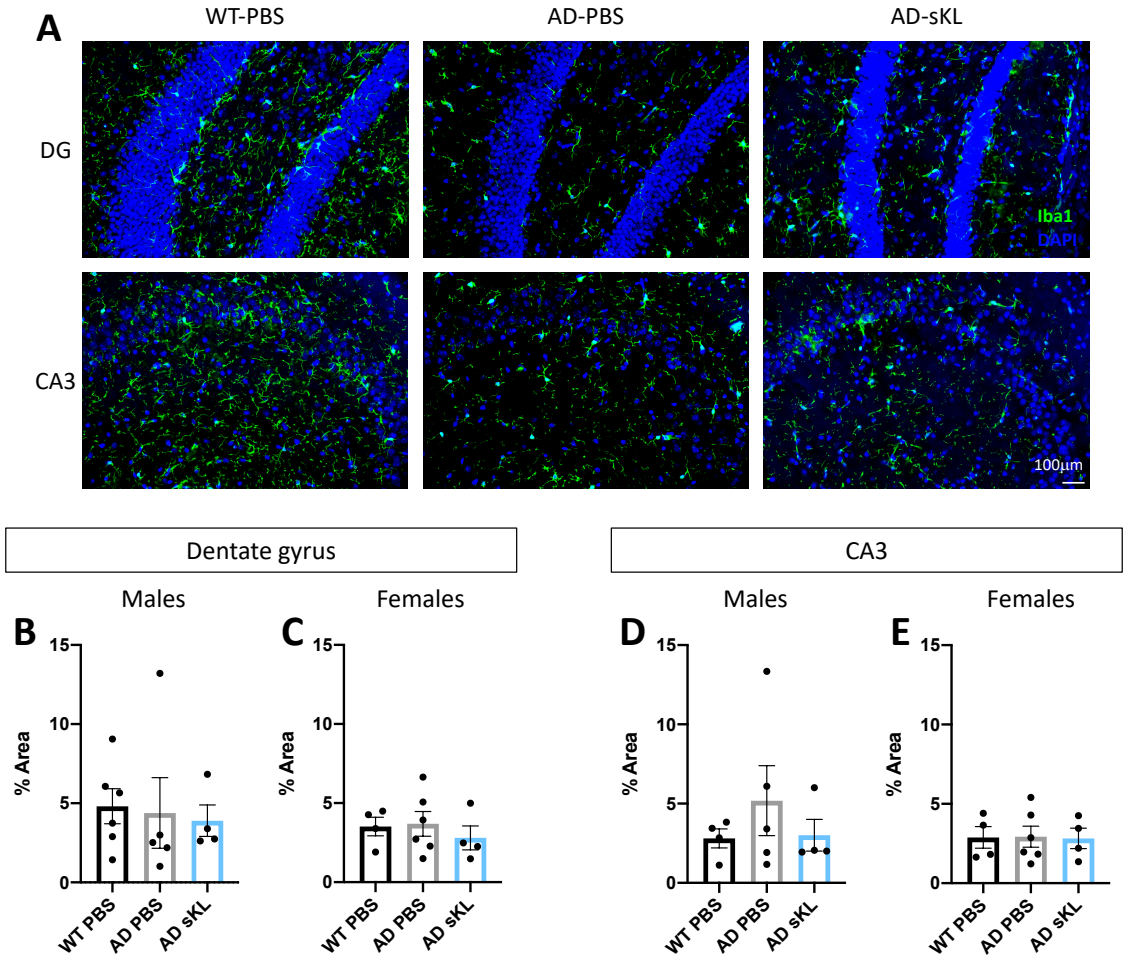



Figure 50. Iba1 immunofluorescence in hippocampus, dentate gyrus (B, C) and CA3 (D, E). (A) Representative images for immunofluorescence with Iba1 antibody. Green: Iba1 labeling, blue: DAPI. (B, C) Quantification of positive Iba1 area in the dentate gyrus, in males and females, respectively. (E, F) Quantification of positive Iba1 area in the CA3 region, in males and females, respectively. Data are shown as Mean ± SEM, One-way ANOVA and Tukey post-hoc. Sample size for males: WT-PBS=6, AD-PBS=5, AD-sKL=4. Sample size for females: WT-PBS=4, AD-PBS=6, AD-sKL=4.

### 1.6.6.3. pTau

Neurofibrillary tangles, composed of a hyperphosphorylated form of the Tau protein (pTau), are key hallmarks of AD (Fig. 51A). WT mice did not exhibit pTau in the hippocampus, as expected (Fig. 51B-E). However, all AD mice displayed significant levels of pTau in both analyzed areas and sexes. The increased pTau levels were not attenuated in males treated with sKL (Fig. 51B, D), and only in the CA3 area of females was a decrease observed with the treatment (Fig. 51E). These results suggest that sKL did not exert a clear impact on pTau levels in the hippocampus.

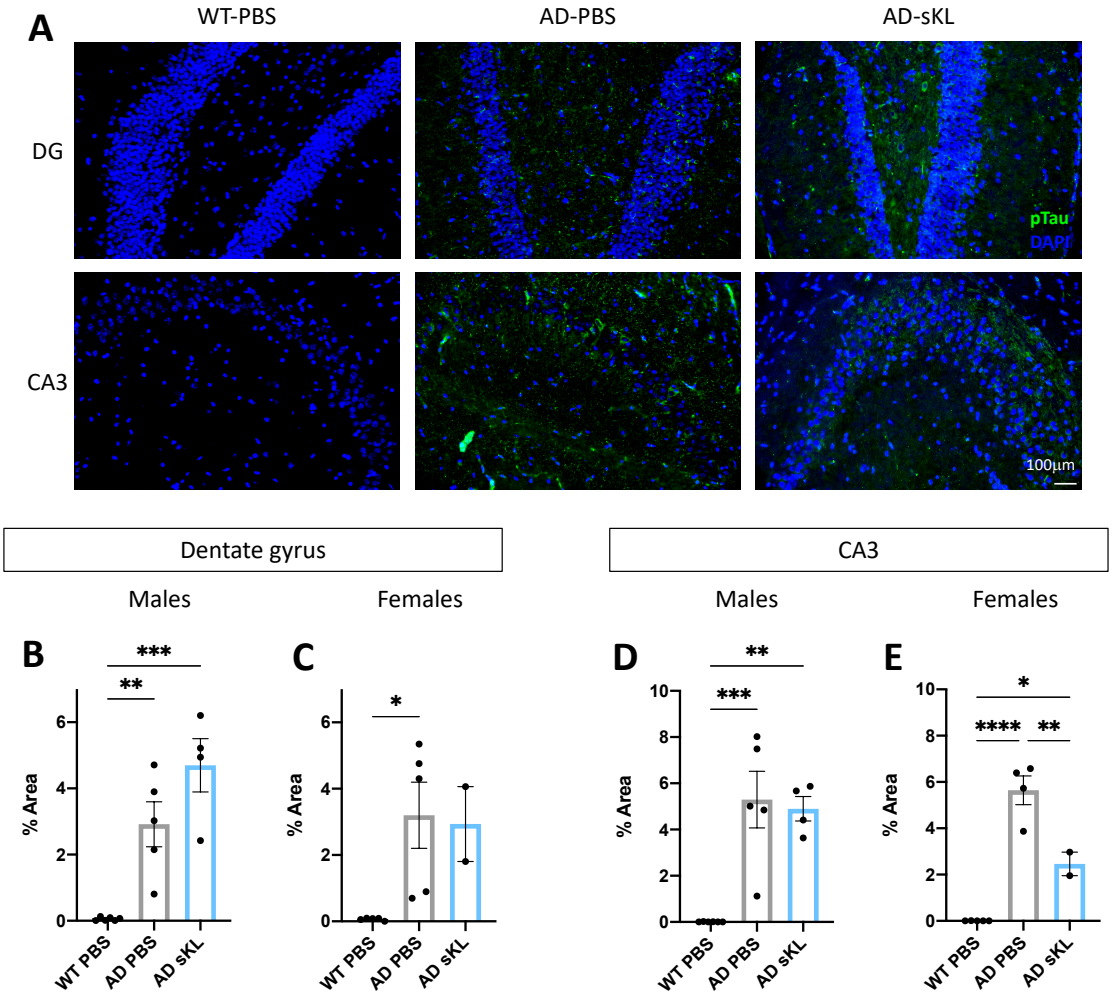



Figure 51. pTau immunofluorescence in hippocampus, dentate gyrus (B, C) and CA3 (D, E). (A) Representative images for immunofluorescence with phospho-Tau (Ser202, Thr205) antibody. Green: pTau labeling, blue: DAPI. (B, C) Quantification of positive pTau area in the dentate gyrus, in males and females, respectively. (E, F) Quantification of positive pTau area in the CA3 region, in males and females, respectively. Data are shown as Mean ± SEM, One-way ANOVA and Tukey post-hoc (*p<0.05, **p<0.01, ***p<0.001, ****p<0.0001). Sample size for males: WT-PBS=6, AD-PBS=5, AD-sKL=4. Sample size for females: WT-PBS=5, AD-PBS=5, AD-sKL=2.

# Chapter 2

## Design, generation, and proof of concept of HEBE

The aim of this study was to develop a novel chimeric chronokine, called HEBE, connecting sKL, sTREM2 and TIMP2, which would combine their therapeutic effects in one secretable molecule. This novel chronokine could simultaneously target multiple mechanisms affected in AD, providing an advantage over other treatments that target a single therapeutic pathway.

### 2.1. Bioinformatic analysis

To generate a functional chimeric chronokine assembling sKL, sTREM2 and TIMP2, a comprehensive bioinformatic analysis was performed in collaboration with Dr Jesús Giraldo's group from the Institute of Neuroscience at Universitat Autònoma de Barcelona. The goal was to examine the structures of these proteins and their potential intermolecular interactions. Human isoforms of these proteins were specifically used in the study to facilitate future translatability to humans.

#### 2.1.1. Analyses of individual chronokines

The proteins were initially analyzed separately to gain insights into their structures and conformational dynamics. Molecular dynamics (MD) simulations were conducted starting from available crystal structures, followed by the construction of all-atom models, and a 520 ns trajectory was calculated for each protein. Additionally, the electrostatic charges of the proteins were assessed.

##### 2.1.1.1. sKL

Analysis of the root-mean-square deviations (RMSD) indicated that sKL exhibits notable flexibility, displaying structural variability throughout the trajectory compared to the reference crystal structure (Fig. 52A). This flexibility was further evident in the principal component analysis (PCA), where the chronokine explored a large conformational space, and therefore adopted distinct conformations during the simulations (Fig. 52B).

Root-mean-square fluctuations (RMSF) analysis allowed for the identification of regions of highest flexibility within the protein (Fig. 52C), with protein structure colored to reflect the relative magnitude of fluctuations, ranging from blue (low amplitude) to red (high amplitude) (Fig. 52D). The flexibility of sKL may be associated with functional motions; therefore, any attempt to combine the proteins should preserve the conformational freedom to avoid disrupting the functions.

Electrostatic charges were also analyzed, as they could indicate the propensity of the proteins to interact with each other. In the case of sKL, two main faces were observed: one with mainly positive charges and the other with mainly negative charges (Fig. 52E).

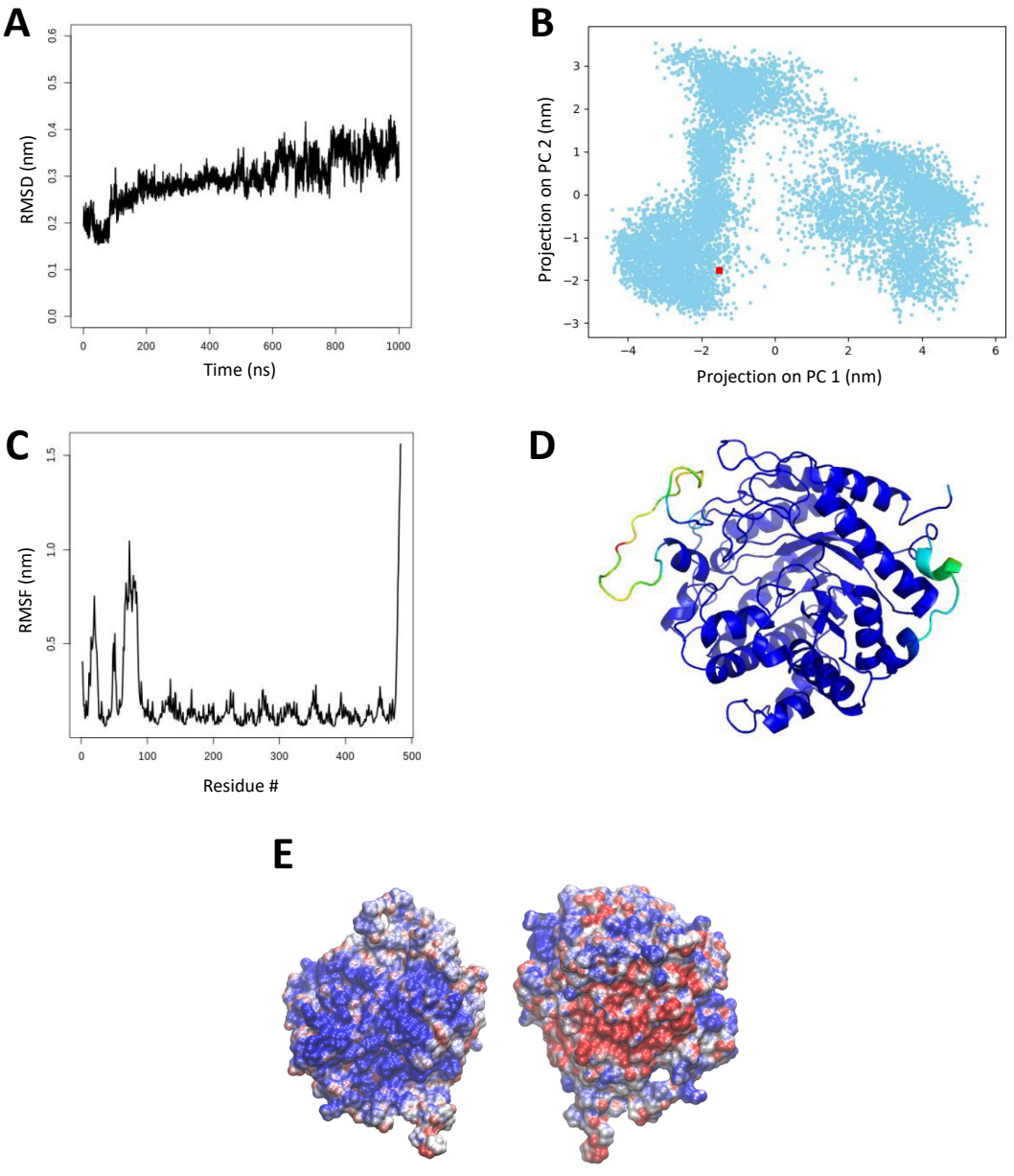
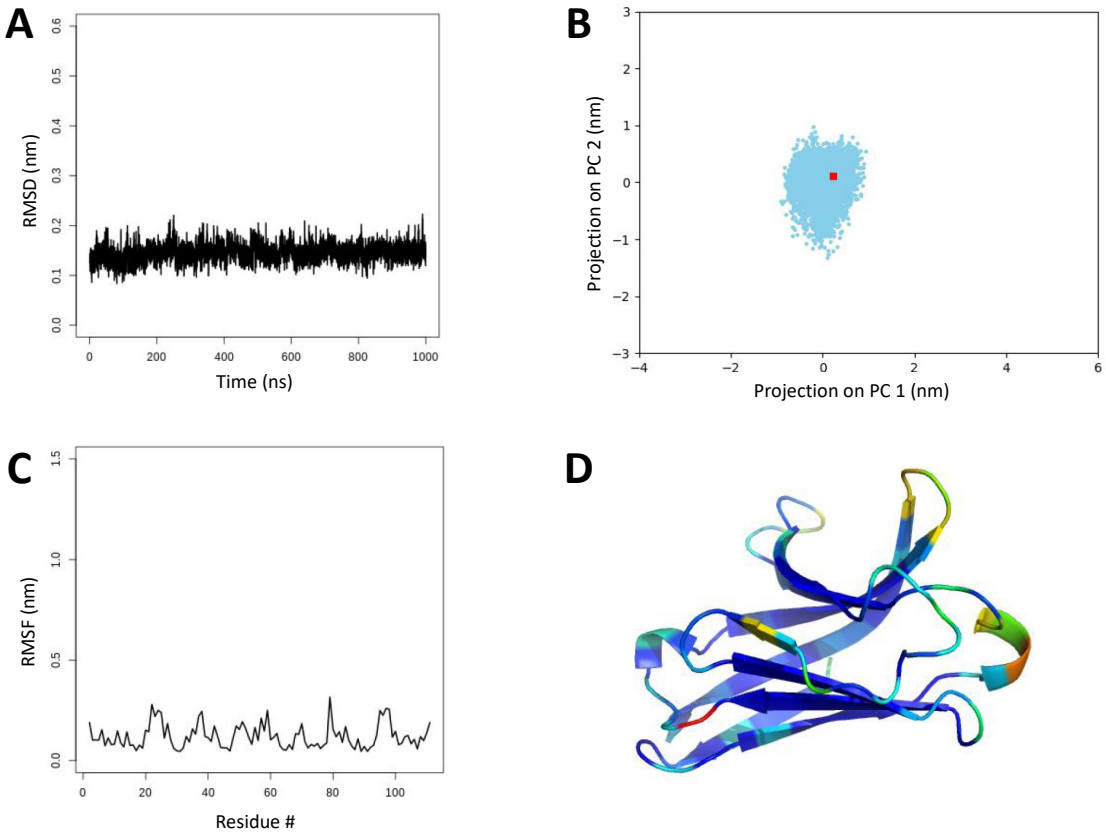


Figure 52. Bioinformatic analysis for sKL. (A) Root-mean-square deviation (RMSD) analysis, indicating how the protein's structure changes over time compared to the initial crystal structure. (B) Principal component analysis (PCA). Projection of trajectory in the space of the first two principal components. The red square denotes the crystal structure used as the starting conformation of the simulation. Conformations visited in the trajectory are represented by blue dots. (C) Root-mean-square fluctuations (RMSF) analysis, indicating the flexibility of individual residues during the simulation. (D) Structure of sKL colored according to the amplitude of the RMSF. The color scale ranges from blue (low amplitude fluctuations, greater rigidity) to red (high amplitude fluctuations, greater flexibility). (E) Distribution of electrostatic charges in the two main faces of the protein, blue indicating positive charge, red indicating negative charge, and white indicating neutral charge.

#### 2.1.1.2. sTREM2

sTREM2 presented less flexibility, as indicated by lower RMSD values (Fig. 53A) and a more restricted dynamic observed in the PCA analysis (Fig. 53B), with a smaller conformational space explored during the simulation and lower amplitude fluctuations (Fig. 53C, D). Electrostatic charge analysis showed sTREM2 to be primarily positively charged (Fig. 53E), which could potentially lead to interactions with the negatively charged face of sKL.



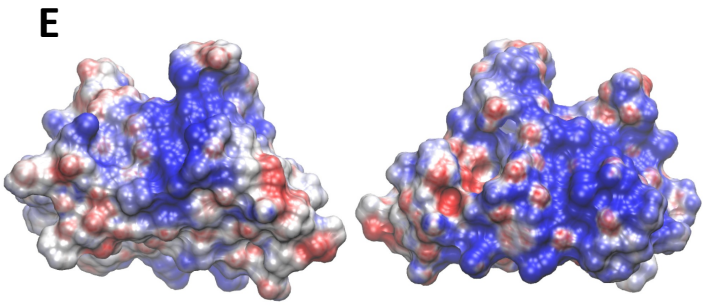



Figure 53. Bioinformatic analysis for sTREM2. (A) Root-mean-square deviation (RMSD) analysis, indicating how the protein's structure changes over time compared to the initial crystal structure. (B) Principal component analysis (PCA). Projection of trajectory in the space of the first two principal components. The red square denotes the crystal structure used as the starting conformation of the simulation. Conformations visited in the trajectory are represented by blue dots. (C) Root-mean-square fluctuations (RMSF) analysis, indicating the flexibility of individual residues during the simulation. (D) Structure of sTREM2 colored according to the amplitude of the RMSF. The color scale ranges from blue (low amplitude fluctuations, greater rigidity) to red (high amplitude fluctuations, greater flexibility). (E) Distribution of electrostatic charges in the two main faces of the protein, blue indicating positive charge, red indicating negative charge, and white indicating neutral charge.

#### 2.1.1.3. TIMP2

TIMP2 exhibited more flexibility, similar to sKL, as evidenced by higher RMSD values (Fig. 54A) and the PCA analysis, indicating a larger conformational space explored during the MD simulation (Fig. 54B), along with greater amplitude fluctuations (Fig. 54C, D). Electrostatic charge analysis revealed that one side of TIMP2 is positively charged, while the other side shows a more neutral charge (Fig. 54E). This suggests that the positively charged side could be prone to contacts with the negatively charged side of sKL.

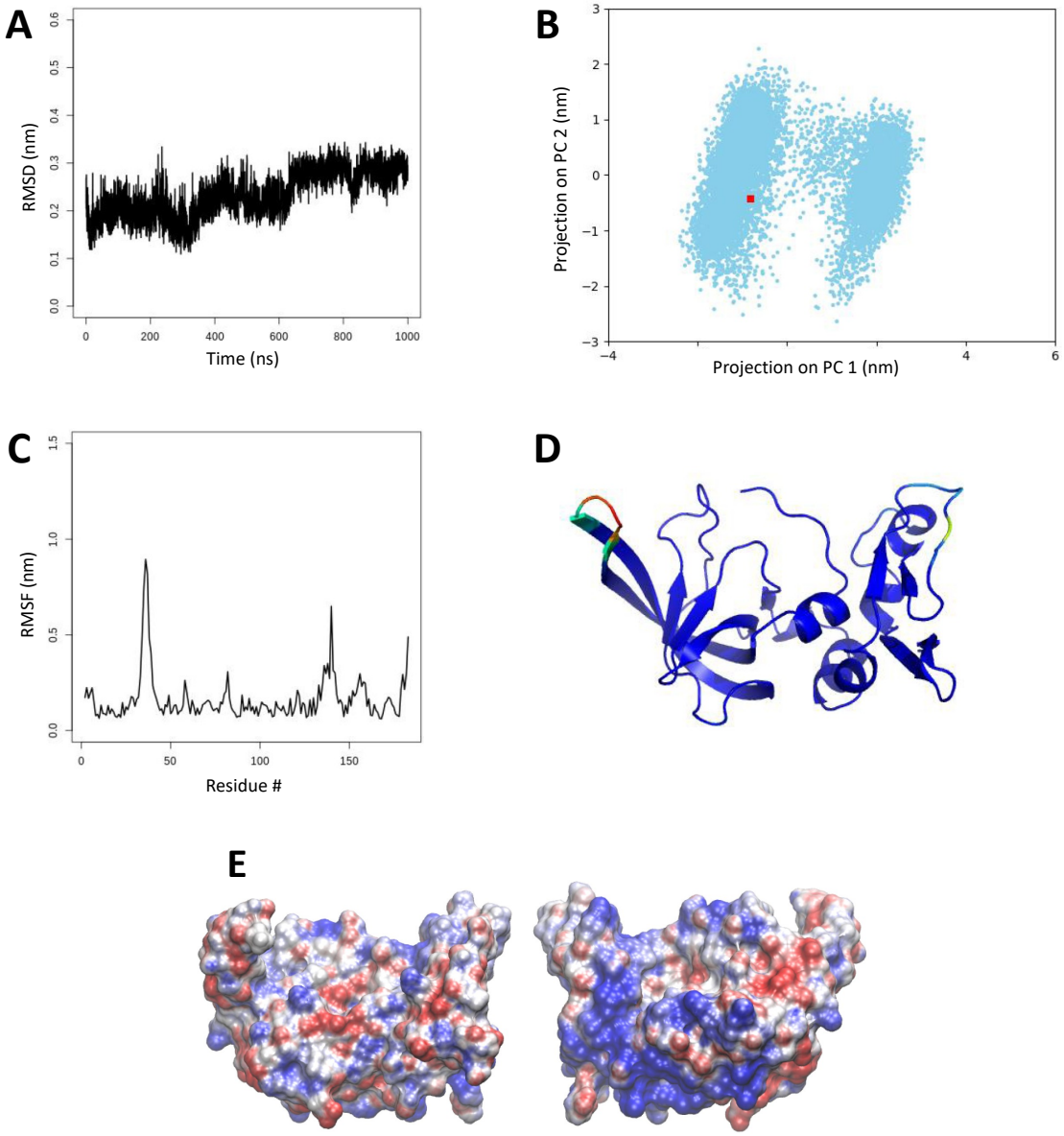



Figure 54. Bioinformatic analysis for TIMP2. (A) Root-mean-square deviation (RMSD) analysis, indicating how the protein's structure changes over time compared to the initial crystal structure. (B) Principal Component Analysis (PCA). Projection of trajectory in the space of the first two principal components. The red square denotes the crystal structure used as the starting conformation of the simulation. Conformations visited in the trajectory are represented by blue dots. (C) Root-mean-square fluctuations (RMSF) analysis, indicating the flexibility of individual residues during the simulation. (D) Structure of TIMP2 colored according to the y amplitude of the RMSF. The color scale ranges from blue (low amplitude fluctuations, greater rigidity) to red (high amplitude fluctuations, greater flexibility). (E) Distribution of electrostatic charges in the two main faces of the protein, blue indicating positive charge, red indicating negative charge, and white indicating neutral charge.

### 2.1.2. Analyses of HEBE candidates

#### 2.1.2.1. Candidate 1

The first attempt to connect the proteins involved joining the three chronokines without any linkers. sKL, being the largest protein, was positioned centrally with the other two proteins placed on either side. Given the unstructured nature of the C-terminal regions of these proteins, these regions were used as natural linkers, colored in grey (Fig. 55A). MD simulations revealed protein interactions leading to aggregation that could potentially hinder their biological activity (Fig. 55B). As a result, this initial candidate was discarded.

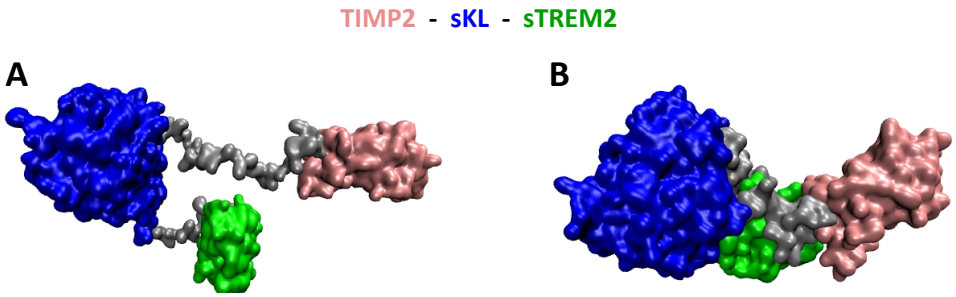



Figure 55. Representation of the first candidate. (A) Structure of the protein before molecular dynamic simulations. (B) Structure of the protein after molecular dynamic simulations.

#### 2.1.2.2. Candidate 2

For the second simulation, linkers were introduced between the proteins to keep them spatially separated from each other and prevent interactions that could lead to aggregation. Linkers can be either flexible or rigid, and for the present simulation a rigid helical linker was chosen ($EAAAK_X$), with the aim to reduce the flexibility of the overall protein and prevent interactions among the subunits. However, after running MD simulations, this arrangement of the proteins also resulted in aggregation (Fig. 56). This aggregation tendency could be attributed to the electrostatic properties of sKL, which features both predominantly positive and negative faces, as previously discussed, potentially attracting the other proteins.

sTREM2 - $(EAAAK)_3$ - sKL - $(EAAAK)_3$ - TIMP2

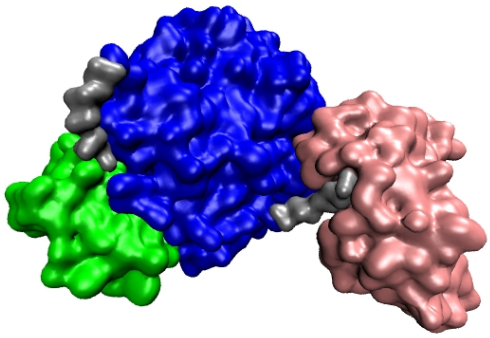


Figure 56. Representation of the second candidate after running molecular dynamic simulations.

#### 2.1.2.3. Candidate 3

The previous arrangement of the proteins, with sKL in the middle, did not lead to a viable candidate as proteins aggregated, prompting a new arrangement. Therefore, sKL was positioned at the C-terminal end of the protein to prevent interactions with the other proteins, and the second linker was extended to further separate sKL from sTREM2 and TIMP2 (Fig. 57). This new arrangement did not result in aggregation, as inter-protein contacts were less frequently observed. Consequently, this candidate was named HEBE and used for subsequent assays.

As the protein was intended to be secreted by the cells, the N-terminal signal peptide of sTREM2 was retained, while the signal peptides of TIMP2 and sKL were omitted from the final construct.

sTREM2 - $(EAAAK)_3$ - TIMP2 - $(EAAAK)_5$ - sKL

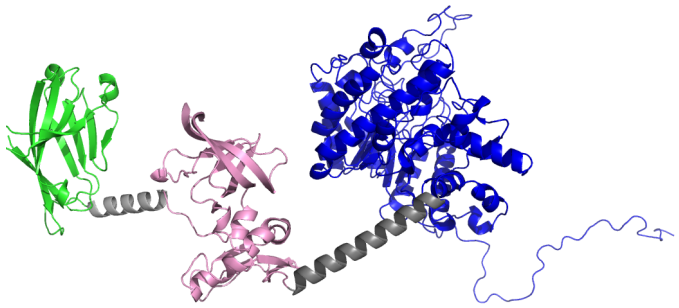


Figure 57. Representation of the third candidate for HEBE.

## 2.2. *In vitro* functional characterization of HEBE

After the bioinformatic analyses led to a viable candidate for HEBE, the protein was produced and subjected to *in vitro* testing prior to evaluation in an animal model.

### 2.2.1. Cloning and production of HEBE

To assess the stability of HEBE, a plasmid encoding the protein was engineered following restriction enzyme cloning techniques (pGG2-HEBE). Subsequent transfection of the plasmid into the HEK293 mammalian cell line, followed by a Western Blot revealed a band of ~130 kDa detected by antibodies against each of the subunits, thus demonstrating that the protein (i) was expressed correctly within cells, (ii) could be secreted by the cells, as evidenced by its presence in the supernatant, and (iii) did not break at the junction of the linkers (Fig. 58); therefore, it was a structurally stable protein in an *in vitro* context.

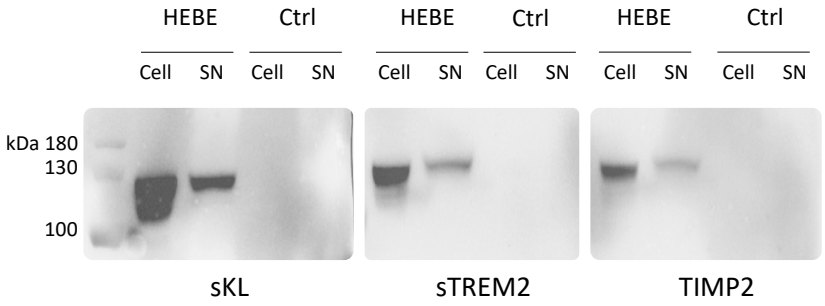



Figure 58. Western Blot of HEK293 cells transfected with a plasmid encoding HEBE or Null as a control. Both cell lysates (Cell) and supernatants (SN) were loaded, and the immunodetection was performed using antibodies against each of the subunits as indicated below each membrane. Theoretical molecular weight of HEBE without posttranslational modifications is 100,1 kDa.

### 2.2.2. Production of recombinant proteins

To test the *in vitro* functionality of HEBE, recombinant proteins were produced and purified. Adenoviral vectors encoding each individual protein and HEBE were produced for this purpose. A polyhistidine tag was added to the 3' end of each gene through an overlapping PCR reaction to facilitate downstream purification of the proteins (Fig. 59).

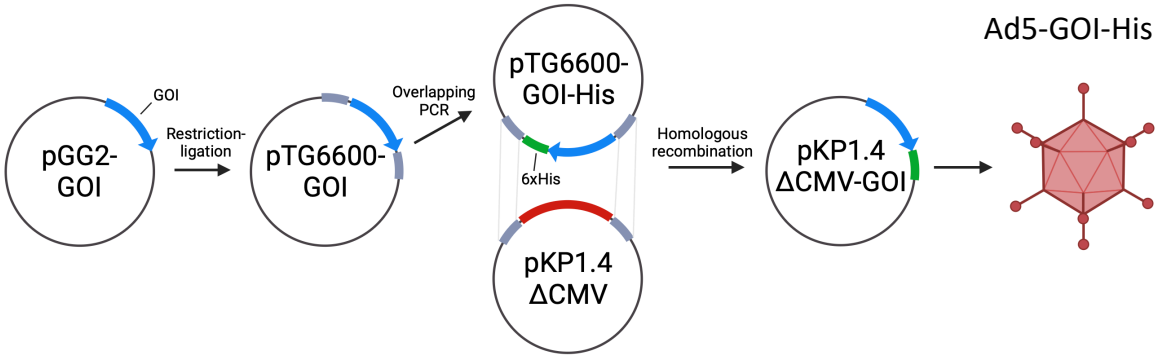



Figure 59. Schematic representation of the adenoviral vector generation for sKL, sTREM2, TIMP2 and HEBE. Each gene of interest (GOI) was cloned into a pTG6600 shuttle vector through a restriction enzyme cloning. A C-terminal polyhistidine tag was introduced through an overlapping PCR reaction, and the resulting GOI-His cassette was introduced into the pKP plasmid through homologous recombination. This last plasmid encodes all the genes necessary for the production of adenoviral vectors when transfected into HEK293 cells.

These adenoviral vectors were then used to transduce CHO cells. The correct expression of each protein was confirmed through a Western Blot (Fig. 60, fig. 24, results for sTREM2 and TIMP2 vectors not shown). The supernatants were purified, resulting in highly purified proteins, suitable for consequent assays.

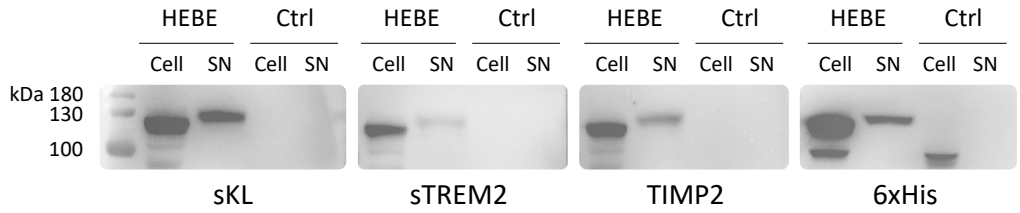



Figure 60. Western Blot of CHO cells transduced with an adenoviral vector encoding HEBE-His or Null as a control. Both cell lysates (Cell) and supernatants (SN) were loaded, and the immunodetection was performed using antibodies against each of the subunits and the His tag, as indicated below each membrane. Theoretical molecular weight of HEBE-His without posttranslational modifications is 101.2 kDa.

### 2.2.3. Testing of biological activity

Three tests were conducted, each targeting one of the subunits comprising HEBE, to elucidate the biological activity of this chimeric chronokine.

#### 2.2.3.1. β-glucuronidase activity

The activity of the sKL subunit was evaluated using an enzymatic assay, where the β-glucuronidase activity of the protein was quantitatively measured as the increase in fluorescence as a result of the hydrolysis of a substrate (Fig. 61). Remarkably, HEBE

presented greater β-glucuronidase activity than sKL alone, while neither of the other proteins displayed this activity, confirming the biological activity of sKL within HEBE.

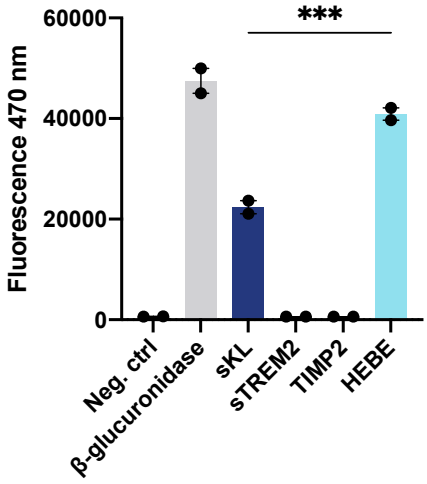



Figure 61. β-glucuronidase activity assay. 10 µg of sKL and equimolar amounts of the other proteins were used. Bovine β-glucuronidase was used as a positive control, while the negative control did not contain any protein. Data are shown as Mean ± SEM, One-way ANOVA and Tukey post-hoc (***p<0.001). Sample size: 2 per condition.

#### 2.2.3.2. MMP1 inhibition activity

Similarly, an enzymatic assay was employed to assess the activity of the TIMP2 subunit. In this assay, activity is measured through a decrease in the fluorescence of the product of the FS-6 fluorogenic substrate resulting from the inhibition of MMP1 by TIMP2. It is noteworthy that TIMP2 alone demonstrated potent efficacy in inhibiting MMP1 (Fig. 62), leading to a notable reduction in fluorescence compared to the control lacking TIMP2. In contrast, neither sKL, sTREM2, nor HEBE exhibited any inhibitory effect on MMP1, indicating that this particular function of the TIMP2 subunit is not retained within HEBE.

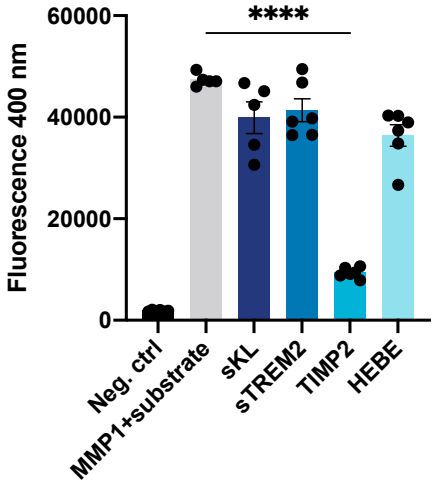


Figure 62. MMP1 inhibition activity assay. 0.8 μg/mL of TIMP2 and equimolar concentrations of the other proteins were used. Only the substrate was used as a negative control, while no TIMP2 was added as a control for the enzymatic reaction (MMP1+substrate). Data are shown as Mean ± SEM, One-way ANOVA and Tukey post-hoc (**p<0.01, ****p<0.0001). Sample size: 6 per condition.

#### 2.2.3.3. Phagocytic activity

The effects of the sTREM2 subunit within HEBE were analyzed by measuring the induction of phagocytic activity in the BV2 murine microglial cell line. Two fluorescent molecules, myelin and Aβ, were used as targets for phagocytosis. Given the increase in β-glucuronidase activity observed in HEBE compared to sKL, a mixture of the three individual chronokines was also tested to assess any potential differences compared to HEBE. A flow cytometer was employed to quantify the phagocytosis of myelin or Aβ by BV2 cells, following the gating strategy illustrated in Fig. 63. After selecting the live cell population (Fig. 63A) and excluding aggregates (Fig. 63B), cell populations labeled with FITC, corresponding to phagocytosed myelin or Aβ (Fig. 63C), as well as CD45, indicative of microglial activation (Fig. 63D), were analyzed.

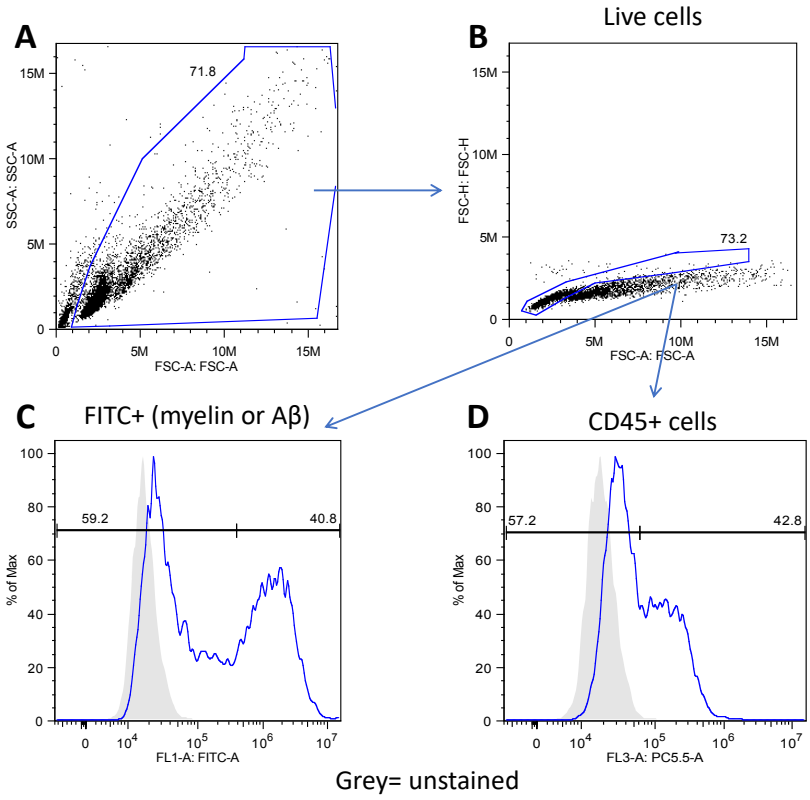
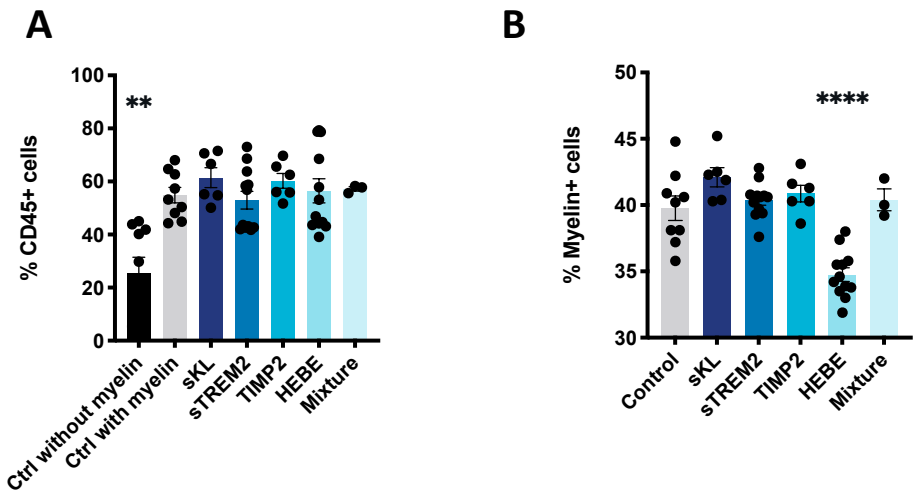



Figure 63. Gating strategy for the phagocytosis assay. (A) Forward and side scatter density plot of the whole BV2 cell population. (B) Forward scatter height versus forward scatter area density plot of live BV2 cells. (C) FITC positive cell histogram. (D) CD45 positive cell histogram.

#### 2.2.3.3.1. Myelin phagocytosis

Upon addition of myelin to the cell culture medium following treatment with recombinant proteins, more than half of the BV2 cells became activated, as indicated by an increase in the number of CD45+ cells (Fig. 64A). However, treatment with individual recombinant chronokines did not appear to influence this parameter. Despite the consistent level of cell activation observed across treatment groups, variations in phagocytic activity were evident. HEBE notably reduced the number of cells engaged in myelin phagocytosis, unlike the individual chronokines (Fig. 64B). Notably, HEBE displayed this effect despite the mixture of the three individual chronokines failing to do so, suggesting distinct behavior of HEBE compared to the chronokine mixture. Treatment with recombinant chronokines did not impact the degree of cell activation, as evidenced by consistent mean fluorescence in CD45+ cells across treatment groups (Fig. 64C). Moreover, the recombinant chronokines did not alter the amount of myelin phagocytosed per individual cell, as indicated by consistent mean myelin fluorescence per cell (Fig. 64D). Intriguingly, sTREM2 did not demonstrate the expected changes in myelin phagocytosis or BV2 cell activation under the tested conditions.



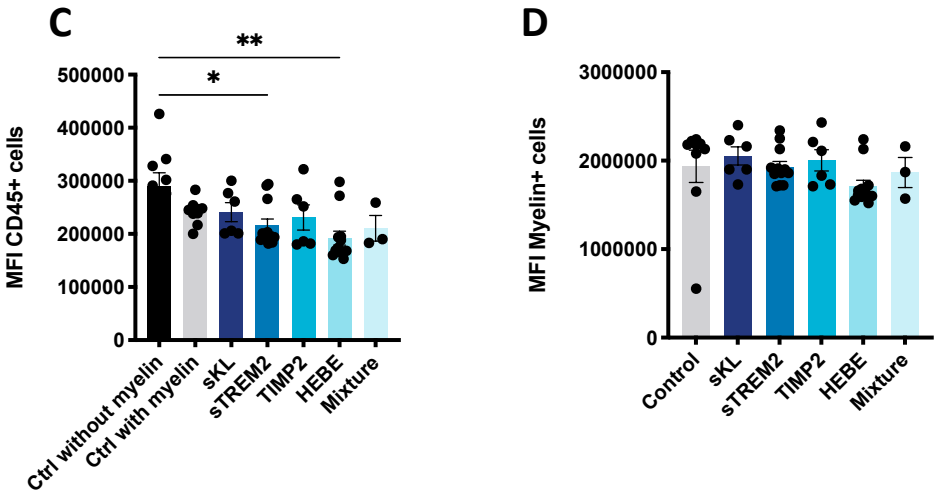



Figure 64. Myelin phagocytosis assay in BV2 cells. (A) Percentage of BV2 cells with positive CD45 labeling. (B) Percentage of BV2 cells with phagocytosed myelin. (C) Mean fluorescence intensity (MFI) of CD45 positive BV2 cells. (D) Mean fluorescence intensity of myelin positive BV2 cells. Data are shown as Mean ± SEM, One-way ANOVA and Tukey post-hoc (*p<0.05, **p<0.01, ****p<0.0001). Sample size: 9 for controls, 6 for sKL and TIMP2, 12 for sTREM2 and HEBE, 3 for the mixture.

#### 2.2.3.3.2. Aβ peptide phagocytosis

Upon addition of the Aβ peptide to the cell culture medium, distinct outcomes were observed compared to myelin. Firstly, a higher percentage of cells became activated, around 80% (Fig. 65A), suggesting that under the tested conditions, Aβ is a greater activator of BV2 compared to myelin. Treatment with individual recombinant chronokines also influenced cell activation in the presence of Aβ. Specifically, sKL slightly decreased the number of activated cells, whereas HEBE increased it. Additionally, the mixture of the three chronokines also decreased the number of activated cells. Importantly, similar to the observations with myelin, HEBE exhibited different activity compared to the mixture of individual proteins, further confirming distinct behavior of HEBE from the chronokine mixture. The decrease in the number of activated cells observed with sKL and the mixture was accompanied by a reduction in the number of cells phagocytosing Aβ, while HEBE did not appear to affect this parameter despite the slight increase in the number of activated cells (Fig. 65B). However, due to the high percentage of activated cells following incubation with Aβ, detecting significant effects on activation and phagocytosis mediated by HEBE proved challenging. Interestingly, although the activation level of CD45+ cells was not significantly altered (Fig. 65C), all treatments with chronokines appeared to decrease

the amount of Aβ phagocytosed per cell compared to control cells (Fig. 65D). Moreover, once again, sTREM2 did not present functions different from the other chronokines.

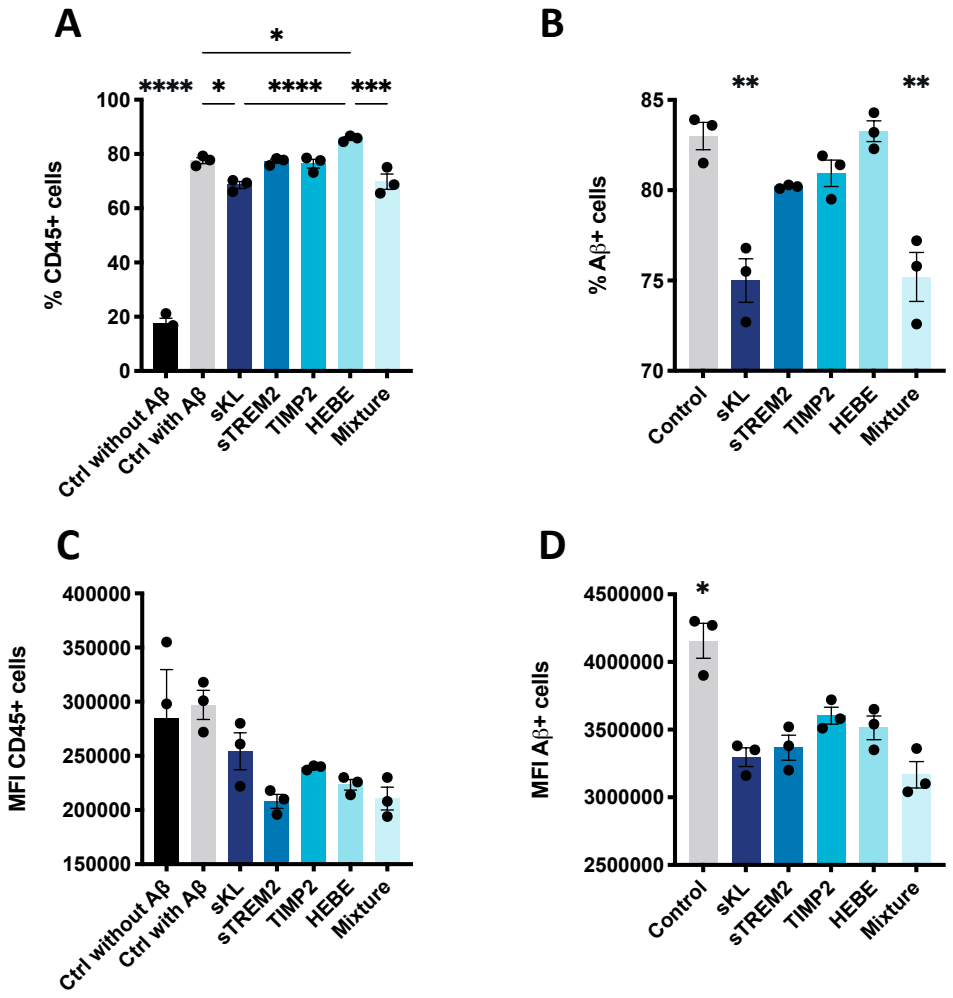



Figure 65. Aβ peptide phagocytosis assay in BV2 cells. (A) Percentage of BV2 cells with positive CD45 labeling. (B) Percentage of BV2 cells with phagocytosed Aβ. (C) Mean fluorescence intensity of CD45 positive BV2 cells. (D) Mean fluorescence intensity of Aβ positive BV2 cells. Data are shown as Mean ± SEM, One-way ANOVA and Tukey post-hoc (*p<0.05, **p<0.01, ***p<0.001, ****p<0.0001). Sample size: 3 per condition.

Therefore, the outcomes from the phagocytosis experiments revealed that the effects of the chronokines differ depending on the specific phagocytic molecule used. Importantly, a distinct functional disparity was observed when comparing HEBE to the mixture of individual chronokines in both experimental scenarios, implying that HEBE may possess unique functionalities. Furthermore, it is noteworthy that sTREM2 did not exhibit any discernible effect on phagocytosis modulation under the conditions tested.

## 2.3. *In vivo* therapeutic approach with HEBE

### 2.3.1. AAV9P31 setup

For the *in vivo* experiment, we planned to use the AAV9P31 viral vector, known for its enhanced capability to cross the murine blood-brain barrier and effectively transduce the CNS [293]. This vector offers the advantage of simplified administration and reduced invasiveness, as it can be delivered intravenously rather than intracerebrally. Additionally, the vector presents tropism for the liver, facilitating the secretion of the therapeutic protein to the bloodstream for systemic functions. However, this viral vector had not been tested in the APP/Tau mouse model, and therefore, a small setup experiment was conducted. APP/Tau mice were intravenously injected with $5 \cdot 10^{11}$ vg/mouse of either AAV9P31-eGFP or AAV9-eGFP as a control. While the AAV9 vector is widely used for transducing the CNS, its ability to cross the BBB is limited. Our results showed that the AAV9P31 vector efficiently crossed the BBB and transduced the CNS in the animal model, particularly demonstrating strong transduction in the hippocampus, which is of significant interest in AD (Fig. 66). In contrast, the AAV9 vector did not exhibit comparable efficiency to the new vector, confirming the suitability of the AAV9P31 vector for the *in vivo* testing of HEBE in our animal model.

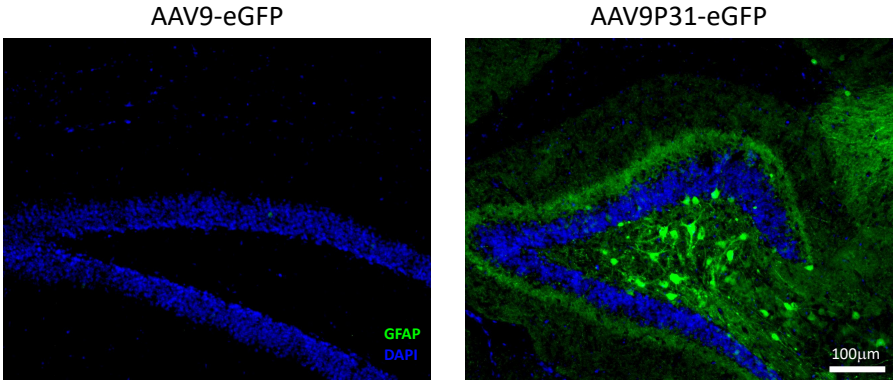



Figure 66. Hippocampus of APP/Tau mice injected with AAV9-eGFP (left) and mice injected with AAV9P31-eGFP (right). Green corresponds to eGFP signal, while blue corresponds to DAPI.

### 2.3.2. Experimental design

In this study, we evaluated the effects of HEBE on the APP/Tau transgenic mouse model of AD. Male and female APP/Tau mice and WT littermate controls were used, resulting in eight experimental groups as outlined in Table 11. Notably, the inclusion of the WT-HEBE

group was solely for assessing potential toxicity of HEBE, and no behavioral tests were conducted on these mice. Due to the large number of mice required for the study, simultaneous testing of all animals was not feasible. Therefore, two independent cohorts of mice were used and tested at different times to manage experimental logistics. Nonetheless, both cohorts were subjected to identical experimental conditions, and no discernible differences were observed between them, thereby validating the combined analysis of results.

Table 11. Experimental groups of the experiment, and number of animals used.

| | | Males | | Females | | **Total** | |
|---|---|---|---|---|---|---|---|
| | | Set 1 | Set 2 | Set 1 | Set 2 | **Males** | **Females** |
| **WT** | **Null** | 6 | 6 | 9 | 2 | **12** | **11** |
| | **HEBE** | - | 5 | - | 5 | **5** | **5** |
| **AD** | **Null** | 3 | 7 | 3 | 6 | **10** | **9** |
| | **HEBE** | 4 | 8 | 3 | 8 | **12** | **11** |

Twenty-four-week-old male and female APP/Tau mice were intravenously injected with $5 \cdot 10^{11}$ vg/mouse of either an AAV9P31 expressing HEBE (AAV9P31-HEBE) or a non-coding Null sequence (AAV9P31-Null) as a control (Fig. 68). Twelve weeks post-injection, at 36 weeks of age, behavioral and cognitive functions were assessed with the OF, NORT and MWM tests. Subsequently, mice were euthanized, and tissue samples were collected for biochemical and histological analyses (Fig. 67).

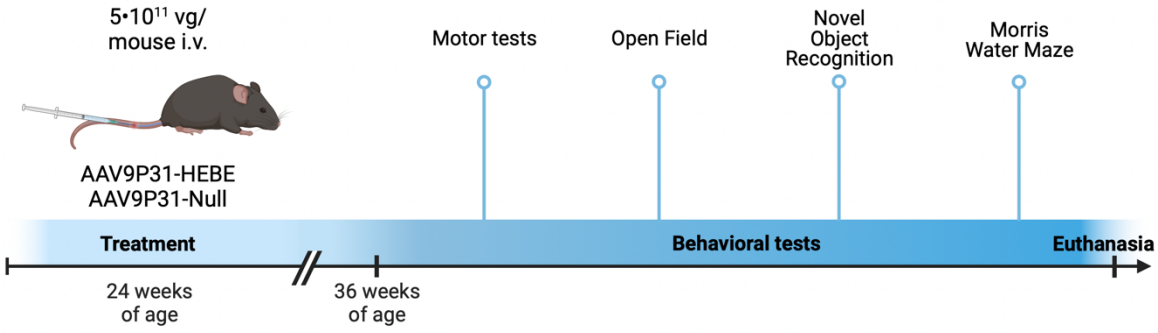



Figure 67. Experimental design of the *in vivo* experiment for HEBE in APP/Tau mice.

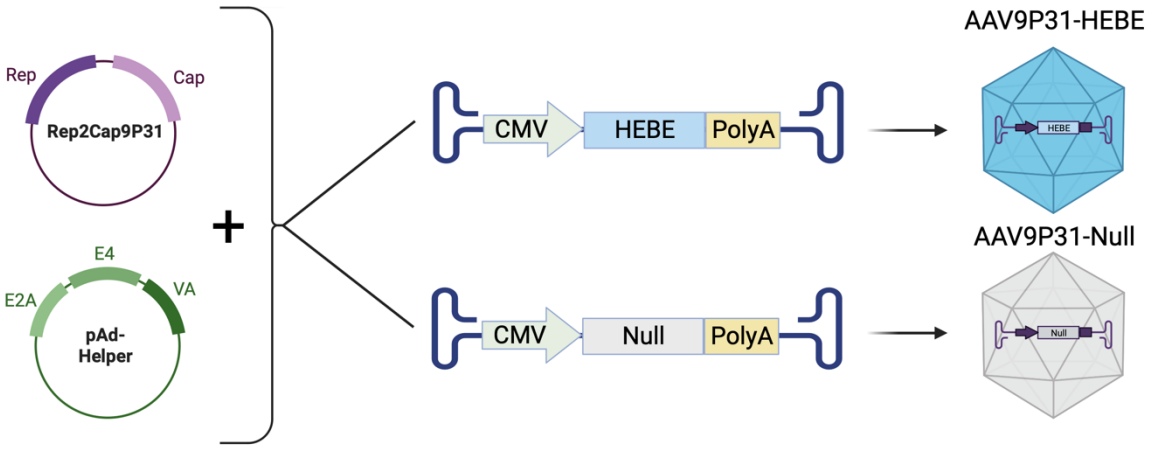



Figure 68. Viral vector production process. pRep2Cap9P31 and the pAd-Helper were co-transfected along with either the HEBE or Null-encoding plasmid into HEK293 cells, and the viral vectors were produced and purified.

### 2.3.3. Viral vector verification

To verify the correct transduction of viral vectors within the CNS, the viral genomes per cell and gene expression were analyzed.

#### 2.3.3.1. Viral genomes

Quantification of viral genomes per cell serves as an indicator of viral vector transduction efficiency, which was evaluated using a RT-qPCR, as described in the methods section. Viral genomes were analyzed in both the liver and the brain, as not all the vectors cross the BBB, and some transduce the liver (Fig. 69). Correct transduction of the HEBE viral vector was confirmed in both tissues and sexes, with no detection of HEBE-expressing viral vector presence in the control groups. Notably, the viral genome count was significantly lower in the liver of female mice (Fig. 69B), consistent with previous studies [332].

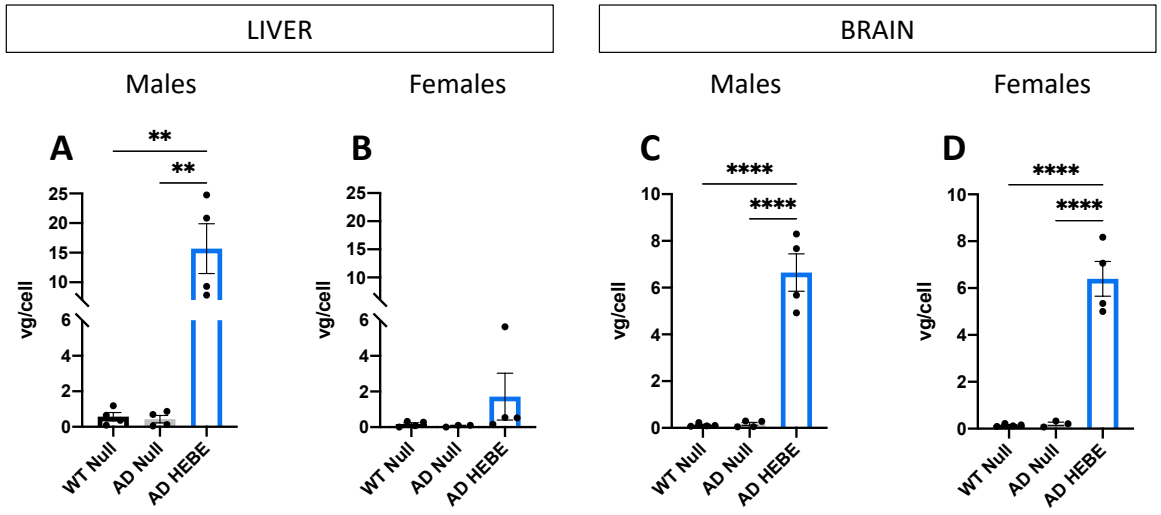



Figure 69. AAV9P31-HEBE viral genomes per cell in liver (A, B) and brain (C, D). Data are shown as Mean ± SEM, One-way ANOVA and Tukey post-hoc (**p<0.01, ****p<0.0001). Sample size of 4 per group.

### 2.3.3.2. Expression of viral vector

Viral genomes must undergo transcription to mRNA before translation into proteins. To confirm the correct expression of the viral vector, a RT-qPCR was performed using RNA samples extracted from the liver and brain of mice (Fig. 70). Expression of the HEBE gene was confirmed in both tissues and sexes, although lower expression levels were detected in the liver of female mice (Fig. 70B), consistent with the reduced transduction efficiency previously observed.

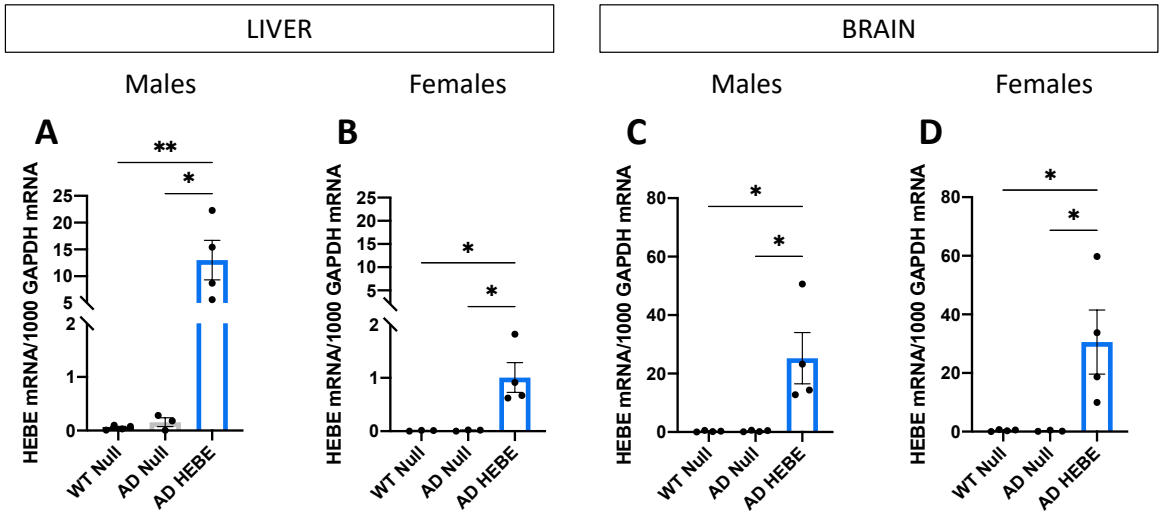



Figure 70. HEBE mRNA molecules normalized to 1000 GAPDH mRNA molecules in liver (A, B) and brain (C, D). Data are shown as Mean ± SEM, One-way ANOVA and Tukey post-hoc (*p<0.05, **p<0.01). Sample size of 4 per group.

### 2.3.4. HEBE toxicity

Since HEBE is a newly generated protein, its potential toxicity was evaluated in WT mice injected with the HEBE vector. This assessment involved macroscopic examination and analysis of blood samples to detect any potential HEBE-related toxicity.

#### 2.3.4.1. Macroscopic observations

Upon euthanasia of the HEBE-injected WT mice 12 weeks post-treatment, macroscopic observation of their internal organs did not reveal any visible differences compared to WT mice injected with the Null vector; no tumoral masses were detected, and the organs exhibited no abnormalities (results not shown).

#### 2.3.4.2. Analysis of blood samples

Blood samples collected from these mice were analyzed using a comprehensive panel encompassing a wide range of parameters (Fig. 71). No notable alterations were detected in the blood of WT mice injected with HEBE, regardless of sex. The only parameters showing a slight increase were sodium and chloride in male mice. However, despite the statistical significance of these increases, the values remained within the expected reference ranges [333]. In conclusion, these findings indicate that HEBE does not induce toxic effects that significantly impact blood parameters, supporting its safety as a therapeutic strategy.

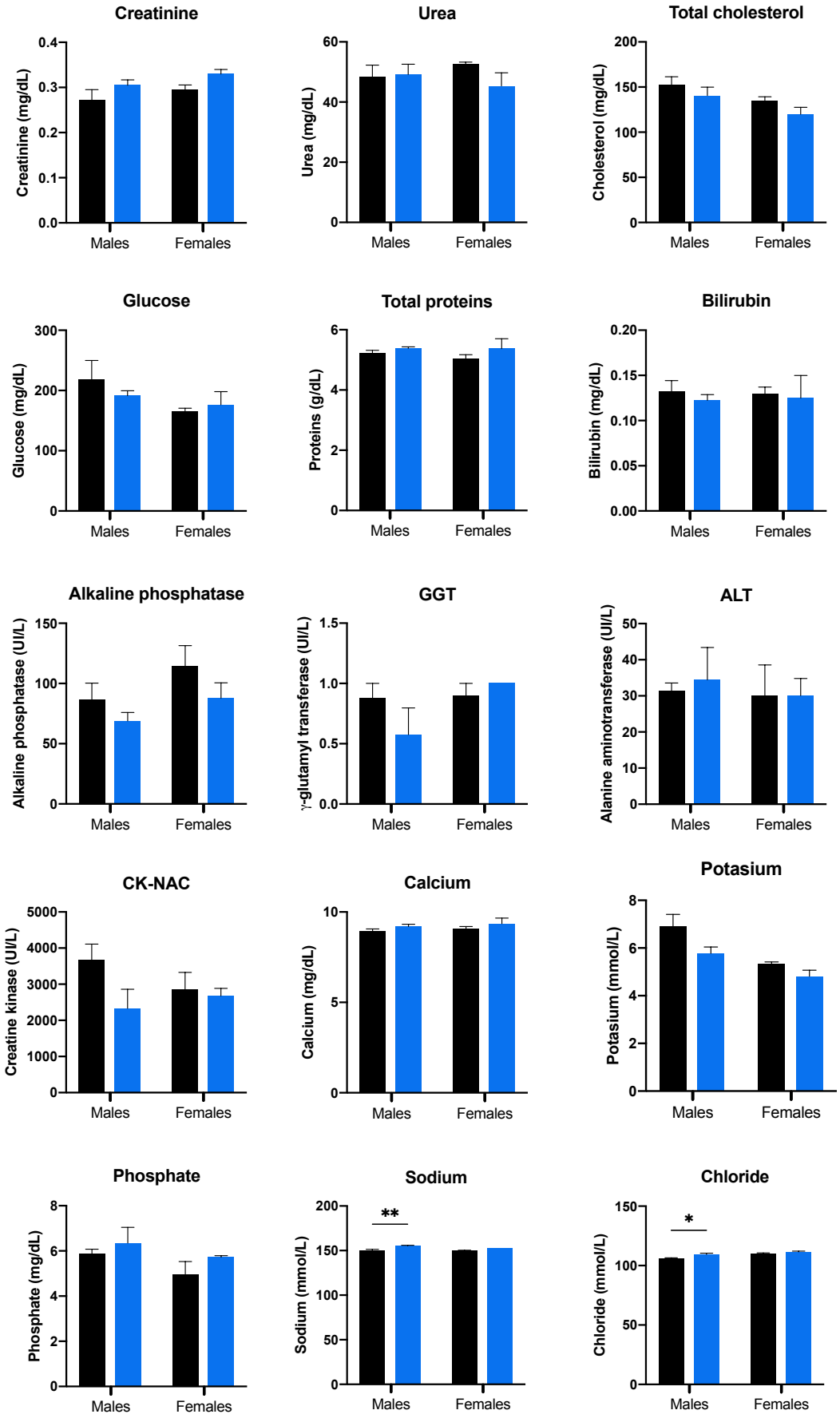

Creatinine
Creatinine (mg/dL)
0.4
0.3
0.2
0.1
0.0
Males
Females
Urea
Urea (mg/dL)
60
40
20
0
Males
Females
Total cholesterol
Cholesterol (mg/dL)
200
150
100
50
0
Males
Females
Glucose
Glucose (mg/dL)
300
200
100
0
Males
Females
Total proteins
Proteins (g/dL)
6
4
2
0
Males
Females
Bilirubin
Bilirubin (mg/dL)
0.20
0.15
0.10
0.05
0.00
Males
Females
Alkaline phosphatase
Alkaline phosphatase (UI/L)
150
100
50
0
Males
Females
GGT
γ-glutamyl transferase (UI/L)
1.5
1.0
0.5
0.0
Males
Females
ALT
Alanine aminotransferase (UI/L)
50
40
30
20
10
0
Males
Females
CK-NAC
Creatine kinase (UI/L)
5000
4000
3000
2000
1000
0
Males
Females
Calcium
Calcium (mg/dL)
10
5
0
Males
Females
Potasium
Potasium (mmol/L)
8
6
4
2
0
Males
Females
Phosphate
Phosphate (mg/dL)
8
6
4
2
0
Males
Females
Sodium
Sodium (mmol/L)
**
200
150
100
50
0
Males
Females
Chloride
Chloride (mmol/L)
*
150
100
50
0
Males
Females
WT Null
WT HEBE

Figure 71. Blood parameters analyzed in WT mice treated with Null or HEBE. Data are shown as Mean ± SEM, One-way ANOVA and Tukey post-hoc (*p<0.05, **p<0.01). Sample size for males: WT-Null=4, WT-HEBE=4. Sample size for females: WT-Null=4, WT-HEBE=2.

A proteinogram is a valuable diagnostic test used to aid in the clinical assessment of conditions marked by dysproteinemia or to detect inflammation [334]. Blood samples were analyzed to obtain a proteinogram, and no significant differences were found among groups (Fig. 72), indicating that HEBE did not induce inflammation.

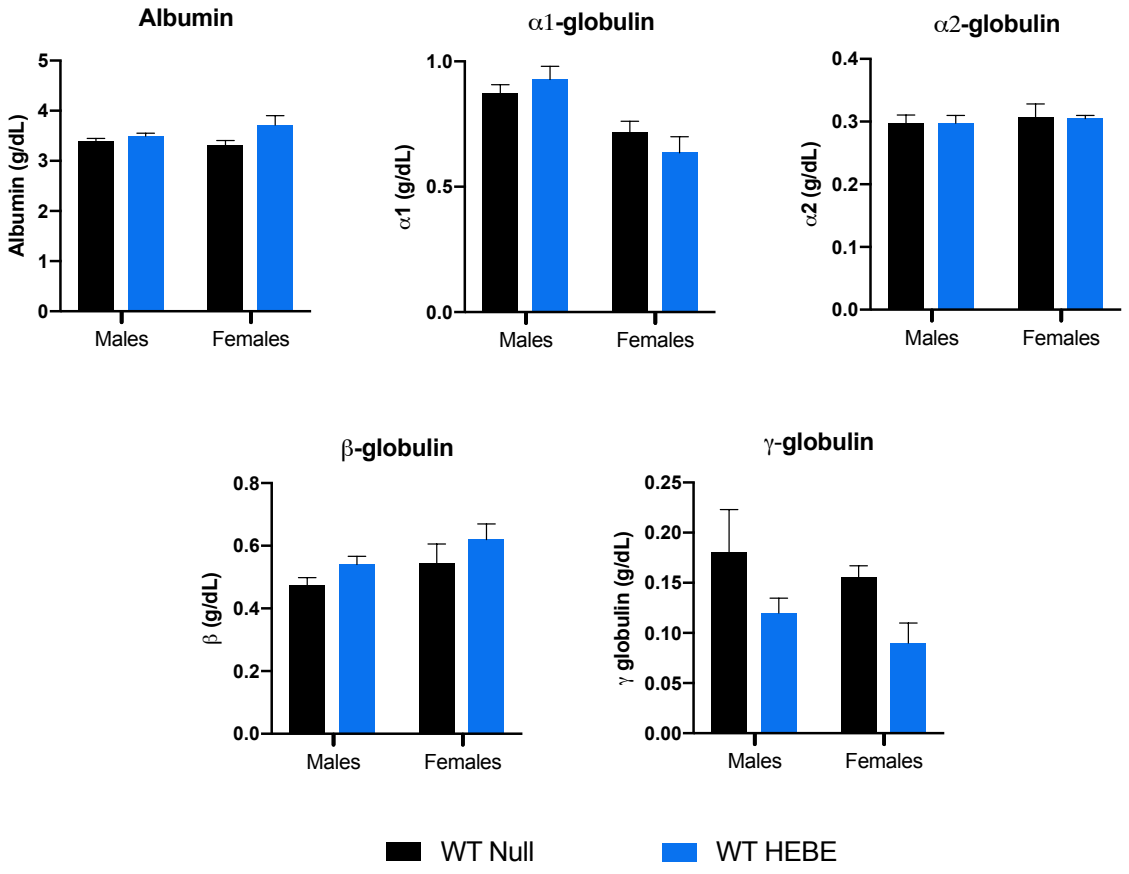



Figure 72. Proteinogram parameters analyzed in WT mice treated with Null or HEBE. Data are shown as Mean ± SEM, One-way ANOVA and Tukey post-hoc. Sample size for males: WT-Null=4, WT-HEBE=4. Sample size for females: WT-Null=4, WT-HEBE=2.

### 2.3.5. Body weights

Mice were weighed at 36 weeks of age, three months post-injection, and before the start of the behavioral and cognitive test battery to minimize potential stress-related weight fluctuations resulting from the tests (Fig. 73). Consistent patterns were observed in both male (Fig. 73A) and female (Fig. 73B) mice, where WT mice displayed higher body weights compared to the AD groups. Importantly, no significant changes in body weight were

observed in HEBE-treated mice relative to the control AD group. These findings suggest that HEBE administration did not impact the body weight of the animals.

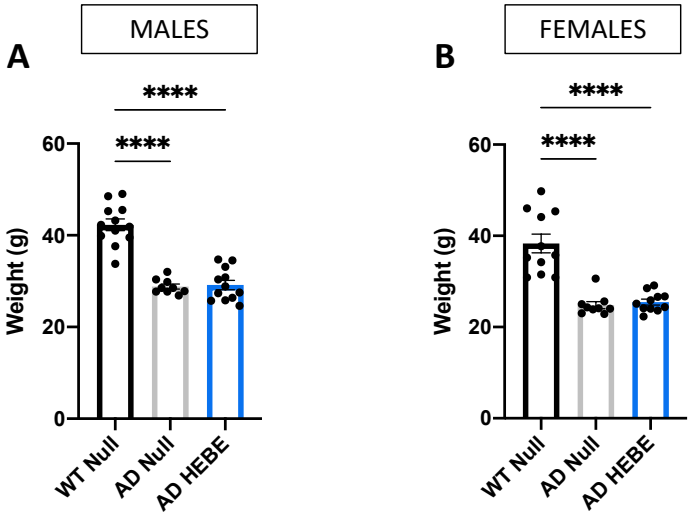



Figure 73. Weights of male (A) and female (B) mice 3 months post-injection. Data are shown as Mean ± SEM, One-way ANOVA and Tukey post-hoc (****p<0.0001). Sample size of 4 per group. Sample size for males: WT-Null=12, AD-Null=9, AD-HEBE=12. Sample size for females: WT-Null=11, AD-Null=9, AD-HEBE=11

### 2.3.6. Behavioral and cognitive tests

Prior to conducting behavioral and cognitive tests, mice underwent assessments of sensorimotor functions, which included evaluations of visual and hindlimb reflexes, equilibrium, and strength. No discernible differences were observed among groups in either sex, indicating that neither genotype nor HEBE treatment affected sensorimotor functions (results not shown). Therefore, it was assumed that all groups presented the same physical conditions, and any difference observed in the behavioral tests could be attributed to behavioral and/or cognitive functions.

#### 2.3.6.1. Open Field

The OF was used to evaluate locomotor activity and anxiety-like behaviors in mice. The traveled distance and mean speed were analyzed, as indicators of general locomotor activity. In males, no differences were observed among the groups (Fig. 74A, B), indicating the absence of locomotor impairments in the animal model, or related to the treatment.

Anxiety levels were assessed by examining the percentage of time spent in motion, as immobility can be indicative of fear. Male mice across all groups exhibited similar levels of movement, spending approximately 75% of the test in motion (Fig. 74C). Thigmotaxis, another measure of anxiety, was evaluated by assessing the time spent in the peripheral zone of the maze. The control AD group did not significantly differ from the WT group in thigmotaxis (Fig. 74D), spending approximately 75% of the time in the outer zone. However, a modest increase in thigmotaxis was observed in HEBE-treated male mice, spending around 85% of the time in the peripheral zone.

Overall, male mice did not demonstrate locomotor impairments, although a mild increase in anxiety-like behavior was noted in the HEBE-treated group based on thigmotaxis measurements.

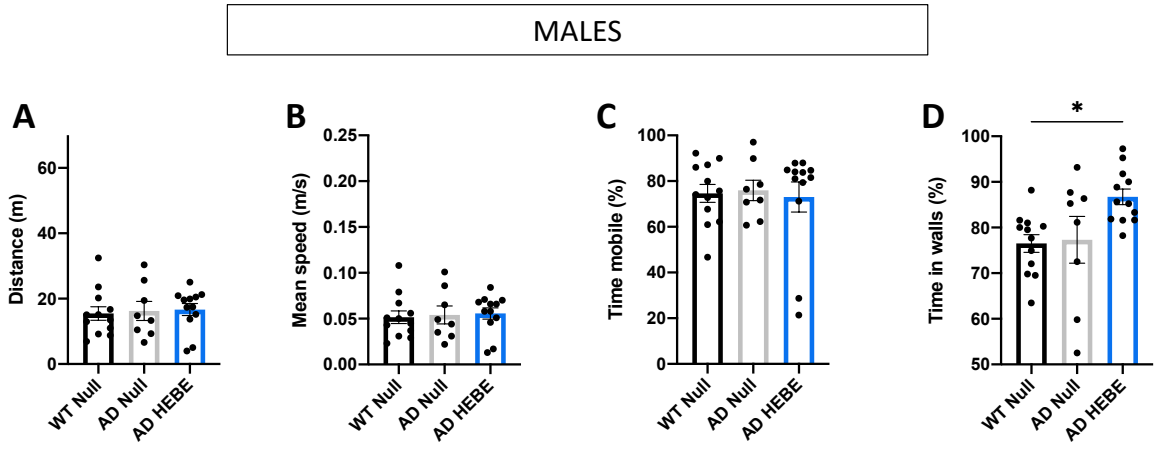



Figure 74. Open Field test in males. (A) Distance traveled in the Open Field. (B) Mean speed in the Open Field. (C) Percentage of time mice spend mobile during the test. (D) Percentage of time mice spend around the walls of the Open Field. Data are shown as Mean ± SEM, One-way ANOVA and Tukey post-hoc (*p<0.05). Sample size after discarding outliers: WT-Null=12, AD-Null=8, AD-HEBE=12.

In the case of females, no significant differences in locomotor activity were detected, as evidenced by similar traveled distances and mean speeds across all experimental groups (Fig. 75A, B). With respect to anxiety-like behaviors, there were no notable differences observed in the percentage of time spent in motion, as all groups spent approximately 70% of the test mobile (Fig. 75C). Furthermore, in contrast to male mice, thigmotaxis analysis revealed no differences among groups for females (Fig. 75D), suggesting that HEBE did not elicit an increase in anxiety-like behaviors in female mice.

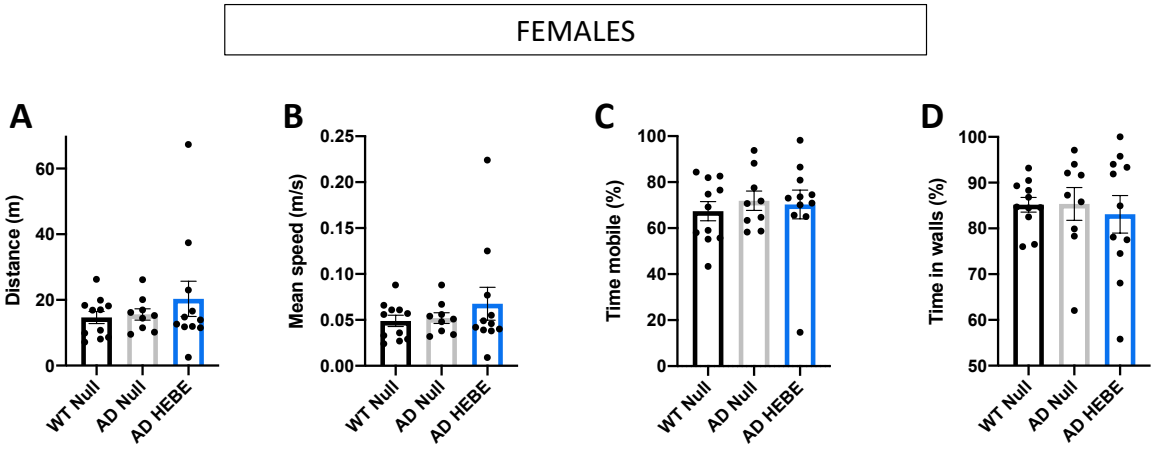



Figure 75. Open Field test in females. (A) Distance traveled in the Open Field. (B) Mean speed in the Open Field. (C) Percentage of time mice spend mobile during the test. (D) Percentage of time mice spend around the walls of the Open Field. Data are shown as Mean ± SEM, One-way ANOVA and Tukey post-hoc. Sample size: WT-Null=11, AD-Null=9, AD-HEBE=11

#### 2.3.6.2. Novel Object Recognition Test

The NORT was used to assess recognition memory in mice. The total exploration time was used as an exclusion criterion, requiring mice to explore the objects for a minimum of 5 seconds to be included in the analysis. As a result, only mice meeting this criterion were included in following analyses.

In male mice, on the initial day of the test, they exhibited no distinct preference for any of the identical objects (Fig. 76A). However, on the subsequent day, when one of the objects was replaced with a novel item, differences in the preference index were evident, despite the absence of variations in the total object exploration time (Fig. 76B, C). AD-Null mice did not display a preference for the new object, suggesting a lack of memory retention for the objects explored the previous day (Fig. 76B). In contrast, HEBE-treated AD mice presented a trend towards preferring the new object, reaching preference index values comparable to WT mice. Comparison of preference indexes between the first and second day revealed a notable increase in preference for the new object in both WT and HEBE-treated mice, whereas no such increase was observed in the AD-Null group (Fig. 76D). These findings suggest an enhancement in recognition memory in HEBE-treated AD male mice.

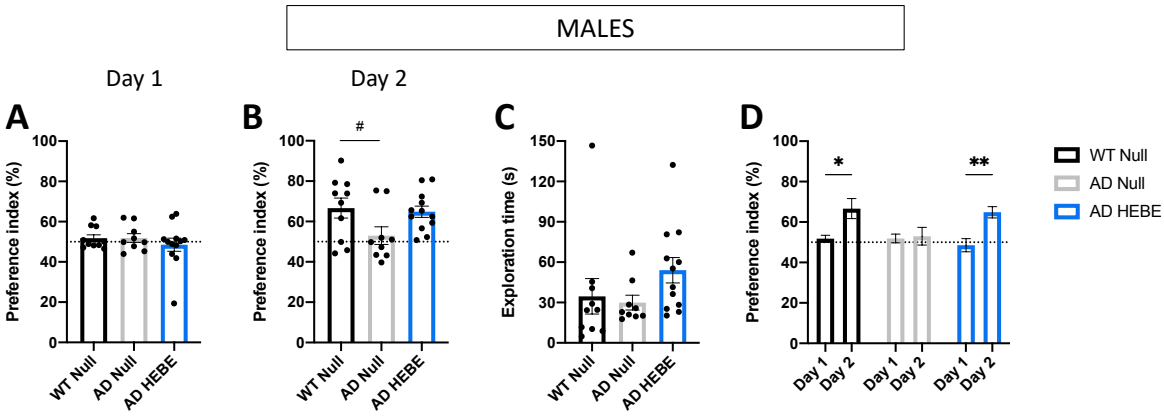



Figure 76. Novel Object Recognition Test for males. (A) Preference index on the first day of the test, when both objects are identical. (B) Preference index for the new object on the second day of the test. (C) Total time mice spend exploring the objects. (D) Comparison of the preference index between both test days. Data are shown as Mean ± SEM, One-way ANOVA and Tukey post-hoc, comparisons between days analyzed by 2-way ANOVA and Tukey post-hoc (*p<0.05, **p<0.01, #<0.07). Sample size after discarding outliers: WT-Null=10, AD-Null=9, AD-HEBE=12.

In female mice, no significant differences among experimental groups were evident in the preference index on the first day of the test, as expected (Fig. 77A). However, on the second day, notable differences emerged, with the AD group showing no preference for the new object compared to the other groups (Fig. 77B), despite similar exploration times for the objects (Fig. 77C). Comparison of preference indexes between the first and second day revealed a significant preference for the new object in both WT and HEBE-treated mice, while no such difference was observed in the AD-Null group (Fig. 77D), confirming the improvement in recognition memory in HEBE-treated AD mice observed in males.

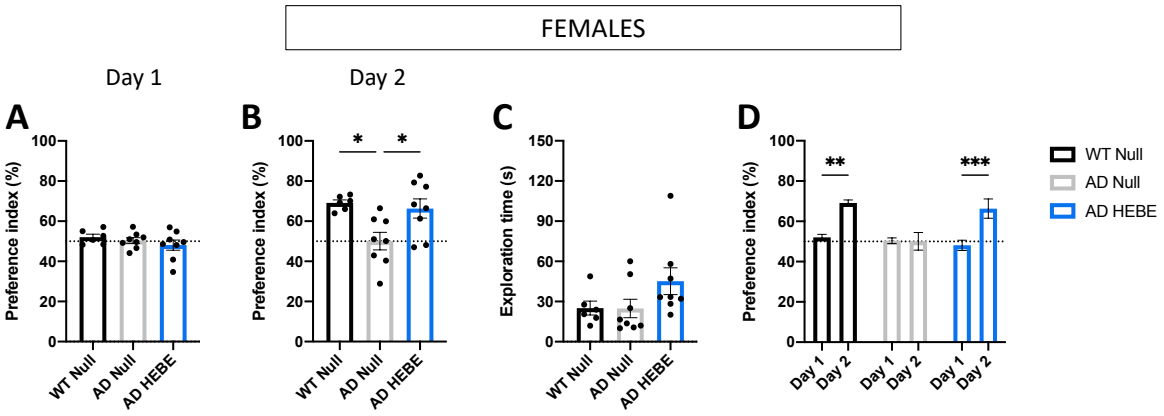



Figure 77. Novel Object Recognition Test for females. (A) Preference index on the first day of the test, when both objects are identical. (B) Preference index for the new object on the second day of the test. (C) Total time mice spend exploring the objects. (D) Comparison of the preference index between both test days. Data are shown as Mean ± SEM, One-way ANOVA and Tukey post-hoc, comparisons between days analyzed by 2-way ANOVA and Tukey post-hoc (*p<0.05,

**p<0.01, ***p<0.001). Sample size after discarding outliers for females: WT-Null=6, AD-Null=9, AD-HEBE=9

#### 2.3.6.3. Morris Water Maze

The MWM was used to assess spatial learning and memory in mice. Male WT mice performed well from the first learning day, evident from their short latency to reach the platform (Fig. 78A) and high number of platform entries (Fig. 78B). Consequently, they swam short distances to reach the platform (Fig. 78C). In contrast, both AD groups started at similar levels on the first day, with apparently longer latencies and fewer platform entries compared to WT mice, although not statistically significant (Fig. 78A, B). Mice treated with HEBE demonstrated a significant improvement over subsequent days, achieving performance levels comparable to WT mice, while control AD mice did not display such improvements. HEBE-treated mice presented a decrease in the latency to reach the target platform (day 2 vs day 5, p=0.0311) and an increase in the number of platform entries (day 2 vs day 5, p=0.0286) (Fig. 78A, B). Consequently, the distances covered by WT and HEBE-treated mice were shorter than those covered by AD mice (Fig. 78C). Importantly, these observed differences were not attributable to variations in locomotor abilities, as all three groups exhibited similar swimming speeds (Fig. 78D). In conclusion, male mice treated with HEBE demonstrated improved spatial learning, achieving performance levels comparable to WT mice, unlike AD mice, which presented impaired learning.

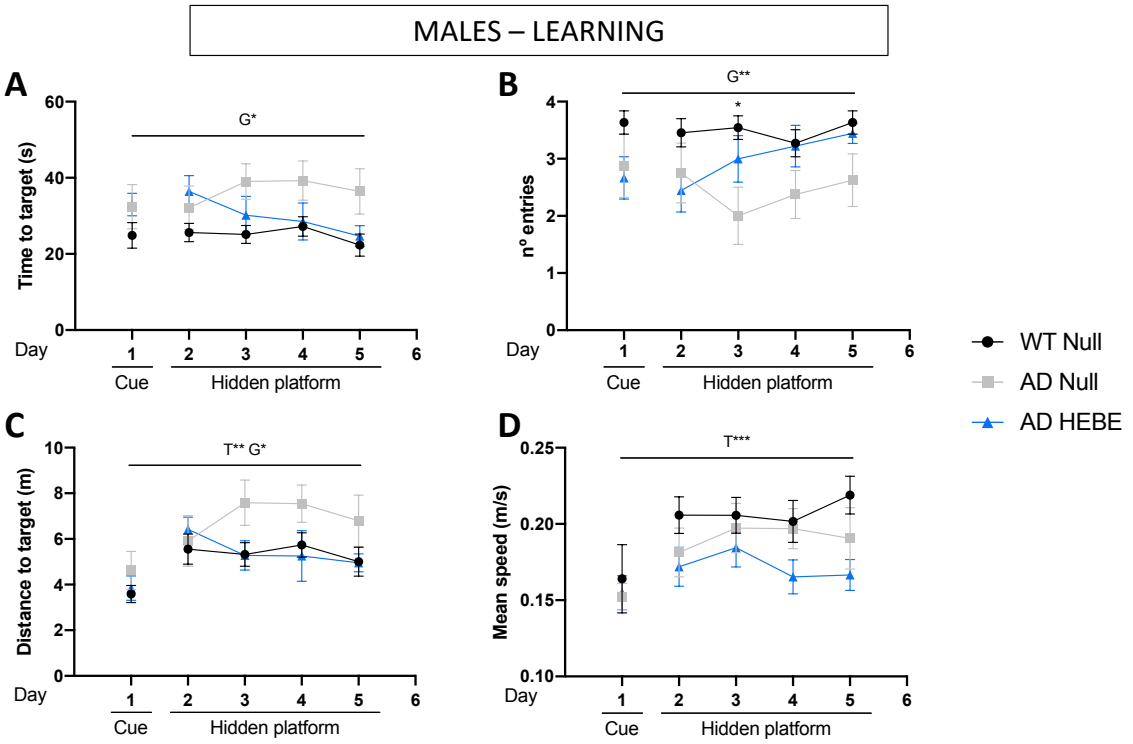



Figure 78. Learning phase of the Morris Water Maze for males. (A) Time to reach the target platform inside the pool. (B) Average of entries to the platform in each training day. (C) Distance traveled to reach the platform. (D) Mean swimming speed. Data are shown as Mean ± SEM, 2-way ANOVA and Tukey post-hoc (*p<0.05, **p<0.01, ***p<0.001). T-test for comparisons of means within groups among test days. G: group factor. T: time factor. Sample size after discarding outliers: WT-Null=11, AD-Null=8, AD-HEBE=9.

Short-term memory was assessed two hours after the last learning trial in the 2 h probe test, by removing the platform and recording the animal for 60 seconds (Fig. 79A-D). In male mice, no significant differences were observed in the number of entries into the target zone among experimental groups (Fig. 79A). However, a slight trend towards reduced latency to reach the platform zone for the first time was noted in the HEBE-treated group (Fig. 79B). The time spent in each of the pool's quadrants was also analyzed to determine if mice spent more time in the quadrant where the platform was (Fig. 79C), although no differences were observed among groups. Notably, HEBE-treated mice exhibited a lower mean swimming speed compared to the WT group (Fig. 79D). Despite impaired performance in the learning phase, AD mice did not display significant deficits in short-term spatial memory during the 2 h probe test, suggesting that profound deficits were not present at the tested age.

Long-term memory was assessed 24 h after the last learning trial, in the 24 h probe test (Fig. 79E-H). In males, a modest trend towards increased entries into the target zone was observed in HEBE-treated mice (Fig. 79E). Notably, a significant decrease in latency to reach the target for the first time was observed in the HEBE-treated group, although AD mice did not present increased latencies compared to WT mice (Fig. 79F). Time spent in the target quadrant was comparable among groups (Fig. 79G), as was the mean swimming speed (Fig. 79H). Collectively, these results suggest that male AD mice did not exhibit significant long-term spatial memory impairments at the tested age, which may have made it challenging to observe substantial improvements in the AD-HEBE group.

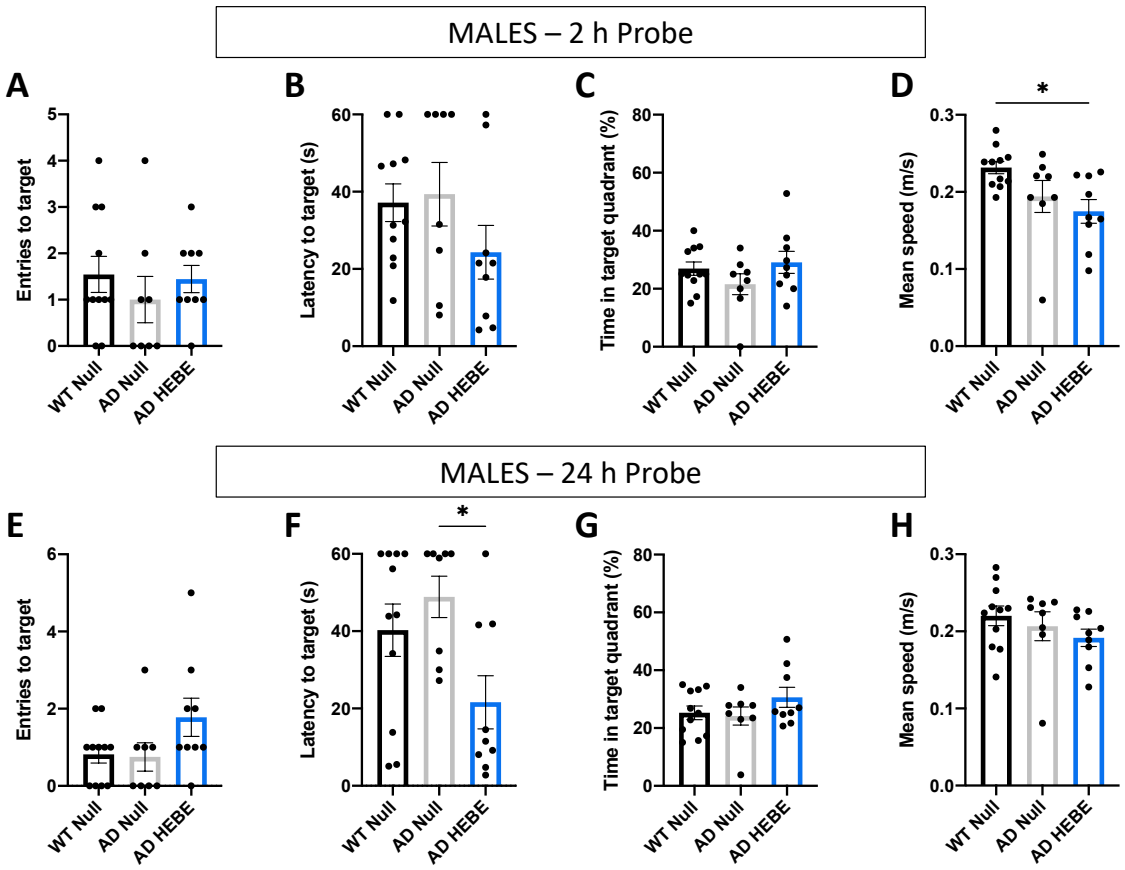



Figure 79. Probe phase of the MWM for males, 2 h probe (A-D) and 24 h probe (E-H). (A, E) Number of entries to the area where the platform was. (B, F) Latency to the first entry into the target area. (C, G) Percentage of time in the target quadrant were the platform used to be. (D, H) Mean swimming speed along the test. Data are shown as Mean ± SEM, 2-way ANOVA and Tukey post-hoc (*p<0.05). G: group factor. Sample size after discarding outliers for males: WT-Null=11, AD-Null=8, AD-HEBE=9.

In females, WT mice performed well from the first learning day, as evidenced by their short latency to reach the platform (Fig. 80A) and high number of platform entries (Fig.

80B). Consequently, they swam short distances to reach the platform (Fig. 80C). However, similar to observations in males, AD mice exhibited different performance levels. Both AD groups started at comparable levels on the first day, taking longer than WT mice to reach the platform (Fig. 80A) and showing fewer platform entries (Fig. 80B). Nevertheless, mice treated with HEBE displayed significant improvement over subsequent days, achieving performance levels equivalent to WT mice. HEBE-treated mice reached the platform in less time than Null-treated AD mice (day 2 vs day 5, p=0.0059) and also increased the number of platform entries (day 2 vs day 5, p=0.0055) (Fig. 80A, B). Consequently, the distances covered by WT and HEBE-treated mice were shorter than those covered by AD mice (Fig. 80C). Notably, these differences were not attributable to variations in locomotor abilities, as all three groups showed similar swimming speeds (Fig. 80D). In summary, female mice treated with HEBE demonstrated improved spatial learning, reaching performance levels comparable to WT mice, unlike AD mice, which presented impaired learning.

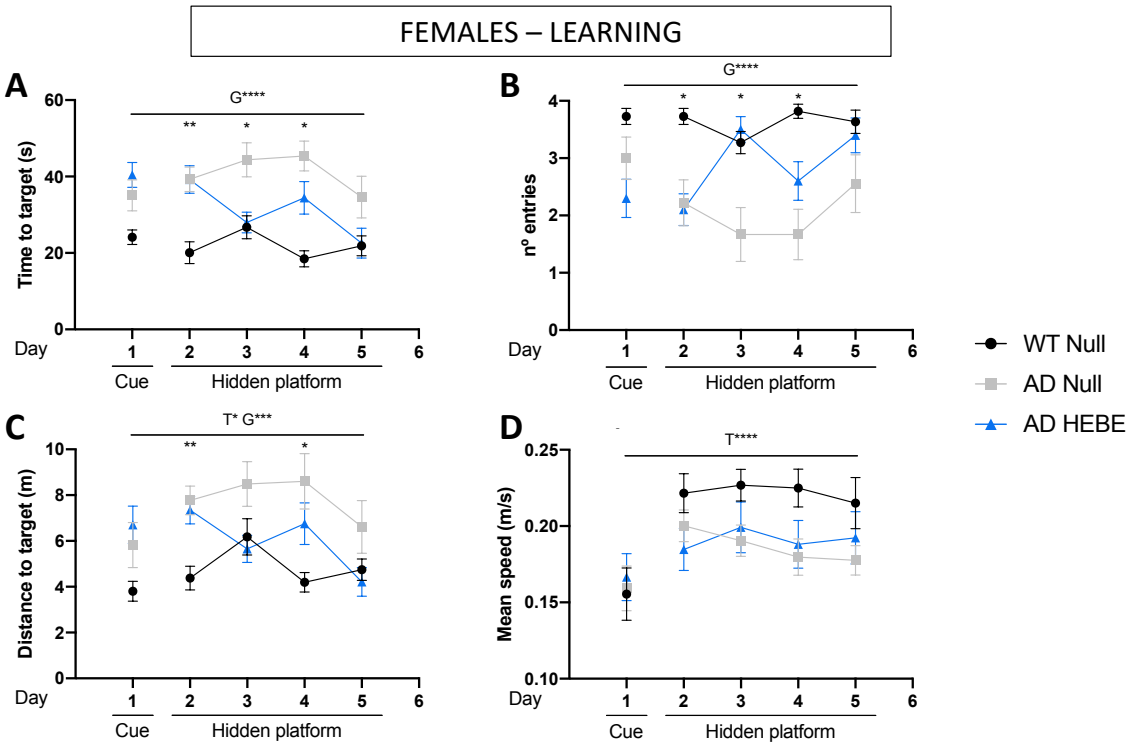



Figure 80. Learning phase of the Morris Water Maze for females. (A) Time to reach the target platform inside the pool. (B) Average of entries to the platform in each training day. (C) Distance traveled to reach the platform. (D) Mean swimming speed. Data are shown as Mean ± SEM, 2-way ANOVA and Tukey post-hoc (*p<0.05, ***p<0.001, ****p<0.0001). T-test for comparisons of means within groups among test days. G: group factor. T: time factor. Sample size after discarding outliers: WT-Null=11, AD-Null=9, AD-HEBE=10.

In the 2 h probe test (Fig. 81A-D), no significant differences were observed in the number of entries to the target zone, although a slight decrease was noted in HEBE-treated mice (Fig. 81A). Likewise, the latency to reach the platform was similar among groups (Fig. 81B), as was the time spent in the target quadrant (Fig. 81C). No differences in locomotor activity were observed either, as all groups showed similar mean swimming speeds (Fig. 81D). These findings suggest that female AD mice did not exhibit significant short-term spatial memory impairments.

In the 24 h probe test (Fig. 81E-H), similar results were obtained. No differences were observed in the number of entries or the latency to reach the target zone (Fig. 81E, F). Additionally, the time spent in the target quadrant was comparable among groups (Fig. 81G), and locomotor activity remained consistent (Fig. 81H). Taken together, these results indicate the absence of long-term spatial memory deficits in female AD mice, which may have hindered the ability to observe improvements with HEBE.

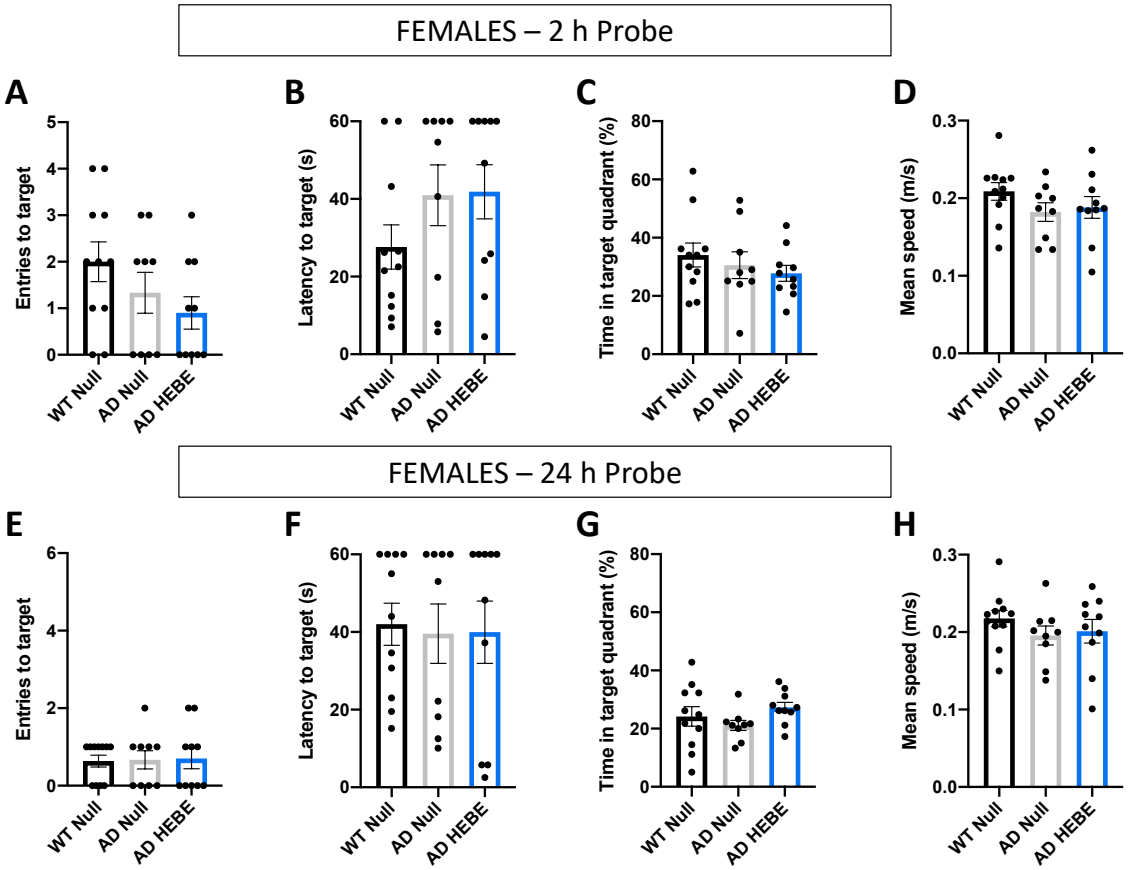


Figure 81. Probe phase of the MWM for females, 2 h probe (A-D) and 24 h probe (E-H). (A, E) Number of entries to the area where the platform was. (B, F) Latency to the first entry into the target area. (C, G) Percentage of time in the target quadrant were the platform used to be. (D, H) Mean swimming speed along the test. Data are shown as Mean ± SEM, 2-way ANOVA and Tukey post-hoc. G: group factor. Sample size after discarding outliers for females: WT-Null=11, AD-Null=9, AD-HEBE=10

### 2.3.7. RNA-seq analysis

To elucidate the molecular mechanisms contributing to the observed memory-related effects, an RNA-seq analysis was conducted on two key brain regions implicated in AD, the hippocampus and the entorhinal cortex.

#### 2.3.7.1. Hippocampus

First, a PCA plot was employed to discern the expression patterns across the experimental groups (Fig. 82A, Fig. 83A). Notably, a consistent pattern was observed in both male and female cohorts. As anticipated, the expression profile of the WT group markedly differed from that of the AD-Null group. However, the expression patterns between the two AD groups displayed a notable degree of similarity, suggesting that treatment-induced transcriptional changes were modest. To gain insights into the differences between the AD mouse model and the WT group, KEGG pathway enrichment analysis was performed (Fig. 82B, C, Fig. 83B, C). A total of 5935 DEGs were identified in males, while 3203 DEGs were detected in females. These upregulated and downregulated DEGs were subsequently categorized into various biological pathways.

Certain pathways were shared between both sexes, prominently associated with the pathophysiological features of Alzheimer's disease. "Lysosome", "phagosome", "Fcγ R-mediated phagocytosis", "apoptosis" and "cellular senescence" were upregulated in control AD mice (Fig. 82B, Fig. 83B), while several synapse types and the long-term potentiation involved in memory formation were downregulated (Fig. 82C, Fig. 83C). This indicates that the animal model used in the study recapitulates some of the key molecular signature characteristics of AD.

Regarding the differences between HEBE-treated mice and control AD mice, a total of 395 DEGs were found in males, and 422 in females, which were assigned to different pathways

(Fig. 82D, E, Fig. 83D, E). Surprisingly, no clear evidence of a substantial effect was observed at a transcriptional level. In males, the most significant improvement could be the downregulation of Aβ formation (Fig. 82E), although the rest of the upregulated pathways could also contribute to an enhancement of overall hippocampal functions. In females, no downregulation of Aβ formation was evident (Fig. 83E), and although various pathways with a potential positive impact were upregulated (Fig. 83D), others were downregulated (Fig. 83E), indicating no major improvement.

These findings suggest that HEBE does not exert a pronounced impact at the transcriptional level, at least within the hippocampal region of mice.

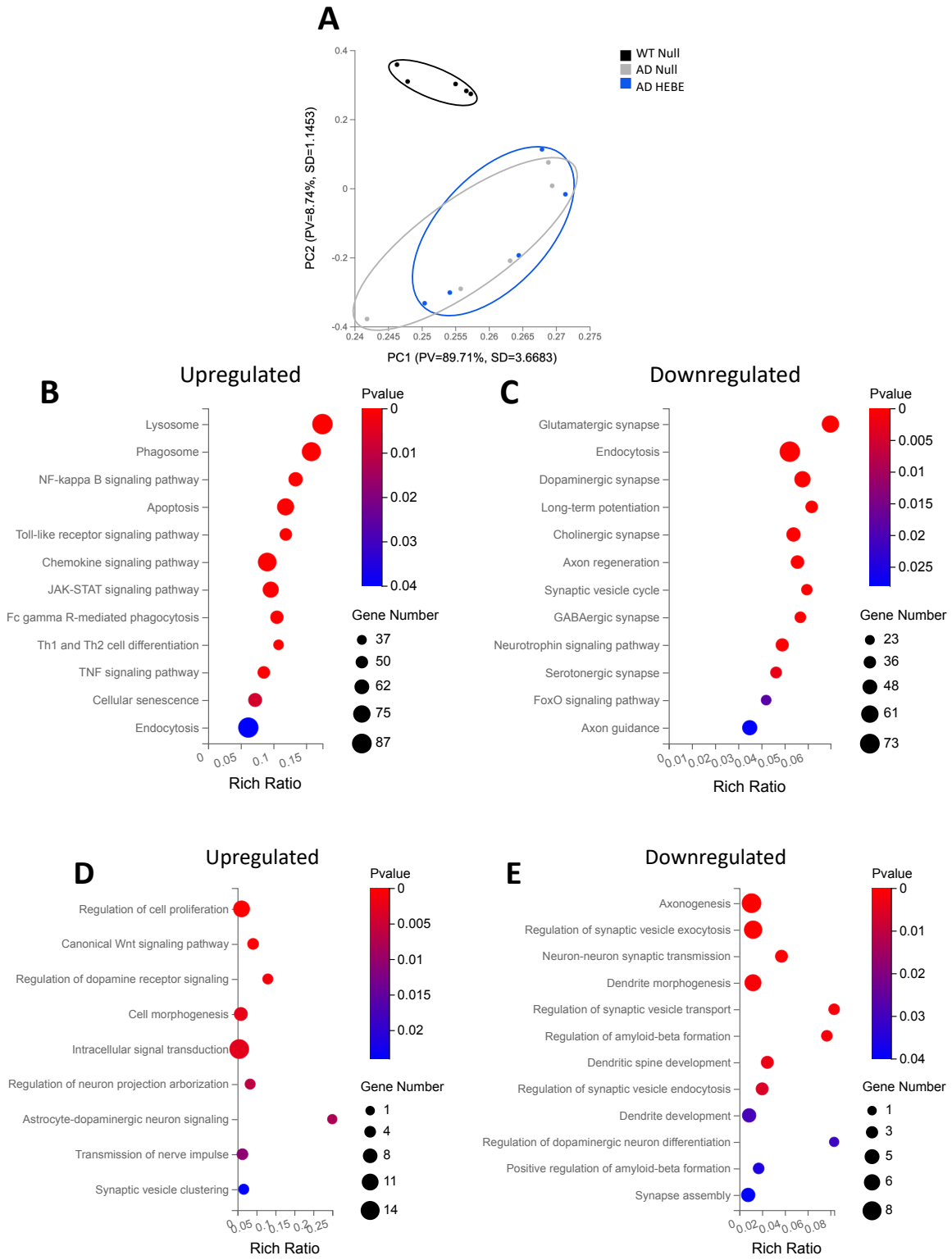



Figure 82. RNA-seq analysis of hippocampus samples for males. (A) Principal component analysis (PCA) plot. (B) KEGG pathways enriched in AD-Null vs WT-Null upregulated genes. (C) KEGG pathways enriched in AD-Null vs WT-Null downregulated genes. (D) GO pathways enriched in AD-HEBE vs AD-Null upregulated genes. (E) GO pathways enriched in AD-HEBE vs AD-Null downregulated genes. The abscissa represents the rich ratio, indicating the proportion of DEGs in each pathway. The number of DEGs in each pathway is represented by the circle area, and the color represents the corrected p-value. Sample size of 5 per group.

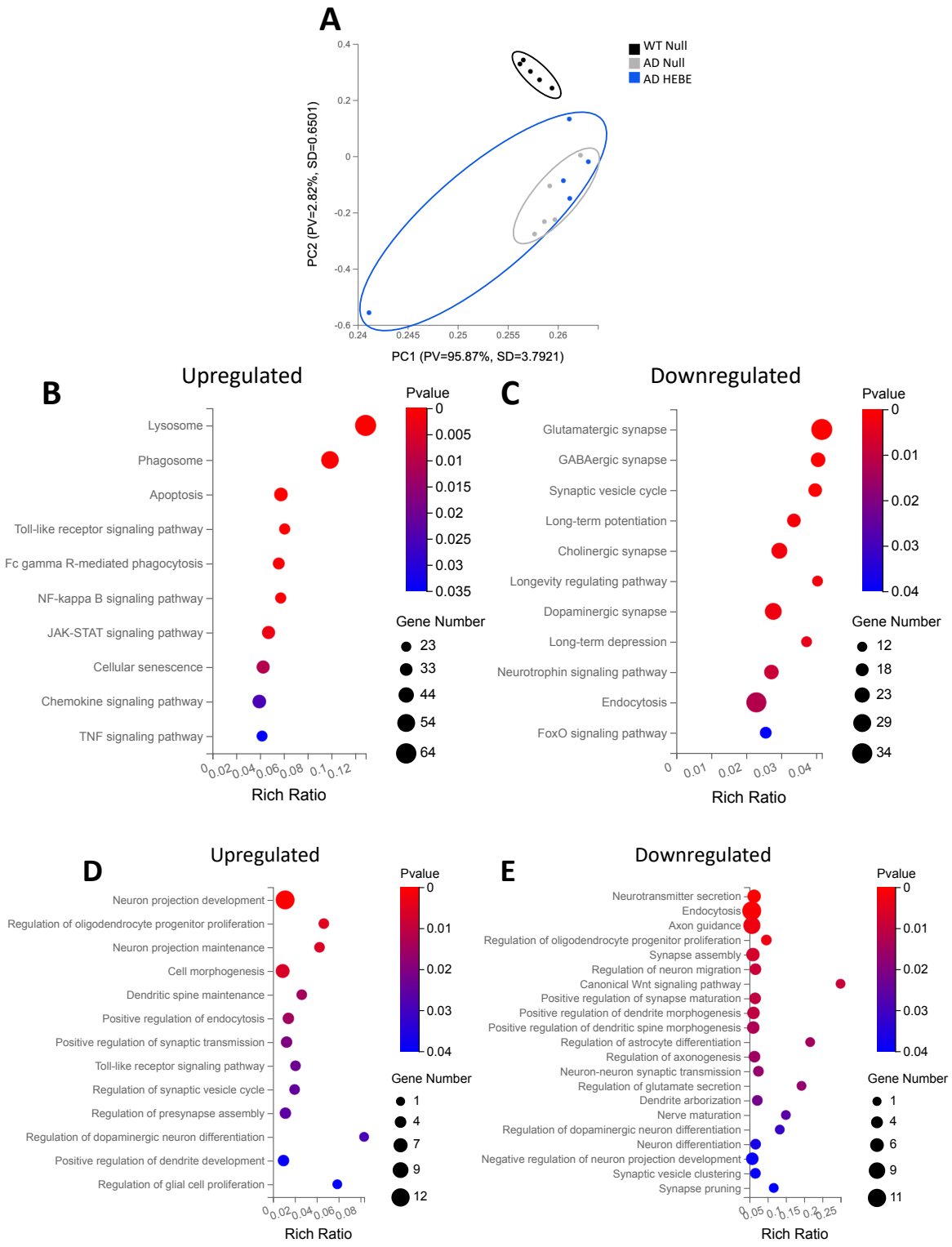



Figure 83. RNA-seq analysis of hippocampus samples for females. (A) Principal component analysis (PCA) plot. (B) KEGG pathways enriched in AD-Null vs WT-Null upregulated genes. (C) KEGG pathways enriched in AD-Null vs WT-Null downregulated genes. (D) GO pathways enriched in AD-HEBE vs AD-Null upregulated genes. (E) GO pathways enriched in AD-HEBE vs AD-Null downregulated genes. The abscissa represents the rich ratio, indicating the proportion of DEGs in each pathway. The number of DEGs in each pathway is represented by the circle area, and the color represents the corrected p-value. Sample size of 5 per group.

#### 2.3.7.2. Entorhinal cortex

In the entorhinal cortex, PCA analysis revealed a consistent pattern across both male and female subjects (Fig. 84A, Fig. 85A). As anticipated, the expression profile of the WT group diverged from that of the other experimental groups. However, similar to the hippocampus, the patterns between the two AD groups exhibited similarities, indicating modest treatment-induced transcriptional changes. When comparing AD-Null mice with WT mice, KEGG pathway enrichment analysis identified a total of 2888 DEGs in males and 660 in females (Fig. 84B, C, Fig. 85B, C), which were subsequently categorized into various biological pathways.

Most of the upregulated and downregulated pathways in control AD males were similar to those identified in the hippocampus (Fig. 84B, C), suggesting a comparable impact on both cerebral regions. However, in females, the affectations to the entorhinal cortex appeared to be less pronounced, with few pathways showing upregulation (Fig. 85B), and the downregulated pathways did not reach statistical significance (Fig. 85C).

Regarding the differences between HEBE-treated mice and AD mice, a total of 335 DEGs were found in males and 696 in females, which were assigned to different pathways (Fig. 84D, E, Fig. 85D, E). In males, HEBE's effects appeared to predominantly target neurons, regulating their activity and synaptic transmission (Fig. 84D, E). In females, despite affected pathways indicating an improvement in disease-related features similar to males (Fig. 85D, E), the AD model presented few affected pathways, making it challenging to draw clear conclusions from these results.

These findings suggest that HEBE improved important disease hallmarks in the entorhinal cortex of male mice, while the effects in females were less definitive.

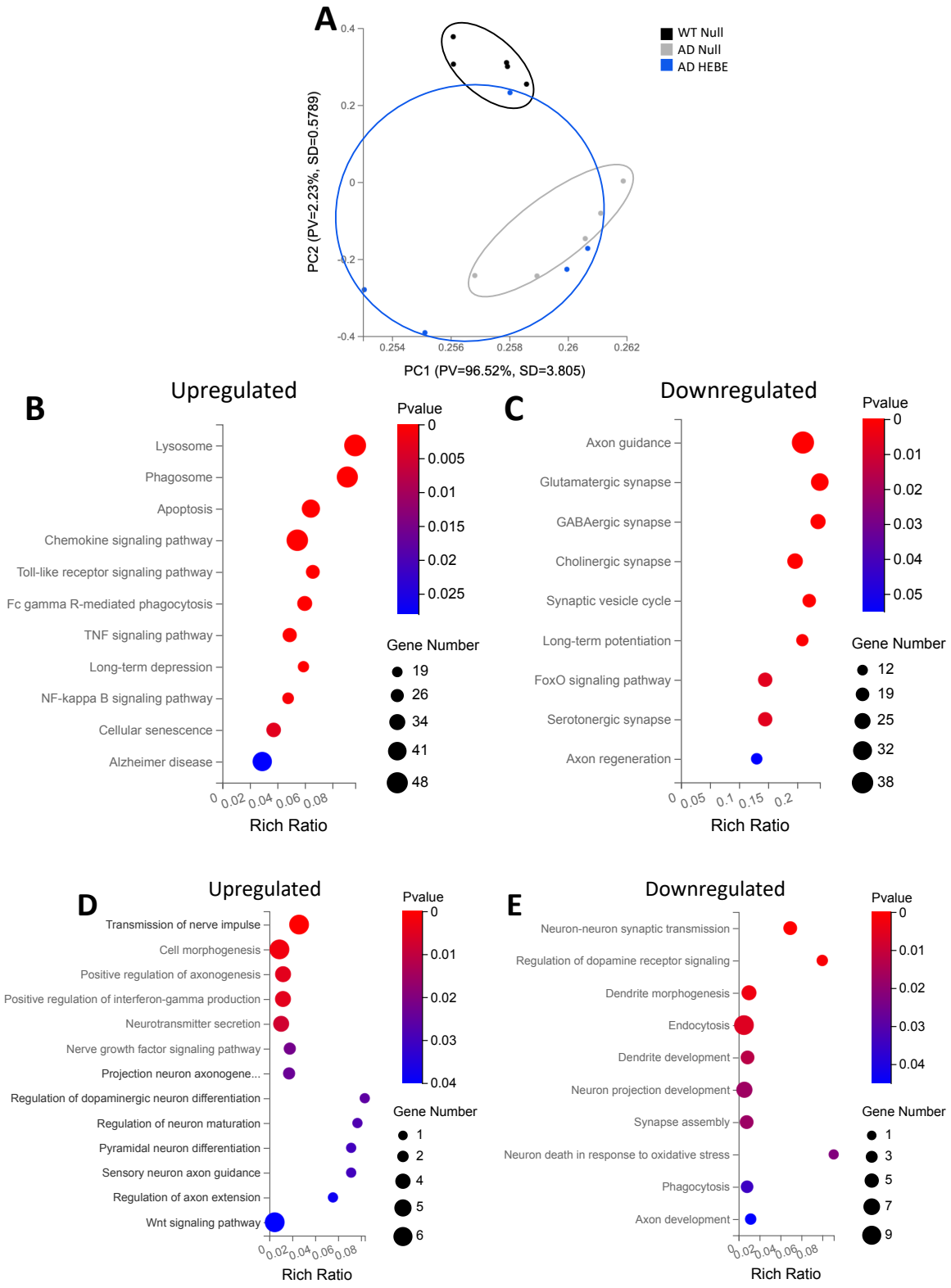



Figure 84. RNA-seq analysis of entorhinal cortex samples for males. (A) Principal component analysis (PCA) plot. (B) KEGG pathways enriched in AD-Null vs WT-Null upregulated genes. (C) KEGG pathways enriched in AD-Null vs WT-Null downregulated genes. (D) GO pathways enriched in AD-HEBE vs AD-Null upregulated genes. (E) GO pathways enriched in AD-HEBE vs AD-Null downregulated genes. The abscissa represents the rich ratio, indicating the proportion of DEGs in each pathway. The number of DEGs in each pathway is represented by the circle area, and the color represents the corrected p-value. Sample size of 5 per group.

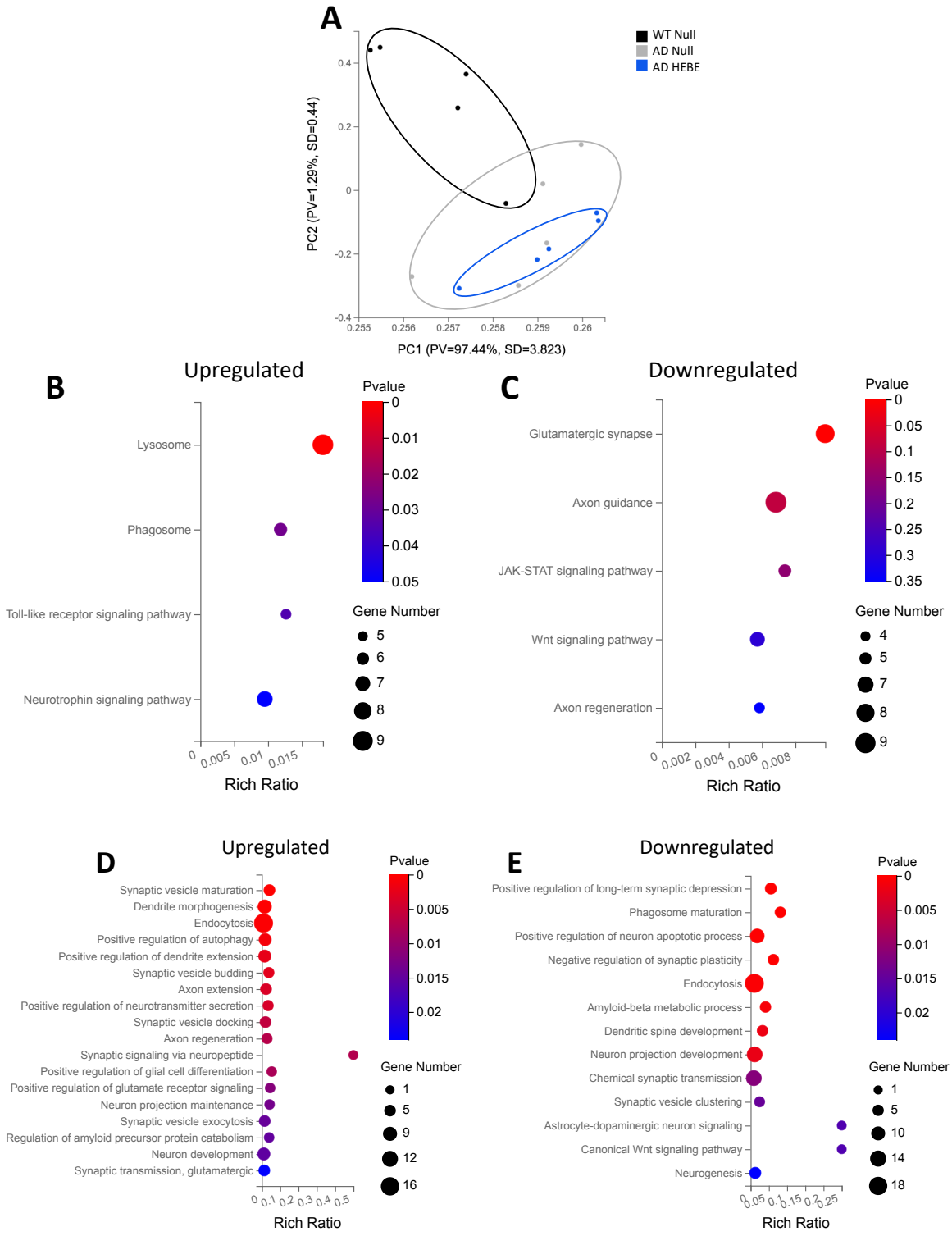



Figure 85. RNA-seq analysis of entorhinal cortex samples for females. (A) Principal component analysis (PCA) plot. (B) KEGG pathways enriched in AD-Null vs WT-Null upregulated genes. (C) KEGG pathways enriched in AD-Null vs WT-Null downregulated genes. (D) GO pathways enriched in AD-HEBE vs AD-Null upregulated genes. (E) GO pathways enriched in AD-HEBE vs AD-Null downregulated genes. The abscissa represents the rich ratio, indicating the proportion of DEGs in each pathway. The number of DEGs in each pathway is represented by the circle area, and the color represents the corrected p-value. Sample size of 5 per group.

### 2.3.8. Histopathology

Histopathological studies are helpful to visually determine changes in tissues. In this study, we conducted brain analyses focusing on the hippocampal region due to its relevance in AD.

#### 2.3.8.1. GFAP

GFAP is an astrocytic marker used to assess reactive astrogliosis in the brain. A moderate increase in astrogliosis was observed in AD mice (Fig. 86A), which appeared to be associated with the animal model rather than the treatment with HEBE. This increase was evident in both the dentate gyrus (Fig. 86B, C) and the CA3 region (Fig 86D, E). Therefore, the APP/Tau animal model exhibited increased astrogliosis compared to WT mice.

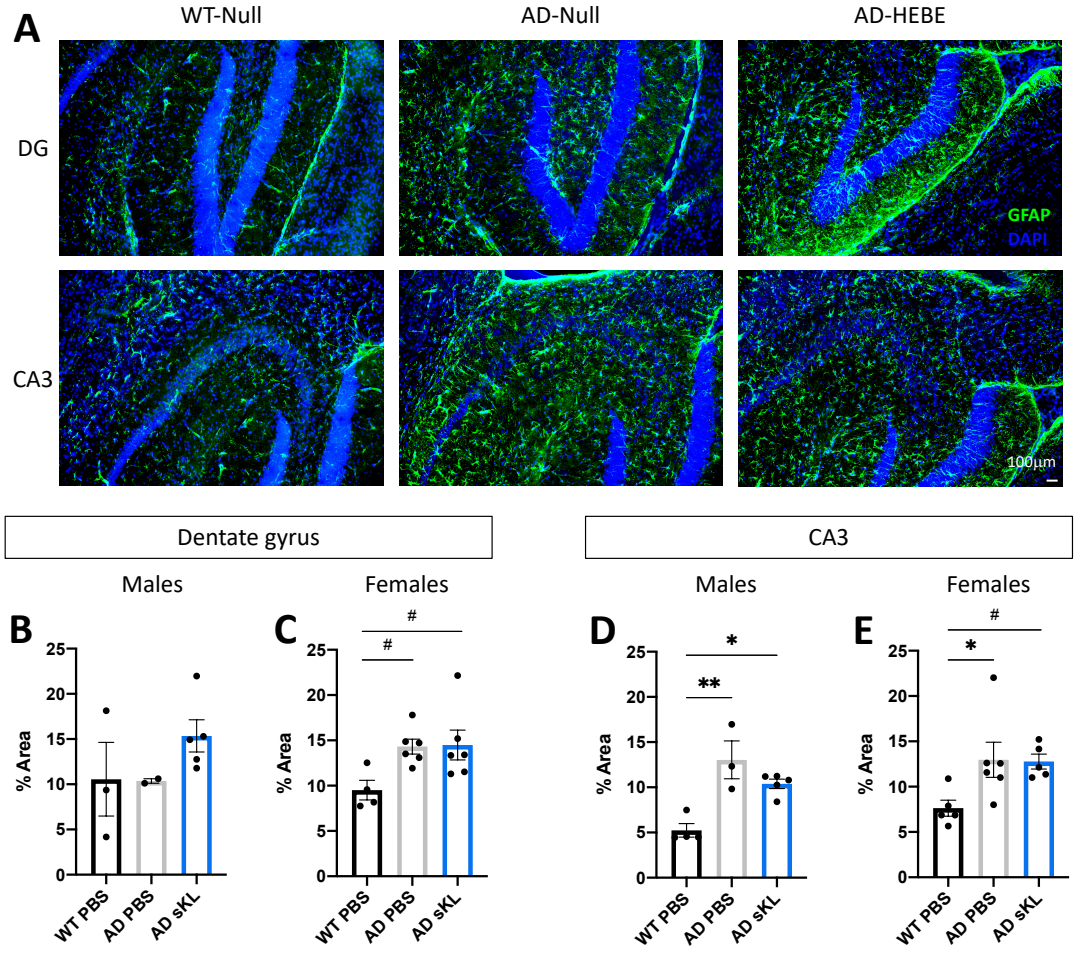



Figure 86. GFAP immunofluorescence in hippocampus, dentate gyrus (B, C) and CA3 (D, E). (A) Representative images for immunofluorescence with GFAP antibody. Green: GFAP labeling, blue: DAPI. (B, C) Quantification of positive GFAP area in the dentate gyrus, in males and females, respectively. (E, F) Quantification of positive GFAP area in the CA3 region, in males and females, respectively. Data are shown as Mean ± SEM, One-way ANOVA and Tukey post-hoc (*p<0.05, **p<0.01, #<0.07). Sample size for males: WT-Null=4, AD-Null=3, AD-HEBE=5. Sample size for females: WT-Null=5, AD-Null=6, AD-HEBE=5.

### 2.3.8.2. Iba1

Iba1 is a microglial marker, used to determine the microglial activation in brain. In AD males, we observed a trend towards increased microglial activation in the dentate gyrus (Fig. 87B) and a significant increase in the CA3 region (Fig. 87D). Interestingly, this heightened microglial activation in AD males appeared to normalize with the treatment. In females, no significant changes were noted in the dentate gyrus (Fig. 87C), although there was a trend towards increased activation in the CA3 region in HEBE-treated females (Fig. 87E). These findings suggest that AD mice may present elevated microglial activation, which could potentially be mitigated with HEBE treatment.

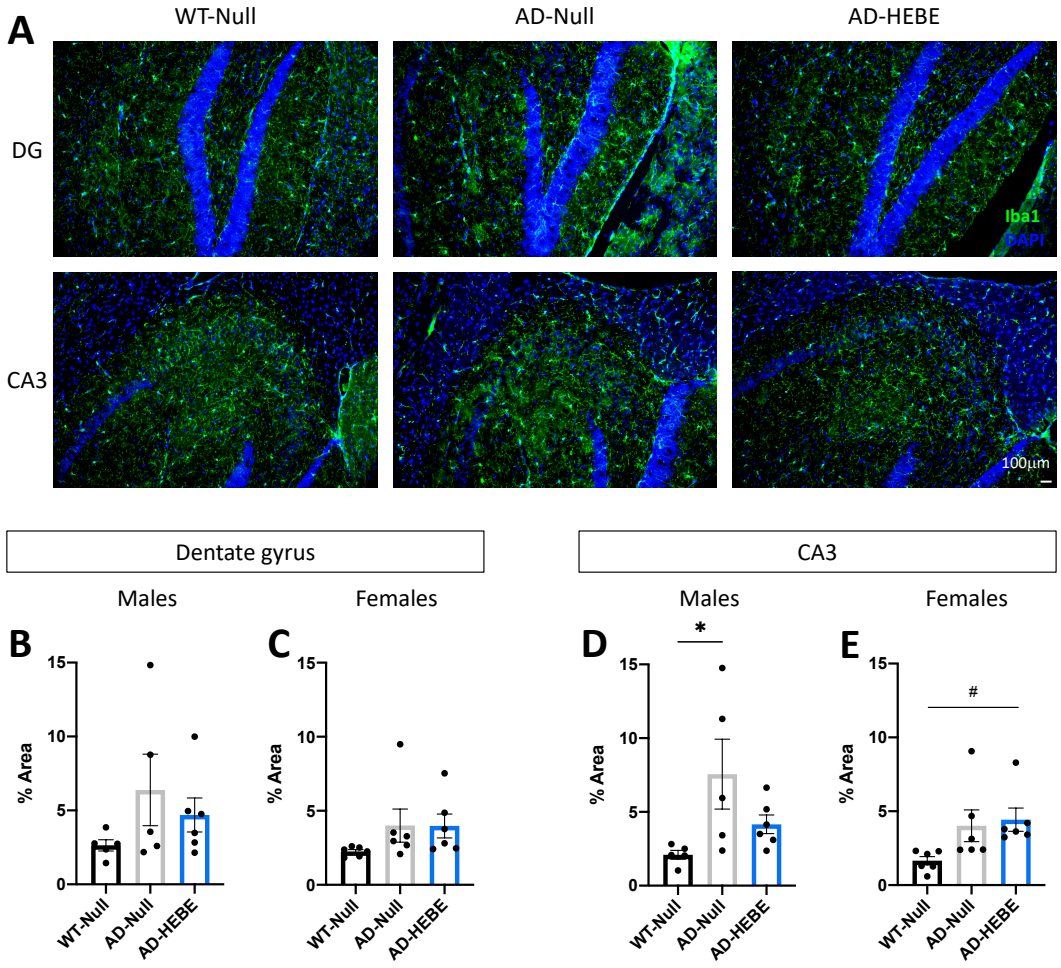



Figure 87. Iba1 immunofluorescence in hippocampus, dentate gyrus (B, C) and CA3 (D, E). (A) Representative images for immunofluorescence with Iba1 antibody. Green: Iba1 labeling, blue: DAPI. (B, C) Quantification of positive Iba1 area in the dentate gyrus, in males and females, respectively. (E, F) Quantification of positive Iba1 area in the CA3 region, in males and females, respectively. Data are shown as Mean ± SEM, One-way ANOVA and Tukey post-hoc (*p<0.05, #<0.06). Sample size for males: WT-Null=5, AD-Null=5, AD-HEBE=6. Sample size for females: WT-Null=6, AD-Null=6, AD-HEBE=6.

### 2.3.8.3. pTau

Neurofibrillary tangles are one of the main hallmarks in AD, composed of pTau. Analysis of pTau levels (Fig. 88A) in WT mice displayed negligible levels (Fig. 88B-E), as expected. In contrast, AD mice exhibited significant pTau accumulation in pyramidal and granular neurons, independent of gender or hippocampal subregion. Treatment with HEBE attenuated these elevated pTau levels, indicating a beneficial effect of the treatment. Notably, females displayed lower pTau levels (Fig. 88C, E) compared to males (Fig. 88B, D).

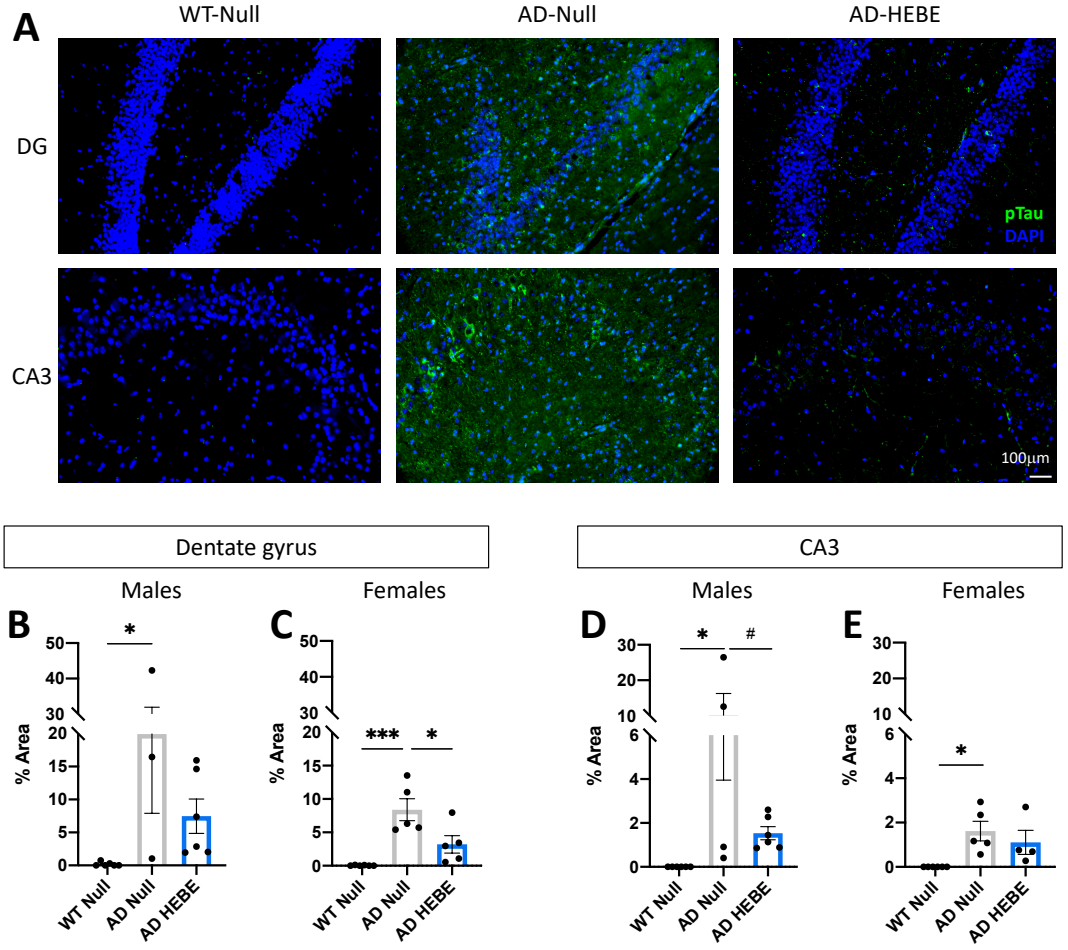



Figure 88. pTau immunofluorescence in hippocampus, dentate gyrus (B, C) and CA3 (D, E). (A) Representative images for immunofluorescence with phospho-Tau (Ser202, Thr205) antibody. Green: pTau labeling, blue: DAPI. (B, C) Quantification of positive pTau area in the dentate gyrus, in males and females, respectively. (E, F) Quantification of positive pTau area in the CA3 region, in males and females, respectively. Data are shown as Mean ± SEM, One-way ANOVA and Tukey post-hoc (*p<0.05, ***p<0.001, #<0.1). Sample size for males: WT-Null=6, AD-Null=5, AD-HEBE=6. Sample size for females: WT-Null=6, AD-Null=5, AD-HEBE=5.

### 2.3.8.4. Aβ

Amyloid plaques, composed of the Aβ peptide, represent another hallmark of AD. Assessment of Aβ peptide levels (Fig. 89A) revealed minimal to absent amyloid protein in WT mice (Fig. 89B-E). In contrast, AD mice displayed elevated Aβ levels, with HEBE treatment showing a modest trend towards reduction, particularly in the dentate gyrus of males (Fig. 89B) and the CA3 region in females (Fig. 89E), although these trends did not reach statistical significance.

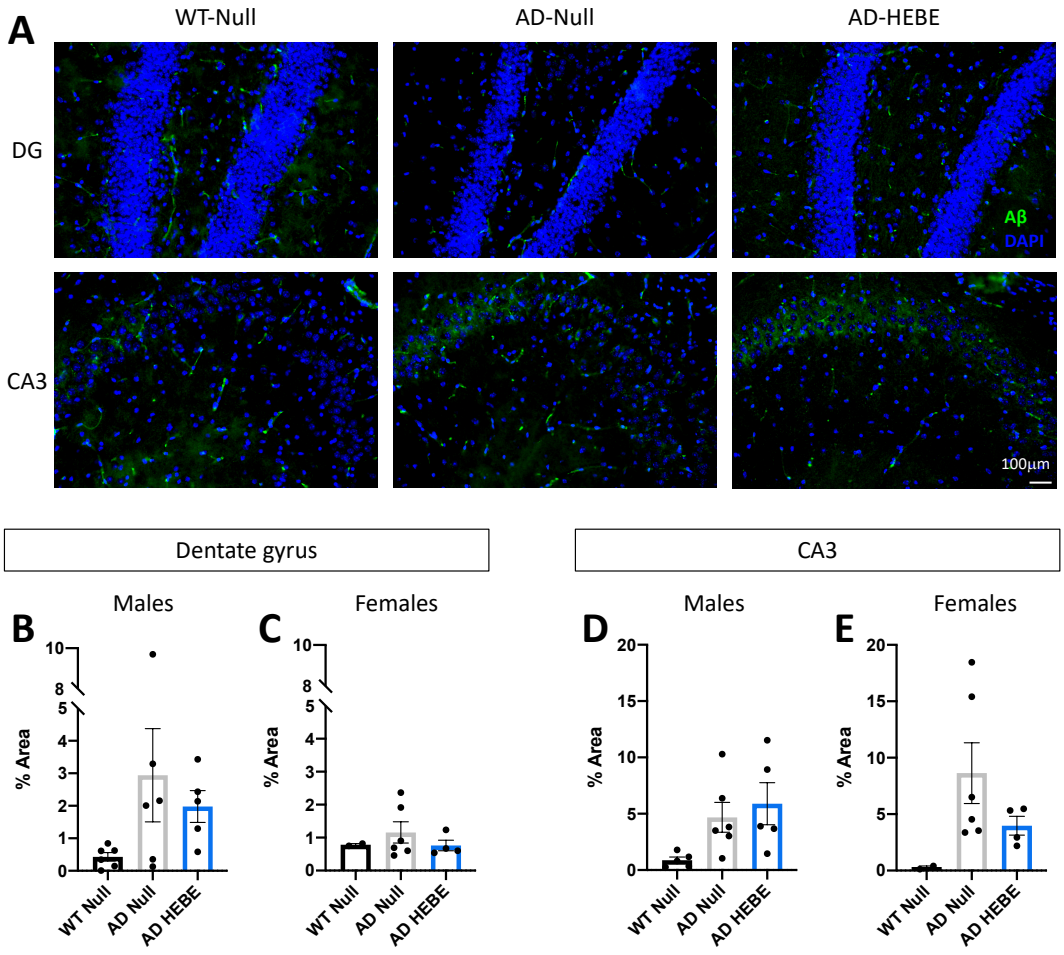



Figure 89. Amyloid-β immunofluorescence in hippocampus, dentate gyrus (B, D) and CA3 (D, E). (A) Representative images for immunofluorescence with amyloid-β 1-16 antibody. Green: Aβ labeling, blue: DAPI. (B, C) Quantification of positive Aβ area in the dentate gyrus, in males and females, respectively. (D, E) Quantification of positive Aβ area in the CA3 region, in males and females, respectively. Data are shown as Mean ± SEM, One-way ANOVA and Tukey post-hoc. Sample size for males: WT-Null=6, AD-Null=5, AD-HEBE=5. Sample size for females: WT-Null=2, AD-Null=6, AD-HEBE=4.

## 2.4. HEBE2 generation

HEBE exhibited a significant improvement in learning and memory in mice, accompanied by an amelioration of the Tau pathology. The absence of MMP inhibitory activity through the TIMP2 subunit *in vitro* with HEBE may have positive implications, considering that constitutive MMP inhibition could impact various physiological pathways. However, to test the potential activity of HEBE if it was able to inhibit MMPs, a second version of the chimeric chronokine, named HEBE2, was generated following an additional bioinformatic analysis.

### 2.4.1. Bioinformatic analysis

TIMP2 exerts its MMP-inhibitory function through its N-terminal domain [335]. In the first version of HEBE, the placement of TIMP2 in the middle of the protein structure hindered its N-terminal domain from inhibiting MMPs. Consequently, for the next iteration of HEBE, an alternative arrangement of the three chronokines was explored by swapping the positions of sTREM2 and TIMP2, resulting in the development of a new model (Fig. 90). In HEBE2, the signal peptide of sTREM2 was excluded, while that of TIMP2 was retained to preserve the protein's secretion properties. The new bioinformatic model was generated in collaboration with Dr Xavier Daura's group from the Department of Biochemistry and Molecular Biology at Universitat Autònoma de Barcelona. AlphaFold, a newly described software tool for accurately predicting protein structures [329], was used for this analysis, revealing no indication of protein aggregation.

TIMP2 - $(EAAAK)_3$ - sTREM2 - $(EAAAK)_5$ - sKL

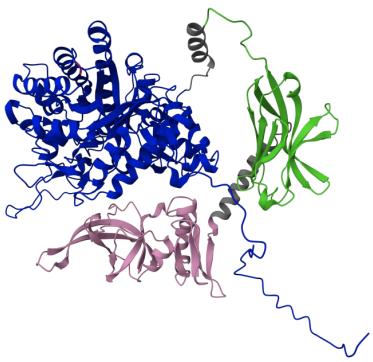


Figure 90. Representation of HEBE2.

### 2.4.2. Cloning and production of recombinant HEBE2

A plasmid encoding the new HEBE2 was engineered with restriction enzyme cloning techniques (pGG2-HEBE2). Subsequent transfection of the plasmid into the HEK293 mammalian cell line, followed by a Western Blot revealed a band of ~130 kDa detected by antibodies against each of the subunits. This demonstrated that the protein (i) was correctly expressed in cells, (ii) could be secreted by the cells, as evidenced by its presence in the supernatant, and (iii) did not break at the junction of the linkers (Fig. 91). Therefore, it was a structurally stable protein in an *in vitro* context.

The HEBE2 protein will be used for further studies to assess its *in vitro* functional activities and to compare its efficacy *in vivo* with that of the original HEBE protein.

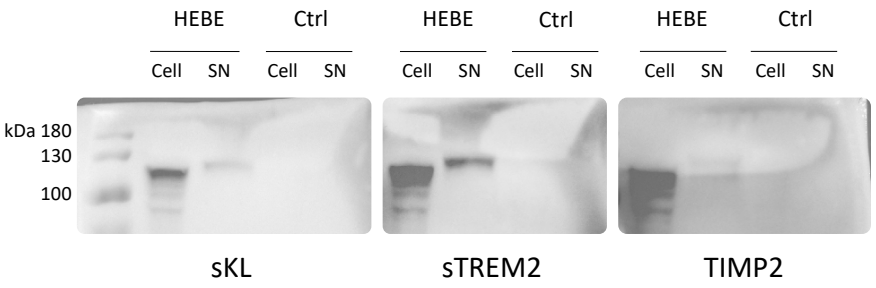



Figure 91. Western Blot of HEK293 cells transfected with a plasmid encoding HEBE2 or Null as a control. Both cell lysates (Cell) and supernatants (SN) were loaded, and the immunodetection was performed using antibodies against each of the subunits as indicated below each membrane. Theoretical molecular weight of HEBE2 without posttranslational modifications is 102,2 kDa.

# DISCUSSION

Until recently, available therapeutics for Alzheimer's disease provided symptomatic relief without addressing the underlying biological mechanisms driving the pathology [336]. However, in recent years, disease-modifying treatments have gained interest due to their potential to ameliorate the biological processes implicated in AD, improving treatment outcomes. Predominantly, clinical trials using disease-modifying treatments focus on modulating the Aβ biological pathway, based on the already disputed amyloid cascade hypothesis [100,337]. Notably, the FDA has only approved two disease-modifying treatments, namely lecanemab [98] and aducanumab [96], which are monoclonal antibodies aimed at inhibiting amyloid aggregation. However, a significant limitation of these treatments lies in the targeting of a specific pathway, overlooking the complexity of the disease [338]. The lack of a broader targeting is one of the reasons many of the treatments in clinical trials result in limited clinical efficacy and do not achieve approval by regulatory agencies [337,339]. In this context, we believe that using pleiotropic chronokines capable of simultaneously improving multiple mechanisms could offer greater therapeutic potential for the treatment of AD.

## 1. Recombinant sKL as a therapy for Alzheimer's disease

αKlotho is a protein known for its significant anti-aging properties [104,107,176,177]. It exists in various isoforms, as discussed in the introduction. However, the functional differences among these isoforms remain unclear, with many studies failing to differentiate between them. Most studies on Klotho's neuroprotective role in the brain focus on the transmembrane (mKL) or processed isoform (pKL) [107,159,160,340], but the contribution of the secreted isoform (sKL) remains poorly understood. Nonetheless, it is believed that the KL2 domain (present only in pKL) may confer different properties compared to sKL. Recent findings indicate that while pKL adversely affects mineral metabolism and bone microstructure, sKL appears to have no such effect [341], implying that sKL might offer a safer therapeutic option compared to pKL. Furthermore, previous studies have demonstrated that a therapeutic strategy using sKL is safe [167,169,177,342], even presenting antitumor effects [140–142].

Given the association between altered Klotho expression and Alzheimer's disease [118–120,159,342], permanently maintaining elevated Klotho levels presents a suitable therapeutic strategy. *In vivo* gene therapy using AAV vectors has emerged as a promising approach for achieving sustained Klotho expression in the brain and has been previously tested in mice [138,167,177,342]. However, viral vectors still present drawbacks. Despite the availability of some gene therapy strategies in the market for human patients suffering from various diseases, the number is limited due to the high economic cost, potential cytotoxicity at high doses, and pre-existing immunity against AAVs in patients [270,343]. These challenges can be circumvented by using recombinant proteins that do not present the aforementioned limitations and typically have shorter approval times. Consequently, the first objective of this thesis was to evaluate the beneficial effects of systemically administered recombinant sKL, specifically the human isoform, which has shown efficacy in mice [344] and could facilitate future translatability to human patients.

### 1.1. Recombinant sKL production and characterization

Recombinant human sKL was produced in-house, by infecting CHO cells with adenoviral vectors. This protein production system yields substantial quantities of recombinant proteins due to the efficient transduction of cell lines by adenoviral vectors. The CHO cell line was selected based on previous findings indicating that CHO-derived sKL exhibited greater biological activity compared to HEK293-derived sKL [345]. For purification purposes, the protein was engineered with a C-terminal polyhistidine tag. Placing the tag at the C-terminal position prevents interference with the N-terminal signal peptide responsible for protein secretion, ensuring that the protein could be purified from the cell medium with all necessary posttranslational modifications for its functionality. Although the polyhistidine tag was not removed after purification, its small size (0.8 kDa) was not expected to impact the protein's biological activity or elicit an immunogenic response in mice.

sKL is a pleiotropic protein, complicating the comprehensive *in vitro* assessment of all its activities. Therefore, a straightforward method employed to confirm protein stability and activity was the β-glucuronidase enzymatic assay. Despite previous studies reporting a

weak β-glucuronidase activity for recombinant Klotho [345,346], we observed significant activity, comparable to pure bovine β-glucuronidase. This result suggests that sKL indeed possesses notable β-glucuronidase activity, likely influenced by the production and purification process of the protein, as our methods differed from those used in other studies. Furthermore, this result confirmed the suitability of using the produced recombinant sKL for an *in vivo* experiment.

Understanding the half-life of a recombinant protein is crucial for determining optimal dosing and administration intervals in therapeutic strategies. Following intravenous administration, our recombinant sKL exhibited a terminal half-life of 8.65 h. This duration is comparable to the reported half-life of pKL, ranging from approximately 7.2 h [347] to 12.2 h [345] in rats, depending on the study. Given the similarities between these proteins, we anticipated similar terminal half-lives for sKL, although to our knowledge, this study represents the first determination of this parameter for sKL. The observed longer half-life of 10.53 h following intraperitoneal administration was advantageous for our purposes, allowing for extended administration intervals in the *in vivo* experiment.

We selected an administration interval of 24 h based on our calculations. A longer interval would not sustain consistent protein presence in the bloodstream, potentially compromising therapeutic efficacy. Since the protein's half-life is less than 12 h, when administered once daily, the accumulation index is low, resulting in minimal concerns regarding protein accumulation and associated toxicity [318]. Therefore, the 24-h interval was deemed optimal, ensuring sufficient protein levels in the bloodstream without complete depletion before the subsequent administration. The dose was determined based on the physiological soluble Klotho levels in humans. Despite declining with age, healthy young individuals typically have around 1500 pg/mL [330,331]. Thus, our therapeutic approach aimed to maintain sKL levels at or above this threshold. A dose of 10 μg/kg was calculated to achieve this target, resulting in a minimum of 3000 pg/mL of sKL in the blood. This dosage has been previously used in studies involving pKL, which demonstrated cognitive improvements [160,340,344].

### 1.2. *In vivo* assessment of sKL's effects

The study presented in this thesis serves as a proof of concept. However, the translatability of this therapeutic approach is limited by the need for daily administration of the protein. While the half-life of sKL in human plasma is unknown, it is not expected to significantly differ from that in mice. Therefore, to apply this strategy in humans, it is essential to extend the protein's half-life. Several strategies have been explored for this purpose, including attaching carbohydrates, polymers, polypeptides, or bioactive proteins to the therapeutic protein, introducing point mutations to prevent protease-mediated degradation, or delivering the protein encapsulated within nanoparticles [348]. These strategies should be tested with sKL, aiming to reduce the frequency of drug administration and facilitate translation to human therapies.

The APP/Tau mouse model was selected due to its ability to recapitulate the AD-like pathology by developing both the Aβ and Tau pathologies, overcoming the limitation of other mouse models that only develop one of the pathologies [311]. Recombinant sKL therapy was proposed as a preventive measure to delay or halt disease onset. Treatment started at approximately 5 months of age, prior to symptom onset. Mice received intraperitoneal injections of 10 μg/kg of recombinant human sKL for four weeks before undergoing behavioral and cognitive assessments to allow elevated sKL levels to exert a protective effect.

No significant changes in physical condition were observed among mice groups, as evidenced by consistent weight throughout the experiment, consistent with previous sKL studies [177,341]. Additionally, sensorimotor abilities remained unchanged, indicating that sKL does not affect physical capabilities in mice.

In the Open Field test, locomotor activity did not differ among groups, suggesting that sKL had no impact on this parameter. However, female mice injected with sKL displayed a moderate increase in thigmotaxis, an indicator of anxiogenic behavior [349], suggesting higher anxiety levels in females. Notably, this moderate increase may be attributable to the animal model itself, as females have been reported to exhibit higher anxiety levels

[312]. Nevertheless, it is important to note that the trend towards an increase observed in control AD mice compared to WT mice was not statistically significant in our study. Therefore, it is unlikely that sKL directly induces anxiety-like behaviors in these mice, a finding consistent with other studies [107,177,342].

Recognition memory impairment was observed only in male mice, as evidenced by the Novel Object Recognition Test. Male AD mice presented impaired recognition memory, which was normalized in sKL-treated mice. However, female AD mice did not display this impairment, hindering the observation of sKL-induced changes. Recognition memory is closely associated with the medial temporal lobe, particularly the hippocampus and perirhinal cortex [350,351]. It is possible that the pathology was not well established at the age the animals were tested, even showing differences in the establishment pace between sexes, with more pronounced affectations in the hippocampal region of males than females.

In the case of spatial learning and memory in the Morris Water Maze, results differed from those of recognition memory. AD males did not display clear impairment during the learning phase. However, in the memory test, while short-term memory appeared unaffected in AD males, a moderate impairment in long-term memory was observed, which was not alleviated by the sKL treatment. In contrast, AD females displayed generalized spatial learning and memory impairment across all tests performed. These impairments, however, were not alleviated by sKL. These results contrast with previous studies, which showed a modest enhancement in long-term spatial memory performance in the MWM tests conducted on 3xTg-AD and APP/Tau mice expressing sKL via an AAV vector within the brain [342], as well as in aged WT mice [177]. Similarly, improvements in spatial memory were noted in the APP/PS1 model of AD following intracerebroventricular administration of a lentiviral vector expressing mKL [167,169]. This indicates that at the conditions used in this study, systemically delivered recombinant sKL is not capable of correcting spatial learning and memory deficits in the APP/Tau model.

Spatial learning and memory are highly dependent on the hippocampus [352], indicating that various memory types associated with this brain region may be differently affected in the APP/Tau model. For instance, males displayed impaired recognition memory but unaffected spatial memory, while females did not show recognition memory impairment but displayed modest spatial memory deficits. As discussed earlier, these contradictory findings may be attributed to incomplete AD phenotype development in 6-month-old mice, underscoring the importance of conducting studies at older ages. Nonetheless, sKL effectively mitigated recognition memory impairment in male AD mice, highlighting its potential as a treatment for cognitive impairment.

### 1.3. sKL-induced changes at a molecular level

A gene expression analysis was conducted to elucidate the underlying mechanisms contributing to observed memory changes. Notably, a downregulation of *Slc17a7* expression was observed in the hippocampus of both male and female AD mice, alongside decreased *Homer1* expression specifically in males, consistent with previous findings in this animal model [312]. The proteins encoded by these genes play critical roles in glutamate neurotransmission at synapses, a process pivotal for memory formation [353,354]. Thus, these downregulations and subsequent reduction in glutamate transmission may underlie the impaired memory performance observed in AD mice during the NORT and MWM tests. Treatment with sKL appeared to normalize the expression of these genes, suggesting that the observed memory enhancements may be mediated by increased glutamate neurotransmission. Similar findings have been reported in other studies, where Klotho was found to increase the levels of the GluN2B protein subunit of the NMDA receptor in postsynaptic densities of the hippocampus, enhancing glutamate neurotransmission and long-term potentiation [107,159]. Collectively, these results indicate that sKL may augment glutamate neurotransmission in the hippocampus, thereby contributing to memory preservation.

An RNA-seq analysis of hippocampal samples provided insights into the affected pathways in AD mice and the functional impact of sKL. Males exhibited upregulated pathways associated with AD pathology, including apoptosis [355], cellular senescence [356],

lysosomes [357] and phagocytosis [358], alongside downregulated pathways related to synapses and LTP [359], confirming males can replicate AD. In contrast, female mice did not display important differences compared to WT mice, further supporting the idea that at 6 months of age female mice may not have fully developed the AD phenotype yet. Despite modest memory improvements in males, the study demonstrated that sKL enhances synaptic transmission involving glutamate, corroborating the previous gene expression findings. It is important to note that RNA-seq analyses provide insight into transcriptional changes but do not offer a comprehensive view of brain alterations. Therefore, a comprehensive proteomic analysis could further elucidate additional Klotho-mediated mechanisms. For instance, as previously mentioned, Klotho has been shown to increase GluN2B protein levels without affecting transcription levels [107], suggesting that sKL could be acting at a posttranscriptional level.

Histopathological examination revealed minimal Aβ levels in the hippocampus of both sexes of the APP/Tau model at 6 months of age, possibly explaining the mild cognitive impairment observed in behavioral tests. In contrast, Tau depositions were evident in the dentate gyrus and CA3 region of the hippocampus in both sexes. sKL treatment did not appear to alleviate Tau pathology in general, with only a significant reduction observed in the CA3 region of females. This was further corroborated by the absence of differences in positive area for microglial cells, which are involved in mediating the clearance of aggregated proteins. Nonetheless, further analyses should explore differences in cell number or morphology indicative of microglial activation, potentially revealing more pronounced effects [360]. Astrocytes also contribute to protein clearance, with a modest increase in positive area observed in sKL-treated males, although this increase may be related to the animal model itself, as a slight elevation was visible in the CA3 region.

### 1.4. Final remarks

Overall, the findings suggest that the pathology in the animal model is not fully developed by 6 months of age, particularly evident in females. Furthermore, disease progression in the APP/Tau model appears to be influenced by sex, underscoring the necessity to repeat the study at more advanced ages when pathology is fully established and treatment

effects with sKL are more apparent. Additionally, the sample size used in this study was insufficient to detect statistically significant differences in many cases, indicating the need for a larger cohort of mice to observe more pronounced effects. Nonetheless, this study concludes that sKL can induce changes in the brain of APP/Tau mice, particularly at the molecular level, ultimately resulting in cognitive improvement.

The mechanisms underlying sKL-induced changes are unclear, as the protein does not cross the BBB to reach the brain. Consistent with earlier research showing that systemically administered pKL fails to cross the BBB [160,347], our findings similarly demonstrate the inability of sKL to breach this barrier, mainly accumulating in the liver. However, despite not reaching the brain, pKL has been shown to modulate mechanisms involved in AD, ameliorating cognitive decline by enhancing glutamate neurotransmission [160]. Therefore, our hypothesis is that sKL could initiate a systemic signaling cascade acting through an intermediate molecule capable of crossing the BBB, ultimately leading to cognitive improvement. Further research is necessary to elucidate the precise mechanism through which sKL acts in the brain.

Studies conducted in the APP/PS1 mouse model of AD have demonstrated that mKL can ameliorate cognitive impairments by inducing autophagy and promoting microglial transition from the M1 phenotype to M2, thereby leading to enhanced Aβ clearance [167,169,171,361]. Additionally, Klotho has been observed to modulate the brain metabolome through its KL1 domain [344] and reduce oxidative stress in the brain [138]. Given that the RNA-seq analysis performed in the APP/Tau model did not reveal changes in these pathways, future research should explore the potential of systemically administered recombinant sKL to influence these pathways for enhanced cognition.

In conclusion, recombinant sKL holds promise as a systemic therapeutic agent capable of inducing changes and improving cognitive abilities in the brains of AD patients. However, further experiments should be conducted using older mice with a well-established pathology and a larger sample size to reduce data variability. Additionally, further studies aiming to extend sKL's half-life could streamline the study design and enhance its potential application in human patients.

## 2. HEBE as a therapy for Alzheimer's disease

Chimeric proteins are being widely studied for several applications, as they offer advantages such as extended half-life and enhanced therapeutic effects, among others. Typically, FDA-approved chimeric proteins consist of a short effector peptide linked to a protein that helps with stability, targeting, and solubility, such as the Fc region of the human IgG1 antibody [362]. The effector peptide typically modulates the activity of a specific receptor either as an agonist or antagonist. Additionally, another area where chimeric proteins find application is in cancer immunotherapy involving CAR T-Cells, where the CAR receptor of the T-Cells is engineered to bind to specific antigens on the surface of cancer cells [363]. AD is a complex disease characterized by the dysregulation of numerous pathways, and while sKL exhibits pleiotropic effects, it may not be sufficient as a standalone therapy for AD. Therefore, leveraging the technology of chimeric proteins, we proposed a strategy combining different chronokines with complementary functions to enhance therapeutic efficacy. In this study, three chronokines were selected based on their complementary actions to potentially contribute to an effective AD treatment.

The beneficial effects of sKL on improving glutamate neurotransmission, reducing oxidative stress in the brain, and providing neuroprotection have been previously discussed. Additionally, sTREM2 could offer further benefits by addressing microglial dysfunction in AD, enhancing Aβ phagocytosis through the transition to disease-associated microglia, and promoting their survival and proliferation. Moreover, sTREM2's potential to decrease Tau depositions would also be advantageous. TIMP2's role in promoting neuronal differentiation and increasing synapse density could also contribute to the therapy for AD. Each of these three chronokines has individually demonstrated beneficial effects in AD [159,167,177,240,248,342,364,365]. Therefore, combining them into a novel drug holds potential for advancing the search for an effective treatment for the pathology. Furthermore, Klotho and TREM2 are said to have beneficial effects in other neurodegenerative diseases such as Parkinson's [160,366,367], suggesting that the combination of proteins could potentially have a broad therapeutic scope for various disorders. Therefore, this study aimed to develop a chimeric chronokine combining all

three proteins, referred to as HEBE, inspired by the Greek goddess of youth and rejuvenation *Hebe*.

## 2.1. HEBE design

A thorough bioinformatic analysis was conducted to engineer a viable candidate for the chimeric chronokine HEBE. Initially, individual analyses were performed on each chronokine to assess their molecular dynamics in a physiological context and the distribution of electrostatic charges across their protein surfaces. Previous studies had only assessed the structure and flexibility for the sTREM2 protein [368], yielding RMSD and RMSF plots similar to those observed in our study, and confirming the limited flexibility of the protein. In contrast, studies on sKL and TIMP2 had predominantly explored their structures and flexibilities within the context of protein-protein interactions. Notably, investigations into Klotho have centered on its full-length structure when interacting with either FGF23 [369,370] or VEGFR2 and TRCP1 [371]. Similarly, previous examinations of TIMP2 did not assess its flexibility upon crystal structure determination [372], and subsequent studies have focused on its interactions with matrix metalloproteinases [335,373]. Hence, our study represents the first comprehensive analysis of sKL and TIMP2's structures and flexibilities to our knowledge. Our analysis revealed that both chronokines are flexible, a trait likely crucial for their functional roles. Therefore, preserving the conformational freedom of these proteins was imperative during the assembly of the chronokines to maintain their functionality. Additionally, understanding the electrostatic charge distribution was critical for designing the chimeric chronokine, as arrangements leading to electrostatic attraction between proteins might induce aggregation. Given the complexity of these analyses, the human versions of each protein were selected to enhance translatability to humans, considering the demonstrated beneficial effects of each individual protein in mice, where HEBE would be later evaluated [240,248,344].

Since several initial attempts to combine the proteins resulted in aggregation, rigid linkers were introduced between the proteins to maintain spatial separation, thereby reducing the likelihood of interactions and consequent aggregation. Ultimately, a version of HEBE

was developed that did not aggregate, and its stability was confirmed through *in vitro* analyses. Therefore, this study highlights the importance of conducting comprehensive bioinformatic analyses to engineer fusion proteins, providing insights into their dynamics and yielding candidates with improved success rates.

## 2.2. *In vitro* functional characterization

To determine the biological activity of HEBE, recombinant proteins of each individual chronokine and HEBE itself were produced and purified with a C-terminal polyhistidine tag. The β-glucuronidase activity of sKL was retained in HEBE, showing even greater activity than sKL alone at equimolar concentrations, suggesting a potential synergistic effect upon combining the chronokines.

Subsequently, phagocytic activity analysis associated with sTREM2 in BV2 cells revealed that HEBE's impact on phagocytosis varied depending on the targeted molecule. Specifically, HEBE led to a reduction in myelin phagocytosis, whereas it did not affect Aβ phagocytosis. Additionally, a moderate increase in cell activation was observed upon HEBE addition, although this did not translate into enhanced phagocytic activity. The limited effects observed with Aβ could be attributed to the already high cell activation state in the presence of Aβ, making it challenging to discern further increases in phagocytic activity. Unfortunately, contrary to previous findings [240,374], neither commercial recombinant sTREM2 proteins nor our in-house-produced protein showed alterations in phagocytic activity in our experiments. Hence, in the absence of a working control for our test, we cannot confirm sTREM2's function on phagocytosis modulation. Some studies indicate that sTREM2 may have greater impact on the activation of microglia and inflammatory responses rather than phagocytic activity [238,375,376], contrary to the transmembrane form of the protein. Therefore, conducting a comprehensive analysis of microglial activation in future experiments could provide insights into sTREM2's mechanisms of action. Furthermore, sKL's unexpected effect of reducing phagocytic activity in the presence of Aβ has not been previously described to our knowledge. Despite differences depending on the phagocytosed molecule, a consistent and noteworthy conclusion emerged: HEBE exhibited distinct activity compared to the mixture of

individual chronokines. This suggests that the conformation resulting from the union of the three proteins could enhance existing functions or confer new ones, potentially increasing HEBE's therapeutic potential compared to the administration of the three chronokines individually.

In the case of MMP1 inhibition mediated by the TIMP2 subunit, HEBE did not achieve the level of inhibition observed with TIMP2 alone, indicating that HEBE does not preserve MMP inhibitory activity. The underlying reasons for this discrepancy will be addressed later. However, it is important to note that the *in vitro* activities tested in this study do not encompass all the functions of these proteins due to their pleiotropic nature. Therefore, although HEBE may not efficiently inhibit MMP1, it may retain other known functions of TIMP2 [263–265] that could contribute to improving the pathology. Further experiments are warranted to fully elucidate more *in vitro* functions of HEBE.

### 2.3. *In vivo* assessment of HEBE's activities

For the *in vivo* proof of concept with HEBE, a gene therapy strategy using AAV vectors was selected, as viral vectors allow for a long-term expression of the transgene after a single administration and efficient transduction of cells in the brain. Given the advantages these vectors present, they are currently being employed in some clinical trials for the treatment of AD [100,377,378], indicating the suitability of evaluating HEBE through this approach. In our study, a variant of AAV9, known as AAV9P31, was chosen due to its capability to cross the BBB in mice [293]. This makes the administration route less invasive than intracerebral injection, as it allows for an intravenous administration of the vector. It also enables the vector to reach the central nervous system and distribute uniformly, achieving more consistent protein expression across the brain, including the hippocampus, an area where we have observed an important expression of the vector, and is adequate for a therapy targeting AD. Additionally, the vector also exhibits tropism for the liver, allowing for protein secretion into the bloodstream, potentially contributing to systemic effects that could benefit AD pathology, as has been observed with recombinant sKL in the previous study of this thesis.

A dose of the viral vector of $5 \cdot 10^{11}$ vg/mouse was administered for two primary reasons. Firstly, as an initial proof of concept approach, a high expression of the protein would allow us to assess potential beneficial effects of HEBE. Secondly, the dose was intended to compensate for potential expression loss due to methylation of the CMV promoter within the expression cassette. The CMV promoter was chosen for its high, rapid, and ubiquitous expression in neural cells. However, it is susceptible to methylation, leading to a decrease in expression over time and subsequent potential loss of therapeutic efficacy [379]. Other strong promoters, such as the CAG promoter, were not suitable in this case, given its size of approximately 1.7 kb. When combined with HEBE's 2.7 kb, ITRs, and polyA signal, the total size would be close to exceed the AAV's packaging capacity. Consequently, this could lead to diminished vector yield and potential incomplete genome packaging, compromising the therapeutic approach [380].

The APP/Tau mouse model was employed, consistent with the previous study involving recombinant sKL, although treatment initiation age differed. Mice were injected with the viral vector at 24 weeks of age (approximately 6 months), coinciding with the onset of initial pathology signs. Evaluation occurred at 36 weeks of age (around 9 months), allowing sufficient time for therapeutic protein expression and function. By this stage, mice were expected to present well-established pathology, facilitating observation of HEBE's effects. Considering the observed variability in the previous sKL study, the sample size was increased. Due to logistical complexities with larger sample sizes, two independent sets were used in this study at different times under identical experimental conditions, enhancing statistical robustness and significance.

The efficient transduction of viral vectors was confirmed in both the liver and brain tissues, with detectable expression of HEBE observed in these tissues. However, the viral vector count and expression levels were notably lower in the livers of female mice compared to males, consistent with previous findings with AAV vectors in females [332]. The potential implications of these gender-based differences on treatment efficacy require further investigation, considering that systemic expression of HEBE may contribute to cognitive enhancement, similar to the effects observed in the study with recombinant sKL. Ultimately, these results indicate effective BBB crossing by viral vectors,

with mice expressing HEBE for approximately three months by the time behavioral and cognitive assessments were conducted.

Given that HEBE is a newly developed molecule, its potential toxicity was assessed. WT mice were injected with the AAV vector expressing HEBE, and subsequent observations revealed no macroscopic changes upon euthanasia. Blood analysis demonstrated that HEBE did not alter any analyzed parameters compared to WT mice injected with a control vector. Furthermore, weight loss is one of the first apparent symptoms in rodents in response to exposure to a toxic substance [381], and HEBE-injected AD mice did not exhibit differences in weight compared to AD mice injected with the control vector. These findings collectively suggest that HEBE does not pose toxic effects and can be safely applied therapeutically. Furthermore, HEBE is not expected to elicit an immunogenic response in humans, as the endogenous forms of the chronokines were used in the design of the chimeric chronokine.

Similar to the previous sKL experiment, no significant differences were observed among groups in physical condition or sensorimotor functions. In the Open Field test, mice did not display differences in locomotor activity upon HEBE treatment, suggesting that HEBE does not impact these parameters. Notably, locomotor activity data was comparable to that obtained in the recombinant sKL experiment, indicating consistency in locomotor activity across experiments in this animal model up to 9 months of age. However, variations were observed in anxiety-like behaviors. Male mice treated with HEBE presented increased thigmotaxis compared to other groups, indicating a potential effect of HEBE on anxiety levels, although thigmotaxis levels were maintained in WT and AD groups compared to the sKL experiment. In contrast, female mice treated with HEBE did not display increased thigmotaxis, although both WT and AD female groups spent considerable time near the walls, indicating high anxiety levels. Compared to the recombinant sKL experiment, all female groups displayed higher anxiety, suggesting age-related increases in anxiety levels in the APP/Tau mouse model.

Recognition memory was evaluated using the Novel Object Recognition Test. At 9 months of age, both male and female AD mice displayed significant memory impairment,

indicating a more established pathology compared to 6 months of age. This provided an ideal scenario to assess HEBE's effect on recognition memory. Treatment with HEBE resulted in a significant improvement in recognizing the new object in both male and female AD mice, with performance levels comparable to WT mice. These findings align with previous studies using individual chronokines, where similar enhancements were observed [364,382,383]. Therefore, these results indicate that the three chronokines in HEBE could act synergistically to enhance hippocampal-dependent recognition memory in the APP/Tau model.

Spatial learning and memory were evaluated using the Morris Water Maze. Both male and female control AD mice exhibited clear impairments in spatial learning. This suggests that the APP/Tau model does not manifest impairment at 6 months of age but develops it by 9 months. During the learning phase, AD mice did not effectively acquire the task. However, HEBE-treated mice demonstrated improved hippocampal-dependent spatial learning. Despite initially performing similarly to AD mice, they progressively learned the task over experimental days, achieving performance levels comparable to WT mice by the final learning day. Notably, AD mice did not present impairment in short and long-term spatial memory, as their performance was similar to that of WT mice. Therefore, no improvement with HEBE could be observed in this aspect. These results indicate that the APP/Tau mouse model may not be suitable for studying short and long-term spatial memory at 9 months of age, despite displaying impairments in spatial learning.

### 2.4. HEBE-induced changes at a molecular level

Understanding the molecular pathways influenced by HEBE is crucial for elucidating its mechanism of action. An RNA-seq analysis was conducted on two brain regions implicated in AD, namely the hippocampus and the entorhinal cortex [384,385]. In the hippocampus, both male and female AD mice presented upregulated pathways associated with the pathology, including apoptosis [355], cellular senescence [356], lysosomes [357] and phagocytosis [358], alongside downregulation of various synapse types and LTP [359]. Unlike the experiment with recombinant sKL, in this case, females also displayed alterations at a molecular level, suggesting that the onset of the disease is slower than in

males, but can be evident by 9 months of age. However, the effects of HEBE at the transcriptomic level appeared to be modest. In males, only a downregulation of Aβ formation was observed, while in females, potential improvements at the synaptic level remain unclear due to the diversity of affected pathways.

In the entorhinal cortex, on the other hand, male AD mice exhibited impairments in various pathways similar to those observed in the hippocampus, including lysosomes, phagosome, apoptosis and cellular senescence. Additionally, impairments in synapses and LTP were also evident. In contrast, differences observed in females were less substantial than in males, suggesting that pathology may progress spatially in the APP/Tau mouse model, beginning in the hippocampus and later expanding to other brain regions, contrasting with humans where alterations in the entorhinal cortex precede those in the hippocampus [384]. These findings support the notion that pathological changes develop earlier in males than in females. HEBE improved several pathways in the entorhinal cortex of males, primarily involving neuronal activity and synaptic transmission.

Overall, these results indicate that HEBE acts on different brain regions, modifying pathways typically affected in AD, although the improvements were modest, particularly in the hippocampus. Despite significant enhancements in cognition, more profound transcriptomic changes were expected. We believe that the lack of more changes may be due to HEBE's primary mechanism of action not involving the generation of significant transcriptional changes, but rather acting at a proteomic level. Studies have suggested that an RNA-seq analysis may offer an incomplete view of molecular changes induced by treatment [386], emphasizing the necessity for further proteomic investigations to elucidate the mechanisms involved, where changes might be more readily detected. Additionally, conducting transcriptomic analyses at more advanced ages and in other brain regions could further contribute to understanding HEBE's functions.

Histopathological assessments revealed significant hippocampal pathology in 9-month-old AD mice. In contrast to the 6-month-old mice in the recombinant sKL experiment, these AD mice exhibited Aβ depositions in the hippocampus, particularly in the CA3 region. HEBE showed a trend towards reducing Aβ levels in the hippocampus, although

statistical significance was not achieved. Further investigations are warranted to confirm the effects of HEBE on Aβ elimination, as literature on sTREM2 suggests that aiding microglia in increasing phagocytosis should lead to a reduction in amyloid plaque depositions [194,243,387]. Tau depositions, on the other hand, were decreased in HEBE-treated mice, indicating an amelioration of the Tau pathology similar to other studies with Klotho and sTREM2 [169,388]. An increase in GFAP labeling was observed in both AD groups, supporting the notion that astrogliosis is a characteristic of this animal model and was not caused by HEBE. Surprisingly, despite the described actions of sTREM2 in microglial activation, no apparent differences were observed in Iba1 labeling. Nevertheless, further analyses should be conducted to determine whether HEBE induces differences in cell number or morphology, which could be a more accurate indicator of microglial activity [360]. In conclusion, HEBE is capable of ameliorating the Tau pathology and presumably the Aβ pathology, with apparently no significant changes to astrocytes or microglial cells.

Overall, results suggest that HEBE has a significant effect on learning and memory, improving both recognition and spatial memories. However, the molecular basis for this improvement has not been elucidated, as few transcriptomic changes have been observed, and only the Tau pathology has been alleviated. A proteomic analysis could provide further insights into how HEBE improves cognition in mice. A possible explanation for the modest molecular changes could be the choice of promoter for HEBE. The selected CMV promoter is a strong ubiquitous promoter, but studies have shown that it is susceptible to methylation *in vivo*, leading to a decrease in transgene expression over time [379]. Consequently, by the time mice were euthanized, a significant decrease in expression could have occurred, hindering the observation of more pronounced molecular changes. Therefore, for future experiments, a different promoter should be used, one that is relatively small and capable of driving strong transgene expression without being susceptible to silencing by methylation.

## 2.5. HEBE2 generation

Given the lack of MMP inhibition by TIMP2 in HEBE, a second version of the chronokine was engineered. TIMP2 exerts MMP inhibition primarily through its N-terminal [335,373]. However, in HEBE, the N-terminal of TIMP2 is positioned in the middle of the protein, thus preventing it from acting on MMPs. To address this limitation, HEBE2 was developed with a modified protein arrangement, relocating TIMP2 to the protein's N-terminal. This strategic adjustment enables the N-terminal domain to effectively inhibit MMPs. HEBE2 demonstrated *in vitro* stability and bioinformatic predictions indicated no aggregation issues. Furthermore, HEBE2 incorporates the CBh promoter in its expression cassette [379]. This promoter is preferable over the CMV promoter as it avoids methylation-induced silencing and is compact enough to fit into an AAV vector along with HEBE2, potentially sustaining higher levels of HEBE2 expression *in vivo* for enhanced therapeutic outcomes. Comprehensive *in vitro* and *in vivo* investigations are necessary to evaluate HEBE2's efficacy compared to HEBE.

However, some factors need to be considered when working with HEBE2. As discussed in the introduction, TIMP2's activities extend beyond MMP inhibition, encompassing neuroprotective functions that operate independently of MMP regulation [263,264,389]. Therefore, despite HEBE's deficiency in MMP inhibition, it may still preserve its neuroprotective properties. This aspect necessitates further examination through additional *in vitro* assays. Moreover, the constitutive inhibition of MMPs may pose risks, as the catalysis of other substrates by MMPs supports physiological functions that could be affected by an inhibition, leading to undesired side effects [390]. Hence, HEBE's incapacity to inhibit MMPs might be advantageous, provided it retains its other beneficial functions. During experiments with HEBE2, it will be critical to evaluate any adverse effects resulting from MMP inhibition. If such effects are observed, but it overall exhibits more positive effects than HEBE, one strategy to prevent MMP inhibition while retaining therapeutic efficacy could involve introducing an alanine residue at the N-terminal of TIMP2 [264,389,391].

## 2.6. HEBE versus sKL

Two different therapeutic strategies were evaluated in this thesis. However, it is challenging to draw a clear conclusion as to which of the two presents greater therapeutic efficacy. Initially, we expected more pronounced effects with HEBE compared to sKL, as HEBE would combine sKL's effects with sTREM2 and TIMP2's. HEBE demonstrated improvements in recognition memory and spatial learning, alongside decreases in pTau levels and transcriptional improvements. However, the effects were not as pronounced with sKL. One possible explanation for these differences may be the animal model itself, as the age at which mice were treated was different in each approach. In the sKL experiment, mice had not developed a complete phenotype of the disease by the time cognitive functions and molecular alterations were assessed, potentially hindering the observation of significant changes with sKL. In contrast, in the case of HEBE, mice exhibited a more advanced disease stage by the time they were tested, facilitating the observation cognitive improvements with HEBE. Another critical consideration is the mode of treatment delivery. HEBE was administered using a viral vector, ensuring sustained protein expression in the brain for approximately three months. sKL, however, was administered as a recombinant protein over a period of six weeks, without reaching the brain. Consequently, HEBE had more time to exert its functions, and to do it directly in the brain, unlike sKL, which could not act directly within the brain, likely decreasing therapeutic efficacy.

In conclusion, HEBE holds promise for having greater therapeutic efficacy compared to sKL, as it combines the beneficial effects of three chronokines. However, further research will be necessary to elucidate their functions and to compare their therapeutic efficacies.

## 2.7. Final remarks

The combination of three chronokines in the novel chimeric protein HEBE has demonstrated significant cognitive benefits in the APP/Tau mouse model, making it a promising candidate for addressing memory impairment associated with neurodegenerative diseases. However, the molecular mechanisms underlying this effect have not been fully elucidated. Therefore, further research will be necessary to

understand the changes caused by HEBE at the proteomic level. Additionally, studies using iPSCs or alternative animal models may offer valuable insights into HEBE's activities in the brain. Further optimizations of the therapeutic agent may be necessary, such as the change in protein arrangement performed in HEBE2, which could potentially unlock new functions or enhance existing ones. The expression cassette of the viral vector could also be optimized to include a new promoter, such as CBh, which would drive higher expression of HEBE, potentially increasing its therapeutic value and duration of effect. Furthermore, the long-term effects of HEBE should also be tested, to assess any potential toxic effects and long-term therapeutic efficacy.

In conclusion, the proof of concept for HEBE has been successful, opening the way for prospective therapeutic approaches targeting multifactorial diseases by combining multiple beneficial factors.

# CONCLUSIONS

1. Biologically active recombinant human sKL was successfully produced in the CHO cell line. Its half-life following intravenous and intraperitoneal administrations in WT mice was determined for the first time. This data was instrumental in determining the optimal dose and administration interval for the *in vivo* therapeutic application of recombinant sKL.

2. Chronic systemic administration of sKL to the APP/Tau mouse model of Alzheimer's disease led to modest improvements in recognition memory. Molecular analyses revealed improvements in AD-affected pathways within the hippocampus of male mice. However, the AD phenotype in the animal model, particularly in females, was not fully developed, requiring the repetition of the study at more advanced ages.

3. A novel chimeric chronokine named HEBE was developed for Alzheimer's disease treatment, connecting sKL, sTREM2, and TIMP2 via an extensive bioinformatic analysis. This fusion combines their individual beneficial effects into a soluble, stable protein under physiological conditions without aggregation. The biological activity of HEBE was assessed *in vitro*, suggesting that the assembly of the three proteins could confer new functions not present in the individual chronokines.

4. HEBE overexpression in the APP/Tau mouse model via AAV9P31 vectors significantly improved recognition and learning memory without observable toxic effects. Additionally, improvements in AD-affected pathways were observed in the hippocampus, accompanied by reduced Tau depositions. However, effects at a molecular level were more moderate than anticipated, potentially due to reduced transgene expression resulting from promoter methylation.

5. A new version of HEBE, called HEBE2, was generated through a new bioinformatic analysis to potentially enhance the therapeutic effects *in vivo*. TIMP2 was positioned at the N-terminal of the protein to enable MMP inhibition, and the new chimeric chronokine exhibited stability without aggregation.

# REFERENCES

[1] Alzheimer's Association. (2023) '2023 Alzheimer's disease facts and figures', *Alzheimer's & Dementia*, 19(4):1598–695.

[2] Selkoe, DJ., Hardy, J. (2016) 'The amyloid hypothesis of Alzheimer's disease at 25 years', *EMBO Molecular Medicine*, 8(6):595–608.

[3] Holtzman, DM. *et al*. (2011) 'Alzheimer's disease: The challenge of the second century', *Science Translational Medicine*, 3(77).

[4] Nichols, E. *et al*. (2022) 'Estimation of the global prevalence of dementia in 2019 and forecasted prevalence in 2050: an analysis for the Global Burden of Disease Study 2019', *The Lancet Public Health*, 7(2):e105–25.

[5] Alzheimer's Association. (accessed: 2023 Oct 2) 'Causes and Risk Factors for Alzheimer's Disease [Online]', Available from: https://www.alz.org/alzheimers-dementia/what-is-alzheimers/causes-and-risk-factors

[6] Zhu, XC. *et al*. (2015) 'Rate of early onset Alzheimer's disease: A systematic review and meta-analysis', *Annals of Translational Medicine*, 3(3).

[7] Armstrong, RA. (2019) 'Risk factors for Alzheimer's disease', *Folia Neuropathologica*, 57(2):87–105.

[8] Baker, E. *et al*. (2023) 'What does heritability of Alzheimer's disease represent?', *PLoS ONE*, 18(4).

[9] Campion, D. *et al*. (1999) 'Early-Onset Autosomal Dominant Alzheimer Disease: Prevalence, Genetic Heterogeneity, and Mutation Spectrum', *American Journal of Human Genetics*, 65:664–70.

[10] Watts, JC., Prusiner, SB. (2018) 'β-amyloid prions and the pathobiology of alzheimer's disease', *Cold Spring Harbor Perspectives in Medicine*, 8(5).

[11] Li, NM. *et al*. (2019) 'Mutations of beta-amyloid precursor protein alter the consequence of Alzheimer's disease pathogenesis', *Neural Regeneration Research*, 14(4):658–65.

[12] Walker, ES. *et al*. (2005) 'Presenilin 2 familial Alzheimer's disease mutations result in partial loss of function and dramatic changes in Aβ 42/40 ratios', *Journal of Neurochemistry*, 92(2):294–301.

[13] Shimojo, M. *et al*. (2008) 'Enzymatic characteristics of I213T mutant presenilin-1/γ-secretase in cell models and knock-in mouse brains', *Journal of Biological Chemistry*, 283(24):16488–96.

[14] Strittmatter, WJ. *et al*. (1993) 'Apolipoprotein E: High-avidity binding to β-amyloid and increased frequency of type 4 allele in late-onset familial Alzheimer disease', *Proceedings of the National Academy of Sciences of the United States of America*, 90:1977–81.

[15] Corder, EH. *et al*. (1994) 'Protective effect of apolipoprotein E type 2 allele for late onset Alzheimer disease', *Nature Genetics*, 7:180–4.

[16] Li, R. *et al*. (2021) 'The most prevalent rare coding variants of TREM2 conferring risk of Alzheimer's disease: A systematic review and meta-analysis', *Experimental and Therapeutic Medicine*, 21(4).

[17] Jonsson, T. *et al*. (2013) 'Variant of TREM2 Associated with the Risk of Alzheimer's Disease', *New England Journal of Medicine*, 368(2):107–16.

[18] Mielke, MM. (2018) 'Sex and Gender Differences in Alzheimer's Disease Dementia', *Psychiatric Times*, 35(11):14–7.

[19] Scheyer, O. *et al*. (2018) 'Female Sex and Alzheimer's Risk: The Menopause Connection', *The journal of prevention of Alzheimer's disease*, 5(4):225–30.

[20] Thinakaran, G., Koo, EH. (2008) 'Amyloid precursor protein trafficking, processing, and function', *Journal of Biological Chemistry*, 283(44):29615–9.

[21] de Paula, V de JR. *et al*. (2009) 'Neurobiological pathways to Alzheimer's disease: Amyloid-beta, TAU protein or both?', *Dementia e Neuropsychologia*, 3(3):188–94.

[22] Hampel, H. *et al*. (2021) 'The Amyloid-β Pathway in Alzheimer's Disease', *Molecular Psychiatry*, 26(10):5481–503.

[23] Mullan, M. *et al*. (1992) 'A pathogenic mutation for probable Alzheimer's disease in the APP gene at the N-terminus of β-amyloid', *Nature genetics*, 1:345–7.

[24] Di Fede, G. *et al*. (2009) 'A recessive mutation in the APP gene with dominant-negative effect on amyloidogenesis', *Science*, 323(5920):1473–7.

[25] Kim, J. *et al*. (2007) 'Aβ40 inhibits amyloid deposition in vivo', *Journal of Neuroscience*, 27(3):627–33.

[26] Kumar, S., Walter, J. (2011) 'Phosphorylation of amyloid beta (Aβ) peptides – A trigger for formation of toxic aggregates in Alzheimer's disease', *Aging*, 3(8).

[27] Michaels, TCT. *et al*. (2020) 'Dynamics of oligomer populations formed during the aggregation of Alzheimer's Aβ42 peptide', *Nature Chemistry*, 12(5):445–51.

[28] Sanz-Blasco, S. *et al*. (2008) 'Mitochondrial Ca2+ overload underlies Aβ oligomers neurotoxicity providing an unexpected mechanism of neuroprotection by NSAIDs', *PLoS ONE*, 3(7).

[29] Rhein, V., Eckert, A. (2007) 'Effects of Alzheimer's amyloid-beta and tau protein on mitochondrial function - Role of glucose metabolism and insulin signalling', *Archives of Physiology and Biochemistry*, 113(3):131–41.

[30] Hardy, J., Allsop, D. (1991) 'Amyloid deposition as the central event in the aetiology of Alzheimer's disease', *Trends in Pharmacological Science*, 12:383–8.

[31] Vemuri, P. *et al*. (2011) 'Cognitive reserve and Alzheimer's disease biomarkers are independent determinants of cognition', *Brain*, 134(5):1479–92.

[32] Buee, L. *et al*. (2000) 'Tau protein isoforms, phosphorylation and role in neurodegenerative disorders', *Brain Research Reviews*, 33:95–130.

[33] Barbier, P. *et al*. (2019) 'Role of tau as a microtubule-associated protein: Structural and functional aspects', *Frontiers in Aging Neuroscience*, 10.

[34] Haughey, NJ. *et al*. (2002) 'Disruption of neurogenesis by amyloid β-peptide, and perturbed neural progenitor cell homeostasis, in models of Alzheimer's disease', *Journal of Neurochemistry*, 83:1509–24.

[35] Tiwari, S. *et al*. (2019) 'Alzheimer's disease: Pathogenesis, diagnostics, and therapeutics', *International Journal of Nanomedicine*, 14:5541–54.

[36] Wolfe, MS. (2009) 'Tau mutations in neurodegenerative diseases', *Journal of Biological Chemistry*, 284(10):6021–5.

[37] Lyman, M. *et al*. (2014) 'Neuroinflammation: The role and consequences', *Neuroscience Research*, 79(1):1–12.

[38] Norris, GT., Kipnis, J. (2019) 'Immune cells and CNS physiology: Microglia and beyond', *Journal of Experimental Medicine*, 216(1):60–70.

[39] Helmut, K. *et al*. (2011) 'Physiology of microglia', *Physiological Reviews*, 91(2):461–553.

[40] Bar, E., Barak, B. (2019) 'Microglia roles in synaptic plasticity and myelination in homeostatic conditions and neurodevelopmental disorders', *GLIA*, 67(11):2125–41.

[41] Rea, IM. *et al*. (2018) 'Age and age-related diseases: Role of inflammation triggers and cytokines', *Frontiers in Immunology*, 9.

[42] Lee, CYD., Landreth, GE. (2010) 'The role of microglia in amyloid clearance from the AD brain', *Journal of Neural Transmission*, 117(8):949–60.

[43] Hickman, SE. *et al*. (2008) 'Microglial dysfunction and defective β-amyloid clearance pathways in aging alzheimer's disease mice', *Journal of Neuroscience*, 28(33):8354–60.

[44] Preman, P. *et al*. (2021) 'Astrocytes in alzheimer's disease: Pathological significance and molecular pathways', *Cells*, 10(3):1–19.

[45] Hol, EM., Pekny, M. (2015) 'Glial fibrillary acidic protein (GFAP) and the astrocyte intermediate filament system in diseases of the central nervous system', *Current Opinion in Cell Biology*, 32:121–30.

[46] Leng, F., Edison, P. (2021) 'Neuroinflammation and microglial activation in Alzheimer disease: where do we go from here?', *Nature Reviews Neurology*, 17(3):157–72.

[47] Akiyama, H. *et al*. (2000) 'Inflammation and Alzheimer's disease', *Neurobiology of Aging*, 21(3):383–421.

[48] Zhang, Z. *et al*. (2021) 'Autophagy in Alzheimer's disease pathogenesis: Therapeutic potential and future perspectives', *Ageing Research Reviews*, 72.

[49] Malampati, S. *et al*. (2020) 'Targeting Aggrephagy for the Treatment of Alzheimer's Disease', *Cells*, 9(2).

[50] Cavieres, VA. *et al*. (2015) 'Tetrahydrohyperforin inhibits the proteolytic processing of amyloid precursor protein and enhances its degradation by Atg5-dependent autophagy', *PLoS ONE*, 10(8).

[51] Chung, KM. *et al*. (2019) 'Alzheimer's disease and the autophagic-lysosomal system', *Neuroscience Letters*, 697:49–58.

[52] Uddin, MS. *et al*. (2018) 'Autophagy and Alzheimer's disease: From molecular mechanisms to therapeutic implications', *Frontiers in Aging Neuroscience*, 10.

[53] Jack, CR. *et al*. (2018) 'NIA-AA Research Framework: Toward a biological definition of Alzheimer's disease', *Alzheimer's & Dementia*, 14(4):535–62.

[54] Vermunt, L. *et al*. (2019) 'Duration of preclinical, prodromal, and dementia stages of Alzheimer's disease in relation to age, sex, and APOE genotype', *Alzheimer's & Dementia*, 15(7):888–98.

[55] Sperling, RA. *et al*. (2020) 'Association of Factors With Elevated Amyloid Burden in Clinically Normal Older Individuals', *JAMA Neurology*, 77(6):735–45.

[56] Bennett, DA. *et al*. (2006) 'Neuropathology of older persons without cognitive impairment from two community-based studies', *Neurology*, 66:1837–44.

[57] Petersen, RC. *et al*. (2018) 'Practice guideline update summary: Mild cognitive impairment', *Neurology*, 90(3):126–35.

[58] Thal, DR. *et al*. (2002) 'Phases of Aβ-deposition in the human brain and its relevance for the development of AD', *Neurology*, 58:1791–800.

[59] Braak, H., Braak, E. (1991) 'Neuropathological stageing of Alzheimer-related changes', *Acta Neuropathologica*, 82:239–59.

[60] Giannakopoulos, P. *et al*. (2003) 'Tangle and neuron numbers, but not amyloid load, predict cognitive status in Alzheimer's disease', *Neurology*, 60:1495–500.

[61] Serrano-Pozo, A. *et al*. (2011) 'Neuropathological alterations in Alzheimer disease', *Cold Spring Harbor Perspectives in Medicine*, 1(1).

[62] Weintraub, S. *et al*. (2012) 'The neuropsychological profile of Alzheimer disease', *Cold Spring Harbor Perspectives in Medicine*, 2(4).

[63] Bateman, RJ. *et al*. (2012) 'Clinical and Biomarker Changes in Dominantly Inherited Alzheimer's Disease', *New England Journal of Medicine*, 367(9):795–804.

[64] Khan, S. *et al*. (2020) 'Recent Advancements in Pathogenesis, Diagnostics and Treatment of Alzheimer's Disease', *Current Neuropharmacology*, 18(11):1106–25.

[65] Kapoor, V. *et al*. (2004) 'An introduction to PET-CT imaging', *Radiographics*, 24(2):523–43.

[66] Mosconi, L. *et al*. (2006) 'Hypometabolism Exceeds Atrophy in Presymptomatic Early-Onset Familial Alzheimer's Disease', *Journal of Nuclear Medicine*, 47:1778–86.

[67] Chételat, G. *et al*. (2020) 'Amyloid-PET and 18F-FDG-PET in the diagnostic investigation of Alzheimer's disease and other dementias', *The Lancet Neurology*, 19(11):951–62.

[68] Alexander, GE. *et al*. (2002) 'Article Longitudinal PET Evaluation of Cerebral Metabolic Decline in Dementia: A Potential Outcome Measure in Alzheimer's Disease Treatment Studies', *American Journal of Psychiatry*, 159(5).

[69] Chandra, A. *et al*. (2019) 'Applications of amyloid, tau, and neuroinflammation PET imaging to Alzheimer's disease and mild cognitive impairment', *Human Brain Mapping*, 40(18):5424–42.

[70] Ossenkoppele, R. *et al*. (2022) 'Tau biomarkers in Alzheimer's disease: towards implementation in clinical practice and trials', *The Lancet Neurology*, 21(8):726–34.

[71] Ossenkoppele, R. *et al*. (2019) 'Associations between tau, Aβ, and cortical thickness with cognition in Alzheimer disease', *Neurology*, 92(6):e601–12.

[72] Kim, J. *et al*. (2022) 'Neuroimaging Modalities in Alzheimer's Disease: Diagnosis and Clinical Features', *International Journal of Molecular Sciences*, 23(11).

[73] Márquez, F., Yassa, MA. (2019) 'Neuroimaging Biomarkers for Alzheimer's Disease', *Molecular Neurodegeneration*, 14(1).

[74] Dickerson, BC. *et al*. (2011) 'Alzheimer-signature MRI biomarker predicts AD dementia in cognitively normal adults', *Neurology*, 76:1395–402.

[75] Lerch, JP. *et al*. (2005) 'Focal decline of cortical thickness in Alzheimer's disease identified by computational neuroanatomy', *Cerebral Cortex*, 15(7):995–1001.

[76] Silbert, L. *et al*. (2003) 'Changes in premorbid brain volume predict Alzheimer's disease pathology', *Neurology*, 61:487–92.

[77] Bălaşa, AF. *et al*. (2020) 'Body fluid biomarkers for alzheimer's disease-an up-to-date overview', *Biomedicines*, 8(10):1–21.

[78] Boumenir, A. *et al*. (2019) 'CSF level of β-amyloid peptide predicts mortality in Alzheimer's disease', *Alzheimer's Research and Therapy*, 11(1).

[79] Biscetti, L. *et al*. (2019) 'The added value of Aβ42/Aβ40 in the CSF signature for routine diagnostics of Alzheimer's disease', *Clinica Chimica Acta*, 494:71–3.

[80] Lee, JC. *et al*. (2019) 'Diagnosis of Alzheimer's disease utilizing amyloid and tau as fluid biomarkers', *Experimental and Molecular Medicine*, 51(5).

[81] Pawlowski, M. *et al*. (2017) 'Cerebrospinal fluid biomarkers in Alzheimer's disease-From brain starch to bench and bedside', *Diagnostics*, 7(3).

[82] Zetterberg, H., Bendlin, BB. (2021) 'Biomarkers for Alzheimer's disease—preparing for a new era of disease-modifying therapies', *Molecular Psychiatry*, 26(1):296–308.

[83] Altuna-Azkargorta, M., Mendioroz-Iriarte, M. (2021) 'Blood biomarkers in Alzheimer's disease', *Neurología*, 36:704–10.

[84] Hampel, H. *et al*. (2018) 'Blood-based biomarkers for Alzheimer disease: mapping the road to the clinic', *Nature Reviews Neurology*, 14(11):639–52.

[85] Ovod, V. *et al*. (2017) 'Amyloid β concentrations and stable isotope labeling kinetics of human plasma specific to central nervous system amyloidosis', *Alzheimer's & Dementia*, 13(8):841–9.

[86] Milà-Alomà, M. *et al*. (2019) 'Latest advances in cerebrospinal fluid and blood biomarkers of Alzheimer's disease', *Therapeutic Advances in Neurological Disorders*, 12.

[87] Hugon, J. *et al*. (2018) 'Blood-Based Kinase Assessments in Alzheimer's Disease', *Frontiers in Aging Neuroscience*, 10.

[88] Mahaman, YAR. *et al*. (2022) 'Biomarkers used in Alzheimer's disease diagnosis, treatment, and prevention', *Ageing Research Reviews*, 74.

[89] Yiannopoulou, KG., Papageorgiou, SG. (2020) 'Current and Future Treatments in Alzheimer Disease: An Update', *Journal of Central Nervous System Disease*, 12.

[90] Jain, U. *et al*. (2023) 'Current Insights of Nanocarrier-Mediated Gene Therapeutics to Treat Potential Impairment of Amyloid Beta Protein and Tau Protein in Alzheimer's Disease', *Molecular Neurobiology*, 61:1969–89.

[91] Silva, MA. *et al*. (2020) 'Donepezil Inhibits Acetylcholinesterase via Multiple Binding Modes at Room Temperature', *Journal of Chemical Information and Modeling*, 60(7):3463–71.

[92] Hampel, H. *et al*. (2018) 'The cholinergic system in the pathophysiology and treatment of Alzheimer's disease', *Brain*, 141(7):1917–33.

[93] Matsunaga, S. *et al*. (2015) 'Memantine monotherapy for Alzheimer's Disease:A systematic review and meta-analysis', *PLoS ONE*, 10(4).

[94] Huang, LK. *et al*. (2023) 'Clinical trials of new drugs for Alzheimer disease: a 2020–2023 update', *Journal of Biomedical Science*, 30(1):83.

[95] Arndt, JW. *et al*. (2018) 'Structural and kinetic basis for the selectivity of aducanumab for aggregated forms of amyloid-β', *Scientific Reports*, 8(1).

[96] Sevigny, J. *et al*. (2016) 'The antibody aducanumab reduces Aβ plaques in Alzheimer's disease', *Nature*, 537(7618):50–6.

[97] Liu, KY. *et al*. (2021) 'The need to show minimum clinically important differences in Alzheimer's disease trials', *The Lancet Psychiatry*, 8(11):1013–6.

[98] Swanson, CJ. *et al*. (2021) 'A randomized, double-blind, phase 2b proof-of-concept clinical trial in early Alzheimer's disease with lecanemab, an anti-Aβ protofibril antibody', *Alzheimer's Research and Therapy*, 13(1).

[99] Hoy, SM. (2023) 'Lecanemab: First Approval', *Drugs*, 83(4):359–65.

[100] Cummings, J. *et al*. (2023) 'Alzheimer's disease drug development pipeline: 2023', *Alzheimer's & Dementia*, 9(2).

[101] Liu, Y. *et al*. (2017) 'Application of bio-orthogonal proteome labeling to cell transplantation and heterochronic parabiosis', *Nature Communications*, 8(1).

[102] Kheifets, V., Braithwaite, SP. (2019) 'Plasma-Based Strategies for Therapeutic Modulation of Brain Aging', *Neurotherapeutics*, 16(3):675–84.

[103] Kuro-O, M. *et al*. (1997) 'Mutation of the mouse klotho gene leads to a syndrome resembling ageing', *Nature*, 390.

[104] Kurosu, H. *et al*. (2005) 'Suppression of aging in mice by the hormone Klotho', *Science*, 309(5742):1829–33.

[105] Dubal, DB. *et al*. (2014) '1Life Extension Factor Klotho Enhances Cognition', *Cell Reports*, 7(4):1065–76.

[106] Arking, DE. *et al*. (2022) 'Association of human aging with a functional variant of klotho', *PNAS*, 99(2):856–61.

[107] Dubal, DB. *et al*. (2014) 'Life Extension Factor Klotho Enhances Cognition', *Cell Reports*, 7(4):1065–76.

[108] Yokoyama, JS. *et al*. (2015) 'Variation in longevity gene KLOTHO is associated with greater cortical volumes', *Annals of Clinical and Translational Neurology*, 2(3):215–30.

[109] Belloy, ME. *et al*. (2021) 'KL∗VS heterozygosity reduces brain amyloid in asymptomatic at-risk APOE∗4 carriers', *Neurobiology of Aging*, 101:123–9.

[110] Matsumura, Y. *et al*. (1998) 'Identification of the Human Klotho Gene and Its Two Transcripts Encoding Membrane and Secreted Klotho Protein', *Biochemical and Biophysical Research Communications*, 242:626–30.

[111] Bloch, L. *et al*. (2009) 'Klotho is a substrate for α-, β- and γ-secretase', *FEBS Letters*, 583(19):3221–4.

[112] Chen, C Di. *et al*. (2014) 'Identification of cleavage sites leading to the shed form of the anti-aging protein klotho', *Biochemistry*, 53(34):5579–87.

[113] Shiraki-Iida, T. *et al*. (1998) 'Structure of the mouse klotho gene and its two transcripts encoding membrane and secreted protein', *FEBS Letters*, 424:6–10.

[114] Akimoto, T. *et al*. (2012) 'Characteristics of urinary and serum soluble Klotho protein in patients with different degrees of chronic kidney disease', *BMC Nephrology*, 13(155).

[115] Imura, A. *et al*. (2004) 'Secreted Klotho protein in sera and CSF: Implication for post-translational cleavage in release of Klotho protein from cell membrane', *FEBS Letters*, 565(1–3):143–7.

[116] Lim, K. *et al*. (2015) 'α-klotho expression in human tissues', *Journal of Clinical Endocrinology and Metabolism*, 100(10):E1308–18.

[117] Brobey, RK. *et al*. (2015) 'Klotho protects dopaminergic neuron oxidant-induced degeneration by modulating ASK1 and p38 MAPK signaling pathways', *PLoS ONE*, 10(10).

[118] Massó, A. *et al*. (2015) 'Secreted and transmembrane αklotho isoforms have different spatio-temporal profiles in the brain during aging and Alzheimer's disease progression', *PLoS ONE*, 10(11).

[119] Duce, JA. *et al*. (2008) 'Gene profile analysis implicates Klotho as an important contributor to aging changes in brain white matter of the rhesus monkey', *GLIA*, 56(1):106–17.

[120] Semba, RD. *et al*. (2014) 'Klotho in the cerebrospinal fluid of adults with and without Alzheimer's disease', *Neuroscience Letters*, 558:37–40.

[121] Urakawa, I. *et al*. (2006) 'Klotho converts canonical FGF receptor into a specific receptor for FGF23', *Nature*, 444(7120):770–4.

[122] Dalton, GD. *et al*. (2017) 'New insights into the mechanism of action of soluble klotho', *Frontiers in Endocrinology*, 8.

[123] Chen, G. *et al*. (2018) 'α-Klotho is a non-enzymatic molecular scaffold for FGF23 hormone signalling', *Nature*, 553(7689):461–6.

[124] Rausch, S., Föller, M. (2022) 'The regulation of FGF23 under physiological and pathophysiological conditions', *Pflugers Archiv European Journal of Physiology*, 474(3):281–92.

[125] Erben, RG. (2018) 'Physiological actions of fibroblast growth factor-23', *Frontiers in Endocrinology*, 9.

[126] Li, H. *et al*. (2011) 'Compound deletion of Fgfr3 and Fgfr4 partially rescues the Hyp mouse phenotype', *American Journal of Physiology Endocrinology and Metabolism*, 300:508–17.

[127] Kuro-o, M. (2010) 'A potential link between phosphate and aging-Lessons from Klotho-deficient mice', *Mechanisms of Ageing and Development*, 131(4):270–5.

[128] Kurosu, H. *et al*. (2006) 'Regulation of fibroblast growth factor-23 signaling by Klotho', *Journal of Biological Chemistry*, 281(10):6120–3.

[129] Huang, Q. *et al*. (2020) 'Klotho antagonizes pulmonary fibrosis through suppressing pulmonary fibroblasts activation, migration, and extracellular matrix production: a therapeutic implication for idiopathic pulmonary fibrosis', *Aging*, 12(7):5812–31.

[130] Mencke, R. *et al*. (2017) 'Effects of Klotho on fibrosis and cancer: A renal focus on mechanisms and therapeutic strategies', *Advanced Drug Delivery Reviews*, 121:85–100.

[131] Mikuła-Pietrasik, J. *et al*. (2022) 'The functional multipotency of transforming growth factor β signaling at the intersection of senescence and cancer', *Cellular and Molecular Life Sciences*, 79(4).

[132] Doi, S. *et al*. (2011) 'Klotho inhibits transforming growth factor-β1 (TGF-β1) signaling and suppresses renal fibrosis and cancer metastasis in mice', *Journal of Biological Chemistry*, 286(10):8655–65.

[133] Kops, GJPL. *et al*. (2002) 'Forkhead transcription factor FOXO3a protects quiescent cells from oxidative stress', *Nature*, 419(6904):312–6.

[134] Yamamoto, M. *et al*. (2005) 'Regulation of Oxidative Stress by the Anti-aging Hormone', *Journal of Biological Chemistry*, 280(45):38029–34.

[135] Haruna, Y. *et al*. (2007) 'Amelioration of progressive renal injury by genetic manipulation of Klotho gene', *PNAS*, 104(7):2331–6.

[136] Wang, Y. *et al*. (2012) 'Klotho gene delivery suppresses Nox2 expression and attenuates oxidative stress in rat aortic smooth muscle cells via the cAMP-PKA pathway', *Aging Cell*, 11(3):410–7.

[137] Zeldich, E. *et al*. (2014) 'The neuroprotective effect of Klotho is mediated via regulation of members of the redox system', *Journal of Biological Chemistry*, 289(35):24700–15.

[138] Zhou, HJ. *et al*. (2018) 'Lentivirus-mediated klotho up-regulation improves aging-related memory deficits and oxidative stress in senescence-accelerated mouse prone-8 mice', *Life Sciences*, 200:56–62.

[139] Ray, A. *et al*. (2014) 'Insulin Signaling Network in Cancer', *Indian Journal of Biochemistry & Biophysics*, 51:493–8.

[140] Shu, G. *et al*. (2013) 'Restoration of klotho expression induces apoptosis and autophagy in hepatocellular carcinoma cells', *Cellular Oncology*, 36(2):121–9.

[141] Xie, B. *et al*. (2013) 'Restoration of klotho gene expression induces apoptosis and autophagy in gastric cancer cells: tumor suppressive role of klotho in gastric cancer', *Cancer Cell International*, 13(18).

[142] Wolf, I. *et al*. (2008) 'Klotho: A tumor suppressor and a modulator of the IGF-1 and FGF pathways in human breast cancer', *Oncogene*, 27(56):7094–105.

[143] Zhan, T. *et al*. (2017) 'Wnt signaling in cancer', *Oncogene*, 36(11):1461–73.

[144] Kaus, A., Birchmeier, W. (2008) 'Wnt signalling and its impact on development and cancer', *Nature Reviews*, 8:387–98.

[145] Liu, H. *et al*. (2007) 'Augmented Wnt Signaling in a Mammalian Model of Accelerated Aging', *Science*, 317(803):799–803.

[146] Tang, X. *et al*. (2016) 'Klotho: A tumor suppressor and modulator of the Wnt/β-catenin pathway in human hepatocellular carcinoma', *Laboratory Investigation*, 96(2):197–205.

[147] Camilli, TC. *et al*. (2011) 'Loss of Klotho during melanoma progression leads to increased filamin cleavage, increased Wnt5A expression, and enhanced melanoma cell motility', *Pigment Cell and Melanoma Research*, 24(1):175–86.

[148] Chen, B. *et al*. (2012) 'Inhibition of lung cancer cells growth, motility and induction of apoptosis by Klotho, a novel secreted Wnt antagonist, in a dose-dependent manner', *Cancer Biology and Therapy*, 13(12):1221–8.

[149] Fulop, T. *et al*. (2023) 'Immunology of Aging: the Birth of Inflammaging', *Clinical Reviews in Allergy and Immunology*, 64(2):109–22.

[150] Buendía, P. *et al*. (2016) 'Klotho Prevents Translocation of NFκB', *Vitamins and Hormones*, Elsevier Inc.; p. 119–50.

[151] Typiak, M., Piwkowska, A. (2021) 'Antiinflammatory actions of klotho: Implications for therapy of diabetic nephropathy', *International Journal of Molecular Sciences*, 22(2):1–15.

[152] King, GD. *et al*. (2012) 'Promoter methylation and age-related downregulation of Klotho in rhesus monkey', *Age*, 34(6):1405–19.

[153] Chen, C Di. *et al*. (2015) 'The Anti-Aging and Tumor Suppressor Protein Klotho Enhances Differentiation of a Human Oligodendrocytic Hybrid Cell Line', *Journal of Molecular Neuroscience*, 55(1):76–90.

[154] Chen, C Di. *et al*. (2013) 'The antiaging protein klotho enhances oligodendrocyte maturation and myelination of the CNS', *Journal of Neuroscience*, 33(5):1927–39.

[155] Zeldich, E. *et al*. (2015) 'The Anti-Aging Protein Klotho Enhances Remyelination Following Cuprizone-Induced Demyelination', *Journal of Molecular Neuroscience*, 57(2):185–96.

[156] Huerta, PT. *et al*. (2000) 'Formation of Temporal Memory Requires NMDA Receptors within CA1 Pyramidal Neurons', *Neuron*, 25:473–80.

[157] Rondi-Reig, L. *et al*. (2001) 'CA1-specific N-methyl-D-aspartate receptor knockout mice are deficient in solving a nonspatial transverse patterning task', *PNAS*, 98(6):3543–8.

[158] Abraham, CR. *et al*. (2016) 'Klotho Is a Neuroprotective and Cognition-Enhancing Protein', *Vitamins and Hormones*, Elsevier Inc.; p. 215–38.

[159] Dubal, DB. *et al*. (2015) 'Life extension factor klotho prevents mortality and enhances cognition in hAPP transgenic mice', *Journal of Neuroscience*, 35(6):2358–71.

[160] Leon, J. *et al*. (2017) 'Peripheral Elevation of a Klotho Fragment Enhances Brain Function and Resilience in Young, Aging, and α-Synuclein Transgenic Mice', *Cell Reports*, 20(6):1360–71.

[161] Heneka, MT. *et al*. (2013) 'NLRP3 is activated in Alzheimer's disease and contributes to pathology in APP/PS1 mice', *Nature*, 493(7434):674–8.

[162] Halle, A. *et al*. (2008) 'The NALP3 inflammasome is involved in the innate immune response to amyloid-β', *Nature Immunology*, 9(8):857–65.

[163] Saresella, M. *et al*. (2016) 'The NLRP3 and NLRP1 inflammasomes are activated in Alzheimer's disease', *Molecular Neurodegeneration*, 11(1).

[164] Mankan, AK. *et al*. (2012) 'The NLRP3/ASC/Caspase-1 axis regulates IL-1β processing in neutrophils', *European Journal of Immunology*, 42(3):710–5.

[165] Kinney, JW. *et al*. (2018) 'Inflammation as a central mechanism in Alzheimer's disease', *Alzheimer's & Dementia*, 4:575–90.

[166] Stancu, IC. *et al*. (2022) 'The NLRP3 inflammasome modulates tau pathology and neurodegeneration in a tauopathy model', *GLIA*, 70(6):1117–32.

[167] Zhao, Y. *et al*. (2020) 'Klotho overexpression improves amyloid-β clearance and cognition in the APP/PS1 mouse model of Alzheimer's disease', *Aging Cell*, 19(10).

[168] Hanson, K. *et al*. (2021) 'Exploiting The Neuroprotective Effects Of α-klotho To Tackle Ageing- And Neurodegeneration-related Cognitive Dysfunction', *Neuronal Signaling*, 5(2):1–13.

[169] Zeng, CY. *et al*. (2019) 'Lentiviral vector–mediated overexpression of Klotho in the brain improves Alzheimer's disease–like pathology and cognitive deficits in mice', *Neurobiology of Aging*, 78:18–28.

[170] Fernández, ÁF. *et al*. (2018) 'Disruption of the beclin 1-BCL2 autophagy regulatory complex promotes longevity in mice', *Nature*, 558(7708):136–40.

[171] Fung, TY. *et al*. (2022) 'Klotho an Autophagy Stimulator as a Potential Therapeutic Target for Alzheimer's Disease: A Review', *Biomedicines*, 10(3).

[172] Gaitán, JM. *et al*. (2022) 'Circulating Klotho Is Higher in Cerebrospinal Fluid than Serum and Elevated Among KLOTHO Heterozygotes in a Cohort with Risk for Alzheimer's Disease', *Journal of Alzheimer's Disease*, 90(4):1557–69.

[173] Neitzel, J. *et al*. (2021) 'KL-VS heterozygosity is associated with lower amyloid-dependent tau accumulation and memory impairment in Alzheimer's disease', *Nature Communications*, 12(1).

[174] Driscoll, I. *et al*. (2021) 'Age-related tau burden and cognitive deficits are attenuated in Klotho KL-VS heterozygotes', *Journal of Alzheimer's Disease*, 79(3):1297–305.

[175] Cararo-Lopes, MM. *et al*. (2017) 'The relevance of α-KLOTHO to the central nervous system: Some key questions', *Ageing Research Reviews*, 36:137–48.

[176] Li, D. *et al*. (2019) 'Enhanced expression of secreted α-klotho in the hippocampus alters nesting behavior and memory formation in mice', *Frontiers in Cellular Neuroscience*, 13.

[177] Massó, A. *et al*. (2018) 'Secreted αKlotho isoform protects against age-dependent memory deficits', *Molecular Psychiatry*, 23(9):1937–47.

[178] Dalton, G. *et al*. (2017) 'Soluble klotho binds monosialoganglioside to regulate membrane microdomains and growth factor signaling', *Proceedings of the National Academy of Sciences of the United States of America*, 114(4):752–7.

[179] Guerreiro, R. *et al*. (2013) 'TREM2 Variants in Alzheimer's Disease ', *New England Journal of Medicine*, 368(2):117–27.

[180] Yeh, FL. *et al*. (2017) 'TREM2, Microglia, and Neurodegenerative Diseases', *Trends in Molecular Medicine*, 23(6):512–33.

[181] Klesney-Tait, J. *et al*. (2006) 'The TREM receptor family and signal integration', *Nature Immunology*, 7(12):1266–73.

[182] Schlepckow, K. *et al*. (2017) ' An Alzheimer-associated TREM2 variant occurs at the ADAM cleavage site and affects shedding and phagocytic function ', *EMBO Molecular Medicine*, 9(10):1356–65.

[183] Piccio, L. *et al*. (2008) 'Identification of soluble TREM-2 in the cerebrospinal fluid and its association with multiple sclerosis and CNS inflammation', *Brain*, 131(11):3081–91.

[184] Del-Aguila, JL. *et al*. (2019) 'TREM2 brain transcript-specific studies in AD and TREM2 mutation carriers', *Molecular Neurodegeneration*, 14(1).

[185] Wunderlich, P. *et al*. (2013) 'Sequential proteolytic processing of the triggering receptor expressed on myeloid cells-2 (TREM2) protein by ectodomain shedding and γ-secretase-dependent intramembranous cleavage', *Journal of Biological Chemistry*, 288(46):33027–36.

[186] Forabosco, P. *et al*. (2013) 'Insights into TREM2 biology by network analysis of human brain gene expression data', *Neurobiology of Aging*, 34(12):2699–714.

[187] Zheng, H. *et al*. (2016) 'Opposing roles of the triggering receptor expressed on myeloid cells 2 and triggering receptor expressed on myeloid cells-like transcript 2 in microglia activation', *Neurobiology of Aging*, 42:132–41.

[188] Hickman, SE., El Khoury, J. (2014) 'TREM2 and the neuroimmunology of Alzheimer's disease', *Biochemical Pharmacology*, 88(4):495–8.

[189] Schmid, CD. *et al*. (2002) 'Heterogeneous expression of the triggering receptor expressed on myeloid cells-2 on adult murine microglia', *Journal of Neurochemistry*, 83(6):1309–20.

[190] Ma, L. *et al*. (2016) 'Expression and processing analyses of wild type and p.R47H TREM2 variant in Alzheimer's disease brains', *Molecular Neurodegeneration*, 11(1):1–9.

[191] Lue, LF. *et al*. (2015) 'TREM2 Protein Expression Changes Correlate with Alzheimer's Disease Neurodegenerative Pathologies in Post-Mortem Temporal Cortices', *Brain Pathology*, 25(4):469–80.

[192] Slattery, CF. *et al*. (2014) 'R47H TREM2 variant increases risk of typical early-onset Alzheimer's disease but not of prion or frontotemporal dementia', *Alzheimer's & Dementia*, 10(6):602-608.e4.

[193] Zhong, L. *et al*. (2018) 'Amyloid-beta modulates microglial responses by binding to the triggering receptor expressed on myeloid cells 2 (TREM2)', *Molecular Neurodegeneration*, 13(1).

[194] Qiao, W. *et al*. (2023) 'Trem2 H157Y increases soluble TREM2 production and reduces amyloid pathology', *Molecular Neurodegeneration*, 18(1).

[195] Deczkowska, A. *et al*. (2020) 'The Physiology, Pathology, and Potential Therapeutic Applications of the TREM2 Signaling Pathway', *Cell*, 181(6):1207–17.

[196] Kawabori, M. *et al*. (2015) 'Triggering receptor expressed on myeloid cells 2 (TREM2) deficiency attenuates phagocytic activities of microglia and exacerbates ischemic damage in experimental stroke', *Journal of Neuroscience*, 35(8):3384–96.

[197] Yeh, FL. *et al*. (2016) 'TREM2 Binds to Apolipoproteins, Including APOE and CLU/APOJ, and Thereby Facilitates Uptake of Amyloid-Beta by Microglia', *Neuron*, 91(2):328–40.

[198] Takahashi, K. *et al*. (2005) 'Clearance of apoptotic neurons without inflammation by microglial triggering receptor expressed on myeloid cells-2', *Journal of Experimental Medicine*, 201(4):647–57.

[199] Popescu, AS. *et al*. (2023) 'Alzheimer's disease-associated R47H TREM2 increases, but wild-type TREM2 decreases, microglial phagocytosis of synaptosomes and neuronal loss', *GLIA*, 71(4):974–90.

[200] Takahashi, K. *et al*. (2007) 'TREM2-Transduced Myeloid Precursors Mediate Nervous Tissue Debris Clearance and Facilitate Recovery in an Animal Model of Multiple Sclerosis', *PLOS Medicine*, 4(4).

[201] Song, WM. *et al*. (2018) 'Humanized TREM2 mice reveal microglia-intrinsic and -extrinsic effects of R47H polymorphism', *Journal of Experimental Medicine*, 215(3):745–60.

[202] Jay, TR. *et al*. (2017) 'Disease progression-dependent effects of TREM2 deficiency in a mouse model of Alzheimer's disease', *Journal of Neuroscience*, 37(3):637–47.

[203] Leyns, CEG. *et al*. (2017) 'TREM2 deficiency attenuates neuroinflammation and protects against neurodegeneration in a mouse model of tauopathy', *Proceedings of the National Academy of Sciences of the United States of America*, 114(43):11524–9.

[204] Gratuze, M. *et al*. (2020) 'Impact of TREM2R47Hvariant on tau pathology-induced gliosis and neurodegeneration', *Journal of Clinical Investigation*, 130(9):4954–68.

[205] Lee, SH. *et al*. (2021) 'Trem2 restrains the enhancement of tau accumulation and neurodegeneration by β-amyloid pathology', *Neuron*, 109(8):1283–301.

[206] Haass, C. (2021) 'Loss of TREM2 facilitates tau accumulation, spreading, and brain atrophy, but only in the presence of amyloid pathology', *Neuron*, 109(8):1243–5.

[207] Nabizadeh, F. (2023) 'sTREM2 is associated with attenuated tau aggregate accumulation in the presence of amyloid-β pathology', *Brain Communications*, 5(6).

[208] Ulland, TK. *et al*. (2017) 'TREM2 Maintains Microglial Metabolic Fitness in Alzheimer's Disease', *Cell*, 170(4):649–63.

[209] Wang, Y. *et al*. (2015) 'TREM2 lipid sensing sustains the microglial response in an Alzheimer's disease model', *Cell*, 160(6):1061–71.

[210] Wang, Y. *et al*. (2016) 'TREM2-mediated early microglial response limits diffusion and toxicity of amyloid plaques', *Journal of Experimental Medicine*, 213(5):667–75.

[211] Zheng, H. *et al*. (2017) 'TREM2 promotes microglial survival by activating wnt/β-catenin pathway', *Journal of Neuroscience*, 37(7):1772–84.

[212] Bouchon, A. *et al*. (2001) 'A DAP12-mediated Pathway Regulates Expression of CC Chemokine Receptor 7 and Maturation of Human Dendritic Cells', *Journal of Experimental Medicine*, 194(8):1111–22.

[213] Kleinberger, G. *et al*. (2017) 'The FTD-like syndrome causing TREM 2 T66M mutation impairs microglia function, brain perfusion, and glucose metabolism', *The EMBO Journal*, 36(13):1837–53.

[214] Nugent, AA. *et al*. (2020) 'TREM2 Regulates Microglial Cholesterol Metabolism upon Chronic Phagocytic Challenge', *Neuron*, 105(5):837–54.

[215] Bailey, CC. *et al*. (2015) 'The triggering receptor expressed on myeloid cells 2 binds apolipoprotein E', *Journal of Biological Chemistry*, 290(43):26033–42.

[216] Atagi, Y. *et al*. (2015) 'Apolipoprotein E is a ligand for triggering receptor expressed on myeloid cells 2 (TREM2)', *Journal of Biological Chemistry*, 290(43):26043–50.

[217] Rapp, A. *et al*. (2006) 'Implication of apoE isoforms in cholesterol metabolism by primary rat hippocampal neurons and astrocytes', *Biochimie*, 88(5):473–83.

[218] Andreone, BJ. *et al*. (2020) 'Alzheimer's-associated PLCγ2 is a signaling node required for both TREM2 function and the inflammatory response in human microglia', *Nature Neuroscience*, 23(8):927–38.

[219] Ellwanger, DC. *et al*. (2021) 'Prior activation state shapes the microglia response to antihuman TREM2 in a mouse model of Alzheimer's disease', *PNAS*, 118(3).

[220] Cantoni, C. *et al*. (2015) 'TREM2 regulates microglial cell activation in response to demyelination in vivo', *Acta Neuropathologica*, 129(3):429–47.

[221] Cignarella, F. *et al*. (2020) 'TREM2 activation on microglia promotes myelin debris clearance and remyelination in a model of multiple sclerosis', *Acta Neuropathologica*, 140(4):513–34.

[222] Keren-Shaul, H. *et al*. (2017) 'A Unique Microglia Type Associated with Restricting Development of Alzheimer's Disease', *Cell*, 169(7):1276–90.

[223] Rangaraju, S. *et al*. (2018) 'Identification and therapeutic modulation of a pro-inflammatory subset of disease-associated-microglia in Alzheimer's disease', *Molecular Neurodegeneration*, 13(1).

[224] Jay, TR. *et al*. (2017) 'TREM2 in Neurodegenerative Diseases', *Molecular Neurodegeneration*, 12(1).

[225] Wang, Y. *et al*. (2020) 'TREM2 ameliorates neuroinflammatory response and cognitive impairment via PI3K/AKT/FoxO3a signaling pathway in Alzheimer's disease mice', *Aging*, 12(20):20862–79.

[226] Cardozo, PL. *et al*. (2019) 'Synaptic Elimination in Neurological Disorders', *Current Neuropharmacology*, 17(11):1071–95.

[227] Ricklin, D. *et al*. (2016) 'Complement in disease: a defence system turning offensive', *Nature Reviews Nephrology*, 12(7):383–401.

[228] Qin, Q. *et al*. (2022) 'The Specific Mechanism of TREM2 Regulation of Synaptic Clearance in Alzheimer's Disease', *Frontiers in Immunology*, 13.

[229] Zhong, L. *et al*. (2023) 'TREM2 receptor protects against complement-mediated synaptic loss by binding to complement C1q during neurodegeneration', *Immunity*, 56(8):1794–808.

[230] Qu, W., Li, L. (2020) 'Loss of TREM2 confers resilience to synaptic and cognitive impairment in aged mice', *Journal of Neuroscience*, 40(50):9552–63.

[231] Liu, D. *et al*. (2018) 'Soluble TREM2 changes during the clinical course of Alzheimer's disease: A meta-analysis', *Neuroscience Letters*, 686:10–6.

[232] Piccio, L. *et al*. (2016) 'Cerebrospinal fluid soluble TREM2 is higher in Alzheimer disease and associated with mutation status', *Acta Neuropathologica*, 131(6):925–33.

[233] Gu, L. *et al*. (2023) 'Soluble TREM2 in body fluid in Alzheimer's disease and Parkinson's disease', *Neurological Sciences*, 44(8):2743–51.

[234] Suárez-Calvet, M. *et al*. (2016) 'sTREM2 cerebrospinal fluid levels are a potential biomarker for microglia activity in early-stage Alzheimer's disease and associate with neuronal injury markers', *EMBO Molecular Medicine*, 8(5):466–76.

[235] Suárez-Calvet, M. *et al*. (2019) 'Early increase of CSF sTREM2 in Alzheimer's disease is associated with tau related-neurodegeneration but not with amyloid-β pathology', *Molecular Neurodegeneration*, 14(1).

[236] Franzmeier, N. *et al*. (2020) 'Higher CSF sTREM2 attenuates ApoE4-related risk for cognitive decline and neurodegeneration', *Molecular Neurodegeneration*, 15(1).

[237] Edwin, TH. *et al*. (2020) 'A high cerebrospinal fluid soluble TREM2 level is associated with slow clinical progression of Alzheimer's disease', *Alzheimer's & Dementia*, 12(1).

[238] Zhong, L. *et al*. (2017) 'Soluble TREM2 induces inflammatory responses and enhances microglial survival', *Journal of Experimental Medicine*, 214(3):597–607.

[239] Fassler, M. *et al*. (2021) 'Engagement of TREM2 by a novel monoclonal antibody induces activation of microglia and improves cognitive function in Alzheimer's disease models', *Journal of Neuroinflammation*, 18(1).

[240] Zhong, L. *et al*. (2019) 'Soluble TREM2 ameliorates pathological phenotypes by modulating microglial functions in an Alzheimer's disease model', *Nature Communications*, 10(1).

[241] Kober, DL. *et al*. (2021) 'Functional insights from biophysical study of TREM2 interactions with ApoE and Aβ 1-42', *Alzheimer's & Dementia*, 17:475–88.

[242] Belsare, KD. *et al*. (2022) 'Soluble TREM2 inhibits secondary nucleation of Aβ fibrillization and enhances cellular uptake of fibrillar Aβ', *Biophysics and Computational Biology*, 119(5).

[243] Vilalta, A. *et al*. (2021) 'Wild-type sTREM2 blocks Aβ aggregation and neurotoxicity, but the Alzheimer's R47H mutant increases Aβ aggregation', *Journal of Biological Chemistry*, 296.

[244] Parhizkar, S. *et al*. (2019) 'Loss of TREM2 function increases amyloid seeding but reduces plaque-associated ApoE', *Nature Neuroscience*, 22(2):191–204.

[245] Zhang, X. *et al*. (2023) 'Soluble TREM2 ameliorates tau phosphorylation and cognitive deficits through activating transgelin-2 in Alzheimer's disease', *Nature Communications*, 14(6670).

[246] Villeda, SA. *et al*. (2011) 'The ageing systemic milieu negatively regulates neurogenesis and cognitive function', *Nature*, 477(7362):90–6.

[247] Villeda, SA. *et al*. (2014) 'Young blood reverses age-related impairments in cognitive function and synaptic plasticity in mice', *Nature Medicine*, 20(6):659–63.

[248] Castellano, JM. *et al*. (2017) 'Human umbilical cord plasma proteins revitalize hippocampal function in aged mice', *Nature*, 544(7651):488–92.

[249] Kobusiak-Prokopowicz, M. *et al*. (2018) 'MMP-2 and TIMP-2 in patients with heart failure and chronic kidney disease', *Open Medicine*, 13(1):237–46.

[250] Gomes, VA. *et al*. (2011) 'Imbalanced circulating matrix metalloproteinases in polycystic ovary syndrome', *Molecular and Cellular Biochemistry*, 353:251–7.

[251] Lorenzl, S. *et al*. (2002) 'Expression of MMP-2, MMP-9, and MMP-1 and their endogenous counterregulators TIMP-1 and TIMP-2 in postmortem brain tissue of Parkinson's disease', *Experimental Neurology*, 178(1):13–20.

[252] Cabral-Pacheco, GA. *et al*. (2020) 'The roles of matrix metalloproteinases and their inhibitors in human diseases', *International Journal of Molecular Sciences*, 21(24):1–53.

[253] Peeney, D. *et al*. (2022) 'Unravelling the distinct biological functions and potential therapeutic applications of TIMP2 in cancer', *Carcinogenesis*, 43(5):405–18.

[254] Albert, C. *et al*. (2020) 'Biomarker-Guided Risk Assessment for Acute Kidney Injury: Time for Clinical Implementation?', *Annals of Laboratory Medicine*, 41(1):1–15.

[255] Bruno, MA. *et al*. (2009) 'Increased matrix metalloproteinase 9 activity in mild cognitive impairment', *Journal of Neuropathology and Experimental Neurology*, 68(12):1309–18.

[256] Jourquin, J. *et al*. (2003) 'Neuronal activity-dependent increase of net matrix metalloproteinase activity is associated with MMP-9 neurotoxicity after kainate', *European Journal of Neuroscience*, 18(6):1507–17.

[257] Bell, RD. *et al*. (2012) 'Apolipoprotein e controls cerebrovascular integrity via cyclophilin A', *Nature*, 485(7399):512–6.

[258] Giannoni, P. *et al*. (2016) 'Cerebrovascular pathology during the progression of experimental Alzheimer's disease', *Neurobiology of Disease*, 88:107–17.

[259] Sweeney, MD. *et al*. (2018) 'Blood-brain barrier breakdown in Alzheimer disease and other neurodegenerative disorders', *Nature Reviews Neurology*, 14(3):133–50.

[260] Montaner, J. *et al*. (2019) 'Matrix metalloproteinases and ADAMs in stroke', *Cellular and Molecular Life Sciences*, 76(16):3117–40.

[261] Terni, B., Ferrer, I. (2015) 'Abnormal expression and distribution of MMP2 at initial stages of alzheimer's disease-related pathology', *Journal of Alzheimer's Disease*, 46(2):461–9.

[262] Xu, L. *et al*. (2022) 'Fibroblasts repair blood-brain barrier damage and hemorrhagic brain injury via TIMP2', *Cell Reports*, 41(8).

[263] Pérez-Martínez, L., Jaworski, DM. (2005) 'Tissue inhibitor of metalloproteinase-2 promotes neuronal differentiation by acting as an anti-mitogenic signal', *Journal of Neuroscience*, 25(20):4917–29.

[264] Britton, R. *et al*. (2023) 'Noncanonical Activity of Tissue Inhibitor of Metalloproteinases 2 (TIMP2) Improves Cognition and Synapse Density in Aging', *eNeuro*, 10(6).

[265] Ferreira, AC. *et al*. (2023) 'Neuronal TIMP2 regulates hippocampus-dependent plasticity and extracellular matrix complexity', *Molecular Psychiatry*, 28:3943–54.

[266] Anguela, XM., High, KA. (2019) 'Entering the Modern Era of Gene Therapy', *Annual Review of Medicine*, 70:273–88.

[267] The Journal of Gene Medicine. (accessed: 2024 Apr 15) 'Gene Therapy Clinical Trials Worldwide [Online]', Available from: https://a873679.fmphost.com/fmi/webd/GTCT

[268] American Society of Gene + Cell Therapy. (accessed: 2023 Oct 30) ' Gene, Cell, + RNA Therapy Landscape Report, Q3 2023 Quarterly Data Report [Online]', Available from: https://asgct.org/global/documents/asgct-citeline-q3-2023-report.aspx

[269] Wang, C. *et al*. (2023) 'Emerging non-viral vectors for gene delivery', *Journal of Nanobiotechnology*, 21(1).

[270] Mingozzi, F., High, KA. (2011) 'Therapeutic in vivo gene transfer for genetic disease using AAV: Progress and challenges', *Nature Reviews Genetics*, 12(5):341–55.

[271] Thomas, CE. *et al*. (2003) 'Progress and problems with the use of viral vectors for gene therapy', *Nature Reviews Genetics*, 4(5):346–58.

[272] Meier, AF. *et al*. (2020) 'The interplay between adeno-associated virus and its helper viruses', *Viruses*, 12(6).

[273] Hamilton, H. *et al*. (2004) 'Adeno-Associated Virus Site-Specific Integration and AAVS1 Disruption', *Journal of Virology*, 78(15):7874–82.

[274] Ylä-Herttuala, S. (2012) 'Endgame: Glybera finally recommended for approval as the first gene therapy drug in the European union', *Molecular Therapy*, 20(10):1831–2.

[275] Ghauri, MS., Ou, L. (2023) 'AAV Engineering for Improving Tropism to the Central Nervous System', *Biology*, 12(186).

[276] Kotterman, MA. *et al*. (2015) 'Viral Vectors for Gene Therapy: Translational and Clinical Outlook', *Annual Review of Biomedical Engineering*, 17:63–89.

[277] Sonntag, F. *et al*. (2011) 'The Assembly-Activating Protein Promotes Capsid Assembly of Different Adeno-Associated Virus Serotypes', *Journal of Virology*, 85(23):12686–97.

[278] Zolotukhin, S. *et al*. (2002) 'Production and purification of serotype 1, 2, and 5 recombinant adeno-associated viral vectors', *Methods*, 28:158–67.

[279] Xiao, X. *et al*. (1998) 'Production of High-Titer Recombinant Adeno-Associated Virus Vectors in the Absence of Helper Adenovirus', *Journal of Virology*, 72(3):2224–32.

[280] Allen, JM. *et al*. (2000) 'Improved Adeno-Associated Virus Vector Production with Transfection of a Single Helper Adenovirus Gene, E4orf6', *Molecular Therapy*, 1(1):88–95.

[281] Smith, RH. (2008) 'Adeno-associated virus integration: Virus versus vector', *Gene Therapy*, 15(11):817–22.

[282] Asaad, W. *et al*. (2023) 'AAV genome modification for efficient AAV production', *Heliyon*, 9(4).

[283] Wang, D. *et al*. (2019) 'Adeno-associated virus vector as a platform for gene therapy delivery', *Nature Reviews Drug Discovery*, 18(5):358–78.

[284] Agbandje-McKenna, M., Kleinschmidt, J. (2011) 'AAV Capsid Structure and Cell Interactions', *Methods in Molecular Biology*, Humana Press Inc.; p. 47–92.

[285] Li, C., Samulski, RJ. (2020) 'Engineering adeno-associated virus vectors for gene therapy', *Nature Reviews Genetics*, 21(4):255–72.

[286] Atchison, RW. *et al*. (1965) 'Adenovirus-Associated Defective Virus Particles', *Science*, 149(3685):754–6.

[287] David Hoggan, M. *et al*. (1966) 'Studies of small DNA viruses found in various adenovirus preparations: physical, biological, and immunological characteristics', *Proceedings of the National Academy of Sciences of the United States of America*, 55(6):1467–74.

[288] Grimm, D. *et al*. (2008) 'In Vitro and In Vivo Gene Therapy Vector Evolution via Multispecies Interbreeding and Retargeting of Adeno-Associated Viruses', *Journal of Virology*, 82(12):5887–911.

[289] Hudry, E., Vandenberghe, LH. (2019) 'Therapeutic AAV Gene Transfer to the Nervous System: A Clinical Reality', *Neuron*, 101(5):839–62.

[290] Aschauer, DF. *et al*. (2013) 'Analysis of Transduction Efficiency, Tropism and Axonal Transport of AAV Serotypes 1, 2, 5, 6, 8 and 9 in the Mouse Brain', *PLoS ONE*, 8(9).

[291] Cearley, CN., Wolfe, JH. (2006) 'Transduction characteristics of adeno-associated virus vectors expressing cap serotypes 7, 8, 9, and Rh10 in the mouse brain', *Molecular Therapy*, 13(3):528–37.

[292] Deverman, BE. *et al*. (2018) 'Gene therapy for neurological disorders: Progress and prospects', *Nature Reviews Drug Discovery*, 17(9):641–59.

[293] Nonnenmacher, M. *et al*. (2021) 'Rapid evolution of blood-brain-barrier-penetrating AAV capsids by RNA-driven biopanning', *Molecular Therapy*, 20:366–78.

[294] Tornabene, P. *et al*. (2019) 'Intein-mediated protein trans-splicing expands adeno-associated virus transfer capacity in the retina', *Science Translational Medicine*, 11(492).

[295] McClements, ME., MacLaren, RE. (2017) 'Adeno-associated Virus (AAV) Dual Vector Strategies for Gene Therapy Encoding Large Transgenes', *Yale Journal of Biology and Medicine*, 90:611–23.

[296] Ferrari, FK. *et al*. (1996) 'Second-Strand Synthesis Is a Rate-Limiting Step for Efficient Transduction by Recombinant Adeno-Associated Virus Vectors', *Journal of Virology*, 70(5):3227–34.

[297] Flotte, TR. (2020) 'Revisiting the "new" inflammatory toxicities of adeno-associated virus vectors', *Human Gene Therapy*, 31(7–8):398–9.

[298] Chand, D. *et al*. (2021) 'Hepatotoxicity following administration of onasemnogene abeparvovec (AVXS-101) for the treatment of spinal muscular atrophy', *Journal of Hepatology*, 74(3):560–6.

[299] Chowdhury, EA. *et al*. (2021) 'Current progress and limitations of AAV mediated delivery of protein therapeutic genes and the importance of developing quantitative pharmacokinetic/pharmacodynamic (PK/PD) models', *Advanced Drug Delivery Reviews*, 170:214–37.

[300] Calcedo, R. *et al*. (2009) 'Worldwide epidemiology of neutralizing antibodies to adeno-associated viruses', *Journal of Infectious Diseases*, 199(3):381–90.

[301] Meliani, A. *et al*. (2018) 'Antigen-selective modulation of AAV immunogenicity with tolerogenic rapamycin nanoparticles enables successful vector re-administration', *Nature Communications*, 9(1).

[302] Mingozzi, F., High, KA. (2013) 'Immune responses to AAV vectors: Overcoming barriers to successful gene therapy', *Blood*, 122(1):23–36.

[303] Mingozzi, F. *et al*. (2007) 'CD8+ T-cell responses to adeno-associated virus capsid in humans', *Nature Medicine*, 13(4):419–22.

[304] Rogers, GL. *et al*. (2011) 'Innate immune responses to AAV vectors', *Frontiers in Microbiology*, 2.

[305] Takahashi, K. *et al*. (2007) 'Induction of Pluripotent Stem Cells from Adult Human Fibroblasts by Defined Factors', *Cell*, 131(5):861–72.

[306] Cenini, G. *et al*. (2021) 'Dissecting Alzheimer's disease pathogenesis in human 2D and 3D models', *Molecular and Cellular Neuroscience*, 110.

[307] Chen, ZY., Zhang, Y. (2022) 'Animal models of Alzheimer's disease: Applications, evaluation, and perspectives', *Zoological Research*, 43(6):1026–40.

[308] Alzforum. (accessed: 2024 Apr 15) 'Alzheimer's disease research models [Online]', Available from: https://www.alzforum.org/research-models/alzheimers-disease

[309] Braidy, N. *et al*. (2012) 'Recent rodent models for Alzheimer's disease: Clinical implications and basic research', *Journal of Neural Transmission*, 119(2):173–95.

[310] Webster, SJ. *et al*. (2014) 'Using mice to model Alzheimer's dementia: An overview of the clinical disease and the preclinical behavioral changes in 10 mouse models', *Frontiers in Genetics*, 5.

[311] Myers, A., McGonigle, P. (2019) 'Overview of Transgenic Mouse Models for Alzheimer's Disease', *Current Protocols in Neuroscience*, 89(1).

[312] Capilla-López, MD. *et al*. (2023) 'Differential neural circuit vulnerability to β-amyloid and tau pathologies in novel Alzheimer's disease mice', *BioRxiv*

[313] Mucke, L. *et al*. (2000) 'High-Level Neuronal Expression of Aβ1-42 in Wild-Type Human Amyloid Protein Precursor Transgenic Mice: Synaptotoxicity without Plaque Formation', *The Journal of Neuroscience*, 20(11):4050–8.

[314] Yoshiyama, Y. *et al*. (2007) 'Synapse Loss and Microglial Activation Precede Tangles in a P301S Tauopathy Mouse Model', *Neuron*, 53(3):337–51.

[315] Alba, R. *et al*. (2007) 'Differential amplification of adenovirus vectors by flanking the packaging signal with attB/attP-ΦC31 sequences: Implications for helper-dependent adenovirus production', *Virology*, 367(1):51–8.

[316] Delenda, C. *et al*. (2007) 'Cells for Gene Therapy and Vector Production', *Methods in Biotechnology*, Humana Press; p. 23–91.

[317] Hellemans, J. *et al*. (2008) 'qBase relative quantification framework and software for management and automated analysis of real-time quantitative PCR data', *Genome Biology*, 8(2).

[318] Toutain, PL., Bousquet-Mélou, A. (2004) 'Plasma terminal half-life', *Journal of Veterinary Pharmacology and Therapeutics*, 27:427–39.

[319] Piedra, J. *et al*. (2015) 'Development of a rapid, robust, and universal PicoGreen-based method to titer adeno-associated vectors', *Human Gene Therapy Methods*, 26(1):35–42.

[320] Webb, B., Sali, A. (2016) 'Comparative protein structure modeling using MODELLER', *Current Protocols in Bioinformatics*, 2016:5.6.1-5.6.37.

[321] Doerr, S. *et al*. (2016) 'HTMD: High-Throughput Molecular Dynamics for Molecular Discovery', *Journal of Chemical Theory and Computation*, 12(4):1845–52.

[322] Maier, JA. *et al*. (2015) 'ff14SB: Improving the Accuracy of Protein Side Chain and Backbone Parameters from ff99SB', *Journal of Chemical Theory and Computation*, 11(8):3696–713.

[323] Jorgensen, WL. *et al*. (1983) 'Comparison of simple potential functions for simulating liquid water', *The Journal of Chemical Physics*, 79(2):926–35.

[324] Harvey, MJ. *et al*. (2009) 'ACEMD: Accelerating biomolecular dynamics in the microsecond time scale', *Journal of Chemical Theory and Computation*, 5(6):1632–9.

[325] Abraham, MJ. *et al*. (2015) 'Gromacs: High performance molecular simulations through multi-level parallelism from laptops to supercomputers', *SoftwareX*, 1–2:19–25.

[326] Jo, S. *et al*. (2008) 'CHARMM-GUI: A web-based graphical user interface for CHARMM', *Journal of Computational Chemistry*, 29(11):1859–65.

[327] De Jong, DH. *et al*. (2013) 'Improved parameters for the martini coarse-grained protein force field', *Journal of Chemical Theory and Computation*, 9(1):687–97.

[328] Periole, X. *et al*. (2009) 'Combining an elastic network with a coarse-grained molecular force field: Structure, dynamics, and intermolecular recognition', *Journal of Chemical Theory and Computation*, 5(9):2531–43.

[329] Jumper, J. *et al*. (2021) 'Highly accurate protein structure prediction with AlphaFold', *Nature*, 596(7873):583–9.

[330] Espuch-Oliver, A. *et al*. (2022) 'References Values of Soluble α-Klotho Serum Levels Using an Enzyme-Linked Immunosorbent Assay in Healthy Adults Aged 18–85 Years', *Journal of Clinical Medicine*, 11(9).

[331] Abraham, CR., Li, A. (2022) 'Aging-suppressor Klotho: Prospects in diagnostics and therapeutics', *Ageing Research Reviews*, 82.

[332] Davidoff, AM. *et al*. (2003) 'Sex significantly influences transduction of murine liver by recombinant adeno-associated viral vectors through an androgen-dependent pathway', *Blood*, 102(2):480–8.

[333] Otto, GP. *et al*. (2016) 'Clinical chemistry Reference Intervals for C57BL/6J, C57BL/6N, and C3HeB/FeJ Mice (Mus musculus)', *Journal of the American Association for Laboratory Animal Science*, 55(4):375–86.

[334] Tothova, C. *et al*. (2016) 'Serum proteins and their diagnostic utility in veterinary medicine: A review', *Veterinarni Medicina*, 61(9):475–96.

[335] Batra, J. *et al*. (2013) 'Matrix Metalloproteinase-10/TIMP-2 Structure and Analyses Define Conserved Core Interactions and Diverse Exosite Interactions in MMP/TIMP Complexes', *PLoS ONE*, 8(9).

[336] Peng, Y. *et al*. (2023) 'Current and future therapeutic strategies for Alzheimer's disease: an overview of drug development bottlenecks', *Frontiers in Aging Neuroscience*, 15.

[337] Kim, CK. *et al*. (2022) 'Alzheimer's Disease: Key Insights from Two Decades of Clinical Trial Failures', *Journal of Alzheimer's Disease*, 87(1):83–100.

[338] Self, WK., Holtzman, DM. (2023) 'Emerging diagnostics and therapeutics for Alzheimer disease', *Nature Medicine*, 29:2187–99.

[339] Boxer, AL., Sperling, R. (2023) 'Accelerating Alzheimer's therapeutic development: The past and future of clinical trials', *Cell*, 186(22):4757–72.

[340] Castner, SA. *et al*. (2023) 'Longevity factor klotho enhances cognition in aged nonhuman primates', *Nature Aging*, 3:931–7.

[341] Roig-Soriano, J. *et al*. (2023) 'Differential toxicity profile of secreted and processed α-Klotho expression over mineral metabolism and bone microstructure', *Scientific Reports*, 13(4211).

[342] Blanch, R. (2023) 'AAV-mediated expression of Secreted Klotho as a therapeutic strategy for Alzheimer's disease', Universitat Autònoma de Barcelona

[343] Kohn, DB. *et al*. (2023) 'Successes and challenges in clinical gene therapy', *Gene Therapy*, 30(10–11):738–46.

[344] Gupta, S. *et al*. (2022) 'KL1 Domain of Longevity Factor Klotho Mimics the Metabolome of Cognitive Stimulation and Enhances Cognition in Young and Aging Mice', *Journal of Neuroscience*, 42(19):4016–25.

[345] Zhong, X. *et al*. (2020) 'Structure-function relationships of the soluble form of the antiaging protein Klotho have therapeutic implications for managing kidney disease', *Journal of Biological Chemistry*, 295(10):3115–33.

[346] Tohyama, O. *et al*. (2004) 'Klotho Is a Novel β-Glucuronidase Capable of Hydrolyzing Steroid β-Glucuronides', *Journal of Biological Chemistry*, 279(11):9777–84.

[347] Hu, MC. *et al*. (2016) 'Renal Production, Uptake, and Handling of Circulating αklotho', *Journal of the American Society of Nephrology*, 27(1):79–90.

[348] Zaman, R. *et al*. (2019) 'Current strategies in extending half-lives of therapeutic proteins', *Journal of Controlled Release*, 301:176–89.

[349] Simon, P. *et al*. (1994) 'Thigmotaxis as an index of anxiety in mice. Influence of dopaminergic transmissions', *Behavioural Brain Research*, 61:59–64.

[350] Squire, LR. *et al*. (2007) 'Recognition memory and the medial temporal lobe: a new perspective', *Nature Reviews Neuroscience*, 8(11):872–83.

[351] Brown, MW., Aggleton, JP. (2001) 'Recognition memory: what are the roles of the perirhinal cortex and hippocampus?', *Nature Reviews Neuroscience*, 2:51–61.

[352] Othman, MZ. *et al*. (2022) 'Morris water maze: a versatile and pertinent tool for assessing spatial learning and memory', *Experimental Animals*, 71(3):264–80.

[353] Gasbarri, A., Pompili, A. (2014) 'Involvement of Glutamate in Learning and Memory', *Identification of Neural Markers Accompanying Memory*, Elsevier Inc.; p. 63–77.

[354] Riedel, G. *et al*. (2003) 'Glutamate receptor function in learning and memory', *Behavioural Brain Research*, 140:1–47.

[355] Obulesu, M., Lakshmi, MJ. (2014) 'Apoptosis in Alzheimer's Disease: An Understanding of the Physiology, Pathology and Therapeutic Avenues', *Neurochemical Research*, 39(12):2301–12.

[356] Guerrero, A. *et al*. (2021) 'Cellular senescence at the crossroads of inflammation and Alzheimer's disease', *Trends in Neurosciences*, 44(9):714–27.

[357] Udayar, V. *et al*. (2022) 'Lysosomal dysfunction in neurodegeneration: emerging concepts and methods', *Trends in Neurosciences*, 45(3):184–99.

[358] Butler, CA. *et al*. (2021) 'Microglial phagocytosis of neurons in neurodegeneration, and its regulation', *Journal of Neurochemistry*, 158(3):621–39.

[359] Mango, D. *et al*. (2019) 'Targeting synaptic plasticity in experimental models of Alzheimer's disease', *Frontiers in Pharmacology*, 10.

[360] Wittekindt, M. *et al*. (2022) 'Different Methods for Evaluating Microglial Activation Using Anti-Ionized Calcium-Binding Adaptor Protein-1 Immunohistochemistry in the Cuprizone Model', *Cells*, 11(11).

[361] Kuang, X. *et al*. (2017) 'Neuroprotective effect of ligustilide through induction of α-secretase processing of both APP and Klotho in a mouse model of Alzheimer's disease', *Frontiers in Aging Neuroscience*, 9.

[362] Baldo, BA. (2015) 'Chimeric Fusion Proteins Used for Therapy: Indications, Mechanisms, and Safety', *Drug Safety*, 38(5):455–79.

[363] Sun, D. *et al*. (2024) 'CAR-T cell therapy: A breakthrough in traditional cancer treatment strategies (Review)', *Molecular Medicine Reports*, 29(3).

[364] Price, BR. *et al*. (2020) 'Therapeutic Trem2 activation ameliorates amyloid-beta deposition and improves cognition in the 5XFAD model of amyloid deposition', *Journal of Neuroinflammation*, 17(1).

[365] Lu, Y. *et al*. (2023) 'Regulation of TREM2 expression by transcription factor YY1 and its protective effect against Alzheimer's disease', *Journal of Biological Chemistry*, 299(5).

[366] Li, XX., Zhang, F. (2021) 'Targeting TREM2 for Parkinson's Disease: Where to Go?', *Frontiers in Immunology*, 12.

[367] Baluchnejadmojarad, T. *et al*. (2017) 'The anti-aging protein klotho alleviates injury of nigrostriatal dopaminergic pathway in 6-hydroxydopamine rat model of Parkinson's disease: Involvement of PKA/CaMKII/CREB signaling', *Experimental Gerontology*, 100:70–6.

[368] Dash, R. *et al*. (2020) 'Mechanistic insights into the deleterious roles of Nasu-Hakola disease associated TREM2 variants', *Scientific Reports*, 10(1).

[369] Chen, L. *et al*. (2023) 'Structural basis for FGF hormone signalling', *Nature*, 618(7966):862–70.

[370] Chen, G. *et al*. (2018) 'α-Klotho is a non-enzymatic molecular scaffold for FGF23 hormone signalling', *Nature*, 553(7689):461–6.

[371] Fakhar, M. *et al*. (2022) 'Structural basis of Klotho binding to VEGFR2 and TRPC1 and repurposing calcium channel blockers as TRPC1 antagonists for the treatment of age-related cardiac hypertrophy', *Archives of Biochemistry and Biophysics*, 719.

[372] Tuuttila, A. *et al*. (1998) 'Three-dimensional Structure of Human Tissue Inhibitor of Metalloproteinases-2 at 2.1 A Resolution', *Journal of Molecular Biology*, 284(4):1133–40.

[373] Morgunova, E. *et al*. (2002) 'Structural insight into the complex formation of latent matrix metalloproteinase 2 with tissue inhibitor of metalloproteinase 2', *Proceedings of the National Academy of Sciences of the United States of America*, 99(11):7414–9.

[374] Kim, SM. *et al*. (2017) 'TREM2 promotes Aβ phagocytosis by upregulating C/EBPα-dependent CD36 expression in microglia', *Scientific Reports*, 7(1).

[375] Sheng, X. *et al*. (2021) 'Identification of the minimal active soluble TREM2 sequence for modulating microglial phenotypes and amyloid pathology', *Journal of Neuroinflammation*, 18(1).

[376] Filipello, F. *et al*. (2022) 'Soluble TREM2: Innocent bystander or active player in neurological diseases?', *Neurobiology of Disease*, 165.

[377] ClinicalTrials. (accessed: 2024 May 10) 'A Clinical Trial of AAV2-BDNF Gene Therapy in Early Alzheimer's Disease and Mild Cognitive Impairment [Online]', Available from: https://clinicaltrials.gov/study/NCT05040217?cond=Alzheimer%20Disease&intr=aav&rank=4

[378] ClinicalTrials. (accessed: 2024 May 10) 'Evaluation of Safety and Tolerability of Libella Gene Therapy for Alzheimer's Disease: AAV- hTERT [Online]', Available from: https://clinicaltrials.gov/study/NCT04133454?cond=Alzheimer%20Disease&intr=aav&rank=1

[379] Gray, SJ. *et al*. (2011) 'Optimizing promoters for recombinant adeno-associated virus-mediated gene expression in the peripheral and central nervous system using self-complementary vectors', *Human Gene Therapy*, 22(9):1143–53.

[380] Wu, Z. *et al*. (2010) 'Effect of genome size on AAV vector packaging', *Molecular Therapy*, 18(1):80–6.

[381] Hoffman, WP. *et al*. (2002) 'Analysis of Rodent Growth Data in Toxicology Studies', *Toxicological Sciences*, 66:313–9.

[382] Roig-Soriano, J. *et al*. (2022) 'AAV-mediated expression of secreted and transmembrane αKlotho isoforms rescues relevant aging hallmarks in senescent SAMP8 mice', *Aging Cell*, 21(4).

[383] Ferreira, AC. *et al*. (2023) 'MAL Neuronal TIMP2 regulates hippocampus-dependent plasticity and extracellular matrix complexity', *Molecular Psychiatry*, 28:3943–54.

[384] Igarashi, KM. (2023) 'Entorhinal cortex dysfunction in Alzheimer's disease', *Trends in Neurosciences*, 46(2):124–36.

[385] Setti, SE. *et al*. (2017) 'Alterations in hippocampal activity and Alzheimer's disease.', *Translational Issues in Psychological Science*, 3(4):348–56.

[386] Takemon, Y. *et al*. (2021) 'Proteomic and transcriptomic profiling reveal different aspects of aging in the kidney', *eLife*, 10.

[387] Zhao, N. *et al*. (2022) 'Elevating microglia TREM2 reduces amyloid seeding and suppresses disease-associated microglia', *Journal of Experimental Medicine*, 219(12).

[388] Fassler, M. *et al*. (2023) 'TREM2 Agonism with a Monoclonal Antibody Attenuates Tau Pathology and Neurodegeneration', *Cells*, 12(11).

[389] Seo, DW. *et al*. (2003) 'TIMP-2 Mediated Inhibition of Angiogenesis: An MMP-Independent Mechanism', *Cell*, 114:171–80.

[390] Zipfel, P. *et al*. (2020) 'Matrix metalloproteinases as new targets in Alzheimer's disease: Opportunities and Challenges', *Journal of Medicinal Chemistry*, 63(19):10705–25.

[391] Wingfield, PT. *et al*. (1999) 'Biophysical and functional characterization of full-length, recombinant human tissue inhibitor of metalloproteinases-2 (TIMP-2) produced in Escherichia coli', *Journal of Biological Chemistry*, 274(30):21362–8.

# PATENT

GOBIERNO DE ESPAÑA
MINISTERIO DE INDUSTRIA, COMERCIO Y TURISMO
Oficina Española de Patentes y Marcas

## Acknowledgement of receipt

We hereby acknowledge receipt of your request for grant of a European patent as follows:

| | |
|---|---|
| Submission number | 300485809 |
| Application number | EP23382593.4 |
| File No. to be used for priority declarations | EP23382593 |
| Date of receipt | 15 June 2023 |
| Your reference | P6330EP00 |
| Applicant | UNIVERSITAT AUTÒNOMA DE BARCELONA |
| Country | ES |
| Title | KLOTHO FUSION PROTEIN AND USES THEREOF |